1-1-2012

Spectroscopy and Dynamics of Transient Species, the Vinyl Radical and Highly Vibrationally Excited Acetylene

Matt Nikow
University of Pennsylvania, matt_nikow@agilent.com

Spectroscopy and Dynamics of Transient Species, the Vinyl Radical and Highly Vibrationally Excited Acetylene

Abstract
Time-resolved Fourier transform infra-red spectroscopy has been employed to identify vibrational modes of several transient molecular and radical species. IR emission from the vinyl radical generated by five different precursor molecules utilizing different dissociation pathways has been observed. An analytical method, two-dimensional cross spectral correlation, has been employed to verify the low energy bending modes of the vinyl radical as well as one stretching mode. Isotopic substitution has allowed several bending modes to be compared to their non-isotopically substituted analog.

Highly vibrationally excited acetylene has also been generated via photochemical reaction. IR emission is modeled according to known harmonic and anharmonic terms of the linear ground electronic state of acetylene. An unexpectedly strong combination band is found in the modeling. Through collisionally induced vibrational energy transfer, energy transfer rates, collisional mass dependence, and the vibrational energy content of acetylene can be obtained.

The production of highly vibrationally excited acetylene has presented the opportunity to study a short lived isomer of acetylene, vinylidene. The influence of vinylidene on acetylene is observed in the energy transfer rates at high energy. An enhancement in the energy transfer rate is observed above the acetylene-vinylidene isomerization barrier. An energy transfer model is used to verify this observation. A theoretical model is postulated which involves a mixing of vibrational states of acetylene and vinylidene above the isomerization barrier thus accounting for the enhancement of the energy transfer rate at high energies.

Another method involving collisions between translationally hot hydrogen atoms and room temperature acetylene molecules generate a significant amount of vibrationally hot acetylene. Possible mechanisms are proposed and tested via isotopic substitution. A mechanism proceeding through a short lived vinyl intermediate dissociating to form a highly vibrationally excited acetylene molecule was found. A combined statistical/impulsive model and classical trajectory calculation confirm the production of a short lived vinyl radical intermediate.

Degree Type
Dissertation

Degree Name
Doctor of Philosophy (PhD)

Graduate Group
Chemistry

First Advisor
Hai-Lung Dai

Keywords
Dynamics, Radical, Spectroscopy, Vibrational

Subject Categories
Chemistry | Physical Chemistry

SPECTROSCOPY AND DYNAMICS OF TRANSIENT SPECIES, THE VINYL RADICAL AND HIGHLY VIBRATIONALLY EXCITED ACETYLENE

Matthew Nikow

A DISSERTATION

in

Chemistry

Presented to the Faculties of the University of Pennsylvania
in Partial Fulfillment of the Requirements for the Degree of
Doctor of Philosophy

2012

_____

Supervisor of Dissertation
Hai-Lung Dai, Professor of Chemistry,
Temple University

_____

Graduate Group Chairperson
Gary Molander, Professor of Chemistry

Dissertation Committee

Marsha I. Lester, Ph.D., Professor of Chemistry
Michael Topp, Ph.D., Professor Chemistry
Feng Gai, Ph.D., Professor of Chemistry

Dedication

To my wife Adeline

my father Atanas

my brother Andrew

and

in loving memory of

my mother Iona

Acknowledgements

There are numerous scientists and professionals that have aided in my research efforts presented in this dissertation. First and foremost I would like to thank my wife, Dr. Adeline Kojtari, who has helped guide me through all of my personal and professional issues while simultaneously focusing on her work and completion of her PhD. My good friends in and out of the lab, Dr. Min Zhang, Dr. Michael J. Wilhelm, and Dr. Jonathan M. Smith, have provided good dialogue and insight into problems I have encountered over the years. My committee members, Prof. Marsha Lester, Prof. Michael Topp, Prof. Andrew Rappe, and Prof. Feng Gai, have been especially important in my graduate career providing insight and helpful suggestions guiding me down the correct path.

I must provide a special acknowledgement to my advisor, Dean Hai-Lung Dai for all he has done for me in my personal and professional career thus far. I would always look forward to interesting perspectives and dialogues, and sometimes arguments, during our meetings. I appreciate all the help and support from the group members I have worked with who have provided excellent guidance and feedback through my tenure. The successes from the countless hours of work that I have achieved would not have been possible without the aid of those individuals. Dr. Grazia Gonella, Dr. Wei Gan, Dr. Jun Han, Dr. Susan Dounce, Dr. Thomas Rockey, Dr. Heather Eckenrode, Dr. William McNavage, Dr. Shih-Hui Jen, Jia Zeng, Jianqiang Ma, and Dr. Rosa Chou have all played a significant role in my scientific career and helped me mature professionally and personally as well. I would lastly want to thank those graduate students I have had the

privilege to know and work with outside of my research group. Dr. Logan Dempsey, Dr. Erika Derro, Dr. Michelle Bunagan, Dr. Joe Swift, Dr. Aru Hill, and Dr. Andrew Lowell have been good friends and classmates throughout my graduate career.

Abstract

SPECTROSCOPY AND DYNAMICS OF TRANSIENT SPECIES, THE VINYL RADICAL AND HIGHLY VIBRATIONALLY EXCITED ACETYLENE

MATTHEW NIKOW

HAI-LUNG DAI

Time-resolved Fourier transform infra-red spectroscopy has been employed to identify vibrational modes of several transient molecular and radical species. IR emission from the vinyl radical generated by five different precursor molecules utilizing different dissociation pathways has been observed. An analytical method, two-dimensional cross spectral correlation, has been employed to verify the low energy bending modes of the vinyl radical as well as one stretching mode. Isotopic substitution has allowed several bending modes to be compared to their non-isotopically substituted analog.

Highly vibrationally excited acetylene has also been generated via photochemical reaction. IR emission is modeled according to known harmonic and anharmonic terms of the linear ground electronic state of acetylene. An unexpectedly strong combination band is found in the modeling. Through collisionally induced vibrational energy transfer, energy transfer rates, collisional mass dependence, and the vibrational energy content of acetylene can be obtained.

The production of highly vibrationally excited acetylene has presented the opportunity to study a short lived isomer of acetylene, vinylidene. The influence of vinylidene on acetylene is observed in the energy transfer rates at high energy. An

enhancement in the energy transfer rate is observed above the acetylene-vinylidene isomerization barrier. An energy transfer model is used to verify this observation. A theoretical model is postulated which involves a mixing of vibrational states of acetylene and vinylidene above the isomerization barrier thus accounting for the enhancement of the energy transfer rate at high energies.

Another method involving collisions between translationally hot hydrogen atoms and room temperature acetylene molecules generate a significant amount of vibrationally hot acetylene. Possible mechanisms are proposed and tested via isotopic substitution. A mechanism proceeding through a short lived vinyl intermediate dissociating to form a highly vibrationally excited acetylene molecule was found. A combined statistical/impulsive model and classical trajectory calculation confirm the production of a short lived vinyl radical intermediate.

Contents

List of Figures

Chapter 1

Chapter 2

Chapter 3

Chapter 4

Chapter 5

List of Tables

Chapter 2

Chapter 3

Chapter 5

Chapter 6

Introduction

Time-resolved IR emission spectroscopy of transient radicals and molecules

Transient species such as radicals and highly vibrationally excited species play a crucial role in controlling dynamical processes including energy transfer and chemical reactions. The study of these species is difficult due to their inherent short lived nature, in addition to being difficult to produce in significant quantities. In addition, these species are typically present as reaction intermediates or precursors and dynamic and kinetic studies are of vital importance in understanding macroscopic chemical processes.

The detection and identification of these species is the first step in understanding some dynamical information about them. Due to their short lifetimes, they are typically created from an excitation or photolysis laser pulse from a parent/precursor molecule. The photofragments, from a photolysis pulse, thus contain information about the nature

of the photolysis reaction, product branching ratios, product state energy distributions, and energy transfer pathways following photolysis.

There are several available methods to generate and detect these short lived species. Vibrational spectroscopy is of crucial importance in determining molecular structure in the ground state. When compared with electronic spectroscopy, vibrational emission spectroscopy has several disadvantages, including lower emission intensity due to the Einstein A coefficient for spontaneous emission, lower oscillator strength, and typically more congested spectra with larger limitations on spectral resolution. Nonetheless, the benefit of observing at least a partial IR fingerprint of the molecule provides a tremendous amount of spectroscopic and dynamic information about the molecule or radical.

Lasers have been typically used as both reaction initiators, as well as probes to detect molecular properties. Electronic levels can be detected by several different techniques.[1] Following a photolysis pulse (or thermal discharge, or other excitation method) a laser can excite the product into an excited electronic state where either dispersive fluorescence or laser induced fluorescence can be detected. Optical pumping and double resonance spectroscopic techniques include optical-optical double resonance spectroscopy such as stimulated emission pumping (SEP) and pump-probe spectroscopy. Other laser techniques include laser Raman spectroscopy, such as coherent anti-stokes raman spectroscopy (CARS), and stimulated raman spectroscopy. Other coherent spectroscopic methods include Quantum Beat (QB) spectroscopy and correlation spectroscopic methods involving several laser pulses. The majority of these techniques

involve probing the electronic excited state, with a limited amount of information generated about the vibrational ground state.

Absorption spectroscopy of these species proves particularly difficult due to their low density and transient nature. However, great success has been had trapping these molecules at low temperatures in noble gas matricies.[2-4] Once these species are trapped, they can be observed in absorption measurements in the infra-red (IR) region to determine structural information. One drawback of this technique is the static nature of the technique, limiting kinetic and dynamic information about the system. In addition, trapping in the matrix affects the vibrational mode frequencies and intensities due to interactions with the neighboring noble gas atoms.

Other absorption techniques involve the use of IR lasers.[5,6] These techniques are extremely sensitive and can detect very small concentrations of radicals and molecules. Ground state vibrational and rotational information can be obtained by this laser absorption spectroscopy. The main drawback of this method is the limited frequency range of the scanning laser and the resulting high resolution studies only being obtainable if the active mode location is known *a priori*.

Another experimental technique has been employed to study the energetics following a dissociation reaction. Photofragment translational spectroscopy has been employed to detect product translational energies.[7-9] Reaction energetics, branching ratios, and product state energy distributions have been found for numerous systems and has led to a better understanding of the translational, rotational, and vibrational energy distribution in the products. Energetic information is typically obtained in free expansion without collisions, so the only dynamical information available is from the initial

reaction. In addition, the detection method is a mass detector and thus no rotational, vibrational or electronic spectroscopic information is found.

In the method employed here, time-resolved IR emission is collected through a Fourier Transform Interferometer. Transient signals are generated in a vacuum chamber designed to collect and focus IR emission following a UV laser photolysis pulse into a Michelson interferometer. The interferometer is controlled in step-scan mode which allows frequency discrimination, as well as a fast and efficient means of collecting nanosecond time resolved data.

Through time-resolved Fourier transform IR emission spectroscopy (TR-FTIRES) structural and dynamical information can be obtained. The method yields a zero background, low noise, high signal spectra with fast transient signal detection.[10] TR-FTIRES can be used in the study of molecular reactions,[11] photodissociation,[12] spectroscopic identification,[13] and energy transfer processes,[14] among numerous other applications in the gas phase. The method can be used in the condensed phase as a time-resolved absorption technique to study structural and dynamical changes.[15,16]

IR emission can be observed through the TR-FTIRES technique as long as the molecule or radical has some vibrational excitation. This is typically the case following dissociation, as energy is transferred to the translational and internal (rotational, vibrational, electronic) degrees of freedom of the products. In addition, due to scaling rules, emission from highly vibrationally excited states is typically much stronger than emission from the fundamental ($v=1\rightarrow0$) transitions. This technique is therefore perfectly suited for studying ground state molecules with large amounts of vibrational excitation. The TR-FTIRES method is detailed in Chapter 1.

The study of molecular and radical emission in the IR is inherently difficult due to the extremely congested spectra and low oscillator strengths. Two methods introduced here, elaborated on in Chapter 2, and utilized throughout the thesis are 2-dimensional cross spectral correlation (2D-CSC) and vibrational emission modeling. 2D-CSC is an analysis method that has been employed to improve the S/R of the observed emission spectra. 2D-CSC is based on the general 2D correlation method for improving S/R of features with spectral and temporal overlap. The method generates a substantially improved, spectrally accurate, correlation spectra[17] with synchronous and asynchronous plots corresponding to positive and negative correlations. This analysis method is laid out in Chapter 2 and applied to several cases throughout this thesis. In addition, the study of molecular and radical emission is more informative than absorption studies due to the fact that transitions other than fundamental ones exist. This also makes the experimental results more complex. To understand the emission spectra, the vibrational energy manifold is created and emission spectra are generated from allowable transitions. These transitions form the basis of vibrational emission modeling. A general approach will be given in Chapter 2.

IR emission of the vinyl radical is discussed in Chapter 3. Vinyl radicals have been observed following photolysis of five precursor molecules. Five modes of the vinyl-h_3 radical have been identified through the 2D-CSC technique. In addition, three modes of the vinyl-d_3 molecule have also been identified and compare favorably with the assignments made for the vinyl-h_3 molecule based on isotopic frequency shifts of the modes. Several density functional theory (DFT) calculations were also performed and further enforce our vibrational mode assignments.

Vibrational emission of acetylene has also accompanied the reactions which produce vinyl radicals. This emission and subsequent vibrational modeling is described in Chapter 4. It has been found that emission characteristics of acetylene, as well as generalized for other vibrationally hot molecules, are significantly different from absorption measurements. Intensity, in addition to the frequency shifts due to anharmonic effects, alter the appearance of emission spectra. Thermodynamic information following dissociation producing acetylene has been determined as well. The internal energy distribution is consistent with *a priori*, statistical energy distribution calculations.

Based on the vibrational emission modeling calculations and fitting results found for acetylene, energy transfer rates have been determined. Dynamical information on vibration to translation/rotation (V-T/R) processes has been determined. A change in the energy transfer rate near the acetylene-vinylidene isomerization barrier has been found and agrees satisfactorily with the well established isomerization barrier height. An energy transfer model by Schwartz, Slawsky, and Herzfeld[18] (SSH) was used to describe both energy regions. Classical trajectory simulations confirm these results. A mixed state model was postulated to explain the inclusion of vinylidene in the energy transfer rate. General trends found with different collider partners agree qualitatively with accepted models for collisional energy transfer. These energy transfer results are discussed in Chapter 5.

The chemical reaction process producing highly vibrationally excited molecules is also of tremendous importance in high temperature, atmospheric, stellar, and other reaction environments. Reactions of hot hydrogen atoms colliding with cold acetylene

have been shown to produce vibrationally hot acetylene as a product. Single large translational to vibrational (T-V) energy transfer events (~15,000 cm^{-1}) have not been observed previously. A classical trajectory calculation suggests that a small amount of highly vibrationally excited acetylene is formed, while the major contribution comes from a smaller T-V energy transfer collision. A mechanism generating a short-lived, vibrationally hot vinyl radical intermediate is postulated. After the vinyl intermediate dissociates, it leaves a significant quantity of vibrational energy in acetylene while expelling a translationally cold H atom. A combined statistical/impulsive model successfully describes this dissociation. The H + acetylene reaction is discussed in Chapter 6.

References:

(1) Demtroder, W. *Laser Spectroscopy*; Springer: New York, 1996.

(2) Hallam, H. E. *Ann. Rep. Prog. Chem. A* 1970, *67*, 117.

(3) Jacox, M. E. *Acc. Chem. Res.* 2004, *37*, 727.

(4) Jacox, M. E. *Chem. Soc. Rev.* 2002, *31*, 108.

(5) Marr, A. J.; Sears, T. J.; Davies, P. B. *J. Mol. Spec.* 1997, *184*, 413.

(6) Kawaguchi, K.; Ishiwata, T.; Hirota, E.; Tanaka, I. *Chem. Phys.* 1998, *231*, 193.

(7) Lee, Y. T.; Shen, Y. R. *Phys. Today* 1980, *33*, 52.

(8) Wodtke, A. M.; Lee, Y. T. *Mol. Photodiss. Dyn.* 1987, 31.

(9) Ashford, M. N. R.; Lamber, I. R.; Mordaunt, D. H.; Morley, G. P.; Western, C. M. *J. Phys. Chem.* 1992, *96*, 2938.

(10) Hartland, G. V.; Xie, W.; Dai, H.-L.; Simon, A.; Anderson, M. J. *Rev. Sci. Instr.* 1992, *63*, 3261.

(11) McNavage, W.; Dailey, W.; Dai, H.-L. *Can. J. Chem.* 2004, *82*, 925.

(12) Wilhelm, M. J.; Nikow, M.; Letendre, L.; Dai, H.-L. *J. Chem. Phys.* 2009, *130*, 044307.

(13) Wilhelm, M. J.; McNavage, W.; Groller, R.; Dai, H.-L. *J. Chem. Phys.* 2008, *128*, 064313/1.

(14) Qin, D.; Hartland, G. V.; Dai, H.-L. *J. Phys. Chem. A* 2000, *104*, 10460.

(15) Johnson, T. J.; Zachmann, G. *Introduction to Step-Scan FTIR*; Bruker: Billerica, 2001.

(16) Griffiths, P. R.; de Haseth, J. A. *Fourier Transform Infrared Spectrometry*; Wiley-Interscience: New York, 1986; Vol. 83.

(17) Wilhelm, M.; Nikow, M.; Dai, H.-L. *Journal of Molecular Structure* 2008, *883-884*, 242.

(18) Schwartz, R. N.; Slawsky, Z. I.; Herzfeld, K. F. *J. Chem. Phys.* 1952, *20*, 1591.

Chapter 1

Time-resolved Fourier transform spectroscopy

1.1 Introduction

Frequency resolved infra-red spectra are of fundamental importance in the determination of vibrational motion and structure of molecules, ion, and radicals. Temporal resolution of these spectra allow the study of excited state dynamics within the molecule as well as energy transfer processes between other species. Several techniques have been widely used to study infra-red as well as visible/UV emission. Dispersive techniques have been utilized in the infra-red through the visible region to collect spectrally resolved emission spectra through the use of a grating spectrometer, with entrance and exit slits, and a detector. The full temporal and spectral signal may thus be obtained with the only drawback of limitation of the signal to the width of the slit. At increasing resolution, the slit width must be decreased to retain collimation and separation of the different wavelengths of emitted light.

Laser induced fluorescence may sometimes yield information about the vibrational ground state and infra-red active vibrational modes. In this technique a laser is scanned and total fluorescence is collected regardless of frequency. Typically this is done at room temperature in a cell or in a supersonic jet to cool the molecules. However, this technique is more useful for studying the electronic excited states of species due to the laser pumping. Dispersed fluorescence described previously can yield more

information about the structure of the ground state of a species utilizing the excitation wavelength and emission signature recorded.

Stimulated emission pumping may also be used to probe the dynamics of vibrationally excited states. This method is based on the Optical-Optical Double-Resonance (OODR) technique where the two optical fields are tuned to transitions involving a common state. The common state may be the original ground state or an excited state generated by the first laser pulse. Three types of OODR schemes exist: (1) V-type, (2) stepwise excitation, and (3) Λ-type. V-type OODR utilizes a pump and probe laser originating from a common state. The difference in probe laser absorption when the pump laser is on or off yields information about the upper level. Stepwise OODR involve a pump to an excited state and probe absorption of that excited state followed by fluorescence to a lower state. The Λ-type OODR technique involves once again a common excited state, but the probe laser now stimulates emission from the excited state. In all three cases, the technique can be quite sensitive to spectral (<0.01cm-1) and temporal (ns ~ sub-ns) parameters. Stimulated-emission pumping is a type of the later, l-type OODR where the probe laser induces a resonant Raman-type transition. The main difficulties of the technique are the spectral scan range is very narrow and the need to vary the time-delays between pump and probe lasers to determine temporal profiles of the features. Energy states must be known *a priori* to be able to utilize the fine resolution of these techniques.

Other traditional absorption techniques involve commercially available spectrometers. Good S/R is obtained when there is a sufficient population of absorbing states with limited dynamic importance. Transient and short lived species like radicals,

ion, intermediates, and highly vibrationally or electronically excited species are difficult to study under normal conditions. Trapping these species in cold matricies has been employed to study a wide variety of systems, however interactions between the solid matrix noble gas atoms and the species of interest can not be ignored, as well as loss of dynamic information about the process.

Time-Resolved Fourier Transform Spectroscopy (TR FTS) can offer some substantial improvement in experimental efficiency over the previously described techniques. High spectral resolution as well as fast detection can be comparable to the more sensitive techniques of LIF and SEP, with the main advantage of large spectral range. Emission collection through the FTIR offers a multiplexing advantage and eliminates the S/R decreasing slits found in dispersive instruments. Efficient scanning of absorption and emission sources both static and dynamic are possible with no need for calibration and no limit in spectral range.[1]

1.2 Fourier transform spectroscopy

1.2.1 The Michelson interferometer

In order to spectrally resolve specific wavelengths of emission (or absorption) without the use of a grating, an interference within the light must be created to generate an interferogram which can be transformed into a resulting energy unit spectrum. The simplest way to create an interference is to combine two distinct optical fields. The Michelson interferometer, Figure 1.1, utilizes a beam splitter to direct a single optical field to two mirrors, one fixed and one movable. The light reflects off the mirrors and is

Figure 1.1. The Michelson interferometer. The point source light is collimated by L1 (lens 1) onto a BS (beam splitter), which splits the light onto the fixed and movable mirrors. The light is directed back onto the BS, combined and directed to L2 (lens 2), and focused onto the detector.

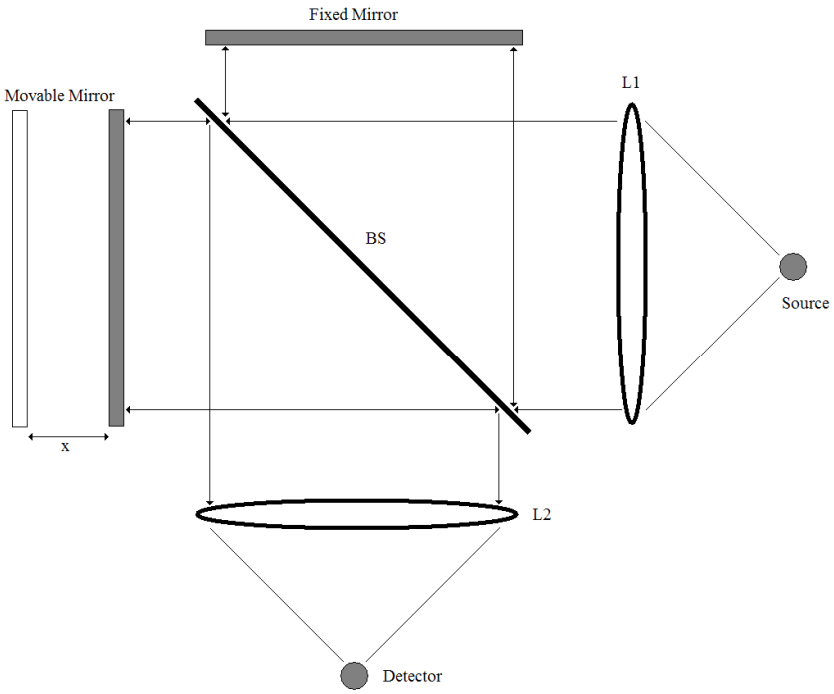

recollected on the backside of the beamsplitter and directed to a detector. The interference pattern is generated by translating the movable mirror as to create constructive and destructive interference patterns between the reflected light. Once the beam is recollected and detected as a function of translated distance, spectral information may be obtained.

1.2.2 Interference of light

The simplest case of interfering light is from a monochromatic source. This incident light traveling in the x direction can be described by:

$$E(x,t) = E_0 e^{-i(\omega t - kx)} \tag{1.1}$$

where $k=2\pi/\lambda$ is the wavevector and λ is the monochromatic wavelength. The source beam is split by the beamsplitter onto the movable and fixed mirrors. The distance the optical field travels to the two mirrors and returns to the beamsplitter is different and defined as x_1 and x_2.

$$E_1(x,t) = E_0 e^{-i(\omega t - kx_1)} \tag{1.2}$$

$$E_2(x,t) = E_0 e^{-i(\omega t - kx_2)} \tag{1.3}$$

The recombined field is just the sum of the two returning fields, while the intensity, I, of the field is proportional to the square of the magnitude of the field strengths.

$$E = E_1 + E_2 \tag{1.4}$$

$$I(\delta) \propto 2\left|E_0\right|^2 \left(1 + \cos\left(k\{x_1 - x_2\}\right)\right) \tag{1.5}$$

$$\text{or} \qquad I(\delta) \propto I_1 + I_2 + 2\left(I_1 I_2\right)^{1/2} \cos\left(k\{x_1 - x_2\}\right) \tag{1.6}$$

The retardation of the beam due to the movable mirror can be defined as $\delta=x_1-x_2$. The intensities of the two incident beams, I_1 and I_2, for an ideal monochromatic collimated source and a 50:50 beamsplitter would be identical making the result:

$$I(\delta) \propto 2I_0\left(\cos(k\delta)+1\right) \tag{1.7}$$

The fundamental theory of interference arises from the retardation of the movable mirror. As δ changes, positive or negative, there are certain discrete values of δ that form constructively and destructively the interferogram.

$$\delta = \frac{2n\pi}{k} = n\lambda \qquad I = 4I_0 \tag{1.8}$$

$$\delta = \frac{(2n+1)\pi}{k} = (n+1/2)\lambda \qquad I = 0 \tag{1.9}$$

If we displace the movable mirror at constant velocity we can observe these constructive and destructive overlaps of the monochromatic light. Constructive interference occurring at integer values of the wavelength, while destructive interference occurs at half integer values of the wavelength. For monochromatic light, it is impossible to determine where $\delta=0$, only integer values of the wavelength. While displacing with constant velocity (δ/t=constant) a sinusoidal pattern will be observed at the detector.

$$I(\delta) = 0.5I(\bar{\nu})(1+\cos(2\pi\delta/\lambda)) \tag{1.10}$$

The interferogram now contains a dc component, $0.5I(\bar{\nu})$, and an ac component, $0.5I(\bar{\nu})\cos(2\pi\delta/\lambda)$. It is this modulated component that is defined as the interferogram, $I(\delta)$. There are several experimental considerations that must be taken into account when determining the interferogram intensity. These include the detector spectral response, the beamsplitter efficiency, amplifier limitations, and spectral response of the optics within

the FTIR. These factors can be combined into a single energy-dependent factor, $H(\bar{\nu})$. Inserted into Eq. 1.10 yields,

$$I(\delta) = 0.5H(\bar{\nu})I(\bar{\nu})\cos(2\pi\delta/\lambda) \tag{1.11}$$

where $0.5H(\bar{\nu})I(\bar{\nu})$ may be set to $B(\bar{\nu})$, defined as the single-beam spectral intensity, which when added to Eq. 1.11,

$$I(\delta) = B(\bar{\nu})\cos(2\pi\delta/\lambda) \tag{1.12}$$

becomes the simplest interferogram defining equation. Eq. 1.12 defines that $I(\delta)$ is the cosine Fourier transform of the spectral response, $B(\bar{\nu})$. The spectral response can be calculated once the interferogram is determined through a Fourier transform of $I(\delta)$.

Once the optical field contains more than one wavelength of light, the trivial task of Fourier transforming the interferogram becomes significantly more complicated and requires the use of computational power. Eq. 1.12 can be expressed as an integral over all energy given by,

$$I(\delta) = \int_{-\infty}^{+\infty} B(\bar{\nu})\cos(2\pi\bar{\nu}\delta)d\bar{\nu} \tag{1.13}$$

where frequency based unit $\bar{\nu}$ is used in place of λ. The Fourier transform conjugate pair is then,

$$B(\bar{\nu}) = \int_{-\infty}^{+\infty} I(\delta)\cos(2\pi\bar{\nu}\delta)d\delta \tag{1.14}$$

One convenience of this function is that it is even and can be expressed as

$$B(\bar{\nu}) = 2\int_{0}^{+\infty} I(\delta)\cos(2\pi\bar{\nu}\delta)d\delta \tag{1.15}$$

It is easy to recognize a dichotomy between spectral resolution and retardation, as well as frequency range and interferogram sampling. An ideal spectrum with infinite spectral resolution sampling the frequencies 0 to $+\infty$ would require an interferogram sample with retardation from 0 to $+\infty$ and infinitesimally small sampling rates. In reality, the result's spectral resolution is limited to a finite retardation, while the frequency range is based on the finite sampling rate of the system.

The result of more than one monochromatic field is shown in Figure 1.2. Four different sources are shown with their corresponding interferometric signal. The interferograms rapidly increase in complexity as more frequencies are added. Both intensity information, seen as a interferometric discrepancy in Figure 1.2 (a) and (b), as well as energetic information including peak width, seen in Figure 1.2 (c) and (d), can be extracted from the interferograms. Monochromatic sources are described by oscillating cosine curves which reach local minimum and maximum as a function of retardation. In addition, the oscillation is symmetric around all of the maxima. It is important to not that when a continuum of frequencies make up a source, the interferogram only reaches a maximum intensity at the zero path difference (ZPD) of retardation.

1.2.3 Finite resolution

There exists a maximum resolution element of the calculated spectrum recorded as an interferogram that is related to the maximum retardation of the interferogram. To give a sense of this resolution element a sample spectrum containing two monochromatic fields is shown is Figure 1.3 (a). The interferometric signal for each field is shown in Figure 1.3 (b) and the combined signal in Figure 1.3 (c).

Figure 1.2. Spectra and interferograms for the following systems, (a) two even strength line spectra, (b) two uneven strength line spectra, (c) thin Lorentzian signal, (d) wide Lorentzian signal.

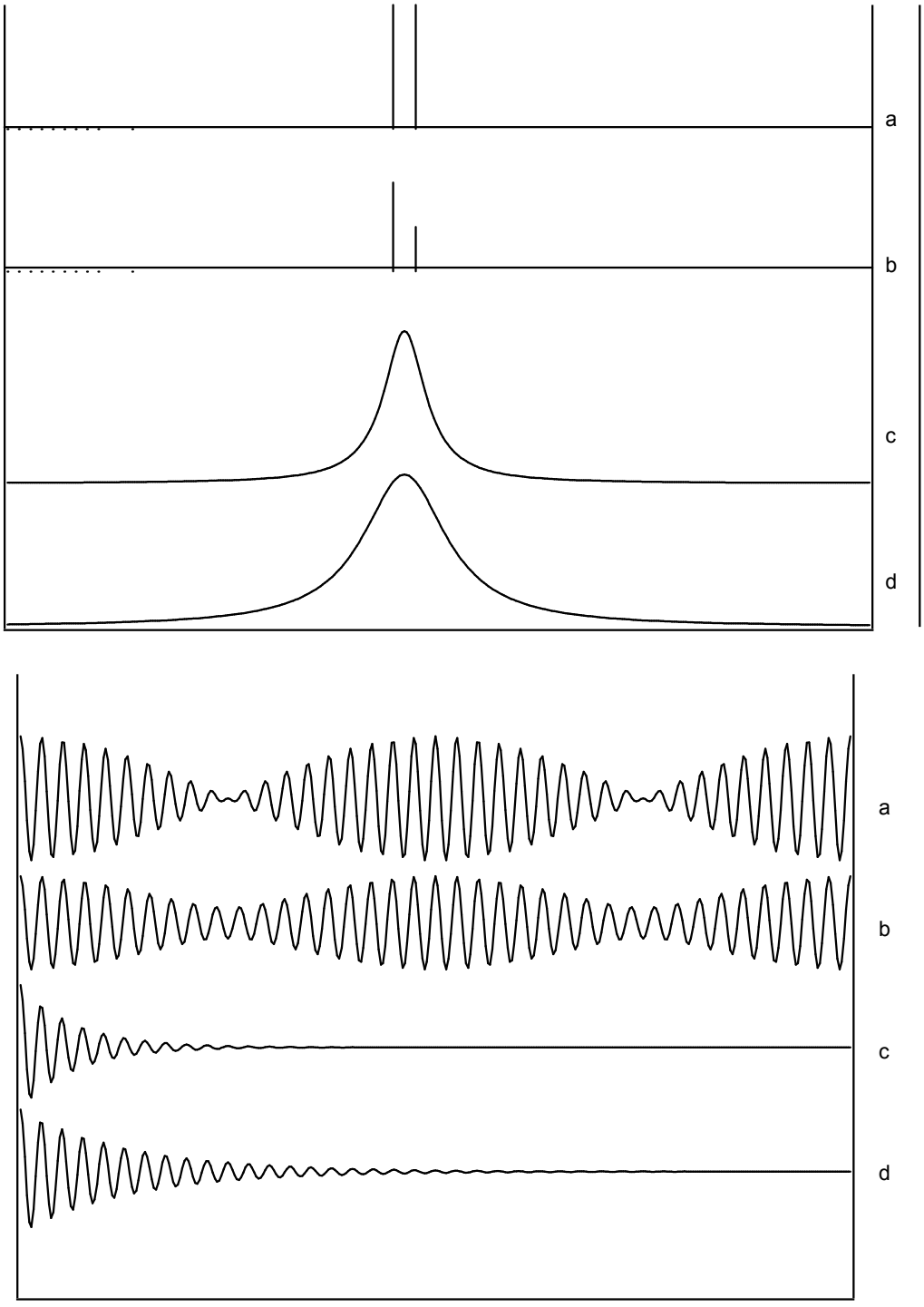

Figure 1.3. Spectra and interferograms for (a) a two line spectra, (b) the two individual cosine interferograms, (c) the sum of the two cosine interferograms.

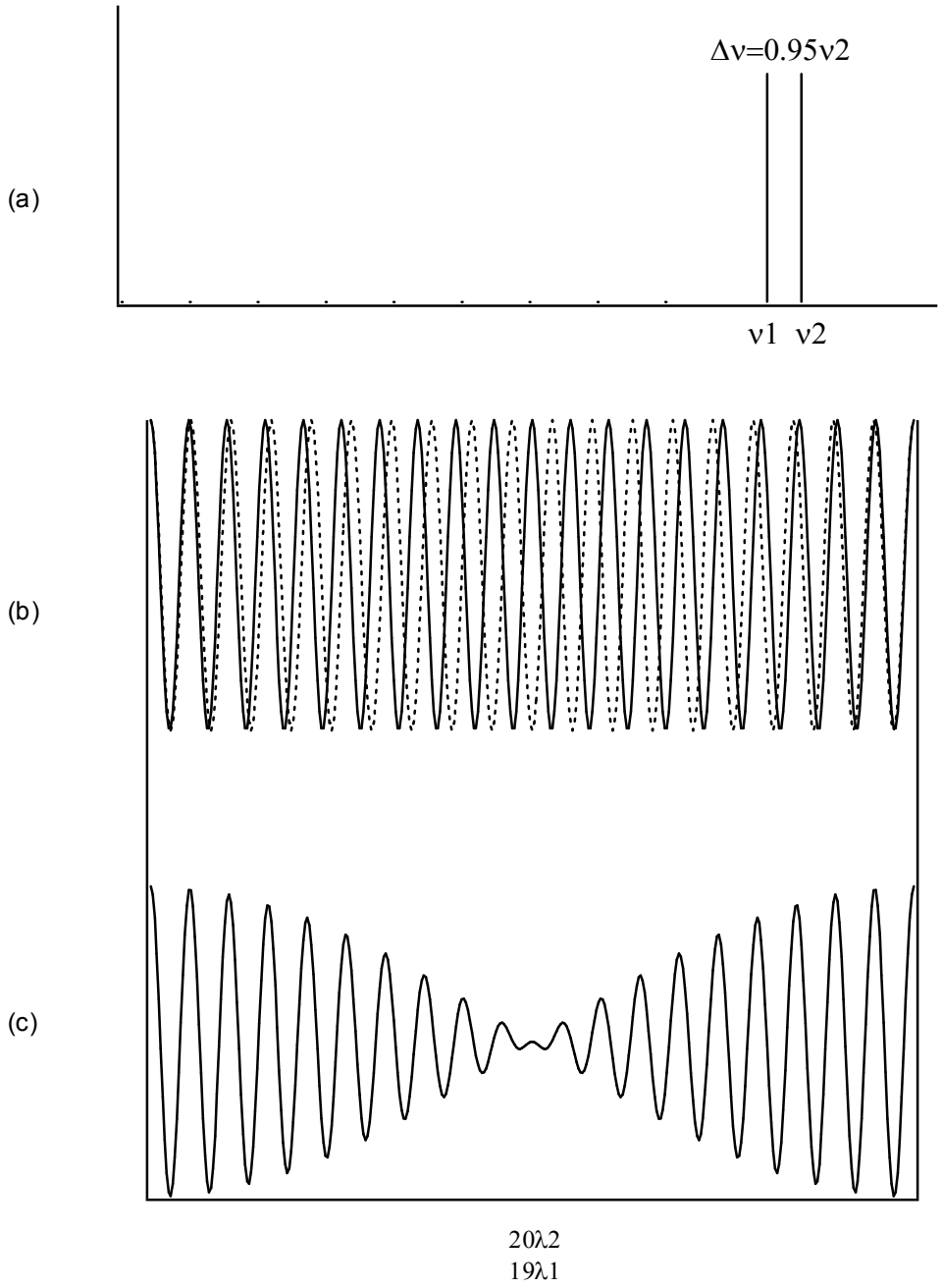

If the two frequencies differ by $\Delta\bar{\nu} = \bar{\nu}_2 - \bar{\nu}_1$, the two fields will go out of phase after a retardation of $0.5(\Delta\bar{\nu})^{-1}$, and are back in phase after a retardation of $(\Delta\bar{\nu})^{-1}$. An interferogram measured only to the half phase retardation, $0.5(\Delta\bar{\nu})^{-1}$, would not yield a completely discernable spectrum. For example, compare the interferograms in Figure 1.3(c) with that of Figure 1.2 (c) both generated from different spectra, one being a continuous function and one a dichromatic source.

We can intuitively conclude that the limit of the method is reliant on the maximum retardation point and since $\delta = (\Delta\bar{\nu})^{-1}$, we can define the maximum retardation $\Delta_{\max}$, as giving the best resolution.

$$\Delta\bar{\nu} = (\Delta_{\max})^{-1} \tag{1.16}$$

A more thorough analysis of the minimum resolution element based on the retardation of the interferogram involves utilizing a complete interferogram from $-\infty$ to $+\infty$ and a truncation function $D(\delta)$.

$$D(\delta) = 1 \qquad \text{if } -\Delta \le \delta \le +\Delta \tag{1.17}$$

$$D(\delta) = 0 \qquad \text{if } \delta > |\Delta|$$

Within this definition of $D(\delta)$, we can conclude that it is a boxcar function centered around a portion of the observable interferogram based on the maximum retardation of the system. Utilizing the result from Eq. 1.14, the resulting spectrum with this truncating function is

$$B(\bar{\nu}) = \int_{-\infty}^{+\infty} I(\delta) D(\delta) \cos(2\pi\bar{\nu}\delta) d\delta \tag{1.18}$$

By a simple mathematical derivation, the Fourier transform of the product of two functions of the same variable can be represented by the convolution of the Fourier transform of each individual function. The result of multiplying $D(\delta)$ with the interferogram function $I(\delta)$ generates a spectrum after Fourier transforming that equals the convolution of the transform of $D(\delta)$ with the transform of $I(\delta)$. The Fourier transform of $I(\delta)$ is the resulting spectrum $B(\bar{\nu})$, while the transform of $D(\delta)$ can be represented by, $f(\bar{\nu})$

$$f(\bar{\nu}) = \frac{2\Delta \sin(2\pi\bar{\nu}\Delta)}{2\pi\bar{\nu}\Delta} \tag{1.19}$$

$$\equiv 2\Delta \operatorname{sinc}(2\pi\bar{\nu}\Delta)$$

Eq. 1.19 is shown in Figure 1.4(a). The narrow function is centered at the origin and has $\bar{\nu}$ axis intercepts at $\bar{\nu} = n/2\Delta$, where n are integer values corresponding to the number of intersections, the first occurring at $(2\Delta)^{-1}$. The convolution of $B(\bar{\nu})$ and $f(\bar{\nu})$ can be described by, $G(\bar{\nu})$

$$G(\bar{\nu}) = B(\bar{\nu}) * f(\bar{\nu}) \tag{1.20}$$

$$= \int_{-\infty}^{+\infty} B(\bar{\nu}') f(\bar{\nu} - \bar{\nu}') d\bar{\nu}'$$

The convolution of $B(\bar{\nu})$ and $f(\bar{\nu})$ can be completed utilizing the symmetric form of $f(\bar{\nu})$. Each point along the frequency axis is multiplied between the functions and then integrated. This is done as $f(\bar{\nu})$ samples all possible displacements of $B(\bar{\nu})$. The instrument line shape of an FTIR spectrometer has thus been defined as $f(\bar{\nu})$, a sinc line shape. This draws an important analogy to the triangular slit function of a

Figure 1.4. A sinc line shape with zero, and ν_1 frequency.

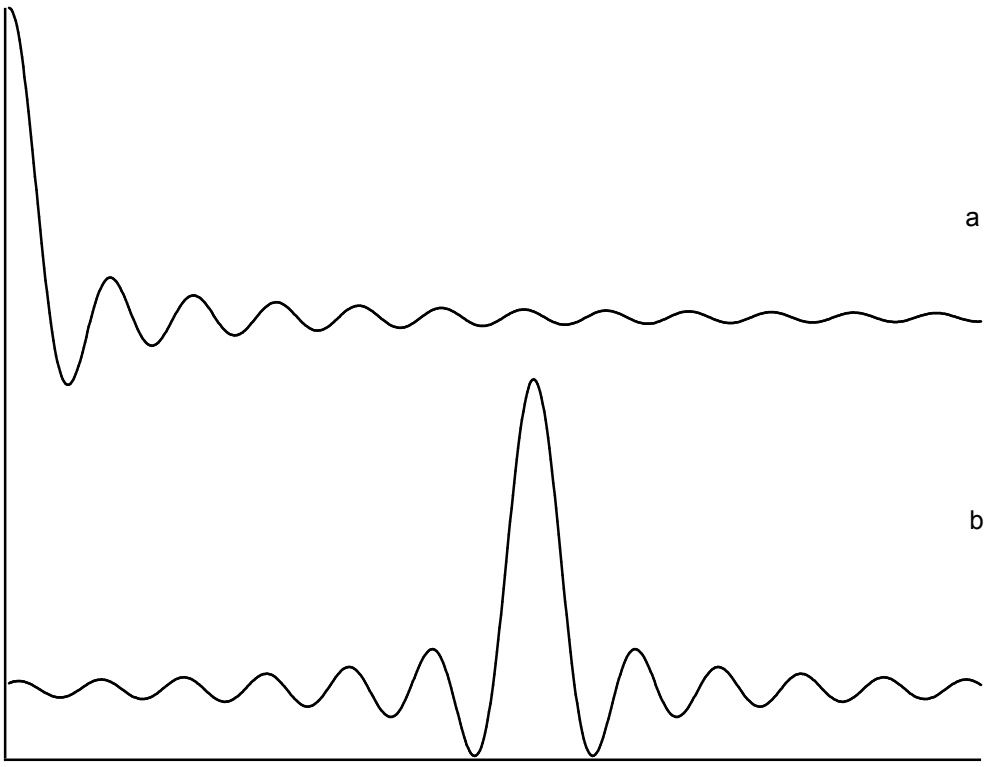

monochromator, where the actual spectrum becomes convoluted with the slit of the monochromator. For a monochromatic source with the single line with frequency, $\overline{\nu}_1$, the spectrum becomes

$$B(\overline{\nu}) = 2\Delta B(\overline{\nu}_1)\sin c(2\pi(\overline{\nu}_1 - \overline{\nu})\Delta) \tag{1.21}$$

as shown in Figure 1.4 (b). Intuitively, since the intersecting lines occur at $(2\Delta)^{-1}$ the resolution is less than twice that amount $< (\Delta)^{-1}$. The limit to the resolution thus requires a criterion for the analysis of separable peaks.

There are two applicable criterion for resolution based on similar types of line shapes and instrument response functions. The first is the Rayleigh criterion. It states that two lines are just resolved for instrument with a sinc^2x line shape, like that from a diffraction-limited grating spectrometer, when the line center of one line appears at the first intersection of the second. This results in approximately a 20% dip between the resulting maxima shown in Figure 1.5 (a). The same method applied to a sinc *x* line shape, however, does not hold true and the two lines are not resolved, as seen in Figure 1.5 (b). The separation between the peak and the first frequency axis intersection is 0.5/Δ as defined by the full width of the feature, 1/Δ.

For the sinc *x* line shape, a more useful definition of resolution is based on the full width at half-maximum of the function. The FWHM of a sinc x line shape given by Eq. 1.19 is 0.605/Δ. The 20% dip associated with the Rayleigh criterion is found at 0.730/D shown in Figure 1.5 (c).

The sinc x line shape associated with the instrumental response used previously is far from ideal for use in the infra-red region due to its side lobes which can reach above

Figure 1.5. Two $sinc^2$ line shapes separated by their minimum resolvable resolution in (a). Two sinc line shapes with the same separation in (b). Two sinc line shapes separated by their minimum resolvable distance in (c).

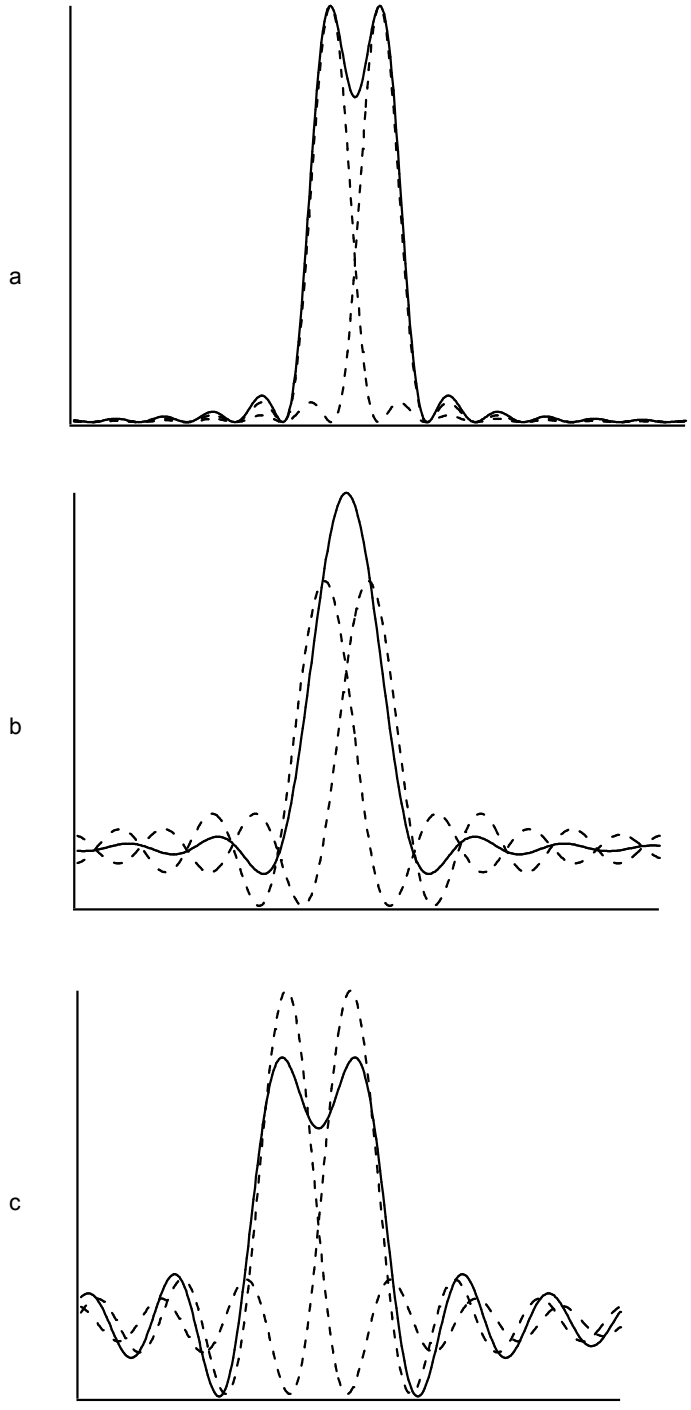

and below zero to as much as 22% of the overall height of the mode. This can interfere constructively and destructively with other lines in close proximity to these oscillations. The removal of these secondary minima and maxima is done through apodization.

1.2.4 Apodization function

The previous assumption that the cosine based interferogram function generates a resulting spectra based on the convolution of the actual spectrum and a sinc function, when presented with a boxcar line shape function is not necessary when performing a Fourier transform. A different function may be applied in place of the boxcar function. For example if we use a simple weighting function,

$$A(\delta) = 1 - |\delta / \Delta| \qquad \text{for} \quad -\Delta \le \delta \le +\Delta \tag{1.22}$$

$$A(\delta) = 0 \qquad \text{for} \qquad \delta > |\Delta|$$

The general form of Eq. 1.22 is known as a triangular function. The function takes the feature and reduces the amplitude linearly and symmetrically away from the center position. The corresponding spectrum based on this weighting function would have the form of the convolution of the true spectrum with the $\text{sinc}^2 x$ instrument line shape.

$$f(\bar{\nu}) = \Delta \frac{\sin^2(\pi \bar{\nu} \Delta)}{(\pi \bar{\nu} \Delta)^2} \tag{1.23}$$

$$= \Delta \text{sinc}^2(\pi \bar{\nu} \Delta)$$

The resulting line shape has noticeably smaller side lobes, as well as no negative intensity oscillations to the baseline. The suppression of these features is known as apodization. The main benefit to this change of functional form to the line shape is to reduce the interference of single features in close proximity to one another. The main drawback is

the width of the main feature increases, both the FWHM and the base width (distance between nodes) increase to 0.88/Δ and 2/Δ from 0.605/Δ and 1/Δ respectively when compared to the sinc *x* line shape function based on the 20% criterion. This can be seen in Figure 1.6.

There are numerous possible apodization functions based on the premise that at the zero path difference (i.e. centerburst) where δ=0, the function must equal one. Then on either side of the interferogram, the function must decay through a known functional form. There is a general rule that most apodization functions follow. The rule is that the further decrease of the sidebands in intensity, the greater the width of the main feature, and likewise the converse, the narrower the main feature, the less the sidebands are suppressed. There has been a substantial amount of work done on apodization functions by Filler[2] who looked at trigonometric functions and the suppression effects and Norton and Beer[3,4] whose functions follow the form,

$$A(\delta) = \sum_{i=0}^{n} C_i \left[1 - \left(\frac{\delta}{\Delta} \right)^2 \right]^i \tag{1.24}$$

These functions had a discernable boundary between main peak width and intensity of the side lobe features. Along this boundary line, the best suppression while retaining the narrowest functional width to the main feature was found. Three functions were selected along this boundary, "weak", "medium", and "strong", based on their side lobe suppression strength.

Figure 1.6. The sinc^2 line shape with parameters corresponding to the maximum signal level Δ.

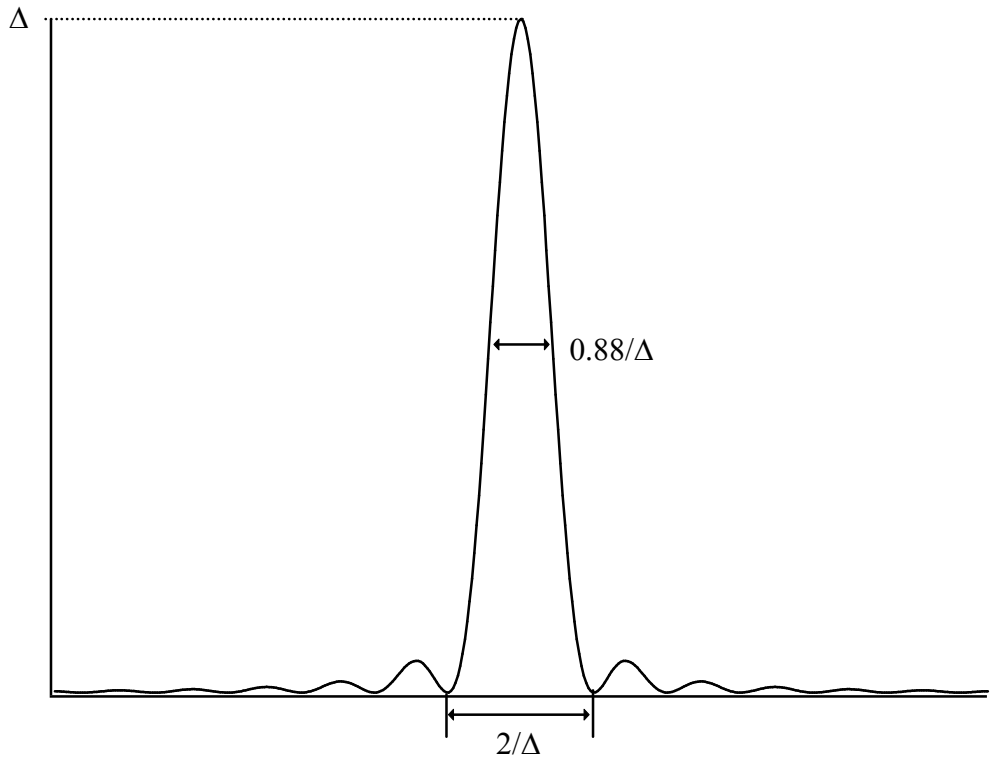

1.2.5 Phase functions

The main premise that the interferogram represents a cosine curve expressed in Eq. 1.13 is predominantly correct. However there are errors caused by electronic or optical issues which may affect the interferogram in the most sensitive area of the interferogram, the centerburst. The portion of the cosine wave, $2\pi\bar{\nu}\delta$, the phase angle, can not represent the complete interferogram based on these errors.

Since the interferogram is totally symmetric around δ=0, but sampling occurs before that point at $\delta = -\varepsilon$ we must correct this factor in Eq. 1.13 as follows,

$$I(\delta) = \int_0^{+\infty} B(\bar{\nu})\cos(2\pi\bar{\nu}(\delta - \varepsilon))d\bar{\nu} \tag{1.25}$$

In addition, a common electronics issue involves removing high frequency noise from the interferograms, artificially adding a phase lag, $\theta_{\bar{\nu}}$, to the result.

$$I(\delta) = \int_0^{+\infty} B(\bar{\nu})\cos(2\pi\bar{\nu}\delta - \theta_{\bar{\nu}})d\bar{\nu} \tag{1.26}$$

Other errors show a similar effect to the interferogram and its symmetry. The correction based on these phase errors can be made to Eq. 1.13 by using the following cosine transform,

$$\cos(\alpha - \beta) = \cos\alpha\cos\beta - \sin\alpha\sin\beta \tag{1.27}$$

$$I(\delta) = \int_0^{+\infty} B(\bar{\nu})e^{-2\pi i\bar{\nu}\delta}d\bar{\nu} \tag{1.28}$$

With the resulting complex Fourier transform of $B(\bar{\nu})$ from $I(\delta)$.

$$B(\bar{\nu}) = \int_0^{+\infty} I(\delta)e^{2\pi i\bar{\nu}\delta}d\delta \tag{1.29}$$

The result is based on the finding that the cosine component produces a real spectrum $\mathrm{Re}(\bar{\nu})$, while the sine component produces and imaginary spectrum $\mathrm{Im}(\bar{\nu})$. The imaginary sine portion of the interferogram can be removed by a phase correction method. As long as the variation in the phase angle is does not change rapidly with increasing frequency, the phase angle can be determined from a low resolution interferogram centered around the zero path difference. A short double sided interferogram is taken and the real and imaginary components are determined by the cosine and sine transforms respectively. The phase spectrum is determined by

$$\theta_{\bar{\nu}} = \arctan \frac{\mathrm{Im}(\bar{\nu})}{\mathrm{Re}(\bar{\nu})} \tag{1.30}$$

A method developed by Mertz[5] involves determining an amplitude spectrum based on the centerburst position. The resulting amplitude is frequency dependent. There is a difference now between the measured phase angle and the reference phase angle. When the cosine of that difference is determined at each frequency point, it can be multiplied by the amplitude spectrum to determine the true phase-corrected spectrum. To eliminate the doubling of the amplitude spectrum by taking a boxcar function around the center burst, a ramp function is used shown in Figure 1.7 (a) with a triangular apodization function and Figure 1.7(b) with a Beer-Norton type apodization function.

1.2.6 Optical beam effects

Beam divergence affects both the resolution and the accuracy of the frequency of a recorded spectrum. The traveling beam thus far has been described as originating from an infinitesimally small point source, and thus could not be detected at our detector. The "real" source, whether a point source or arising as a collimated beam, can exhibit some

Figure 1.7. The phase correction across the ZPD, centered around $\pm\Delta 1$. The full interferogram is taken out to $\Delta 2$.

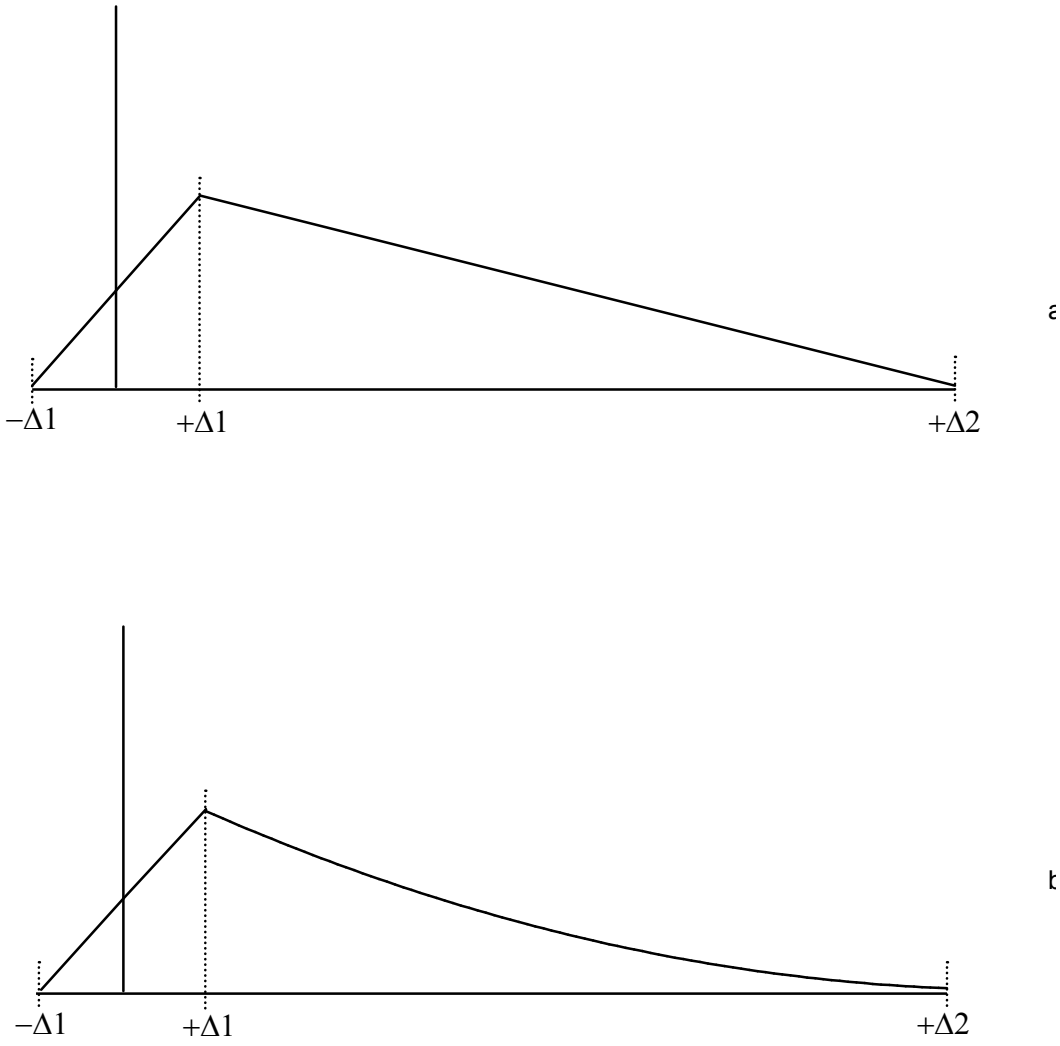

spectral and spatial divergence as it enters and passes through the FTIR. The first effect is from pure divergence of the original optical beam at a half angle α seen in Figure. 1.8. At zero path difference, where the central beam constructively interferes with itself, the diverging ray will also constructively interfere with itself, based on the light path traveled, and the fact that both mirrors are the same distance from the beam splitter and light source. After a small mirror displacement of l, the extreme ray travels an extra distance of $2l/\cos\alpha$ thereby creating a difference in the length traveled of

$$x = \frac{2l}{\cos\alpha} - 2l \tag{1.31}$$

$$= 2l\frac{1-\cos\alpha}{\alpha}$$

Utilizing the cosine series expansion,

$$\cos\alpha = 1 - \frac{\alpha^2}{2!} + \frac{\alpha^4}{4!} - \frac{\alpha^6}{6!} + \ldots$$

and if α is small and thereby $\cos\alpha \approx 1$

$$1 - \cos\alpha \approx \frac{1}{2}\alpha^2$$

$$x = 2l * \frac{1}{2}\alpha^2 = l\alpha^2 \tag{1.32}$$

The divergence may seem small, however when the ray is out of phase by x=1/2λ, the ray will completely destructively interfere with the main feature. Past this point, no further information will be contained in the interferogram. This yields a minimum resolution at a particular frequency based on the maximum retardation at a particular angle, α. Taking another look at Eq. 1.16, we can determine that the resolution is directly affected by the

Figure 1.8. A properly collimated ray and a diverging ray from the same source.

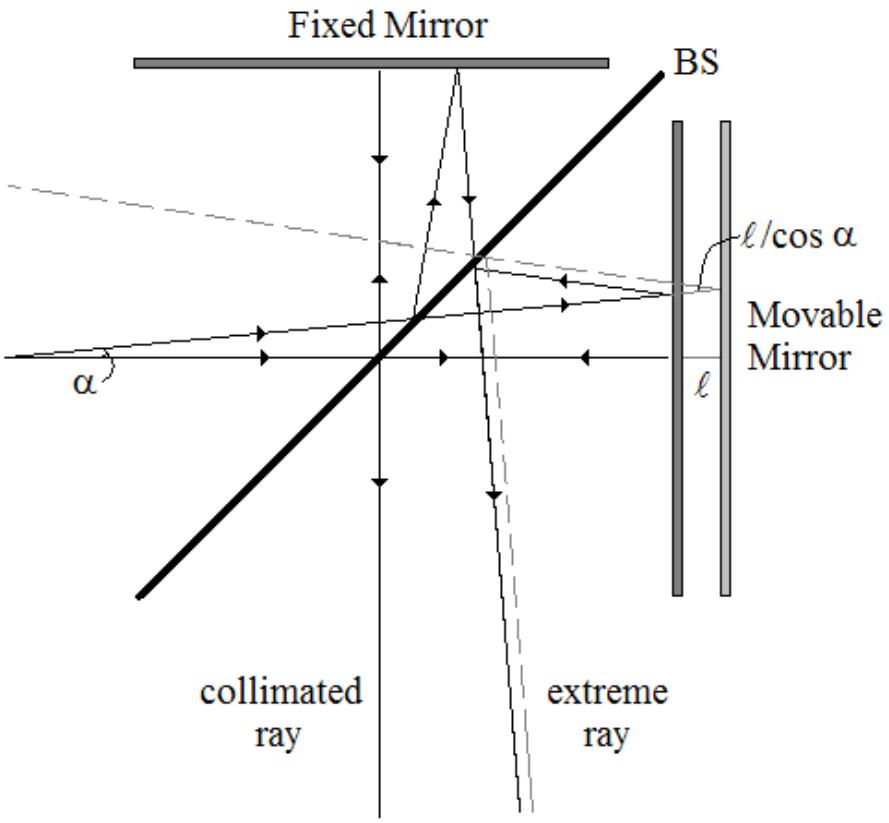

retardation length. To determine the maximum divergence of the solid angle, the maximum frequency and minimum resolution required must be considered.

$$l\alpha_{\max}^2 = \frac{\alpha^2}{2(\Delta\bar{\nu})} = \frac{1}{2\bar{\nu}_{\max}}$$

$$\alpha_{\max} = \left(\frac{\Delta\bar{\nu}}{\bar{\nu}_{\max}}\right)^{\frac{1}{2}} \tag{1.33}$$

The resulting maximum solid angle, Ω_{max}, based on the maximum frequency of the FTIR is therefore

$$\Omega_{\max} = 2\pi\alpha^2 = 2\pi\frac{\Delta\bar{\nu}}{\bar{\nu}_{\max}} \tag{1.34}$$

A diverging beam may not always present a problem when dealing with only resolution broadening. The overall cause of this limitation is due to a self-apodizing effect of the diverging beam. As the mirror displaces further from the centerburst, the interferometric signal is brought down to zero without any calculation or limitation on the signal. With a known solid angle it would be experimentally possible to forgo the apodization requirements described earlier, and only use a boxcar function to truncate the interferogram. Beam divergence, however, must be carefully controlled as it does not only affect resolution, but could also shift frequencies of peaks.

The effect of a diverging beam on the frequency of the detected signal can be seen in Figure. 1.8. As the extreme ray diverges at half angle α, the wavelength of the beam decreases at the detector which is perpendicular to the central ray. The longer path length traveled by this outside ray is given by Eq. 1.32 as

$$x = \frac{1}{2}\alpha^2\Delta \tag{1.35}$$

Using a monochromatic source as the simplest case, between the zero path difference and this particular retardation, Δ, there are *n* maxima in the interferogram.

$$\Delta = n\lambda = \frac{n}{\bar{\nu}} \tag{1.36}$$

Since the outer ray is traveling a further distance while the number of maxima on the interferogram do not change, the wavelength must change to compensate for this difference in length.

$$\Delta + x = n\lambda' = \frac{n}{\bar{\nu}'} \tag{1.37}$$

The difference between the two rays can be combined to determine the frequency, or wavelength shift per given half angle of divergence.

$$\frac{\bar{\nu}'}{\bar{\nu}} = \frac{\Delta}{\Delta + x} = \frac{1}{1 + \alpha^2/2} \tag{1.37}$$

Since α will be small almost all cases, we can solve for the new frequency, $\bar{\nu}'$

$$\frac{\bar{\nu}'}{\bar{\nu}} = 1 - \frac{\alpha^2}{2}$$

$$\bar{\nu}' = \bar{\nu}\left(1 - \frac{\alpha^2}{2}\right) \tag{1.38}$$

If we assume that the measured frequency of a transition is the average of the center and extreme rays (this is a crude assumption as the extreme rays contribute more to the signal than the central rays) the following holds true for the accuracy of the measured frequency. We utilize Eq. 1.33 for the maximum α angle in this result.

$$\bar{\nu}_{meas} \approx \frac{\bar{\nu} + \bar{\nu}'}{2} = \bar{\nu}\left(1 - \frac{\alpha^2}{4}\right) \tag{1.39}$$

$$= \bar{\nu}\left(1 - \frac{\Delta\bar{\nu}}{4\bar{\nu}_{\max}}\right)$$

We can see there is a relationship between the achievable resolution, the maximum spectral frequency, which is based on the sampling rate, and the observed frequency of a particular transition. The deviation from the correct frequency is usually quite small, as the divergence to and through the FTIR is quite well contained by use of apertures and constant *f*/4 optical components. Emission that is focused into the FTIR cavity must therefore match these optical and collimation restraints. One effect that may not be so apparent arises from the He-Ne laser used to track the movable mirror position. The laser is not perfectly positioned inside the cavity thus immediately creating a small deviation from the correct frequency points. This is easily calibrated by using water lines as reference points. The calibration needs to be done whenever the laser is replaced or an optic inside the cavity is moved.

1.2.7 Scan types

There are three main types of scanning that the movable mirror can perform. They are "slow," "rapid," and "stepped." Each will be briefly discussed here with the later in more detail in the next sections.

The slow scanning type FTIR is predominantly used for static collection of a source. The range of these instruments typically runs from the far-IR to the mid-IR range. There has been a good amount of work done on improving the S/R of these systems by utilizing a chopper and lock-in amplifier to combat the increase of 1/*f* noise at

low frequency. The sinusoidal interferogram from a laser source is typically used to track the mirror position.

A rapid scan interferometer has the advantage of being able to detect both static and dynamic responses, as long as the time constants are much longer than the modulation frequency of the moving mirror. The scan ranges in frequency from the mid-IR to the near-IR and visible region. The interferograms must be coadded in a rapid scan system to improve the S/R.

The stepped-scan instrument relies on a He-Ne laser to monitor the moving mirror displacement as it travels using a move-stop-move motion. The benefit of this technique is its ability to measure extremely fast dynamics at a high S/R. During a static scan the signal is integrated at each stepping position improving the S/R over both rapid and slow scanning techniques. The greatest limitation on this technique is the accuracy of the stepping motor as it translates and stops at regular intervals. Sampling errors may be generated because of this as discussed in the next section.

1.2.8 Interferogram sampling and acquisition parameters

The basic premise of interferogram sampling generating a high frequency limit is solely based on sampling frequency. An infinitely long interferogram with infinitesimally small sampling steps is not possible to collect nor compute. A method for calculating the maximum frequency element called the Nyquist Criterion states that a frequency can be sampled without any loss of spectral information utilizing a sampling frequency of twice the frequency element. For a corresponding frequency, $\overline{\nu}$, the cosine transform generates a frequency of $2\upsilon\overline{\nu}$, thus the sampling rate must be at $4\upsilon\overline{\nu}$. When

there is a frequency that is not in the signal, and occurs at equal intervals either around a peak or reflected around a certain point in the spectra, it is known as folding or aliasing of a spectral line. This occurs predominantly where the high frequency limit of the experiment is entered or around peaks of high frequency.

The most common type of error due to folding or aliasing effects arises from under sampling the interferogram data. If a main feature appears at $\overline{\nu}_{max} + \overline{\nu}_1$, and the sampling rate corresponds to $2\overline{\nu}_{max}$, the main feature should be the only apparent peak. However, this peak is not realized because the cut-off for the spectrum is $\overline{\nu}_{max}$. What does appear is a feature at $\overline{\nu}_{max} - \overline{\nu}_1$. This is shown in Figure 1.9. The top curve in Figure. 1.9 shows a sine wave corresponding to $\overline{\nu}_{max}$, sampled at twice its frequency. (twice per oscillation, shown here at each zero point) The middle and bottom curves correspond to $\overline{\nu}_{max} + \overline{\nu}_1$ and $\overline{\nu}_{max} - \overline{\nu}_1$. Note how both bottom curves sample the same intensity values in their corresponding curves. The resulting spectrum will artificially show $\overline{\nu}_{max} - \overline{\nu}_1$ due to this effect.

The folding effect can also occur on the basis of multiple values of a high frequency wave. This high frequency wave will not show up in a spectrum with a lower frequency cut off, F, with corresponding sampling frequency 2F. However, this feature will show up as a folded feature in the lower frequency region due to the sampling rate being too slow to trace an entire wavelength for this species. Multiples of a particular frequency (ν, 2ν, 4ν, 8ν) sine wave are shown in Figure 1.10. It is apparent here that the high frequency oscillation can produce false lower frequency peaks of multiples of its

Figure 1.9. An example of optical folding. Each of the three cosine waves shown here have the same amplitude at each of the dotted intervals. The top sine wave has a frequency, $\overline{\nu}_{max} + \overline{\nu}_1$, the middle wave, $\overline{\nu}_{max}$, and the lower wave, $\overline{\nu}_{max} - \overline{\nu}_1$.

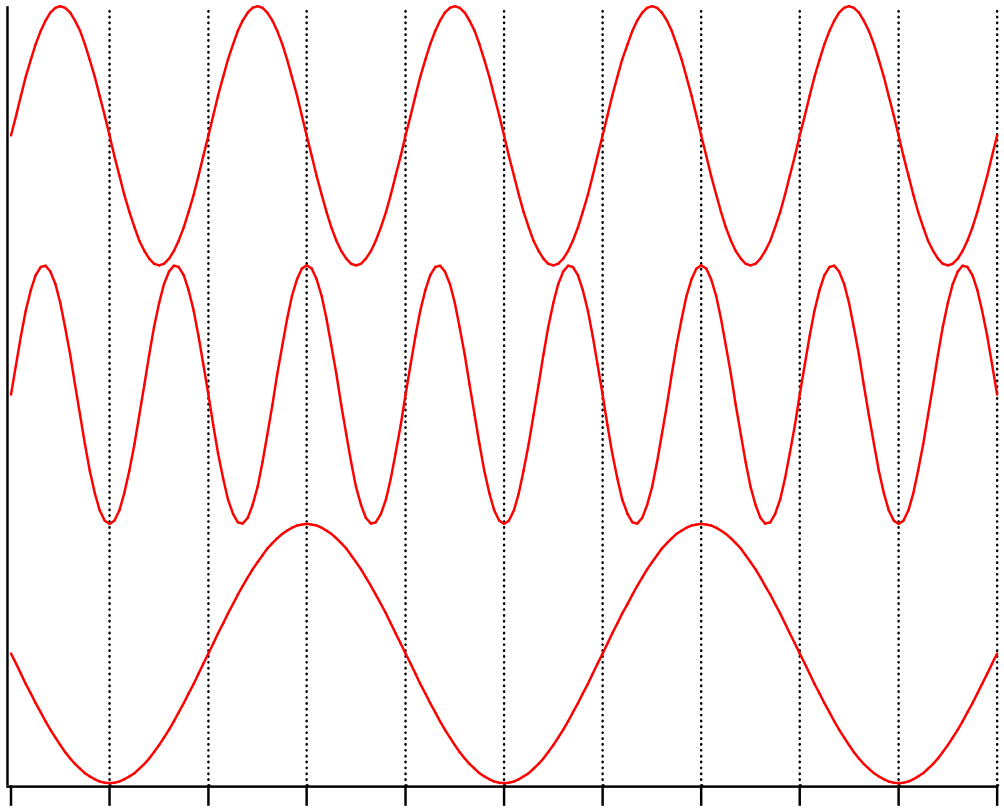

Figure 1.10. Multiple sine waves with identical amplitudes at the intervals shown. Frequencies from the top sine wave are ν, 2ν, 4ν, and 8ν. All pass through the same zero crossing as frequency ν.

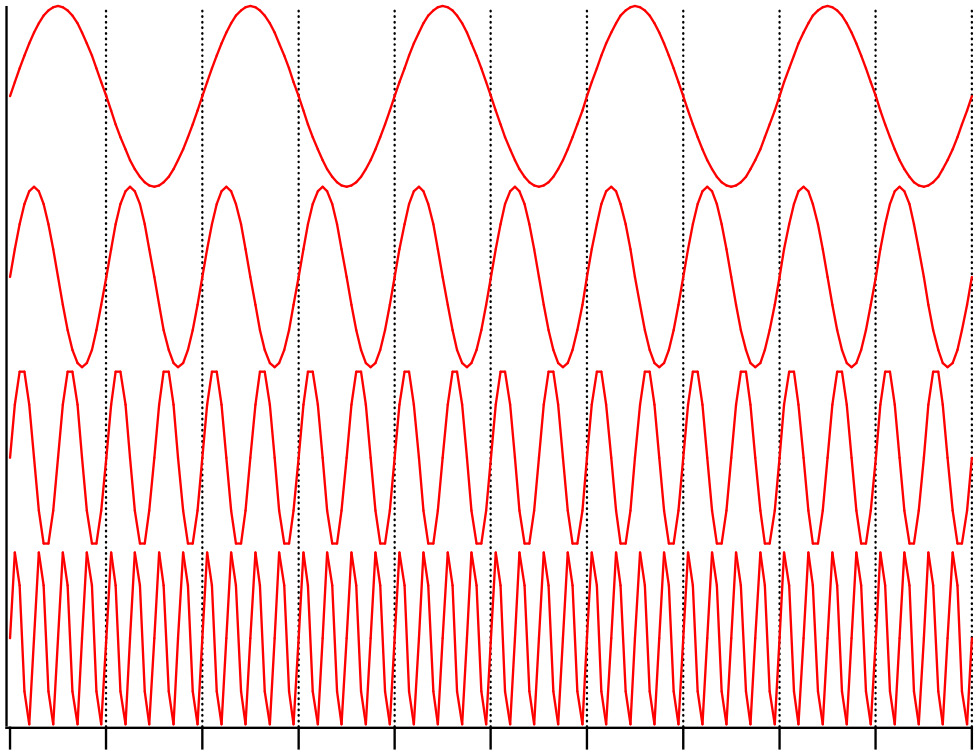

frequency. It is therefore very difficult to use a low frequency result without concern for folding of high frequency features. The false peaks generated by this effect can be removed by utilizing an optical filter at the cut off frequency of the spectrum. This removes those frequencies of light that can enter the detector and whose high frequency oscillations may fold in false lower frequency peaks.

The minimum and maximum frequency limits for the Fourier transformed spectrum are not only important when considering the signal reaching the detector but also the noise. The high frequency noise will act just like low frequency noise within the scanning frequency. This can be removed by limiting amplifier bandwidth. In addition, the optical filter must be of a range that truncates below the highest frequency range scanned. Otherwise, it might be possible to fold in a feature below the maximum frequency.

The mirror tracking system employed in our experiment relies on the sinusoidal oscillation of a He-Ne laser as the moving mirror translates. The wavelength of the laser, 632.816nm, corresponds to a maximum frequency of 15,822.8cm^{-1} with a zero crossing, or half wavelength, occurring every 1/31,645.6 cm. In most cases, the range of frequencies most important in our studies occurs in the mid-IR from 700-4000cm^{-1} thus decreasing the maximum frequency substantially. An experiment containing the entire interferogram sampled out to 15,822.8cm^{-1} would contain extraneous data and increase the time per experiment due to the high sampling rate. To reduce this amount of collected data we can reduce the sampling frequency by *m* times to lower the high frequency limit of the experiment.

$$\Delta\delta = m\Delta\delta_{\min} = m\frac{\lambda}{2} \tag{1.40}$$

with the corresponding folding frequency limit being

$$\bar{\nu}_f = \frac{15{,}822.8 cm^{-1}}{m} \tag{1.41}$$

A further reduction in the sampling rate can be obtained if the lower limit is larger than zero. This creates a minimum frequency in addition to the maximum frequency limit. We can then define the upper and lower folding limits as $\bar{\nu}_f^U$ and $\bar{\nu}_f^L$, respectively.

$$\bar{\nu}_f^U = \frac{n}{n-1}\bar{\nu}_f^L \tag{1.42}$$

The values of *n* here must be integer or natural fractions of the He-Ne frequency. This process is called undersampling and allows a particular range of frequencies to be studied without the need to collect extra data. Optical and electronic methods to control the signal outside of this range can be employed to limit folding and aliasing in the region.

The folding phenomenon can be of tremendous importance for frequencies above the maximum allowed He-Ne limited value. It is possible to record spectral information that is folded over that limit and into the recordable region of the spectra. Of course the spectra will be a mirror image of the actual result and the frequencies will be incorrect, both backwards and shifted, however with prior knowledge of the spectral lines in a particular region, it is possible to obtain results with higher frequency than the He-Ne emission.

There are certain error which can drastically affect the Fourier transformed spectra that are a result of poor sampling. One such error is a missing data point in the interferogram. A missed point near the centerburst can have the negative effect of broadening all the spectral lines in the resulting interferogram. This is due to the phase angle quickly shifting through the missed data point. A missed data point will have less

of an effect further from the centerburst because there is less information contained in those points, in addition to those points being closer in value. This is not the case for a signal that contains only a few monochromatic sources.

A more common sampling error occurs when a "bad" data point is found in the interferogram. Sources for this error may arise from sudden vibration, electronic noise, shock, or other non-continuous disruptions to the recording of data. The result of a "bad" data point is a sinusoidal oscillation in the baseline of the spectrum. This is analogous to the relationship between a delta function (monochromatic) source producing a sinusoidal interferogram. The intensity of this oscillation is dependent on the intensity of the point, as well as its proximity to the centerburst, while the frequency of the oscillation is only dependent on its location relative to the centerburst.

Another common source of error arises from the DC component of the interferogram. The interferogram has an ac and dc component seen in Eq. 1.7. The ac component is Fourier transformed to generate the resulting spectrum. The dc component, while not trivial, is simply removed from the oscillatory signal. After subtraction, if the dc component is not completely removed a low frequency spike will appear in the spectrum. This is usually not of any real concern because it is below the detector limit and out of most experimental limits. The larger concern involves a drifting baseline. This can be caused by temperature changes in the liquid nitrogen cooled detector, experimental drifting, poor mirror alignment, and other continuous sources of error. The result of a drifting baseline is the appearance of an increasing or decreasing dc offset in the interferogram causing a low frequency peak in the Fourier transformed spectrum.

The last source of sampling error involves less the interferometer, but more of the actual emission source utilized in the experiment. Fluctuations in the gas cell pressure, whether static or dynamic, laser power, and gas deposition limiting signal all change the amount of emission that is sent into the FTIR. The decrease in signal can have a dramatic effect on the overall S/R and final spectrum. There are several ways to combat these fluctuations based on normalizing the signal sent into the FTIR. The pressure can be monitored and slow variations over time can be corrected. The laser power can be monitored on a shot-by-shot basis and each data point corrected individually. But the best method of correction involves normalizing the entire emission signal with a static response.[6,7] In this method a small portion of the signal coming from the gas cell was directed onto a detector and used to normalize each interferogram point, correcting for laser fluctuation, gas depletion, deposition, and other signal depleting sources. We have designed a system where the emission collected is not removed from the front of the cell thus reducing the S/R, but rather from the rear of the gas cell. Enough signal has been collected to normalize the interferogram points. More on the setup and method will be explained later.

1.2.9 Interferogram smoothing and zero filling

The process of improving the S/R of the Fourier transformed spectra can be done after the experimental interferogram has been recorded. The first method involves utilizing a shorter interferogram which subsequently has less noise than an identical higher resolution interferogram. This is due to the limitation of the higher frequency

noise that can enter into an interferogram and the resulting spectra as random and oscillatory noise in the baseline.

The first way to improve the S/R is to zero out the last half of the interferogram. This improves the S/R by a factor of $2^{1/2}$. This is however a rather inefficient means to improve the spectra, because the same result could have been obtained in half the time by using the lower resolution spectra in the original experiment. A less desirable effect of this treatment is the possibility of creating side lobes due to this boxcar type of truncation.

A more beneficial and efficient way of improving the spectra is through the use of zero filling the interferogram. Since the resulting spectrum contains a real and imaginary portion as described previously, the original interferogram, with N points, generates a real and imaginary part with $1/2N$ points each. Since the method of improving the S/R depends not only on the length of the interferogram, but the intensity in its wings, adding zero's has the desired effect of smoothing out the data points between the calculated ones. Adding N zero's to the interferogram adds $1/2N$ to each of the components of the resulting spectra. The original $1/2N$ points are linearly independent to each other, while the remaining $1/2N$ that were added in as zero's to the interferogram represent extrapolations between the points.

The number of zeros, R, added to the interferogram depends on the value of m in the following relationship

$$R = \left(2^m - 1\right)N \tag{1.43}$$

where m is an integer greater than 1. The data points in the resulting spectra are understood as arising from $1/2N$ generated from the original interferogram and the rest

being extrapolations between the "real" points. In general $m>3$ is used producing more than 8 output points for every data point in the interferogram. The old limitation of data storage and processing no longer affect the processing of large zero filling values such as 32 or 64 output points (m=5 or 6).

1.2.10 Computing techniques

Computation of the interferogram to yield the resulting spectra can be performed in several ways. An example that will be used throughout this section involves a monochromatic source interferogram of substantial length, and digitized at equal intervals. This is of course the simplest type of interferogram but will provide an excellent description of the mathematical process to generate a spectrum from an interferogram.

An early way of computing an interferogram, called conventional, classical, or discrete Fourier transform, is typically slow and tedious for systems with more than a few emission wavelengths. The basic principle of this technique, applied to the above example, is based on interference with a reference cosine signal. Each point along the interferogram is multiplied by a reference cosine wave with unit amplitude and add the products. For waves with different frequencies, the value will be zero. For waves with the same frequency, the product will have a positive value. The intensity will be proportional to the original cosine wave interferogram. The resolution of the spectra relies greatly on the length of the interferogram. It takes a longer length interferogram for the product of other close by frequencies to reach zero. This can be realized when one starts from the original frequency and slowly changes the frequency value. The

overlap with the original frequency will slowly decrease. Longer interferograms will show this overlap decrease faster thus resulting in higher spectral resolution of the feature. One important requirement for this technique is accurate phase information. If the analyzing or reference cosine wave is 180^0 out of phase with the original frequency, each resulting product will take on a negative value.

The more efficient processing of an interferogram, known as the fast Fourier transform (FFT), is based on an algorithm developed by Cooley and Tukey.[8,9] We start out by utilizing the complex pair notation[10] for the Fourier transform pairs shown below in place of Eq. 1.26.

$$I(\delta) = \int_{-\infty}^{+\infty} B(\bar{\nu}) e^{2\pi i \bar{\nu}} d\bar{\nu} \tag{1.44}$$

$$B(\bar{\nu}) = \int_{-\infty}^{+\infty} I(\delta) e^{-2\pi i \bar{\nu}\delta} d\delta \tag{1.45}$$

In order to compute the FFT, it is required that the interferogram be N equally sampled data points which can produce a spectrum of N points which can be expressed as

$$B(r) = \sum_{k=0}^{N-1} I_0(k) e^{-2\pi i r k / N} \qquad r = 1,2,..., N-1 \tag{1.46}$$

Expressed in this manner, *B(r)* is the discrete Fourier transformed (DFT) spectra of wavenumbers *r*. We can substitute a parameter W defined as

$$W = e^{-2\pi i / N} \tag{1.47}$$

and substituting into Eq. 1.46.

$$B(r) = \sum_{k=0}^{N-1} I_0(k) W^{rk} \tag{1.48}$$

In this DFT, it can be seen that for each *B(r)* value there will be *N-1* additions of *N* multiplications. The FFT technique relies on Eq. 1.48 expressed as a matrix and subsequently factored to reduce the overall number of computations needed. The Cooley-Tukey algorithm is slightly simpler to execute when $N=2^{\alpha}$, where α is a positive integer. For a simple case where $\alpha=2$, Eq. 1.48 is

$$B(r)=\sum_{k=0}^{3} I_0(k)W^{rk} \qquad r=0,1,2,3 \tag{1.49}$$

which when expanded becomes

$$\begin{aligned} B(0) &= I_0(0)W^0 + I_0(1)W^0 + I_0(2)W^0 + I_0(3)W^0 \\ B(1) &= I_0(0)W^0 + I_0(1)W^1 + I_0(2)W^2 + I_0(3)W^3 \\ B(2) &= I_0(0)W^0 + I_0(1)W^2 + I_0(2)W^4 + I_0(3)W^6 \\ B(3) &= I_0(0)W^0 + I_0(1)W^3 + I_0(2)W^6 + I_0(3)W^9 \end{aligned} \tag{1.50}$$

or the matrix representation

$$\begin{vmatrix} B(0) \\ B(1) \\ B(2) \\ B(3) \end{vmatrix} = \begin{vmatrix} W^0 W^0 W^0 W^0 \\ W^0 W^1 W^2 W^3 \\ W^0 W^2 W^3 W^6 \\ W^0 W^3 W^6 W^9 \end{vmatrix} \begin{vmatrix} I_0(0) \\ I_0(1) \\ I_0(2) \\ I_0(3) \end{vmatrix} \tag{1.51}$$

or

$$\mathbf{B}(r)=\mathbf{W}^{rk}\mathbf{I_0}(k) \tag{1.52}$$

The above equation can be simplified by focusing on $\mathbf{W}^{rk}$ and utilizing some recursive relationships to eliminate several calculations. By utilizing the fact that $W^0=1$, and two cyclic relationships of W, we are able to compute the FFT using 1/2N complex multiplications and N(N-1) complex additions as opposed to N^2 complex multiplications and additions for the DFT making the FFT advantage:

$$\frac{N^2}{N\alpha/2} = \frac{2N}{\alpha} \tag{1.53}$$

1.2.11 Advantages and disadvantages of FT spectrometers

Before discussing the benefits of utilizing a FT spectrometer, we must first set up definitions for the signal to noise ratios based on the experimental setup. The signal level is constant in a FT spectrometer due to the fact that the entire signal is being sent to the detector at all times. This is quite different from a dispersive type instrument which selects certain wavelengths to pass as the spectrometer is scanned and thus the signal fluctuates with actual transitions in the system.

For each spectral element, $d\bar{\nu}$, the signal is dependent on the product of the intensity of the feature, $B(\bar{\nu})$ (W/cm^{-1}), and the total collection time at the detector, t.[11]

$$S_{FT} \propto B(\bar{\nu}) t d\bar{\nu} \tag{1.44}$$

When compared with a dispersive instrument, the overall signal must be divided by the total number of spectral elements, N. This is because the signal reaching the detector is only a fraction of the total signal as the dispersive instrument is scanned. The signal for a dispersive instrument is:

$$S_{DIS} \propto B(\bar{\nu}) \frac{t}{N} d\bar{\nu} \tag{1.45}$$

Comparing Eq. 1.44 with 1.45, it is already apparent that the signal in an FT instrument is already greater than that of a dispersive type instrument by a factor of N. We have not yet, however, considered the effect of noise.

Noise can be generated from several sources. There is noise that is inherent to the detector, such as thermal or electronic noise, and is directly proportional to the square

root of the amount of time the detector sees signal. Shot or photon noise is different from detector noise in that it is only related to the signal or photons hitting the detector. This noise is generated due to the fluctuations in the number of photons impacting the detector and is proportional to the square root of the number of photons. Lastly, noise may be generated from the experiment itself, defined as source or modulation noise. This noise is directly proportional to the signal strength.

One particularly interesting and sometimes problematic source of noise occurs in the analog-digital converter (ADC). The analog signal generated by the detector, and sent to the pre-amplifier and amplifier, is sent to an ADC to be processed digitally in a PC. Most static spectra are taken with a 16-bit ADC, with the interferogram signal having 2^{16} possible bit locations to occupy. Digitization in this case is generally not a problem even though the centerburst is significantly more intense than the rest of the spectra. For lower bit ADC, the voltage spacing between bits increases and can reduce or eliminate detector noise. At this point, quantization or digitization noise is generated in the spectrum and information is lost from the result.

We can thus define a parameter, the dynamic range, as being the ratio of the center burst intensity to the RMS value of the noise level. Common dynamic ranges can be 10^4:1 or higher for intense sources. If the dynamic range were 10^4:1, with a 16-bit ADC, six bits of the ADC would sample the noise level. With an 8-bit ADC and 256 possible bit values, no noise would be sampled and information would be lost from the resulting spectra, in addition to digitization noise appearing in the spectra. This concept is extremely important in the time-resolved step-scan method because the ADC temporal

bandwidth is inversely proportional to the data width. For fast detection, an 8-bit ADC must be used.

A common type of detector used are "photon-noise-limited" and just as implied, the level of noise can not be lower than the $\sqrt{signal}$. These detectors collect all the photons emitted from a source like a bucket collecting rain, and integrate over the entire collection, usually based on a fraction of the total collection time. From Eq. 1.45, we can determine the S/R from $d\bar{\nu}$ for a dispersive instrument.

$$(S/R)_{DIS} \propto \sqrt{B(\bar{\nu})\frac{t}{N}d\bar{\nu}} \tag{1.46}$$

While the S/R for the dispersive instrument is straightforward and calculated based on a direct relationship between the signal strength, and the noise, it is slightly more difficult to calculate for the FT instrument. The noise, being proportional to the square root of the total signal, needs to be expressed as a uniform distribution throughout the spectra. For each spectral element, $d\bar{\nu}$, the noise takes an average value of the total signal, $\overline{B}(\bar{\nu})$.

$$Noise = \sqrt{\overline{B}(\bar{\nu})Ntd\bar{\nu}} \tag{1.47}$$

The S/R for the FT spectrometer becomes,

$$(S/R)_{FT} \propto \frac{B(\bar{\nu})td\bar{\nu}}{\sqrt{\overline{B}(\bar{\nu})Ntd\bar{\nu}}} \tag{1.48}$$

And the gain, *G*, in S/R between the FT and dispersive instruments,

$$G_{FT/DIS} \propto \sqrt{\frac{B(\bar{\nu})}{\overline{B}(\bar{\nu})}} \tag{1.49}$$

The above equation shows an improvement to the S/R of the FT over the dispersive instrument known as multiplex or Fellgett's advantage.[12,13] In the above case where the

detector is photon-noise-limited, the gain is a function of the spectral emission at a particular frequency and the overall averaged signal reaching the detector. There are two possible experiment types, namely absorption and emission, which show markedly different behavior when considering Fellgett's advantage.

In an absorption experiment, most absorbing lines are weak and do not remove much intensity from the background emission source. The result is that the gain is limited to values ~1. For strongly absorbing lines, the signal reaching the detector can be much less than the overall average signal and the gain can be >1. Conversely, for emission based experiments, a strong emission band will show a large multiplex gain, while a weaker emission band will show less of a gain. The weak line will still show some advantage over the dispersive result as long as the total emission signal is not generated from a broad continuous source. If there are numerous strong emission bands, the resulting average intensity will increase, limiting the gain of weaker bands.

The multiplexing advantage arises because of the entire signal being sent to the detector at all times during the experiment as opposed to a grating instrument that selectively filters sections of frequencies to pass through to the detector. The drawback to the total signal collection is that the total noise is also sampled throughout the experiment. The multiplexing advantage has been shown to improve the S/R for FT over dispersive instruments based on the presumption that the detector noise is the limiting factor. In fact, detectors especially in the IR, have improved their noise reducing characteristics such that they are limited by random electron motion, called Johnson noise, in resistors in the pre-amplifier and amplifier schemes.

One of the biggest advantages a FT instrument has over a dispersive instrument is in its throughput, known as the Jacquinot advantage. A FT instrument does not require a grating, and thus does not require an entrance and exit slit to separate different frequencies sufficiently. Slits block a majority of the useable emission and therefore a several hundred times gain in signal is not uncommon. One drawback the FT instrument might have is the path length, in general, increases with the use of a Michelson interferometer over gratings. This sometimes required the use of a larger amount of optics and apertures to keep the beam parallel. However, a well collimated beam with low divergence can eliminate the need to apertures in the system.

The last advantage of a FT instrument is it's reproducibility without the need for extensive calibration. The Connes' accuracy, as it is known, is based on a calibrated laser source, a He-Ne source in most cases, to track the mirror position. There may be some inaccuracies generated from a diverging beam, but these can be controlled and calibrated for. Since the interferogram is self tracking, i.e. it does not need a reference point, the resulting spectrum does not need to be calibrated to produce an accurate result.

The sensitivity of the FT instrument may be questioned when compared with a laser based spectroscopy method. The laser based method has the major advantage of being 5-7 orders of magnitude more sensitive due to its high photon flux. Much fewer molecules are needed in a laser absorption event to produce similar results to an FTIR spectrum. Laser lines can also be extremely narrow and therefore produce much better spectral resolution than an FTIR. The main advantage the FTIR has over laser based methods is the scan range. The large scan range of the FTIR makes it a superb experimental tool in analyzing the complete spectral range of molecules.

1.3 Time-resolved Fourier transform spectroscopy

Conventional FT spectrometers provide little temporal information during the standard absorption or emission acquisition. This is due to a number of factors, specifically the time needed for mirror translation and the signal needing to be constant over the scan to produce an accurate interferogram. Even minor temporal changes during at a specific point in the interferogram, collected at a "bucket" type detector can generate errors in the resulting spectra.

In the conventional scanning instrument, the He-Ne laser can not only track mirror position, and the information that is extracted from it, but can be used as a timing device for internal and external components on the FT instrument. The He-Ne laser can trigger laser sources or ADC to digitize signal striking the detector. This timing sequence can therefore be used to generate a high temporal resolution instrument. There is one restriction based on the ADC board, that when sampling, the incident light onto the detector must be constant during the acquisition window. Between events, the signal is not collected and does not interfere with the acquisition, however when the ADC is acquiring in a given window, it must be constant throughout the entire interferogram collection.

Temporally resolved interferograms $I(\delta, t)$ can be collected in two different ways, continuous-scan[14] (CS) and step-scan[15-17] (SS). The main difference between the two methods is the manner in which the movable mirror is adjusted during the signal acquisition process. These methods have been applied to numerous studies from IR emission from collisionally induced vibrational energy transfer,[18,19] photo-induced bimolecular reactions[20,21] to surface studies involving adsorption, desorption, diffusion,

and structure ordering.[22] Biologically relevant processes such as photoreactivity of bacteriorhodopsin,[23] and structural changes in proteins such as hemoglobin[24] and in ordered condensed phase systems such as zeolites[25] and polymers.[26]

1.3.1 Continuous-scan (CS) technique

With the movable mirror position being tracked by the He-Ne laser, time-resolved data can be extracted from a conventional CS technique in two ways. The two acquisition types are based on the bandwidth of emission/absorption and the repetition or lag rate for the system.

For a process that is slow when compared to the scan rate of the interferometer, the temporal information can be extracted by running fast continuous scans while the signal is relatively constant. The full time profile can be extracted by running scans in subsequent progression as seen in Figure 1.11. Scanning bandwidths on current FTIR can run upwards of 300 kHz and faster depending on the spectral resolution and high frequency limit needed. This method is useful for condensed phase reactions or pure IR emission from collisionless gas particles.

Most time-dependent signals decay much faster than the mirror can move. It is thus necessary to generate a stable and constant signal at each retardation point the interferogram is recorded. A method by Sloan and co-workers[27] was developed to a CS/single time delay measurement. Timing for this type of scan begins with the He-Ne laser tracking the movable mirror position. At the zero-crossing of the laser interferogram, the system is initiated. At a certain time *t*, after the zero-crossing, a certain signal is recorded as a point on the interferogram. With a signal that decays faster

Figure 1.11. The AC and DC components from a rapid scan experiment. The AC component has to be several orders of magnitude faster than the emission signal decay to generate a well behaved temporal response.

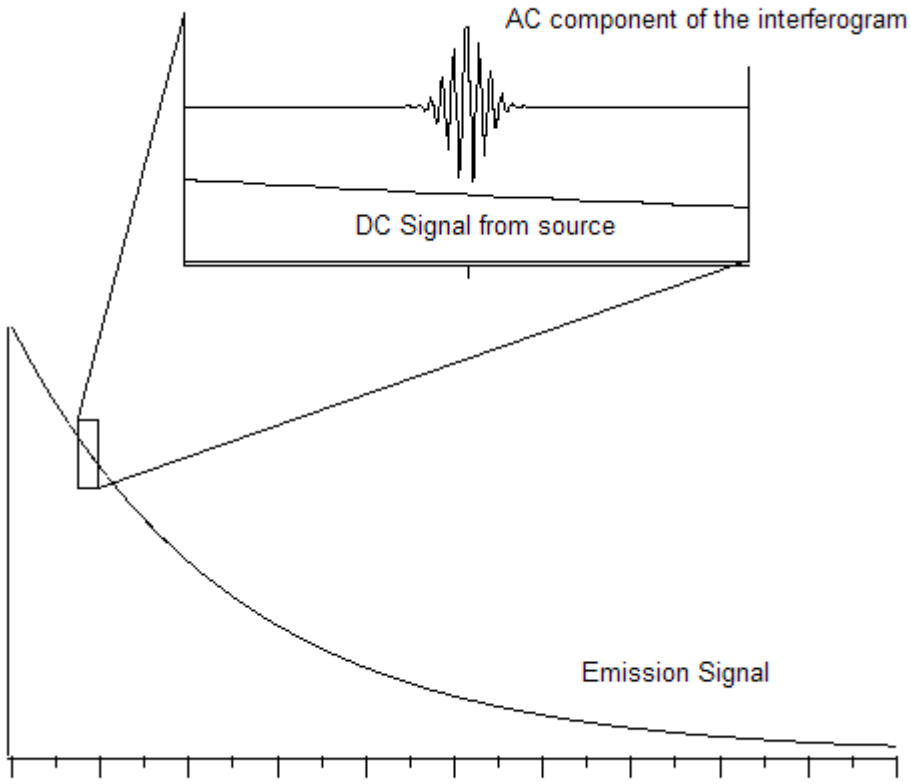

than the mirror scan (He-Ne zero-crossings), an interferogram can be constructed utilizing the same time delay for each interferogram point. The time delay can then be changed to generate a complete temporal response for the system.

Systems initiated by a pulsed laser source are ideal for this method of scanning. A schematic for the temporal synchronization of the He-Ne laser, laser pulse, and emission are shown in Figure 1.12. As the movable mirror displaces, the laser fringe zero-crossing starts a delay generator. At some time later, ΔT_1, the laser is fired, and after another delay, ΔT_2, the interferogram is sampled. This same time delay is used to provide a constant emission source to generate an equally sampled interferogram. The delay time, T_2- T_1, can be changed to observe the entire time decay of the system.

The major disadvantage of this technique is that only one interferogram point is sampled during each laser pulse. Most of the available information is not sampled, thus this method is not as efficient as one that is constantly acquiring signal. The second difficulty in this method arises from the movable mirror speed. At each zero-crossing of a He-Ne fringe, the system needs to generate emission. If not, the resulting interferogram will be incomplete. The oscillating fringe frequency is given by,

$$f = \frac{2\upsilon}{\lambda} \tag{1.50}$$

where f is the zero-crossing frequency (Hz), υ is the mirror speed (cm/s), and λ is the He-Ne wavelength. With a He-Ne laser at 632.8nm, and a minimum mirror speed of 3.16×10^{-5}cm/s, the frequency becomes 100Hz. The laser pulse rate must match the frequency of zero-crossings, otherwise the interferogram will miss data points. This can be avoided by using some interleaved techniques[28] which remove those missing data points. If the decay of the signal is longer than the scan rate frequency, once again, an

Figure 1.12. Temporal step-scan synchronization. Time delays are described in the text.

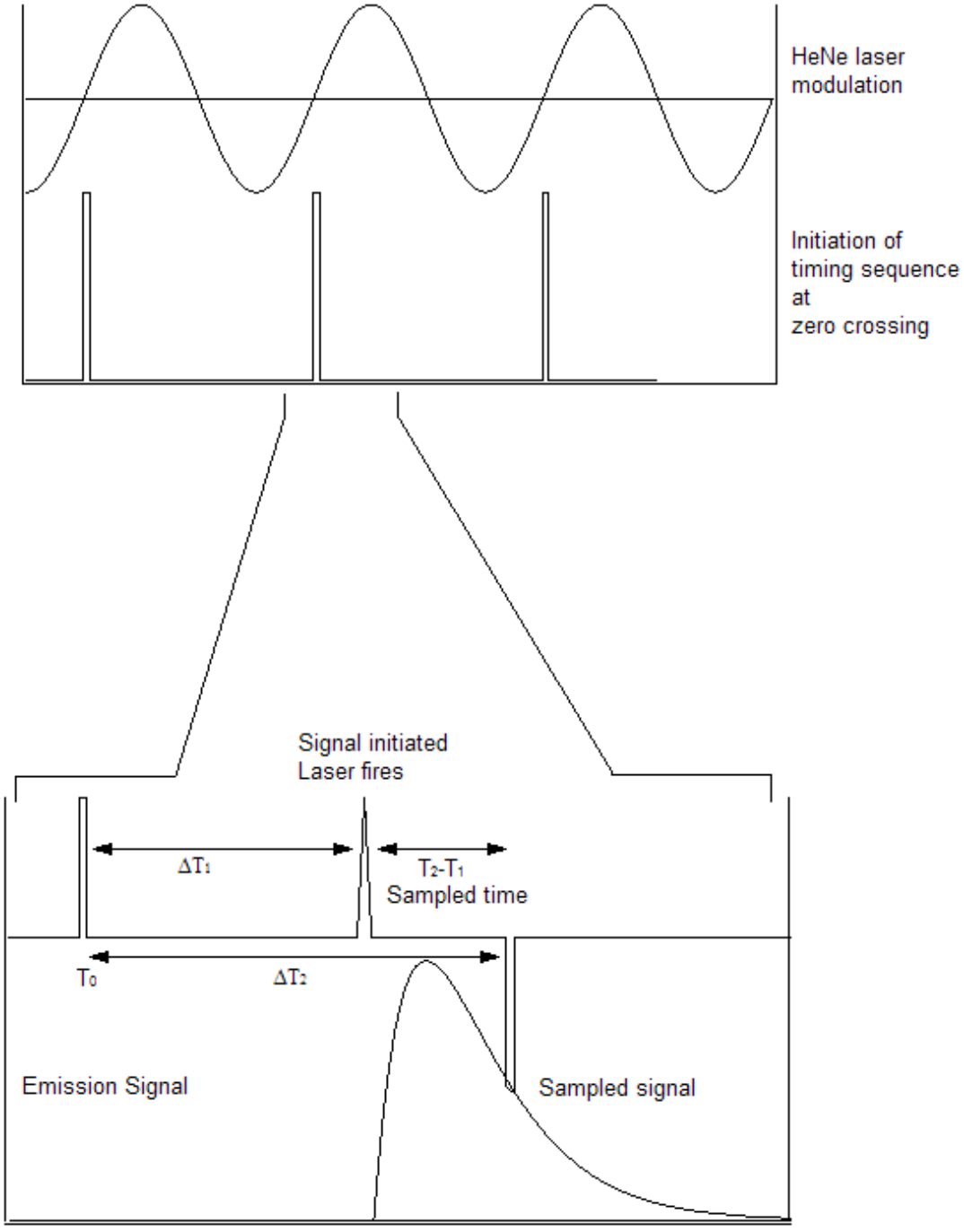

interleaving technique can be used to eliminate those interferogram points where there is missing data and still construct a complete interferogram.

1.3.2 Step-scan technique

The continuous scan technique had the major disadvantage of poor efficiency, as only one time point is taken at each retardation interval. A technique that utilizes the internal He-Ne laser to start and stop the retardation of the movable mirror has been used by many groups.[29-33] The step-scan technique utilizes a mirror that can translate and stop at specific retardations and collect the entire temporal profile. In addition to the sampling of the transient signal, the technique is able to average a significant number of emission events (i.e. laser shots) at each position, before the mirror moves to the next position.

The basic data recording scheme is shown in Figure 1.13. At each mirror position, the movable mirror is stopped and the transient signal is recorded at i^{th} intervals. The array, which contains the time, t, and position, δ, information of the interferogram is recorded at the position δ_j as, $I(\delta_j,t_1)$, $I(\delta_j,t_2)$, $I(\delta_j,t_3)$,… $I(\delta_j,t_m)$. The resulting spectra at time t_k, from the interferometric array, $I(\delta_1,t_k)$, $I(\delta_2,t_k)$, $I(\delta_3,t_k)$,… $I(\delta_p,t_k)$, is $I(\nu_1,t_k)$, $I(\nu_2,t_k)$, $I(\nu_3,t_k)$,… $I(\nu_p,t_k)$. The time component of the interferogram array is uncoupled to the scan or recording parameters, unlike the continuous scan method. The transient signal is therefore unrestricted in its lifetime, as the mirror position can remain stationary as long as the He-Ne zero crossing is held. The fast timescale limit on the signal is restrained by the detector response time, pre-amplifier and amplifier bandwidths, the analog to digital converter, and the initiating pulse. The timing sequence of the step-scan

Figure 1.13. The step-scan mirror delay and digitization rate at each mirror step. The time is on the horizontal axis, the intensity is on the vertical axis, and the mirror retardation is on the z-axis.

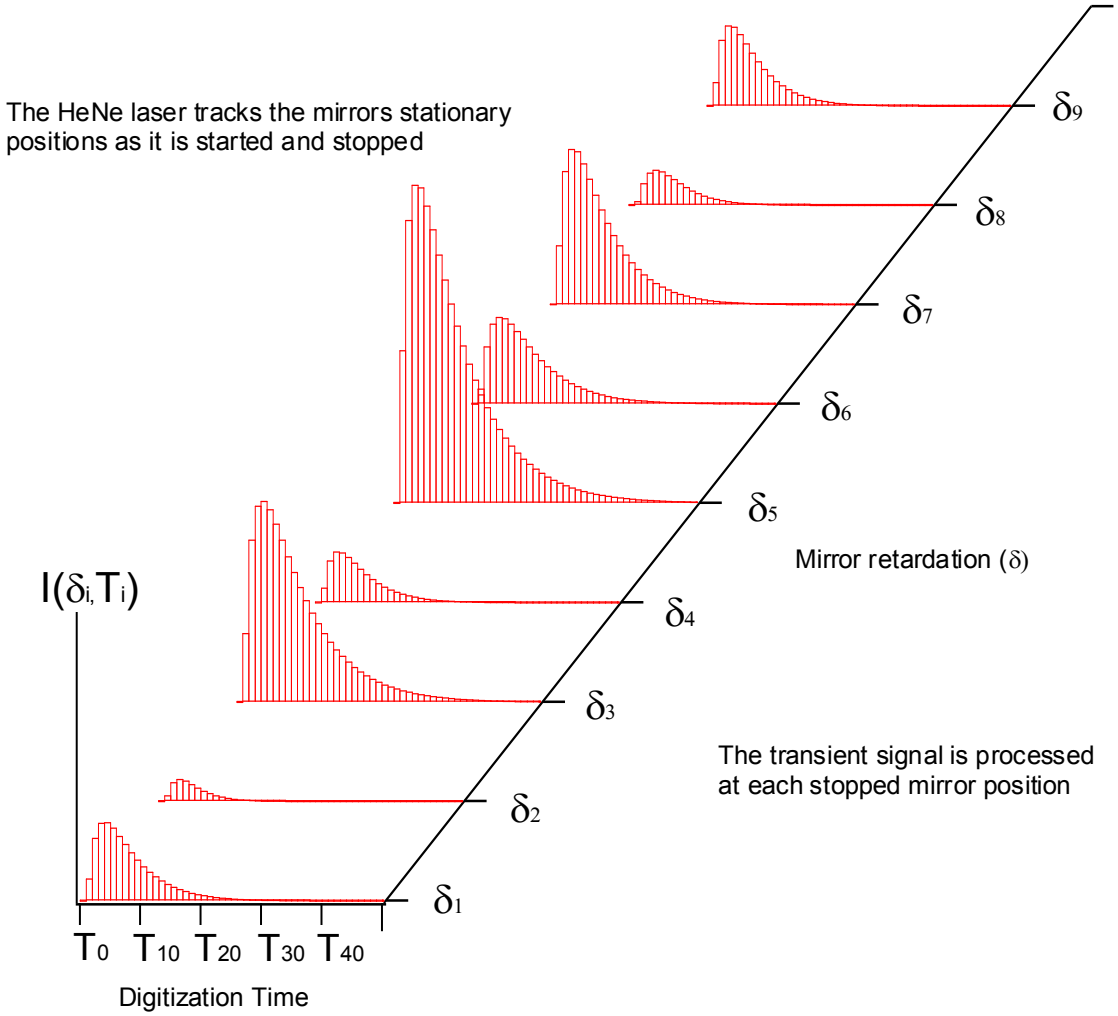

technique is similar to that of the continuous-scan technique, except for the He-Ne laser oscillation becoming a pulse shape that is triggered by the internal computer to move quickly between transient signal events.

A major advantage of the step-scan technique, besides its obvious temporal and efficiency improvements over the continuous-scan method, is the signal averaging that is employed. At each mirror position, the transient signal can be recorded as many times as the computer system's resources can allow. This allows spurious peaks and artifacts to be averaged out of the final interferogram. In addition, a slowly changing signal over the course of the experiment, which could be due to pressure drops in the reaction chamber, laser power fluctuations, or contamination of optics, will not produce or remove features in the final spectra. These errors will only reduce the S/R in the resulting spectra.

The experimental setup used is shown in Figure 1.14. Here, an excimer laser (Lambda-Physik, LPX200), operating at 193nm or 248nm, is used as an excitation source as well as a trigger for the movable mirror and data recording. A Michelson interferometer inside a Bruker IFS/66 FTIR is used in step-scan as well as continuous scan modes. An array of detectors ranging from the far-IR to the UV are employed (200-40,000cm^{-1}) with typically fast response time (<500ns). The spectral range is further limited to the wavelength of the He-Ne laser (632.8nm, 15,798cm^{-1}) since this is the tracking device for the movable mirror, however this can be doubled by a simple programming change to track every half wavelength zero-crossing, instead of every full wavelength zero-crossing. The non-apodized spectral resolution is based on the longest retardation length of the Michelson interferometer, which is 10cm, corresponding to a resolution of 0.1cm^{-1}.

Figure 1.14. The time-resolved step-scan experimental setup.

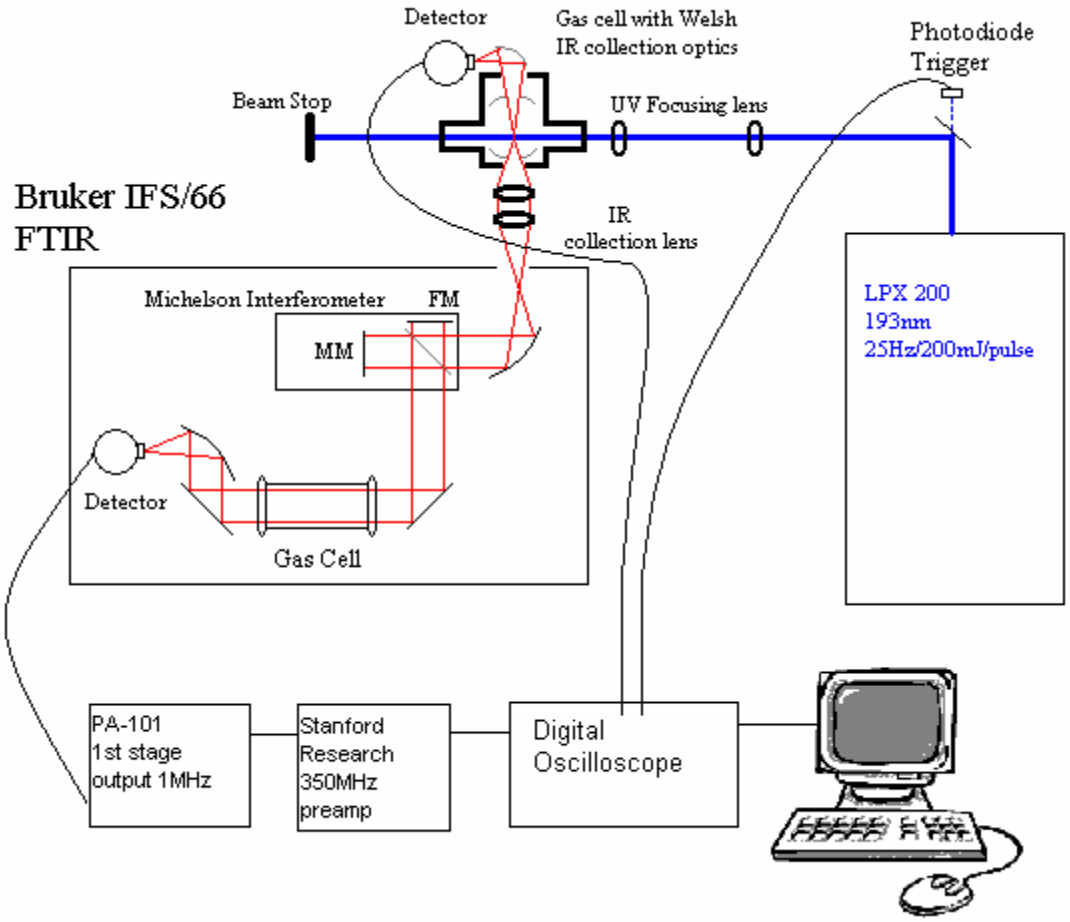

Initiation of the step-scan method first involved the movable mirror displacing to its first retardation distance. The mirror stepping is typically accomplished in 10-30ms depending on the step size, with a few extra ms for the mirror to stabilize. Once the mirror has stabilized, the system awaits a signal to start recording, usually produced externally by a laser pulse. A set number of coadditions are done at the first retardation and then the mirror is moved and the process repeated.

1.3.3 Utilizing a transient digitizer for nanosecond time-resolved spectroscopy

The temporal resolution of the step-scan method is typically restricted by either the detector or ADC bandwidth. In the case of the detector limited response, the observed signal will be a convolution of the actual signal response and the detector rise (or decay) time. For fast detectors, such as PMTs and fast photodiodes, with sub-nanosecond time constants, the digitizer becomes the limiting component. These fast detectors are crucial in examining nanosecond resolved events such as collisional relaxation at high pressures and electronic transitions.

The IFS/66 has an internal 16-bit ADC board capable of 5μs resolution. A faster transient digitizer, an 8-bit/200MHz dual channel (SpectrumGMBH) is employed as an ISA plug-in board in a computer running Bruker's OPUS^{TM} v4.2 software, which controls the acquisition and operation of the optical bench and post processing procedures. The 8-bit PAD82a can digitize signal faster than most IR detectors, however for PMTs and faster photodiodes another method of digitization must be employed. A Digital Storage Oscilloscope[34] (DSO) with 1GHz (and faster) bandwidth, capable of sampling 4GSamples/sec with a stable trigger can be utilized to record the data and, with

the aid of another interface device, transfer the time resolved data to the controlling PC with faster resolution.

In order to sample the data using the Opus program, a transfer module, TM1000 FTIR Transfer Module (McLaren Research), must be used to retrieve the fast data sampled by the DSO and send the data to the computer. The TM1000 transfers data from the DSO via a GPIB connection and to the computer via a parallel connection. The data also receives the signal and trigger data through an analog output and external time output, respectively. The TM1000 operates as a 16-bit ADC. The transfer module can act as a normalization device as well accepting signal from a PMT or IR detector which measure laser power or IR signal. Programmable timers are also available to control other electronics such as gated integrators, laser sources, and delay generators. The hardware is controlled by CODA (COncurrent Data Acquisition) software installed on the PC also running OPUS. CODA intercepts the signal being received through one of its transient digitizers and sends the data retrieved from the DSO instead. The signal pathway can be seen in Figure 1.14.

The external transient digitizer is typically used when the J10D (Judson Technologies, InSb detector element, τ_r=5ns, 1800-8000cm^{-1}) is used. It may also be used to acquire signal from a PMT or other fast detector. A Tektronix TDS 380 DSO is used to collect and average the signal from the detector. The maximum sampling rate of the DSO is 2GSamples/sec, with a bandwidth of 400MHz, at a maximum length of 1000 points. The DSO can operate two 8-bit channels simultaneously. The specific DSO parameters and loaded into the CODA software prior to experimental collection so that CODA may control the DSO while the experiment is running. The CODA software will

control the data acquisition at each new mirror position, send the data through the TM1000, and have OPUS acquire the data.

The OPUS software is "tricked" into running a typical step-scan experiment using the 16-bit, 200kHz, internal ADC board. The factors influencing the interferometer including the resolution and spectral range are inputted into the OPUS software, but must also be inputted to the CODA software, as total number of interferogram points, for controlling the data collection. The number of coadditions is falsely set to one, and the number of time slices is entered as the true total number. The FTIR's sampling clock is typically run at fixed frequency corresponding to fixed time resolution. This is changed to External to allow the internal ADC board to acquire signal determined by the IFS/66 External Time Base (ETB) input.

The FTIR, in step-scan mode, is instructed to proceed to the first mirror position by OPUS and awaits the start pulse from the ETB input. CODA begins to acquire data. The number of coadditions input into CODA are acquired, sent to the TM1000 transfer module, the PC running CODA and OPUS, and then sent to OPUS. An external 16-bit ADC board digitizes the data with a slower time scale. This new slowed signal is then sent back to the IFS/66 internal ADC board input with a time scale set by the ETB input. The data acquisition rate to the internal ADC does not exceed the time resolution of the board (5ms), however the signal is being acquired and digitized much faster on the TDS380 with sub-nanosecond resolution. After the entered number of coadditions has been completed, OPUS receives a signal and the movable mirror steps to the next position. A mirror stabilization time may be initiated, otherwise CODA begins a new signal acquisition.

References:

(1) Griffiths, P. R.; deHaseth, J. A. *Fourier Transform Infrared Spectroscopy*; John Wiley & sons: New York, 1986; Vol. 83.

(2) Filler, A. H. *Journal of the Optical Society of America* **1964**, *54*, 762.

(3) Norton, R. H.; Beer, R. *Journal of the Optical Society of America* **1976**, *66*, 259.

(4) Norton, R. H.; Beer, R. *Journal of the Optical Society of America* **1977**, *67*, 419.

(5) Mertz, L. *Infrared Physics* **1967**, *7*, 17.

(6) Lindner, J.; Lundberg, J. K.; Williams, R. M.; Leone, S. R. *Rev. Sci. Instrum.* **1995**, *66*, 2812.

(7) Johnson, T. J.; Zachmann, G. *Introduction to Step-Scan FTIR*; Bruker Optics: Billerica.

(8) Cooley, J. W.; Tukey, J. W. *Math. Comput.* **1965**, *19*, 297.

(9) Lam, R. B.; Wiebolt, R. C.; Isenhour, T. L. *Anal. Chem.* **1981**, *53*, 889A.

(10) Brigham, E. O. *The Fast Fourier Transform*; Prentice Hall: Englewood Cliffs, N.J., 1974.

(11) Nordstrom, R. J. *In Fourier, Hadamard, and Hilbert Transforms in Chemistry*; Plenum Press: New York, 1982.

(12) Hirschfeld, T. *Appl. Spec.* **1976**, *30*, 68.

(13) Luc, P.; Gerstenkorn, S. *Appl. Opt.* **1978**, *17*, 1327.

(14) Caledonia, G. E.; Green, B. D.; Murphy, R. E. *Journal of Chemical Physics* **1979**, *71*, 4369.

(15) Aker, P. M.; Sloan, J. J. *Journal of Chemical Physics* **1986**, *85*, 1412.

(16) Fletcher, T. R.; Leone, S. R. *Journal of Chemical Physics* **1988**, *88*, 4720.

(17) Hartland, G. V.; Xie, W.; Dai, H.-L.; Simon, A.; Anderson, M. J. *Rev. Sci. Instrum.* **1992**, *63*, 3261.

(18) Hartland, G. V.; Qin, D.; Dai, H.-L. *Journal of Chemical Physics* **1994**, *101*, 1.

(19) Hartland, G. V.; Qin, D.; Dai, H.-L. *Journal of Chemical Physics* **1997**, *107*, 2890.

(20) Neil, W. S.; J.-Y. Li; Sloan, J. J.; Kong, F.-A. *Journal of Chemical Physics* **1997**, *107*, 4537.

(21) Lindner, J.; Loomis, R. A.; Klaassen, J. J.; Leone, S. R. *Journal of Chemical Physics* **1998**, *108*, 6499.

(22) Kasza, R. V.; Shapter, J. G.; Griffiths, K.; Norton, P. R.; Sloan, J. J. *Surface Science* **1994**, *321*, L239.

(23) Rodig, C.; Chizhov, I.; Weidlich, O.; Siebert, F. *Biophysics Journal* **1999**, *76*, 2687.

(24) Hu, X.; Frei, H.; Spiro, T. G. *Biochem.* **1996**, *35*, 13001.

(25) Rosencwaig, A.; Gersho, A. *J. Appl. Phys.* **1976**, *47*, 64.

(26) Dittmar, R. M.; Chao, J. L.; Palmer, R. A. *Appl. Spectroscopy* **1991**, *45*, 1104.

(27) *Time-Resolved Spectroscopy*; Sloan, J. J.; Kruus, E. J., Eds., 1990.

(28) Garrison, A. A.; Crocombe, R. T.; Mamantor, G.; deHaseth, J. A. *Appl. Spec.* **1980**, *34*, 399.

(29) Hancock, G.; Heard, D. E. *Chem. Phys. Lett.* **1989**, *158*, 167.

(30) Palmer, R. A.; Manning, C. J.; Rzepiela, J. A.; Widder, J. M.; Chou, J. L. *Appl. Spec.* **1989**, *43*, 193.

(31) Biggs, P.; Hancock, G.; Heard, D.; Wayne, R. P. *Meas. Sci. and Tech.* **1990**, *1*, 630.

(32) Uhmann, W.; Becker, A.; Taran, C.; Siebert, F. *Appl. Spec.* **1991**, *45*, 390.

(33) Hartland, G. V.; Xie, W.; Dai, H.-L. *Rev. Sci. Instrum.* **1992**, *63*, 3261.

(34) Shepherd, R. A.; Doyle, T. J.; Graham, W. R. *J. Chem. Phys.* **1988**, *89*, 2738.

Chapter 2

2.1 Two-dimensional cross spectral correlation

2.1.1 Introduction

The method of correlating two different spectra to reveal common characteristics in either frequency or temporal space is quite common and has been applied to numerous systems.[1] In the frequency domain, the process involves looking for frequency overlap, while in the temporal domain, lifetimes are the typical correlation feature. The 2D correlation method[2] allows for the simplification of complex spectra with features belonging to different sources evolving with different temporal responses.

Two dimensional correlation spectroscopy has been used extensively in many different disciplines including polymer chemistry,[3] protein folding,[4] interface chemistry,[5] and many others. In the most general approach, the system under study undergoes some perturbation.[6] The perturbation may arise from optical, thermal, mechanical, or other processes which affect the equilibrium of the system. The perturbation typically affects the temporal or frequency response of the system. The system is then subject to monitoring the temporal and/or energetic response.

The change in the system is monitored and Fourier transformed. When two unique systems, each energy (frequency) has a Fourier component generated. The product integral of the Fourier components are analyzed over all recorded frequencies resulting in a complex expression containing the synchronous (positive) and

asynchronous (negative) spectral overlap maps. These plots contain information on the correlation between spectral features, as well as anticorrelation between features. In addition, the diagonal from the synchronous map can be extracted and analyzed with a greatly enhanced S/R when compared with simple averaging.[7]

2.1.2 Fourier components

If we consider a dynamic spectrum with both frequency and time components such that :

$$\tilde{y}(\nu,t)=\begin{cases} y(\nu,t)-\bar{y}(\nu) & for\ T_{\min}\le t\le T_{\max} \\ 0 & otherwise \end{cases} \tag{2.1}$$

where the perturbation induced intensity $\tilde{y}(\nu,t)$, with frequency component, ν, and dynamic and average static spectra, $y(\nu,t)$ and $\bar{y}(\nu)$, respectively, is observed within a time frame. For emission studies, we do not normally observe a background or static spectra thus simplifying Eq. 2.1 by restricting $\bar{y}(\nu)=0$.

The time restriction noted in Eq. 2.1 usually encompasses all of the spectral signal, however there are specific circumstances where limiting the evolution in the spectral signal will be important, e.g. close lying features with very different decay components. This will be discussed in Section 2.1.4.

For two independent sets of dynamic spectra $\tilde{y}(\nu_X,t)$ and $\tilde{y}(\nu_Y,t)$, from system X and Y, the correlation integrals $\tilde{Y}_X(\omega)$ and $\tilde{Y}_Y(\omega)$ are given as the Fourier conjugate in (1) and (2), respectively.

$$\tilde{Y}_X(\omega)=\int_{-\infty}^{\infty}\tilde{y}(\nu_X,t)e^{-i\omega t}dt \tag{2.2}$$

and

$$\widetilde{Y}_Y(\omega) = \int_{-\infty}^{\infty} \widetilde{y}(\nu_Y, t) e^{-i\omega t} dt \tag{2.3}$$

Eqs. 2.2 and 2.3 can originate from the same set of dynamic spectra (self-correlation) or from different spectra (cross-correlation). These two methods will be discussed simultaneously here and independently in section 2.1.5.

The complete two dimensional correlation between system X and Y is shown below. The correlation is defined as the matrix representation of the integral product of the two Fourier components.

$$X(\nu_X, \nu_Y) = \frac{1}{\pi T} \int_0^{\infty} \widetilde{Y}_X(\omega) \bullet \widetilde{Y}_Y^*(\omega) d\omega$$

$$+ \frac{1}{\pi T} \int_0^{\infty} \widetilde{Y}_Y(\omega) \bullet \widetilde{Y}_X^*(\omega) d\omega \tag{2.4}$$

The matrix $X(\nu_X, \nu_Y)$ is a complex number containing both a real and imaginary part, which can be expressed as,

$$X(\nu_X, \nu_Y) = \Phi(\nu_x, \nu_y) + i\Psi(\nu_x, \nu_y) \tag{2.5}$$

The real and imaginary components of the correlation can be determined independently as shown in Eq. 2.6 and Eq. 2.7, respectively yielding the symmetric synchronous and anti-symmetric asynchronous maps.

$$\Phi(\nu_X, \nu_Y) = \frac{1}{\pi T} \int_0^{\infty} (\widetilde{Y}_X^{\mathrm{Re}} \widetilde{Y}_Y^{\mathrm{Re}^*} + \widetilde{Y}_X^{\mathrm{Im}} \widetilde{Y}_Y^{\mathrm{Im}^*}) d\omega$$

$$+ \frac{1}{\pi T} \int_0^{\infty} (\widetilde{Y}_Y^{\mathrm{Re}} \widetilde{Y}_X^{\mathrm{Re}^*} + \widetilde{Y}_Y^{\mathrm{Im}} \widetilde{Y}_X^{\mathrm{Im}^*}) d\omega \tag{2.6}$$

and

$$i\Psi(\nu_X,\nu_Y)=\frac{1}{\pi T}\int_0^{\infty}(\widetilde{Y}_X^{\mathrm{Im}}\widetilde{Y}_Y^{\mathrm{Re}^*}+\widetilde{Y}_X^{\mathrm{Re}}\widetilde{Y}_Y^{\mathrm{Im}^*})d\omega$$

$$+\frac{1}{\pi T}\int_0^{\infty}(\widetilde{Y}_Y^{\mathrm{Im}}\widetilde{Y}_X^{\mathrm{Re}^*}+\widetilde{Y}_Y^{\mathrm{Re}}\widetilde{Y}_X^{\mathrm{Im}^*})d\omega \qquad (2.7)$$

where $\widetilde{Y}_X^{\mathrm{Re}}$ is the cosine Fourier transform of system X, and $\widetilde{Y}_X^{\mathrm{Im}}$, the sine transform of system X. Eqs. 2.6 and 2.7 represent the synchronous and asynchronous correlations of the 2DCSC.[1,8] These two results will be discussed separately in the next section.

Further information can be extracted from these two results, namely the diagonal expressions. The diagonal expression from the synchronous map contains all the common features from both dynamic spectra, while features with accidental overlap will not show up in the diagonal expression. Rather, they will have off-diagonal features. The diagonal of the asynchronous map is null. This is due to the inclusion of the imaginary number, *i*, in Eq. 2.7, causing a discontinuity at $\nu_X=\nu_Y$.

2.1.3 Synchronous and asynchronous maps

The synchronous and asynchronous maps from Eqs. 2.6 and 2.7, respectively, can be obtained independently from the previously derived method. Both maps yield information on the perturbation induced change in the dynamic spectra and both are independently useful for determining spectral features and their correlations.

The synchronous map is useful for identifying commonly evolving features in two spectra. The most important part of the synchronous map is the diagonal expression. The diagonal is always symmetric in the synchronous map, $\nu_X=\nu_Y$, for two systems X and Y. It is representative of the degree of perturbation induced on the spectral components.

For example, if component ν_1 of system X and ν_2 of system Y reside on the same frequency component, and have a similar decay constant, the resulting correlation will be large and show up on the extracted synchronous diagonal. If, however, the two components show a different decay component, even though they may lie at the same frequency component, they will show a negative synchronous correlation with reduced intensity at the diagonal.

The intensity of the diagonal extracted from the synchronous map is approximately proportional to the product of the two intensity contributions from the dynamic spectra. Thus, the square root of the diagonal is the proper method to compare the diagonal to the original spectra.

The off-diagonal components of the synchronous map also yield some information on the dynamic response of the two systems. The off-diagonal components show correlations between two different frequency components with similar temporal constants.

As an example we can consider, emission from system X, Figure 2.1.A and from system Y, Figure 2.1.B. There are two commonly evolving features residing at different frequency components, ν_1=1000 cm^{-1} and ν_2 =2000 cm^{-1}, but evolving with the same decay component and a third band unassociated with the previous two bands. The third band in each system has a unique frequency and decay component. The signal can be described by an exponentially decaying Gaussian function with constant center frequency and width.

Figure 2.1. Two independently generated synthetic spectra, A and B, containing two emission bands with common decay components and one emission band that does not correlate with time or frequency to the other components. Noise is generated through a random noise generator to produce an initial S/R that is the same in both A and B.

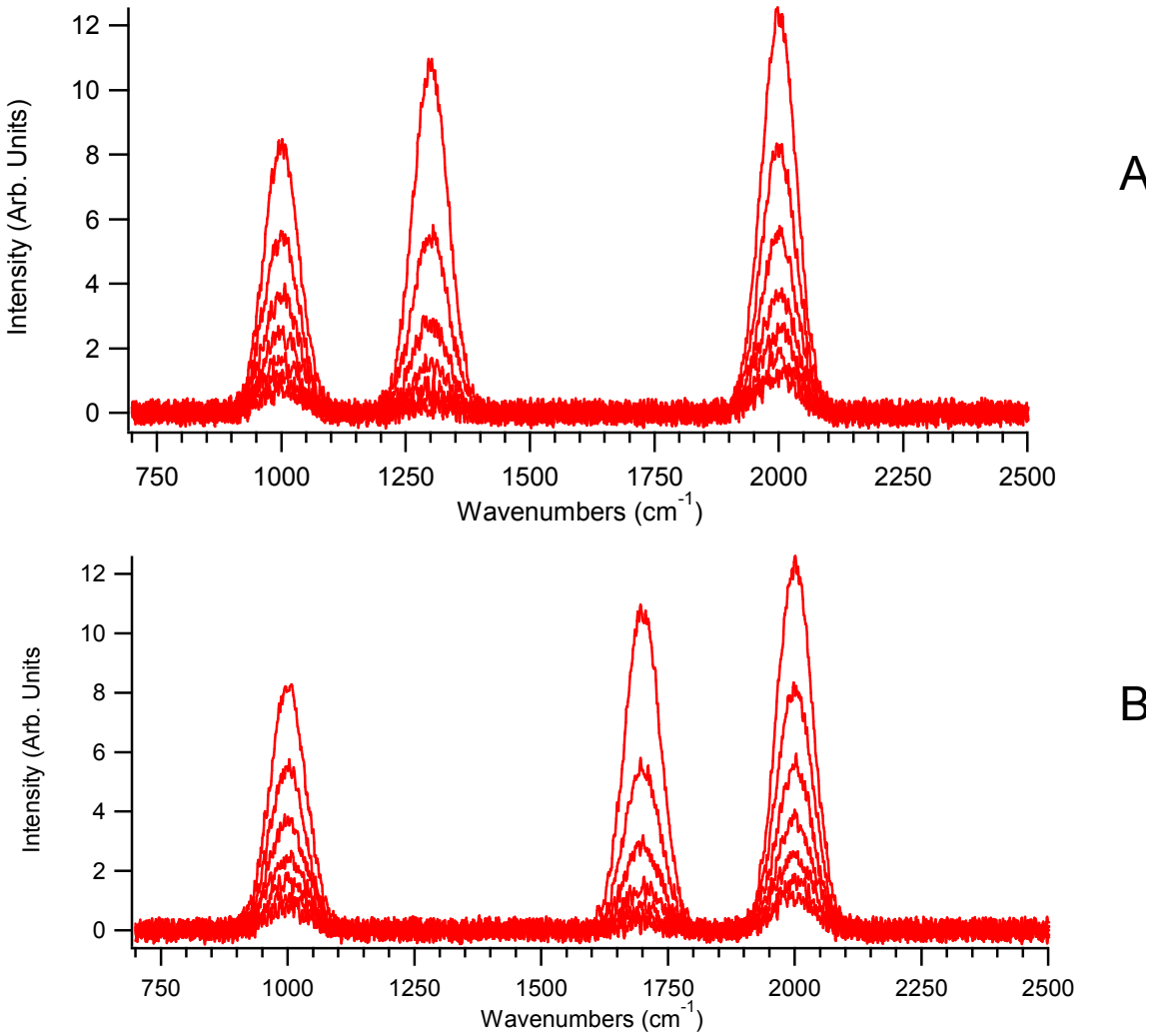

$$y(\nu_X, t) = \sum_i A_X^i e^{-k_X^i t} \exp\left(-\left(\frac{\nu_X - \nu_X^i}{\sigma_X^i} \right)^2 \right) + \tilde{N}(\nu_X) \tag{2.8}$$

where k_X^i is the first order exponential decay constant, A_X^i the intensity factors, ν_X^i, the center frequencies, and σ_X^i the Gaussian widths of the i^{th} band. $\tilde{N}(\nu_X)$ is the noise generation function. The noise level is kept constant through the time evolution of our signal. This is similar to the observed experimental behavior; however there is a slight S/R dependence on the overall signal. For simplicity, we employ a constant noise component throughout this section. An analogous expression exists for $y(\nu_Y, t)$.

Following the above procedure for producing the Fourier components and the product integrals, we can generate the synchronous and asynchronous maps. The synchronous map, as described above, correlates the positive overlap in Fourier space between the two dynamic spectra. This overlap can be observed in both frequency components of the synchronous map. Eq. 2.6 can be solved analytically in phase space for each of the ν_X in system X and ν_Y in system Y as described by Eq. 2.8.

$$\Phi(\nu_X, \nu_Y) = \sum_i \left(\frac{A_X^i A_Y^i}{T} \right) \left(k_X^i + k_Y^i \right)^{-1} \tag{2.9}$$

where the synchronous map is proportional to the product of the amplitudes, A_X and A_Y, and inversely proportional to the sum of the decay rates k_X and k_Y.

The synchronous map is shown in Figure 2.2. A key component of this map is that in the general 2D correlation, the map is symmetric with respect to the diagonal, thus reducing the information obtained. However, in the 2DCSC method, the diagonal contains information on spectral and phase overlap between the two systems. This provides valuable additional information on the correlation between all of the features

Figure 2.2. The 2DCSC synchronous map generated using the spectra simulated in Fig. 2.1. Positive intensities are shown in blue.

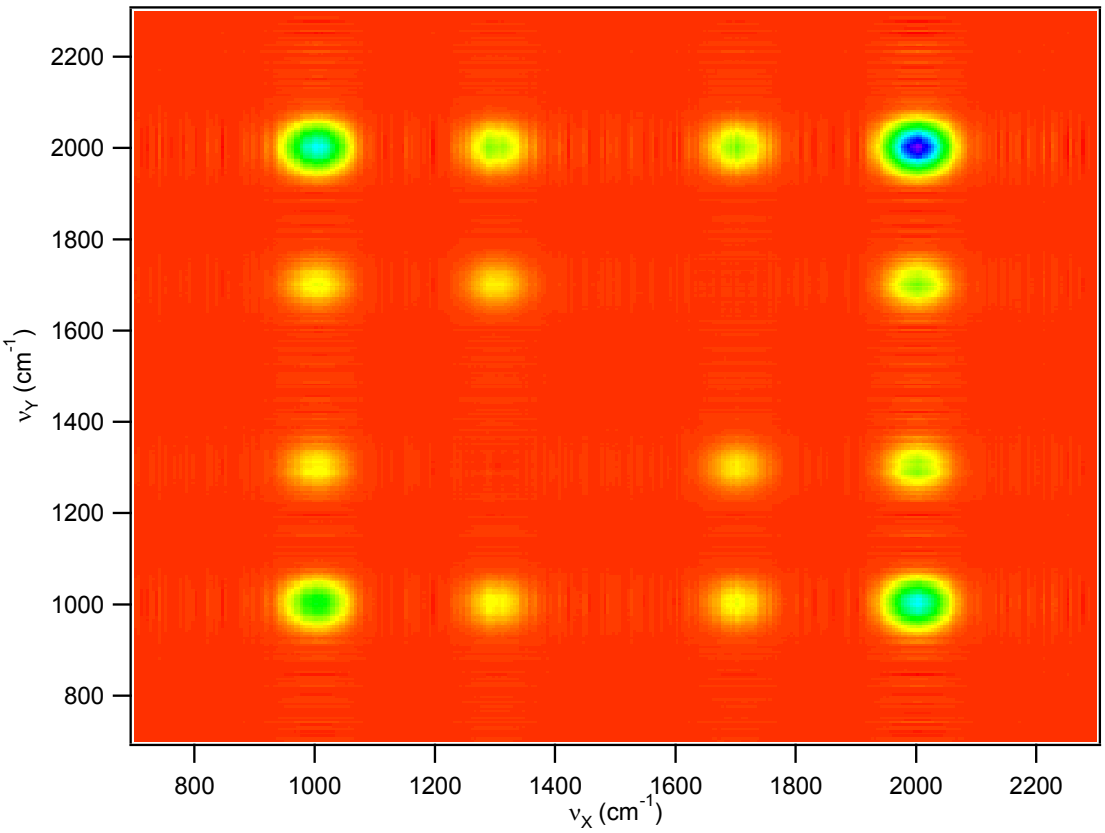

observed in the spectra.

The main features observed in the synchronous map in Figure 2.2 are on the diagonal where $\nu_X=\nu_Y$. These features overlap each other in the frequency domain and show similar time behavior, thus a positive correlation is observed. In contrast to these two features, the two uncorrelated features from Figure 2.1 A and B show a much reduced intensity in the correlation, due to a lack of frequency and phase overlap. The diagonal spectra will be discussed in more detail shortly.

If we analyze the off-diagonal elements in the spectra, each of the features, located at 1000, 1300, 1700, and 2000 cm^{-1} are observed. The off-diagonal elements here show where there is some degree of correlation. Since each of the features is decaying with a somewhat similar decay constant (all within one order of magnitude) there will exist some Fourier component to correlate them. In spite of this, the strongest off-diagonal features lie at $\Phi(1000cm^{-1},2000cm^{-1})$ and $\Phi(2000cm^{-1},1000cm^{-1})$ where the decay rates of these two features are identical. The other off-diagonal peaks involving the 1300 and 1700 cm^{-1} peaks which have different decay components show less correlation, and almost zero correlation along the diagonal.

The most direct way to analyze the synchronous map is to extract the symmetric diagonal. The synchronous diagonal is shown in Figure 2.3. The resulting features show a much improved S/R, discussed further in Section 2.1.5, and positive correlation as expected from the similar decay constant employed here. The reduction in the two uncorrelated features is evident as their intensity is greatly reduced, almost to the level of noise in the spectra.

Figure 2.3. The synchronous correlation map diagonal generated from the emission spectra in Figure 2.1.

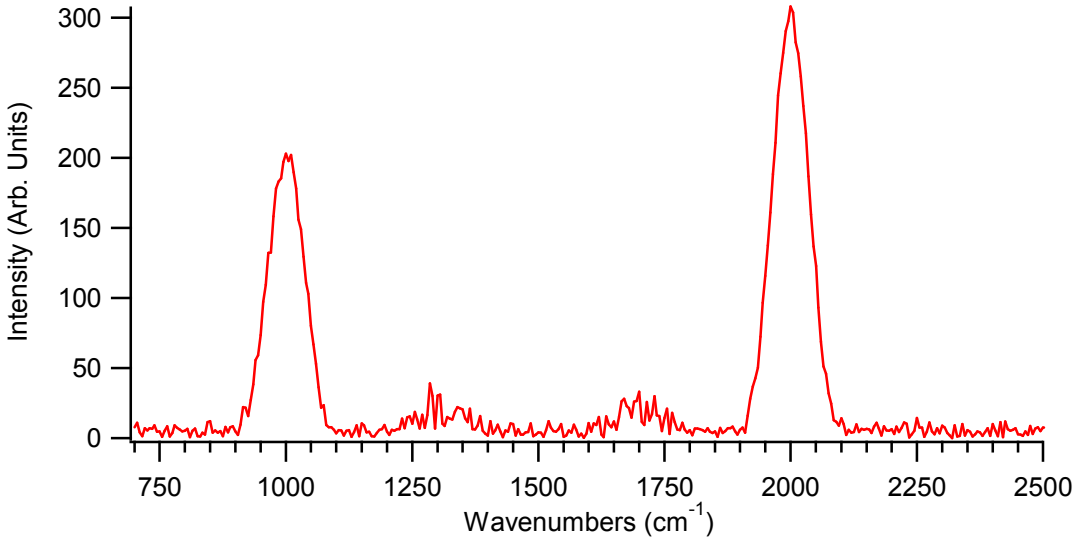

The synchronous diagonal by itself would not however, be able to distinguish whether these features were correlated to each other or not since the diagonal is taken at $\nu_X=\nu_Y$. This is where the off-diagonal components need to be considered.

The asynchronous map is also quite useful in determining spectral correlation. Eq. 2.7 can be solved using the example described by Eq. 2.8 yielding the intensity distribution for the asynchronous map,

$$i\Psi(\nu_X,\nu_Y)=i\sum_i\left(\frac{2A_X^iA_Y^i}{\pi T}\right)\left[\frac{k_X^i-k_Y^i}{\left(k_X^i+k_Y^i\right)^2}\right] \tag{2.10}$$

where the asynchronous correlation is proportional to the product of the amplitude coefficients, A_X and A_Y, and linearly proportional to the difference in the decay rates, k_X and k_Y. This last term is crucial due to the fact the asynchronous map determines the lack of correlation between spectral features.

The asynchronous map of the previous used example from Figure 2.1 is shown in Figure 2.4. The first points that are noticed are the ones missing along the diagonal. The diagonal returns a null value due to the Fourier transform where $\nu_X=\nu_Y$. There is also missing intensity at $i\Psi(1000cm^{-1},2000cm^{-1})$ and $i\Psi(2000cm^{-1},1000cm^{-1})$, which is consistent with Eq. 2.10. Features with the same or similar decay rates will show no or reduced anti-correlation. The 4 positive and 4 negative anti-correlation off-diagonal peaks correspond to peaks that do not correlate with one another.

Let us look into one peak, for example, ν_X=2000 cm^{-1} and examine how the other features are or are not related to this band. From the synchronous plot, the 2000 cm^{-1} feature from system X has the same time profile as the 1000 and 2000 cm^{-1} feature in system Y. Therefore we do not expect to see any anti-correlation features at

Figure 2.4. The 2DCSC asynchronous map generated using the spectra simulated in Fig. 2.1. Positive intensities are shown in blue, while negative intensities are shown in red.

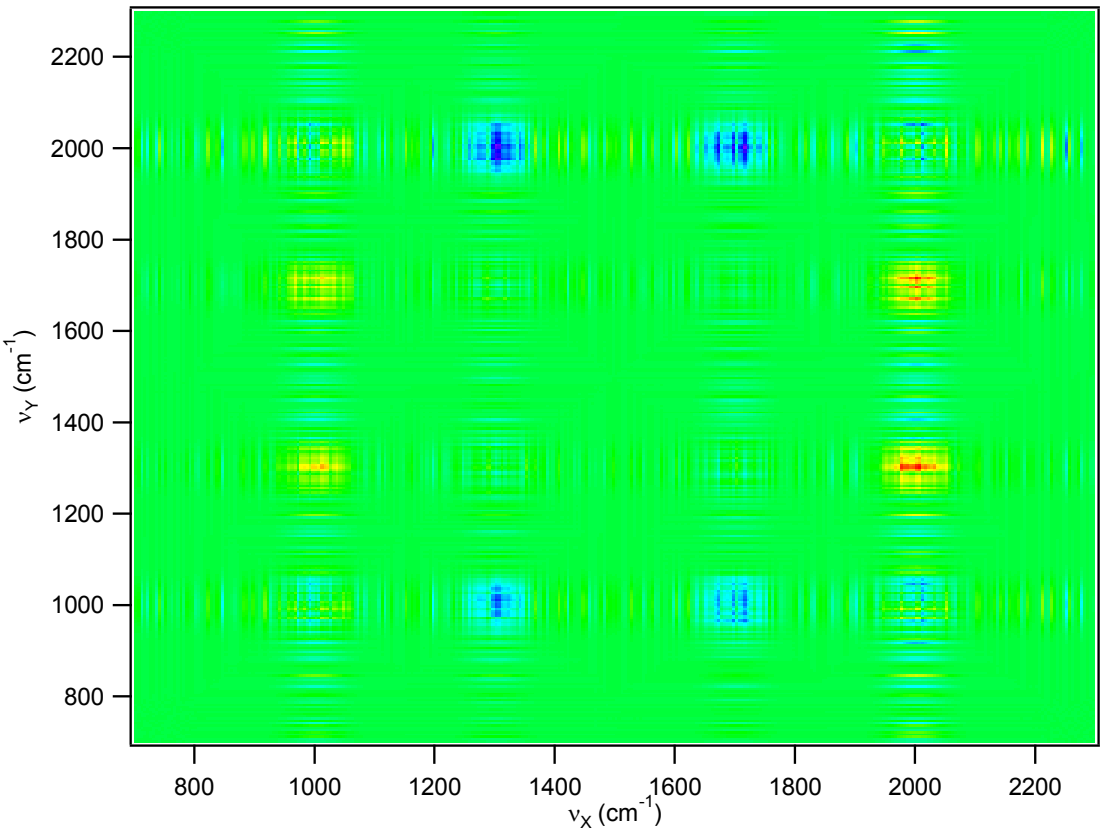

$i\Psi(2000cm^{-1},1000cm^{-1})$ or $i\Psi(2000cm^{-1},2000cm^{-1})$. We do observe that the two features in system X and Y at 1300 and 1700 cm^{-1} do not belong to the same emitter as the peak at 2000 cm^{-1}. Therefore we expect to find two features in the asynchronous map at $i\Psi(2000cm^{-1},1300cm^{-1})$ and $i\Psi(2000cm^{-1},1700cm^{-1})$. These results are consistent with what is observed in Figure 2.4. Further, we can determine some kinetic information about these different systems. If the asynchronous map is negative, $k_Y > k_X$, and conversely if the feature is positive, $k_X > k_Y$ from Eq. 2.10.

2.1.4 Pseudo-time correlations

So far the frequency of the evolving components have been different thus allowing the full correlation between the spectral features. If, however, there are overlapping or close lying emission bands, it would be quite difficult for the full 2DCSC to isolate them. The correlation over the entire temporal range would necessarily involve the complete temporal behavior of both features. We can utilize a technique called "Pseudo-time" correlations to separate the features by taking advantage of their different temporal signatures.

The pseudo-time correlation method employs the same Fourier transforms and product integrals as the full 2DCSC with one minor alteration. The phase component is split into equally spaced phase "bins". These "bins" contain enough phase information to accurately described the evolving system (i.e. if spectra are taken at 100 ns intervals, and the decay component is on the order of tens of μs, the bin size must be large enough to observe a change in the dynamic spectra, probably 10-20 spectra). Each bin is then used to generate a pseudo-time correlation diagonal where the maxima of the spectra show at

what time the correlation reaches the maximum value. For fast time components, the correlation will be large in early time bins, while slower components will show a larger correlation at latter times.

If we consider a system of two features, A and B, located at 1475 and 1550 cm^{-1}, evolving differently in time, with $k_A > k_B$, described by Eq. 2.7, and shown in Figure 2.5, the peaks are unresolvable at early time, and only the late time component is resolvable at late time. If we implement the pseudo-time correlation for the time bins that contain 6 time slices with a duration of 1 μs each, we obtain enough phase information to separate the two features at early time. The result is shown in Figure 2.6.

The early time correlations show a clear separation of the two features, while the later time correlation shows only the slower component. The first time component is fit to a double Gaussian function which returns values of 1470.6(2) and 1549.5(2) cm^{-1} for the two components. The second peak frequency is accurate, however the first peak frequency is slightly off corresponding to limitations with the method. If the decays are similar in magnitude, or if the features are close in amplitude, the pseudo-time correlation will be skewed toward a median value. If the last pseudo-time correlation is fit to a single Gaussian, a value of 1475.4(2) cm^{-1} is found for the center frequency, in much better agreement with the initial emission model.

2.1.5 Signal to noise improvements

As shown in the previous sections, there is a great deal of spectral and dynamic information obtainable from the 2DCSC method. Improvements such as increasing temporal and spectral resolution, determining dynamic information including decay rates,

Figure 2.5. Simulated spectra of two close lying features at 1475 and 1550 cm^{-1}. The decay constants of the two features are 0.2 and 0.06 μs^{-1}, respectively.

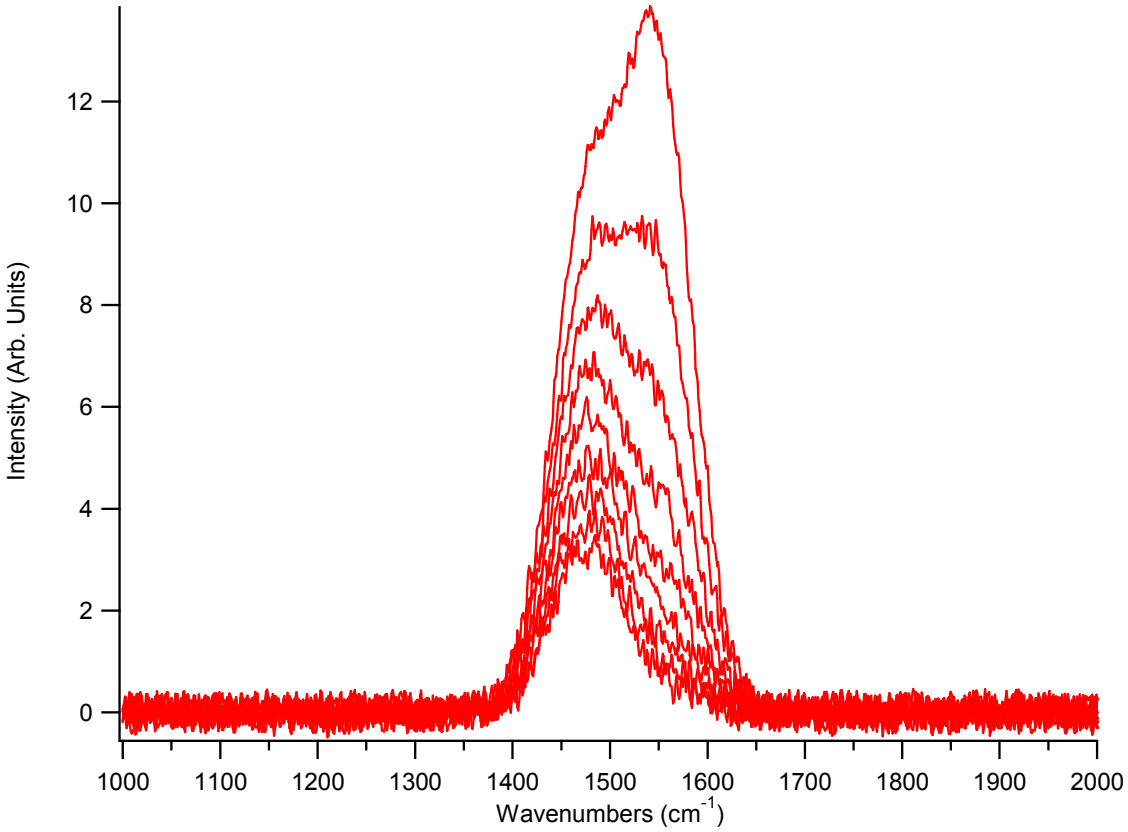

Figure 2.6. The 2DCSC pseudo-time correlation diagonal for the system described by the spectra in Figure 2.5. Each diagonal, shown in red, represents 6 time slices of 1 μs each. The first diagonal is fit to a double Gaussian function, shown in blue.

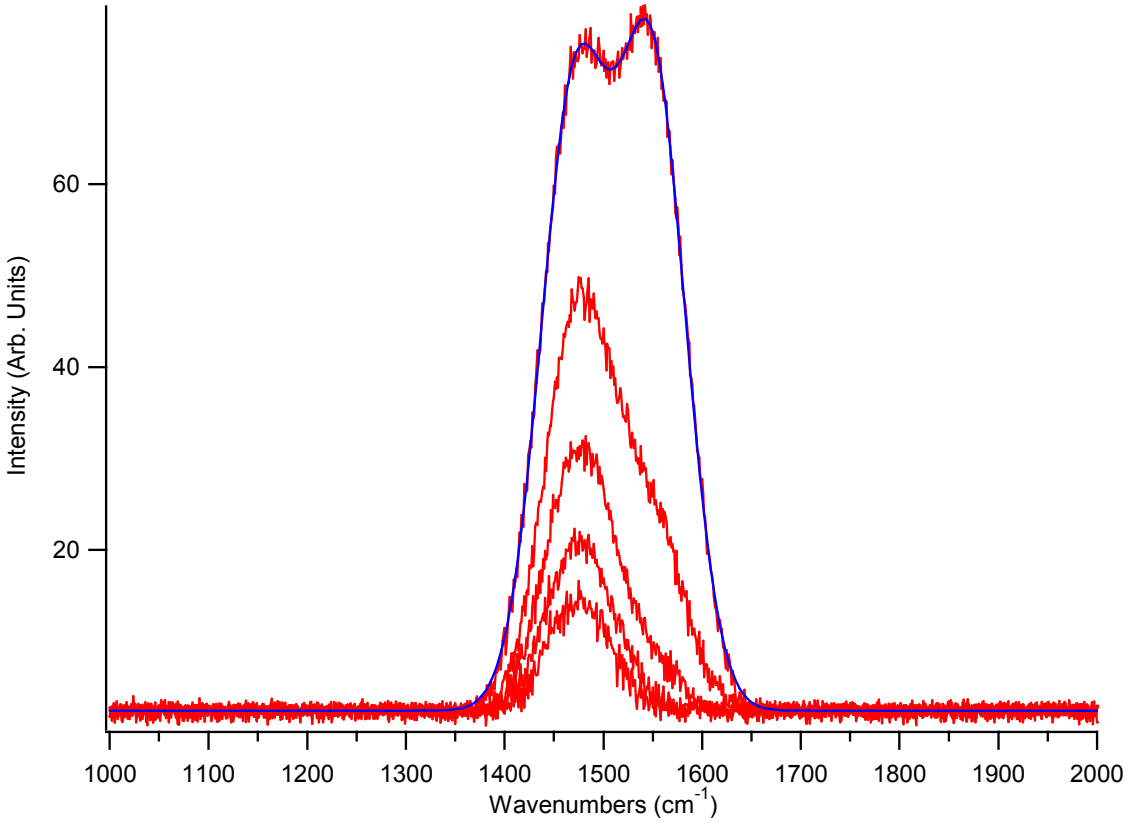

reducing noise, and simplifying complex spectra are all achievable with the methods mentioned thus far. We will now consider the case where we have a common feature with intensity *S* and noise level *N* and compare the 2DCSC result with simple signal averaging.

There are four cases which will be presented here, out of the numerous possible frequency and temporal processes available to the system. The first system will be a Gaussian distribution that does not experience any decay or shift (ND, NS). The second system will incorporate the same distribution that does not decay, but experiences a damped frequency shift (ND, S). The third system utilizes the same distribution but undergoes a decay, without a frequency shift (D, NS). The last system follows a decay and frequency shift (D, S). Each of these systems will undergo a signal averaging method and the 2DCSC method.

In addition, as mentioned previously, the 2DCSC method is typically employed on two separate sets of data, however, a SELF-correlation may be employed to improve the S/N as well. The self and cross correlation methods will also be compared. A summary of the results[7] are listed in Table 2.1. The raw data is the averaged S/N ratio for all the spectra used, normalized to 1. The number of spectra used are kept constant throughout the analysis. The averaging method is the simple linear averaging technique. The correlation method is the one utilized here. The resulting diagonal spectra is used here to determine the S/N enhancement. SELF methods involve using the same data set, while CROSS methods, involve using two data sets with identical features, but containing different noise.

Table 2.1. The S/N enhancement for the following operations on the four simulated spectra: (ND, NS) – no decay, no shift; (ND, S) – no decay, shift; (D, NS) – decay, no shift; (D, S) – decay, shift. The relative enhancement is shown for each grouping independently. Tabulated from Ref. 7.

Data Set	Analytical Method	S/N Enhancement
(ND, NS)	Raw Data	1
	Averaging (SELF)	5
	Correlation (SELF)	5.5
	Averaging (CROSS)	7.3
	Correlation (CROSS)	6.8
(ND, S)	Raw Data	1
	Averaging (SELF)	4.5
	Correlation (SELF)	3.4
	Averaging (CROSS)	6.3
	Correlation (CROSS)	4.1
(D, NS)	Raw Data	1
	Averaging (SELF)	5
	Correlation (SELF)	8
	Averaging (CROSS)	7.1
	Correlation (CROSS)	9.6
(D, S)	Raw Data	1
	Averaging (SELF)	4
	Correlation (SELF)	6.9
	Averaging (CROSS)	5.8
	Correlation (CROSS)	8

For the case of a static signal, (ND, NS), the self-averaging yields a 5-fold enhancement and a cross-averaging (averaging 50 spectra instead of 25) yields an improvement by a factor of 7.3 in line with statistical expectations. The self and cross correlation methods produce a 5.5 and 6.8 times improvement, basically in line with the linear averaging method. This is consistent with the lack of frequency or intensity change, not containing any phase information, therefore not improving the correlation method.

When a shift in the frequency is introduced, (ND, S) the correlation method fails to improve on the basic linear averaging results both for the self and cross methods, 4.5 and 6.3 for the self and cross averaging vs. 3.4 and 4.1 for the self and cross correlation, respectively. This is due to the decrease in overall signal intensity as a result of the frequency shift. The frequency shift broadens the feature, due to the correlations of the shifting feature producing a temporal response. Even in the signal averaging case, the enhancement result is less than what is expected statistically.

A decaying signal substantially changes the enhancement ratios. The correlation method can now take advantage of the phase information within the signal decay. For the case of the decay, no shift, (D, NS), self and cross averaging yield improvements of 5 and 7.1 times, while self and cross correlations improve the S/N by a factor of 8 and 9.6, respectively. The increase in the enhancement is solely due to the correlation method taking advantage of the phase information contained in the system.

In the final example, the signal is both shifting in frequency and decaying in time (D, S). We expect the correlation technique to improve on the results from the no decay, shift (ND, S) case. In addition, we would expect a decrease in the enhancement of the

signal averaging from the (D, NS) case as was observed between the (ND, NS) and (ND, S) case. When a shift is introduced, the enhancement is decreased. For the decaying, shifting case, the self and cross averaging enhance the S/N by a factor of 4 and 5.8, respectively, while the self and cross correlation methods improvethe S/N by 6.9 and 8, respectively. This is consistent with what is expected, when compared with the previous cases, as well as what is expected between the linear averaging and correlation methods. The correlation method is once again aided by the phase information which is contained in the signal decay constant.

2.1.6 Spectral accuracy

The spectral accuracy of the 2DCSC method was briefly discussed in 2.1.4. It was shown in Figure 2.6, that the accuracy of the correlation is related to the relative intensity and proximity of the peak of interest to other nearby peaks. This is extremely important when considering peaks of significantly different intensities. Because the Fourier components are obtained from the complete temporal profile, they may be influenced by the intensity or frequency shift of strong features.

It is easily seen if we consider two cases, one a decaying and shifting peak, and the other only a shifting peak, without decaying. These two cases will be treated separately below.

In the case of the decaying and shifting peak, signal averaging will show a maximum intensity based on the number of spectra and intensity decay rate. In the general case where we obtain all the spectral and temporal information, this will typically yield a signal averaged spectra which has the appearance of the final spectra. If,

however, we utilize the 2DCSC method, we will observe a broadening of the feature toward the early time location. This is due to the intensity of the feature being proportional to the product of the initial intensities, as well as inversely proportional to the sum of the decay constants, as described by Eq. 2.9. Since these initial intensities are much stronger due to the decay rate, there will be some extra intensity seen as a shoulder to the main feature which is still indicative of the final peak position.

In the spectra that only contains a shifting peak, the average value will fall to where the most spectra overlap. This is dependent on the frequency shift rate, whether the shift is damped, and the number of spectra. If we average over a large number of spectra, with a damped frequency shift, the average value will be where the damped shift stops. If, on the other hand, we use the 2DCSC method, the initial signal will appear stronger because that is where the most dynamic information is obtained. From Eq. 2.9, at early time the rate constants *k* will be small, leading to a large amplitude, while at late times the *k* will be large, decreasing the overall signal. As a result, the 2DCSC method will skew the emission feature to the red, while the averaging method will skew the feature to the blue. In terms of accuracy, if the feature is shifting toward it's fundamental transition (typically a blue shift), the signal averaging technique is more accurate.

2.2 Vibrational mode analysis

The assignment of vibrational modes based on absorption results is skewed by the fact that emission processes normally involve transitions other than $v=1 \rightarrow 0$. This fact coupled with other intensity and frequency effects makes vibrational mode determination from emission spectra more difficult.

In order to analyze the vibrational emission from a highly vibrationally excited molecule or radical, an energy level diagram will be generated. From this vibrational manifold, all of the available transitions will be calculated and sorted according to their upper state energy. These transitions will be grouped according to their internal energy and used to fit the observed emission spectra. In addition to determining the vibrational bands, the average internal energy of the molecule, energy transfer rate, and other structural and dynamical information can be obtained through this method.

There exists one large problem with this method that should be addresses here. Even for a simple molecule or radical, the vibrational level density become extremely high even for low levels of vibrational excitation. Vibrational level densities >1 cm are not uncommon in this analysis. In addition, for polyatomic molecules, several of the vibrational modes are IR active, including combination, difference, and overtone bands. This would suggest that all of these different bands would evolve differently with time. The accuracy of this technique at these high densities should then be questioned.

Both of these concerns are easily answered however.[9] The level density, while being a concern, is not as important as the accurate determination of the vibrational energy levels. The determination of these energy levels can be found to very high accuracy with the inclusion of higher terms in the vibrational energy expression. Furthermore, the energy levels are all approximate, as there is a tremendous amount of overlap in the emission spectra even at low energy levels. Small fluctuations of these levels do not affect the overall fitting because of this averaging out. For the case of polyatomics, with several active modes, the vibrational relaxation has been found to be almost universely constant within a given molecule. Almost every polyatomic molecule

shows a constant decay corresponding to its lowest frequency mode, which turns out to be the fastest. In addition, intramolecular vibration-vibration (V-V) energy transfer is much faster than the relaxation rate and thus the molecule equilibrates after each emission event.

2.2.1 The Vibrational energy matrix

The fundamental part of the vibrational manifold is generated through the combination of harmonic, anharmonic, bending, and higher potential energies. These potentials can be combined in a general expression which contains all of the vibrational modes, anharmonic corrections, and bending contributions for the system of interest.

$$G_{\upsilon} = \sum_{i}^{n} \tilde{\omega}_i^0 \upsilon_i + \sum_{i \le j}^{n} x_{ij} \upsilon_i \upsilon_j + \sum_{b \le b'}^{m} g_{bb'} l_b l_{b'} \qquad (2.11)$$

The overall energy of the molecule, G_{υ}, contains contributions from the harmonic frequencies, $\tilde{\omega}_i^0$, anharmonic corrections, x_{ij}, and degenerate bending contribution, $g_{bb'}$ for a molecule with n total modes and m degenerate modes. The vibrational quantum number is designated υ_i or υ_j, and the bending quantum number is l_b or $l_{b'}$. The bending contribution may take on a different form as the symmetry of the molecule changes. The symmetry shown above is $D_{\infty h}$. Higher terms may be added to improve the accuracy of the vibrational energy manifold, however even within this simple expression, vibrational energy levels up to G_{υ}=30,000 cm^{-1} have been generated with surprising accuracy.

The main source of these vibrational energy terms is from experimentally determined vibrational states. Excellent review articles exist for numerous systems[10] describing these harmonic, anharmonic, and higher order terms to great accuracy.

2.2.2 Simulated emission spectra

Utilizing the vibrational matrix expression to generate vibrational states produces an energy manifold that becomes extremely complex at energies as low as 5000 cm^{-1} (7000 K). An example of this is shown in Figure 2.7. For the case of acetylene, the level density is 3.4 cm at 10,000 cm^{-1}, and 23.3 cm at 15,000 cm^{-1}. The accuracy of these densities can be shown by several available methods for calculating the density of states.[11,12]

Accepting some vibrational level discrepancy, calculating the transitions from each level requires further assumptions. For each vibrational state, for e.g. (υ_1=3, υ_2=2^0, υ_3=0) for a system such as CO_2, there exists numerous available transitions. The notation used here, and throughout this thesis is of the form $\left(\upsilon_1^{l_1},\upsilon_2^{l_2},...,\upsilon_n^{l_n}\right)$, where υ_i are the vibrational quantum numbers in the i mode, l_i are the degenerate bending quantum numbers for mode i. Each of the assumptions made here can be broken if other transitions are observed in absorption measurements. The change in the vibrational quantum number is restricted to $\Delta\upsilon = \pm 1$, only single quanta changes are allowed. In addition, only changes of $\Delta l = 0,\pm 1$, will be allowed for the degenerate modes in the linear case. Utilizing these rules we can also determine the rotational structure of the bands, (for e.g. l=0, || band, Σ-Σ or $\Delta l = \pm 1$, $\perp$ band, Π-Σ, Δ-Π, etc…) though for the majority of cases, a constant rotational envelope will be utilized.

Taking the above case for CO_2, the (3, 2^0, 0) state can have several allowed transitions. Final states that generate emission can include (2, 2^0, 0), (3, 1^0, 0), or (3, 1^1, 0). These, however are not the only states observed in absorption measurements.

Figure 2.7. The vibrational manifold generated for acetylene from 0 to 10,000 cm^{-1} of vibrational energy.

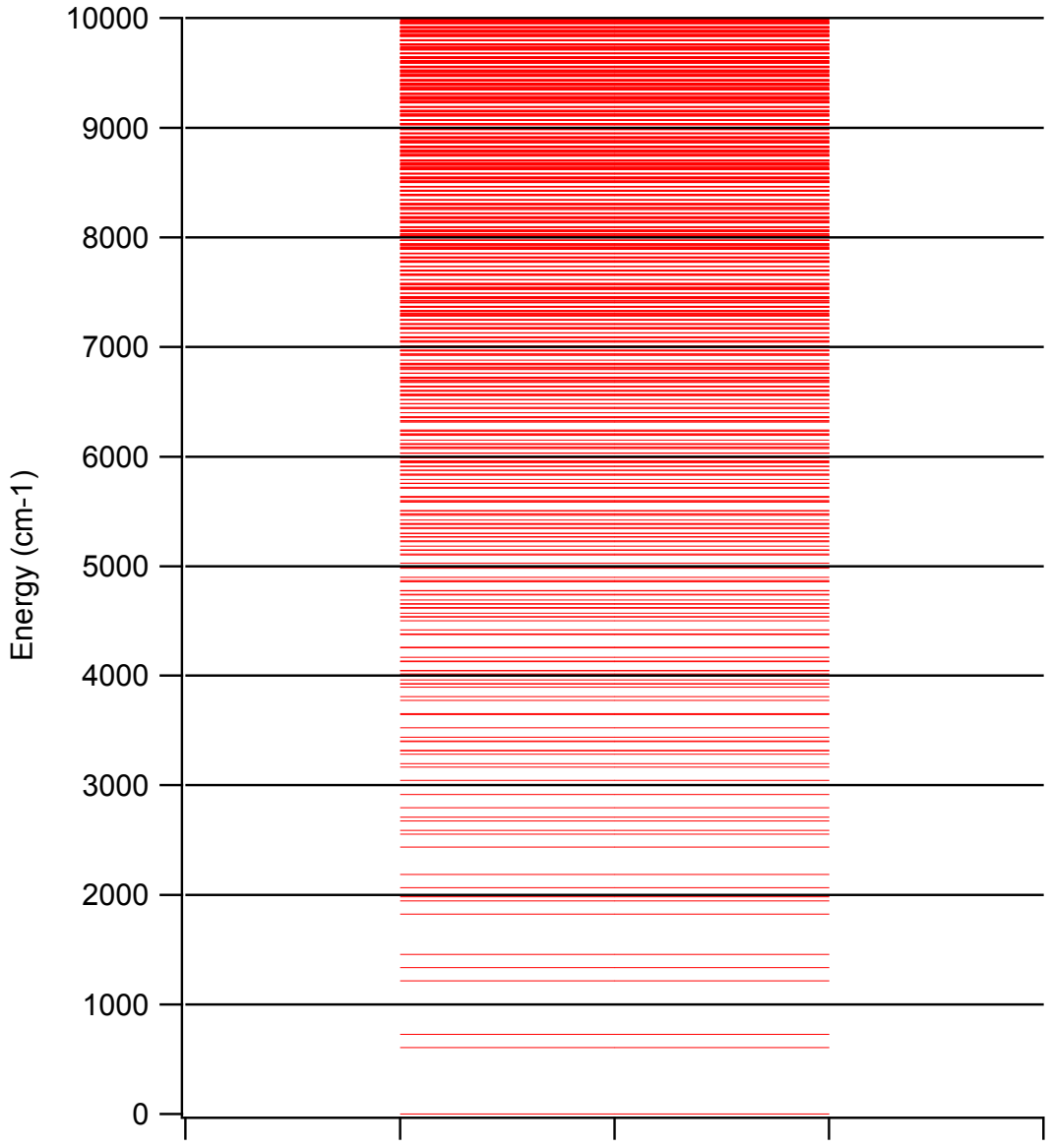

Combination, difference, and overtone bands play a crucial role in the absorption spectra of polyatomic molecules. It is therefore inadequate to limit the number of transitions solely to $\Delta\upsilon = \pm 1$. The actual transition modeled are those that are observed in the absorption spectra from the ground state.

Once all of the transitions are generated, an emission spectrum is generated for each level. The emission spectrum contains several components, each of which is described by a Gaussian distribution with center frequency ν_i^j corresponding to the frequency of mode *i* with *j* quanta of excitation, with width σ_i. Each of the IR active modes are described by their spectral emission function, $S_i^j(\nu)$, for *j* quanta in mode *i*,

$$S_i^j(\nu) = A_i D(\nu) I_i^j \left(\nu_i^0 / \nu_i^j\right)^3 \exp\left\{-\left(\nu - \nu_i^j\right)^2 / 2\sigma_i^2\right\} \tag{2.12}$$

where A_i is the Einstein coefficient for spontaneous absorption taking the value of

$$A_i = A_i^{0\to 1}\left(\nu_i^0\right)^3 \tag{2.13}$$

from the Einstein absorption coefficient $A_i^{0\to 1}$ for mode *i*, and the cube of the fundamental frequency, ν_i^0, and frequency of mode *i* with quanta *j*, ν_i^j. The detector response function *D(ν)* is included in the spectral emission modeling to preserve the S/N in the experimental results. Typical IR detectors have sharp detectivity curves so correcting the emission model with the response preserves the accuracy of the results. The final term I_i^j represents the harmonic oscillator scaling factor for emission from states above the fundamental. This term becomes dominant at increasing internal energies as the number of quanta in each mode increases. This term will be defined here and discussed in section 2.2.4 in this chapter.

$$I \propto \prod_j \left[\left(\upsilon_j + \Delta\upsilon_j \right)! / \left(\Delta\upsilon_j ! \upsilon_j ! \right) \right] \tag{2.14}$$

for non-degenerate mode(s) with lower state quanta υ_j, and the change in vibrational quanta $\Delta\upsilon_j$, which is always positive. The expression for degenerate modes is given by

$$I \propto \prod_j \frac{\left(\upsilon_j \pm l_j + 2 \right)}{2 g_{\upsilon_j}} \tag{2.15}$$

where υ_j is again the lower state quantum number, lj is the degenerate bending quantum number and $g_{\upsilon j}$, is a restriction on the intensity due to having only a P/R branch instead of all three, P, Q, R, branches when l' and $l'' \neq 0$. $g_{\upsilon j}$ takes a value of 1 when l' and $l'' = 0$ or 2 when l' and $l'' \neq 0$. In Eq. 2.15, the $\Delta\upsilon_j$ is restricted to 1. The complete derivation will be shown in section 2.2.4.

Under optimal conditions, we would use these individual emission spectra to model the observed emission spectra. This, however, would be extremely tedious and computationally expensive due to the large number of states and transitions. Instead the individual emission spectra are grouped together in energy "bins" to simulate the average emission spectra with a given energy. The average size of these "bins" is between 500 and 1000 cm^{-1}. Each bin contains the averaged emission spectra from all the transitions which originate at energy levels within that bin.

There are significant differences between the measured absorption spectra and simulated emission spectra that make the relationship between the two difficult to discern. The absorption and simulated emission of acetylene at different vibrational energies is shown in Figure 2.8. In the absorption curve, lower panel, the ν_5 mode at 730 cm^{-1} is the most intense, with the ν_3 mode at 3290 cm^{-1} and $\nu_4 + \nu_5$ combination band at

Figure 2.8. The simulated emission of the ν_5, $\nu_4+\nu_5$, and ν_3 bands, at 730, 1275, and 3000-3300 cm^{-1}, respectively, of acetylene (top panel - A). The absorption spectrum of acetylene is shown in the bottom panel – B, with the same corresponding modes.

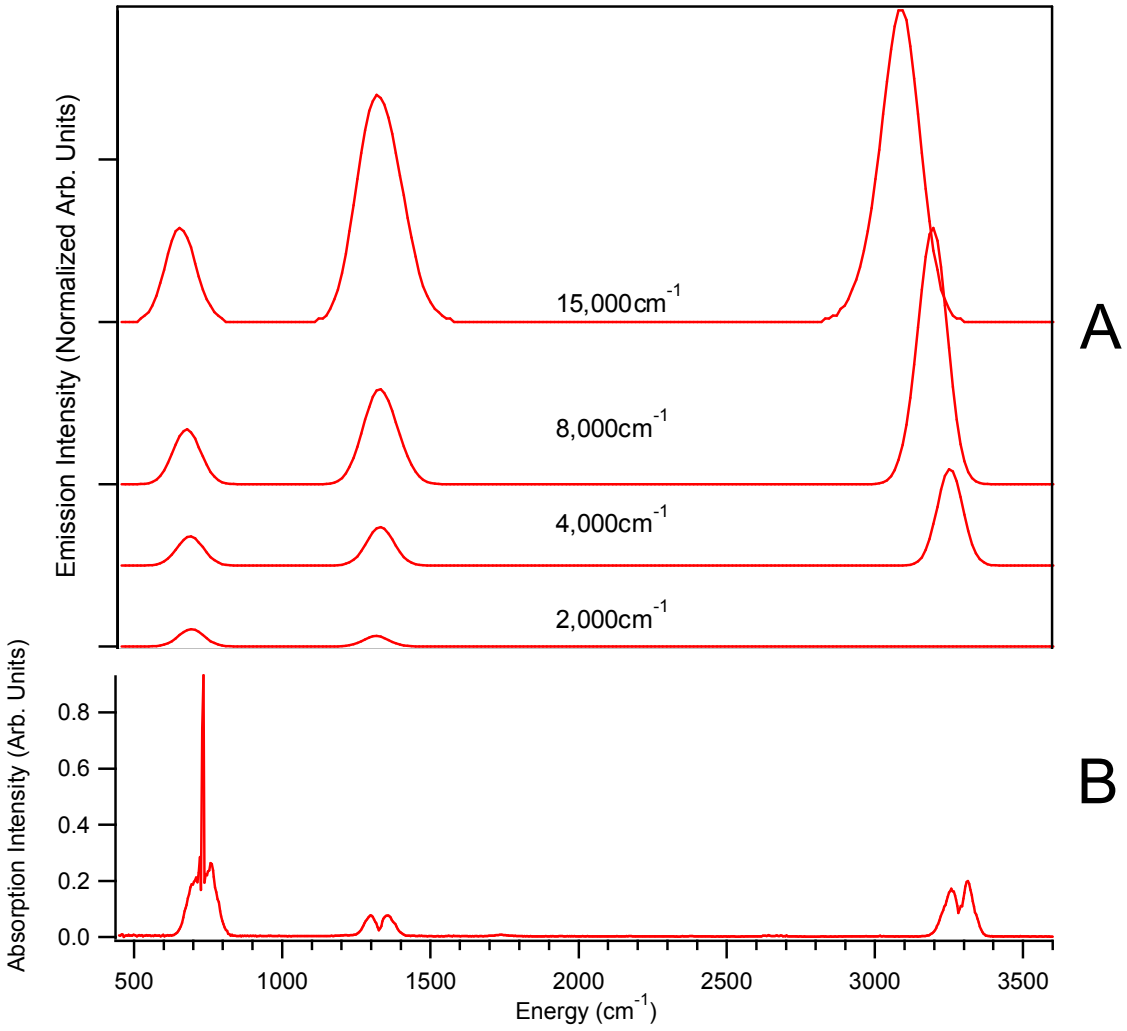

1328 cm^{-1} significantly weaker. However in the emission spectra, the intensity ratios change with the ν_3 mode being the predominant mode with the $\nu_4 + \nu_5$ gaining intensity. In addition, anharmonicity plays a big role in red shifting the emission of the ν_3 mode, as well as the $\nu_4 + \nu_5$ mode to a slightly lesser extent.

This intensity discrepancy is due to several factors. The first is the Einstein A coefficient for spontaneous emission. From Eq. 2.13, the intensity scales as the cube of the frequency, therefore the ν_3 mode will be ~92 times more intense that the ν_5 mode. The next factor is the harmonic oscillator scaling factor. As seen in Eq. 2.14 and 2.15, the intensity of an emission transition increases as the quantum number in each mode increase. Emission from highly excited levels will therefore be more intense that emission from low vibrational levels, or absorption transitions. In addition, the number of quanta in the lower frequency modes will increase faster than the quantum number of the higher frequency vibrations. Therefore, the lower frequency modes will become more intense as the vibrational energy increases.

The final intensity discrepancy between absorption and emission spectra, as seen in Figure 2.8, is the unexpectedly strong $\nu_4 + \nu_5$ combination band. In absorption measurements, the combination band is approximately 30% as intense as the ν_3 mode. In the emission spectra, the combination band grows in intensity and surpasses the ν_3 mode intensity at ~20,000 cm^{-1}. This is due to the intensity of combination bands scaling as the product of the individual band intensities, seen again in Eq. 2.14 and 2.15. Since the combination band of acetylene is made up of two degenerate modes, Eq. 2.15 describes its intensity proportional to the product of the sum of the vibrational quantum numbers and degenerate bending quantum numbers in the two modes.

2.2.3 Vibrational energy distribution

The energy distribution of the evolving features are relatively similar for direct excitation of a molecule, for example a single photon electronic transition followed by internal conversion to the ground state, and the generation of a molecule via photolysis reaction with a large amount of energy in its vibrational ground state. Both systems display a reaction or energetic high excitation population and a low energy thermal population.

The low energy population arises from Franck-Condon pumping or excitation of low energy vibrational states from collisions with highly excited molecules. In either case, we can approximate the low energy feature as a "thermal" or bath gas. The population should show a Boltzman distribution, or a Gaussian distribution centered at $<E>=0$.

The high energy feature, formed directly from the photolysis or excitation pulse, can be considered a Gaussian distribution with varying width. The exact distribution or which states are active can not be determined from this method, as it is not a state specific technique. The method can, however, yield useful information on the ensemble average thermodynamic and kinetic behavior of the system.

The restriction of a particular distribution over the vibrational population depends on several factors including the ground and excited electronic state surface, collisional energy partner, and excitation method. A bimodal distribution was imposed on the emission bins with a low energy Gaussian centered at $E_j=0$, which is considered a thermal sink, and a high energy Gaussian which follows the vibrationally hot acetylene produced in the photolysis reaction. The population distribution is given by

$$\overline{P}^{j} = a \times \exp\left(-\overline{E}_j^2 / 2\sigma_1^2\right) + (1-a) \times \exp\left(-\left(E_j - \langle E \rangle\right)^2 / 2\sigma_2^2\right) / \sqrt{2\pi}\sigma_2 \quad (2.16)$$

in which a corresponds to the populations of the two distributions, σ_1 and σ_2, the widths, and $\langle E \rangle$ the average internal energy of the high energy distribution. The total population is normalized as there is a constant correlation between the coefficients in front of the two distributions, a and $1-a$. This ensures that population is not lost in the process. IR emission is observed for up to 100 μs, which is not enough time for the molecules, except for the lightest ones, H, He, etc…, to leave the active region.

2.2.4 Harmonic oscillator scaling factor

As has been stated previously, the unexpectedly strong $\nu_4 + \nu_5$ combination band arises from several factors, the most important being the harmonic oscillator scaling term. This term has been mentioned in several theoretical papers,[13,14] but since it is not common for this term to play a significant role in molecular spectra, a brief derivation for our collisional relaxation result, where $\Delta\upsilon=1$, should be given. The term has been expanded upon in a work on the hot bands of HCN,[15] and utilizing those early results, we will expand them to include more possible modes.

For the majority of cases, absorption and emission from the ground state dominate spectra due to thermal energies, thereby lessening the impact of the harmonic oscillator scaling factor. However, when non-equilibrium populations are considered, the scaling factor is vital to correctly fit the emission or absorption spectral intensity. The analysis is based on transitions in general and does not matter if you are going up (absorption) or

down (emission) the energy manifold. This allows us to simplify our calculation by defining υ as the lower of the two states.

If we consider the first several terms in the expansion of the electric dipole moment μ,

$$\mu = \mu_0 + \sum_{k=1}^{3N-6} \frac{\partial \mu}{\partial Q_k} Q_k + \sum_{k=1}^{3N-6} \sum_{l=1}^{3N-6} \frac{\partial^2 \mu}{\partial Q_k \partial Q_l} Q_k Q_l + \ldots \tag{2.17}$$

where μ is a vector and the Q's represent the normal coordinates for vibrational motion. To determine the intensity of a given transition between two states, υ' and υ", we can utilize this expansion which yields,

$$\begin{aligned} \sqrt{I} \propto \langle \psi_{\upsilon'} | \mu | \psi_{\upsilon''} \rangle &= \mu_0 \langle \psi_{\upsilon'} | \psi_{\upsilon''} \rangle + \sum_{k=1} \frac{\partial \mu}{\partial Q_k} \langle \psi_{\upsilon'} | Q_k | \psi_{\upsilon''} \rangle \\ &+ \sum_{k=1} \sum_{l=1} \frac{\partial^2 \mu}{\partial Q_k \partial Q_l} \langle \psi_{\upsilon'} | Q_k Q_l | \psi_{\upsilon''} \rangle + \ldots \end{aligned} \tag{2.18}$$

with the first term vanishing unless υ'=υ". We can further benefit from the use of normal mode coordinates to expand the integrals as products by implementing the product expansion of $\psi_\upsilon = \psi(Q_1)\psi(Q_2)\ldots\psi(Q_{3N-6})$. The second term in Eq. 2.18 becomes

$$\begin{aligned} \sum_{k=1} \frac{\partial \mu}{\partial Q_k} \langle \psi_{\upsilon'} | Q_k | \psi_{\upsilon''} \rangle = \sum_{k=1} \frac{\partial \mu}{\partial Q_k} &\left[\prod_{i \neq k} \langle \psi_{\upsilon'}(Q_i) | \psi_{\upsilon''}(Q_i) \rangle \right] \\ &\times \langle \psi_{\upsilon'}(Q_k) | Q_k | \psi_{\upsilon''}(Q_k) \rangle \end{aligned} \tag{2.19}$$

which describes the vibrational mode along Q_k. Additionally, the third term in Eq. 2.18 is simplified to

$$\begin{aligned} \sum_{k=1} \sum_{l=1} \frac{\partial^2 \mu}{\partial Q_k \partial Q_l} \langle \psi_{\upsilon'} | Q_k Q_l | \psi_{\upsilon''} \rangle = \sum_{k=1} \sum_{l=1} \frac{\partial^2 \mu}{\partial Q_k \partial Q_l} &\left[\prod_{i \neq k,l} \langle \psi_{\upsilon'}(Q_i) | \psi_{\upsilon''}(Q_i) \rangle \right] \\ &\times \langle \psi_{\upsilon'}(Q_k) | Q_k | \psi_{\upsilon''}(Q_k) \rangle \langle \psi_{\upsilon'}(Q_l) | Q_l | \psi_{\upsilon''}(Q_l) \rangle \end{aligned} \tag{2.20}$$

which shows the combination or overtone intensity along Q_k and Q_l. Note here that there is no restriction on k or l, and k can be equal to l generating an overtone, while $k \neq l$ generates a combination mode. Replacing expression from Eq. 2.18 with those from Eq. 2.19 and 2.20 yields:

$$\sqrt{I} \propto \sum_{k=1} \frac{\partial \mu}{\partial Q_k} \langle \psi_{\upsilon'}(Q_k) | Q_k | \psi_{\upsilon''}(Q_k) \rangle + \sum_{k=1} \sum_{l=1} \frac{\partial^2 \mu}{\partial Q_k \partial Q_l} \times \langle \psi_{\upsilon'}(Q_k) | Q_k | \psi_{\upsilon''}(Q_k) \rangle \langle \psi_{\upsilon'}(Q_l) | Q_l | \psi_{\upsilon''}(Q_l) \rangle + \ldots \tag{2.21}$$

We can use the cartesian solution to the non-degenerate harmonic oscillator equation to solve Eq. 2.21, whose wavefunction, ψ_{υ_k}, is typically written as

$$\psi_{\upsilon_k}(Q_k) = N_{\upsilon_k} e^{-\gamma_k Q_k^2/2} H_{\upsilon_k}\left(\gamma_k^{1/2} Q_k\right) \tag{2.22}$$

with $N_{\upsilon_k} = \left[(\gamma/\pi)^{1/2}\left(2^{\upsilon_k}\upsilon_k!\right)^{-1}\right]^{1/2}$ being the normalization factor, $\gamma_k = 4\pi^2 \nu_k / h$, and H_{υ_k} the Hermite polynomial of degree υ_k. Upon solving Eq. 2.21 with the above wavefunction it is found that there is a straightforward intensity dependence on the quanta υ in mode k.

$$\begin{aligned} &\sqrt{I} \propto (\upsilon_k + 1)^{1/2}, && \text{for } \Delta\upsilon_k = \pm 1 \\ &\sqrt{I} \propto [(\upsilon_k + 1)(\upsilon_k + 2)]^{1/2}, && \text{for } \Delta\upsilon_k = \pm 2 \\ &\sqrt{I} \propto [(\upsilon_k + 1)(\upsilon_k + 2)(\upsilon_k + 3)]^{1/2}, && \text{for } \Delta\upsilon_k = \pm 3 \end{aligned}$$

The single mode intensity dependence from above simplifies to

$$I \propto [(\upsilon_k + \Delta\upsilon_k)!/\upsilon_k!] \tag{2.23}$$

which needs to be normalized to the fundamental intensity of each mode by dividing Eq. 2.23 by $\Delta\upsilon_k!$. Note, we have dropped the $\partial\mu/\partial Q_k$ and higher terms to simplify the expression. This term remains unchanged throughout the derivation as one would not

expect a change in the dipole moment as the number of quanta in a given mode is changed.

A more general expression can be written to include combination and overtone non-degenerate modes based on solutions obtained from Eq. 2.21 and the expansion of higher order terms:

$$I \propto \prod_k \left[\left(\upsilon_k + \Delta\upsilon_k \right)! / \left(\Delta\upsilon_k ! \upsilon_k ! \right) \right] \tag{2.24}$$

for the case where collisional deactivation promotes relaxation via the lowest quanta (usually single quanta) change we can further simplify Eq. 2.24 to

$$I \propto \prod_k \left(\upsilon_k + 1 \right) \tag{2.25}$$

where υ_k is the lower of the two states. Eq. 2.25 is the harmonic oscillator scaling factor for non-degenerate modes where we only consider single quanta changes.

The above equation is applicable for non-degenerate modes only based on the choice of the harmonic oscillator wavefunction. In order to find a more general expression for degenerate harmonic oscillator levels, we must utilize the solution to the degenerate harmonic oscillator problem in polar coordinates. This has been solved by Pauling and Wilson[16] in the doubly degenerate case generating the wavefunction,

$$\psi_{\upsilon l} = N_\upsilon e^{-\gamma\rho^2/2} F_\upsilon^{|l|} \left(\gamma^{1/2} \rho \right) e^{il\phi} \tag{2.26}$$

where N_υ is the normalization factor, $F_\upsilon^{|l|}$ are the associated Laguerre polynomials of degree υ in ρ, and l taking on values of $0, \pm 2, \pm 4, ..., \pm\upsilon$ if υ is even and $\pm 1, \pm 3, ..., \pm\upsilon$ if υ is odd. ρ and ϕ are coordinates defined as, $Q_a = \rho\cos\phi$ and $Q_b = \rho\sin\phi$. Upon solving,[17] in a similar manor as described above, we obtain those results published by Maki, *et al.*,[15]

$$I \propto \frac{\left[1/2\left(\upsilon_i + l_i + \Delta\upsilon_i\right)\right]!\left[1/2\left(\upsilon_i - l_i + \Delta\upsilon_i\right)\right]!}{\left\{\left[1/2\left(\upsilon_i + l_i\right)\right]!\left[1/2\left(\upsilon_i - l_i\right)\right]!\left[1/2\left(\Delta\upsilon_i\right)\right]!^2\right\}} \tag{2.27}$$

when $\Delta\upsilon_i$ is even, resulting in a parallel band. And the result,

$$I \propto \frac{\left[1/2\left(\upsilon_i + l_i + \Delta\upsilon_i - 1\right)\right]!\left[1/2\left(\upsilon_i - l_i + \Delta\upsilon_i - 1\right)\right]!\left[\upsilon_i + l\Delta l + \Delta\upsilon_i + 1\right]}{\left\{g_\upsilon\left[1/2\left(\upsilon_i + l_i\right)\right]!\left[1/2\left(\upsilon_i - l_i\right)\right]!\left[1/2\left(\Delta\upsilon_i - 1\right)\right]!^2\left[\Delta\upsilon_i + 1\right]\right\}} \tag{2.28}$$

when $\Delta\upsilon_i$ is odd, resulting in a perpendicular band.

We can greatly simplify the expression for the intensity of degenerate modes by considering the system investigated here. The first simplification, which was done for the non-degenerate case, involves fixing $\Delta\upsilon$=1. This term is always takes on a positive value, for absorption or emission. We restrict the angular momentum quantum number to values of $0,\pm2,\pm4,...,\pm\upsilon$ if υ is even and $\pm1,\pm3,...,\pm\upsilon$ if υ is odd. Therefore restricting $\Delta l = \pm 1$ which simplifies the intensity equation for a doubly degenerate mode to:

$$I \propto \frac{\left(\upsilon \pm l + 2\right)}{2g_\upsilon} \tag{2.29}$$

where υ is the lower of the two vibrational quantum numbers υ' and υ", l is equal to l", and g_υ is equal to 1 when either l' or $l'' = 0$, or 2 when l' and $l'' \neq 0$. The g_υ term originates from the restriction of having one of the angular momentum states equal to zero, thus restricting rotational branches to P and R, or Q, and not all three as when l' and $l'' \neq 0$. Since we are assuming a constant rotational envelope function, independent of internal energy and rotational structure, this term only affects the overall intensity of the rovibrational transition. We can forego this term is we consider the exact rotational structure of each band, however in this case of IR emission over a broad range of internal energies, the constant rotational envelope is sufficient. If we consider two or more independent doubly degenerate states, Eq. 2.28 can be generalized to:

$$I \propto \prod_k \frac{\left(\upsilon_k \pm l_k + 2\right)}{2g_{\upsilon_k}} \tag{2.30}$$

for all doubly degenerate bands with $|\Delta\upsilon|=1$.

References

(1) Wang, H.; Palmer, R. A. *Two-Dimensional Correlation Spectroscopy*; American Institute of Physics: Kobe-Sanda, Japan, 1999.

(2) McNavage, W.; Dai, H.-L. *J. Chem. Phys.* **2005**, *123*, 184104/1.

(3) Yu, Z.-W.; Chen, L.; Sun, S.-Q.; Noda, I. *J. Phys. Chem. A* **2002**, *106*, 6683.

(4) Jung, Y. M.; Czarnecki-Matusewicz, B.; Ozaki, Y. *J. Phys. Chem. B* **2000**, *104*, 7812.

(5) Elmore, D. E.; Dluhy, R. A. *Appl. Spectr.* **2000**, *54*, 974.

(6) Noda, I. *Appl. Spectr.* **1990**, *44*, 550.

(7) Wilhelm, M.; Nikow, M.; Dai, H.-L. *Journal of Molecular Structure* **2008**, *883-884*, 242.

(8) Noda, I. *Appl. Spectr.* **1993**, *47*, 1324.

(9) Lambert, J. D. *Vibrational and Rotational Relaxation in Gases*; Clarendon Press: Oxford, 1977.

(10) Herman, M.; Campargue, A.; ElIdrissi, M. I.; Auwera, J. V. *J. Phys. Chem. Ref. Data* **2003**, *32*, 921.

(11) Haarhoff, P. C. *Mol. Phys.* **1963**, *7*, 101.

(12) El Idrissi, M. I.; Zhilinskii, B.; Gaspard, P.; Herman, M. *Mol. Phys.* **2003**, *101*, 595.

(13) Legay-Sommaire, N.; Legay, F. *J. Mol. Spec.* **1962**, *8*, 1.

(14) Tipping, R. H. *J. Mol. Spec.* **1976**, *61*, 272.

(15) Maki, A.; Quapp, W.; Klee, S. *J. Mol. Spec.* **1995**, *171*, 420.

(16) Pauling, L.; Wilson Jr., E. B. *Introduction to Quantum Mechanics*; Dover: New York, 1935.

(17) *Multiple methods are available to solve the problem, including ladder operators as described by Maki.*

Chapter 3

Vibrational modes of the vinyl and deuterated-vinyl radicals

3.1 Introduction

Following the initial report of the detection of fundamental transitions of all nine vibrational modes of the vinyl radical[1] by time-resolved IR emission spectroscopy, we have re-examined the assignments of the vibrational modes through isotope substitution. Precursor molecules vinyl chloride-d_3, vinyl bromide-d_3 and 1,3butadiene-d_6 are used for generating vibrationally excited vinyl-d_3 through 193 nm photolysis. The non-deuterated versions of these molecules along with vinyl iodide and methyl vinyl ketone are used as precursors for the production of vinyl-h_3. IR emission following the 193 nm photolysis laser pulse is recorded with nanosecond time and ~8 cm^{-1} frequency resolution. A room temperature acetylene gas cell is used as a filter to remove the fundamental transitions of acetylene, a photolysis product, in order to reduce the complexity of the emission spectra. Two-Dimensional Cross-Spectra Correlation Analysis is used to identify the emission bands from the same emitting species and improve the S/N of the emission spectra. Isotope substitution allows the identification of several low frequency vibrational modes. For C_2H_3, the assigned modes are the ν_4 (CC stretch) at 1595, ν_5 (CH_2 symmetric bend) at 1401, ν_6 (CH_2 asymmetric + αCH bend) at 1074, ν_8 (CH_2 + αCH symmetric out-of-plane bend) at 944, and ν_9 (CH_2 + αCH asymmetric oop bend) at 897 cm^{-1}. For C_2D_3 the modes are the ν_5 (CD_2 symmetric bend) at 1060, ν_6 (CD_2 asymmetric + αCD bend) at 820, and ν_8 (CD_2 + αCD symmetric out-of-plane bend) at 728 cm^{-1}.

Vinyl radicals in both the condensed and gas phases have been of critical importance in reaction pathways as intermediates in reactions involving small organic molecules.[2] Such small olefinic molecules have also recently garnered much interest as models for larger, more complex systems of reactions.[3,4] On the other hand, radical species such as vinyl are often hard to characterize and identify due to their transient, short lived nature as well as their low abundance. This is particularly true for the observation of these radicals through vibration spectroscopy in the infrared (IR) region due to their small transition dipole moments for vibrational motions.

In contrast to the wealth of information on the excited electronic states[5-15] as well as the production of the vinyl radical,[16-24,25-32] there have been relatively fewer reports on the vibrational modes of the ground state of the vinyl radical.[33-35] Kanamori *et al.*,[33] first detected one pure c-type band, the ν_9 mode, at 895 cm^{-1} by IR diode laser kinetic spectroscopy and determined the barrier height of the double minimum potential of the αC-H in plane oscillation. There has also been work done on ground state vinyl in noble gas matrices.[36-39] Shepherd *et al.*[36] used carbon-13 and deuterium substituted ethylene to generate vinyl radicals and reported an out-of-plane (oop) bending mode at 900 cm^{-1}, labeled the ν_7 band[40], for C_2H_3 and the corresponding frequencies from six other isotopomers. Forney *et al.* also reported the observation of this band in matrices.[39] A more recent work by Tanskanen *et al.*[37] identified the ν_5 and ν_7 bending modes[40] for six isotopomer, including C_2H_3 and C_2D_3, of the vinyl radical in noble gas matrices. The vinyl produced was generated from the photolysis of acetylene and annealing the matrix to mobilize hydrogen atoms. In these prior matrix works, the observed mode was incorrectly assigned to ν_7 which is the lowest energy in-plane (ip) bending mode. It is

now correctly labeled as ν_9, the lowest energy oop bending mode. The most recent work on the IR signature of the vinyl radical was done by using a synchrotron to irradiate ethylene in solid Ne at 3 K.[41] Wu and coworkers found 7 of the 9 modes of the $^{12}C_2H_3$ and $^{13}C_2H_3$ radicals and 6 of the 9 modes of the C_2D_3 radical.

Time-resolved Fourier transform IR emission spectroscopy[42-45] (TR-FTIRES) has been applied for the spectroscopic identification of the vibrational modes of several transient radicals, including vinyl,[1] cyanovinyl[46], HCCO[47] and OCCN.[46,48] In its first application which resulted in the initial report[1] of all nine vibrational modes of the vinyl radical, four different precursor molecules were utilized to generate vibrationally hot vinyl radicals through UV laser photolysis. Vibrationally excited vinyl generated through precursor photolysis would emit IR photons through the IR active modes which can be detected with time and frequency resolution in TR-FTIRES. The experiments were conducted with low pressure (~10-100 mTorr) precursor gas mixed in with >4 Torr Ar buffer gas. Collision with the buffer gas renders less vibrational energy in vinyl. Eventually the IR emission at longer time (10-100 μs) represents the fundamental transitions of the IR active modes. Assignment of the IR emission bands detected in the experiments to the vinyl radical was accomplished through comparison with theoretical calculations and prior studies, and comparison among observations made with the different precursors.

Of the four precursor molecules used in the initial report on the vinyl radical,[1] vinyl bromide and vinyl chloride photolysis yielded significant amounts of vibrationally hot acetylene and other fragments such as HBr/HCl, in addition to vinyl. The 1,3-butadiene precursor also generated some hot acetylene and other unidentifiable fragments

in the photolysis reaction. Methyl vinyl ketone was previously determined to yield vinyl, methyl, and CO with unity quantum yield[18] and no other byproducts. In each of the four cases, a strong band at 1277 cm^{-1} was detected. This band was assigned to the ν_5 CH_2 symmetric bend mode. This assignment caused notable problem in comparison with previous theoretical calculations[49-53] which otherwise have produced both frequencies and intensities in good agreement with experiments for all other modes.

Most recently, Sattelmeyer and Schaefer,[54] using the equation-of-motion coupled cluster theory for ionized states from the anion, calculated the intensity and harmonic frequency of the vinyl vibrational modes with the best theoretical precision. It was found that the ν_5 mode is calculated to be at 1419 cm^{-1}, still much to the blue of the reported 1277 cm^{-1}, with a significantly smaller intensity than in the previous experimental report. This comparison with theoretical calculations called for further examination of the original assignment of the experimentally detected IR emission bands, in particular the one for the ν_5 mode.

It should be mentioned that even though the originally assigned higher frequency CH stretching modes are in much better agreement with theoretical calculations, a recent experimental[55] work by Nesbitt and coworkers using high resolution IR laser absorption of slit-jet cooled sample following photolysis have found the strongest CH_2 symmetric stretching band at 2901 cm^{-1}, much to the red of the originally reported value[1] and the best theoretical harmonic calculation.[54]

In this Chapter, in order to verify the assignment of the previously detected IR emission bands of vinyl, isotopic substitution of three precursors of the vinyl radical and an additional precursor molecule are used. A total of five molecules, vinyl bromide

(VBr), vinyl chloride (VCl), vinyl iodide (VI), 1,3-butadiene (13BD), and methyl vinyl ketone (MVK), and three of their completely deuterated analogs, VBr-d_3, VCl-d_3, and 13BD-d_6 are used as precursors for generating vinyl or deuterated vinyl through photolysis at 193 nm.

Two-dimensional cross spectral correlation (2DCSC) has been developed for deciphering spectral features from different spectra but belonging to the same species.[56] The generalized 2DCSC approach is outlined in Chapter 1. Correlations between spectral features are made based on their frequency and intensity temporal dependence in the time-resolved spectra. The set of emission spectral bands from the same species should share similar time dependence and show positive correlation. Through the application of this method, we should be able to identify the emission features from vinyl and enhance their signal/noise ratio in the spectra obtained from the five precursor molecules.

In order to ensure that the assignment of the emission features to the vinyl radical are not affected by the appearance of emission bands from vibrationally hot acetylene which may be in overlap with the vinyl bands, an IR filter containing room temperature acetylene gas is used to remove fundamental emission from acetylene though absorption. The filter will selectively eliminate emission within the acetylene rovibrational absorption $v=1 \leftarrow v=0$ transitions. This filter is not effective for emission from highly vibrationally excited acetylene. However, as collisions render all excited species to lower energies and emission closer to the fundamental transitions, the acetylene filter can then more effectively remove the acetylene fundamental emission features from the latter-time emission spectra.

The cold chemical filtering experiment reveals that vibrationally hot acetylene is a major product in the photolysis reactions performed. Several emission features can be attributed to vibrationally hot acetylene. Modeling of these features[57] and extraction of the dynamics of highly vibrationally excited acetylene can be used as a starting point to study other acetylenic systems of interest including structural changes, energy transfer, and chemical reaction.[58-61]

In this report, we confirm, with better determined frequency, the assignment of four of the five bending modes and one stretching mode of vinyl (C_2H_3) radical and three bending modes of the deuterated vinyl (C_2D_3) radical. The bending mode, ν_5, is assigned to a band much weaker than the originally assigned, strong band. The new results agree well with recent experimental results and theoretical calculations.

3.2 Experimental

The experimental setup, described in Chapter 1 and previously in the literature,[42,43,45] is briefly outlined here. 193 nm pulses from an excimer laser (Lambda Physik, LPX200, 20 Hz, 10-50 mJ/pulse) were lightly focused into a gas cell with flowing precursor gas mixed in with a noble gas colliding partner. The precursors are vinyl bromide (Aldrich, >98%), vinyl chloride (Aldrich, 99.5%), 1,3-butadiene (Aldrich, >99%), vinyl iodide (Oakwood Products, 90%) or methyl vinyl ketone (Alfa Aesar, 90%). Deuterated precursor molecules include vinyl bromide-d_3 (CDN Isotopes, 99%), vinyl chloride-d_3 (Cambridge Isotopes, 98%), and 1,3-butadiene-d_6 (Cambridge Isotopes, 98%). All precursors were processed with at least one freeze-pump-thaw cycle to improve purity and examined through IR absorption spectroscopy analysis to ensure no

other detectable component present. The colliding gas was typically Ar (Airgas, 99.999%) or He (Airgas, 99.999%). The precursor pressures were kept low (5-20 mTorr) as compared to the noble gas collider (2-8 Torr) to limit secondary reactions and allow quenching of the vibrationally excited molecules before exiting the IR collection area. A cold acetylene gas filter was constructed using a 15 cm long gas cell with KBr windows. Acetylene pressure inside the cell was held between 1 and 10 Torr to provide substantial filtering of the acetylene bands. At 4 Torr acetylene pressure, >90% filtering can be achieved for the moderately strong ν_3 CH stretch mode.

The emitted infrared radiation was collected by a set of 2" curved gold mirrors in a Welsh cell design. The IR emission from the Welsh cell was collected and collimated by a set of KCl lenses, with the focal length, *f*/4, of the last lens matched to the optics in the FTIR (Bruker IFS/66) housing a Michelson interferometer and detector (Judson, J15D14, MCT). The first lens focal length was chosen to accept the largest collection angle from the closest gold mirror based on the separation (approximately 1 cm) between the two halves of the mirror. A 4000 cm^{-1} low pass filter was used to block high frequency emission from folding into the spectra. The signal was amplified by an impedance matched pre-amplifier (Judson, PA-101, DC) coupled to a wide-bandwidth amplifier (Stanford Research, SR-445, 350 MHz, 500 Ω). The amplified signal was sent to a transient digitizer (Spectrum GMBH, PAD82a, 200 MHz, 8 bit) linked to the Opus (Bruker, v4.2) FTIR sampling program. Time resolved step-scan slices were optically triggered and typically taken at 50 or 100 ns intervals with 4-12 cm^{-1} resolution.

3.3 Time resolved IR emission results

3.3.1 IR emission spectra containing vinyl-h_3 features

The products and their energy content from the 193 nm photolysis of each of the five precursor molecules have been characterized via photofragment translational spectroscopy.[16,18-22] All five molecules with the exception of 1,3-butadiene generate a significant quantity of the vinyl radical with acetylene as the other common product. Photolysis of 13BD yields a significant number of possible reaction channels, both molecular and radical, especially evident during the first several μs after photolysis.

The IR emission spectra following the photolysis of the five precursors, obtained without the use of the acetylene gas emission filter, are shown in Figure 3.1. Spectral features assigned to the vinyl radical are given in Table 3.1. The basis for the assignments will be given in the following sections. It should be noted that the relative intensities of the transitions shown in Figure 3.1 as well as subsequent spectra shown are emission intensities which have not been corrected for the experimental response function, and those reported in Table 3.1 are absorption intensities converted from emission intensities that have been corrected for the response function. In the following, the emission spectrum from each precursor is described separately first.

The time evolution of the reaction products of VBr is shown in Figure 3.2. Here, no acetylene filter was used to remove IR emission from the spectra. There are several low energy features that decay rapidly after photolysis with little frequency shift. This is in marked contrast to the two main features at 1100-1400 cm^{-1} and 3000-3300 cm^{-1}. These two features show a slow decay component as well as a large shift in frequency at early times. In the spectra detected following VBr and VCl photolysis, emission from

Figure 3.1. IR emission spectra recorded in between 2 and 3 μs following the photolysis of the five precursor molecules. Spectra are shown without correcting for the detector spectral response. No acetylene filter was used.

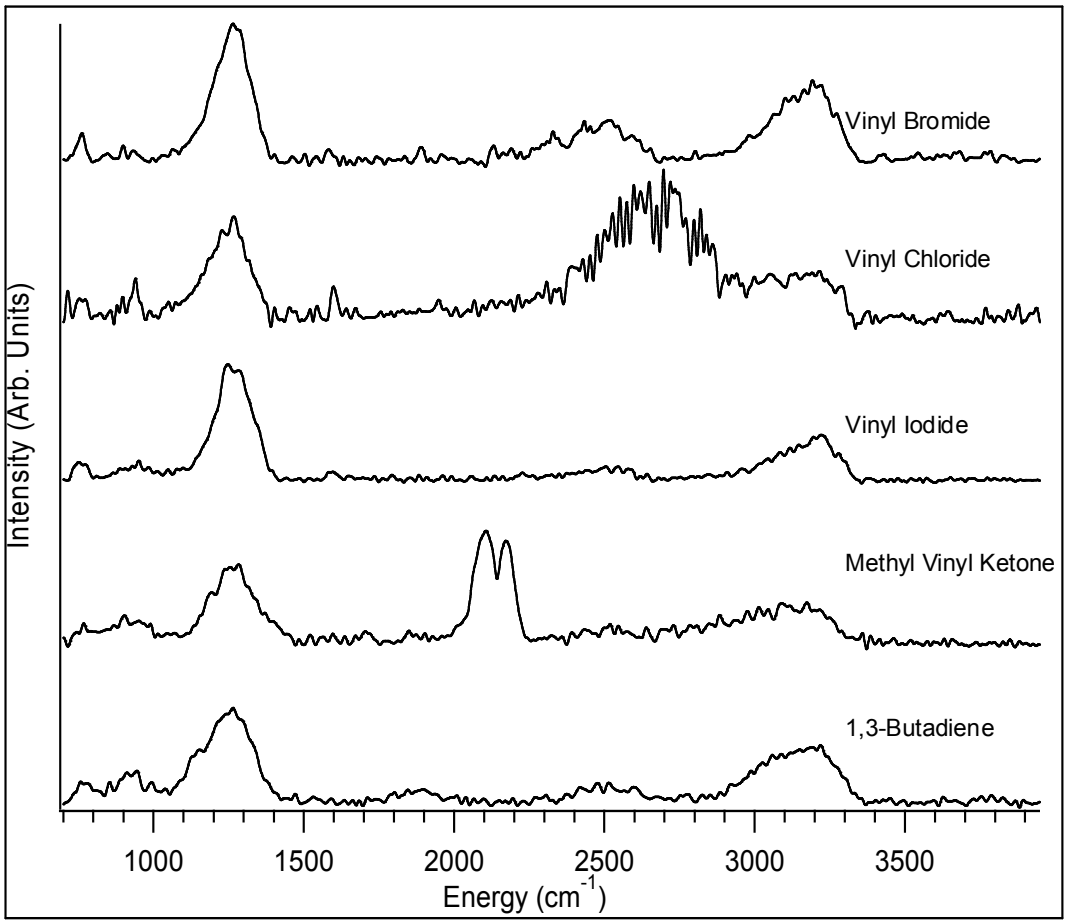

Figure 3.2. Selected time slices, 1, 2, 5, 10, 15, and 20 μs, of IR emission spectra following photodissociation of vinyl bromide. No acetylene filter was used.

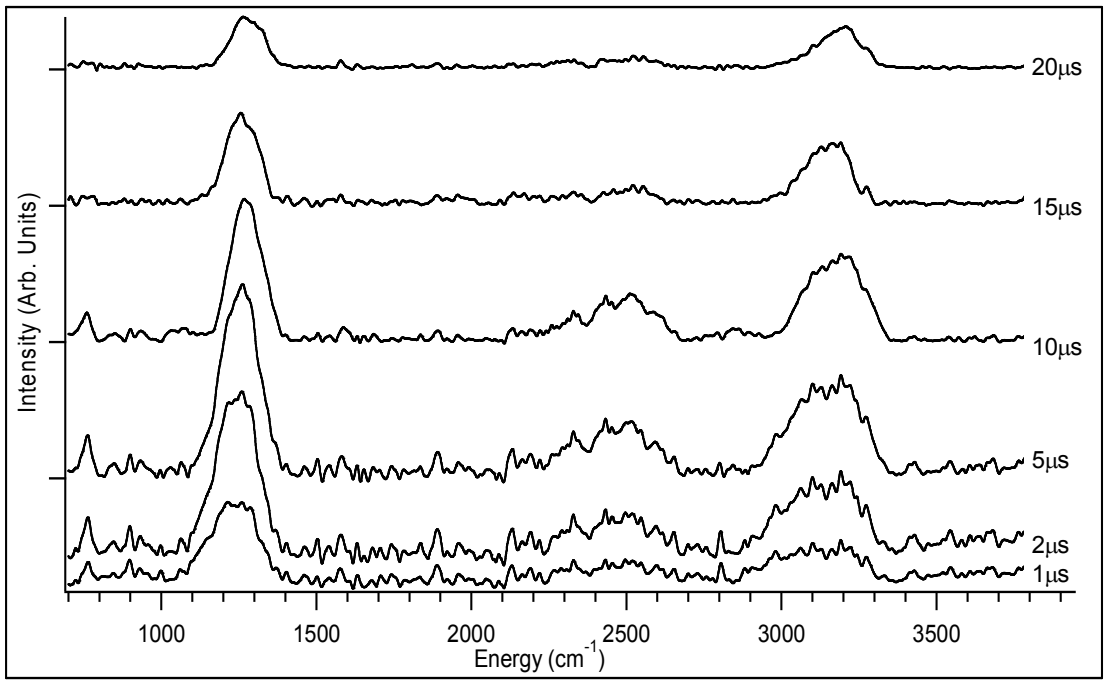

HBr and HCl appear respectively in each case between 2000 and 3000 cm^{-1}. Emission from the υ=6 HBr and the υ=7 HCl have been identified previously in the IR emission observed shortly after photolysis of VBr and VCl.[19,62,63] Accompanying this emission are two main features assignable to acetylene at 1300 cm^{-1} and 3000-3300 cm^{-1}. Some additional low energy emission bands also appear between 1000 cm^{-1} and the detector cut-off around 700 cm^{-1}.

The photolysis of vinyl iodide has been well studied in the condensed phase[38,64] and in the gas phase.[17,65,66] At very low precursor pressures of a few mTorr, atomic iodine emission dominates the spectra. At higher pressures the electronic transitions of iodine are quenched through collisions. Though some iodine emission bands are still apparent at 2500 cm^{-1}, under such experimental conditions vinyl emission could also be detected. Emission assignable to acetylene is apparent in the spectra. HI, however, is not detected.

The dissociation of methyl vinyl ketone[18] leads primarily to methyl and vinyl radicals and CO in a sequential bond breaking mechanism. Emission from hot CO molecules is observed around 2150 cm^{-1}. There may be some emission from methyl radicals, the deformation mode at 1400 cm^{-1} and the CH stretching modes at 3160 cm^{-1}, though these emission bands are masked by the unexpectedly strong emission features of acetylene following the MVK photolysis result as well.

IR emission following 1,3-butadiene photolysis can be complex as there are numerous available reaction channels available for generating molecular and radical products.[21] In addition to the main features attributed to acetylene, there is emission detected as a shoulder on the 1300 cm^{-1} feature. This shoulder may arise from a

vibrationally excited radical other than vinyl, as none of the other precursor photolysis results in emission in this region. There is also extra intensity found on the red side of the CH stretching feature that may also arise from vinyl or other radical products.

The strong feature at 1300 cm^{-1} and a part of the 3000-3300 cm^{-1} bands appearing in all spectra can be assigned to acetylene. The 1300 cm^{-1} feature was previously assigned to vinyl and has been an assignment of contention. This feature is now assigned to the unexpectedly strong $\nu_4 + \nu_5$ combination band. The basis of the assignment which involves substantial modeling of IR emission from vibrationally excited acetylene will appear elsewhere.[57] The same modeling also allows the assignment of part of the group of bands at 3000-3300 cm^{-1} to the acetylene ν_3 mode.

The time-dependence of the emission features provides another consideration for their assignment. In general, primary photolysis reaction products peak within the first several μs, while secondary products and molecules excited though collision energy transfer appear later in the time-resolved spectra. The vinyl features are expected to peak around 1 μs and decay with much faster time constant due to reactions (with the exception in the 13BD case where reactions lead to additional vinyl generation). In contrast, the acetylene emission features should show large anharmonic shifts due to high internal energy content. Its fundamental transitions may occur later (between 2 and 3 μs) and decay with a longer time constant.

Emission from secondary reaction products may become more prominent when the precursor pressure is increased since the amount of these reaction products increases nonlinearly with the pressure. Secondary product emission features also show characteristic, slower rise in time. It has been found that precursor pressures needed to

generate secondary reactions are typically more than 10 times the pressures of the experiments reported here, thus this type of emission has very limited appearance in the spectra. The most apparent secondary product feature found in all five-precursor spectra is the 1600 cm^{-1} C=C stretch of vibrationally excited 1,3-butadiene, which appears most likely through secondary reactions of vinyl with the parent molecules (rather than vinyl-vinyl recombination due to the low vinyl concentration). At even higher pressures, ~100 times the pressures of the experiments shown here, there is collision induced vibrational energy transfer between the excited photoproducts and the parent molecule generating its own molecular IR emission signature of the precursor molecule.

The remaining features common to all five precursors are attributed to the vinyl radical. There are a large number of weak transitions which appear below 2000 cm^{-1}. Assignment can be made based on emission frequency overlap between the different precursor photolysis experiments. Common features exist at ~775, 900, 950, 1050, 1400, and 1600 cm^{-1}. The assignment of these features can be further ascertained utilizing the 2DCSC analysis method discussed below.

3.3.2 IR emission spectra containing features from vinyl-d_3

The reaction energetics and dissociation pathways of the deuterated precursor species should be similar to the non-deuterated ones. The emission spectra recorded, without the acetylene gas filter, for the photolysis of VBr-d_3, VCl-d_3, and 13BD-d_6 is shown in Figure 3.3. These time-resolved IR emission spectra are dominated by two common features at 1000 cm^{-1} and 2300 cm^{-1}. As in the non-deuterated systems, the only

Figure 3.3. IR emission spectra recorded in between 2 and 3 μs following the photolysis of vinyl bromide-d_3, vinyl chloride-d_3, and 1,3-butadiene-d_6. No acetylene-d_2 filter was used.

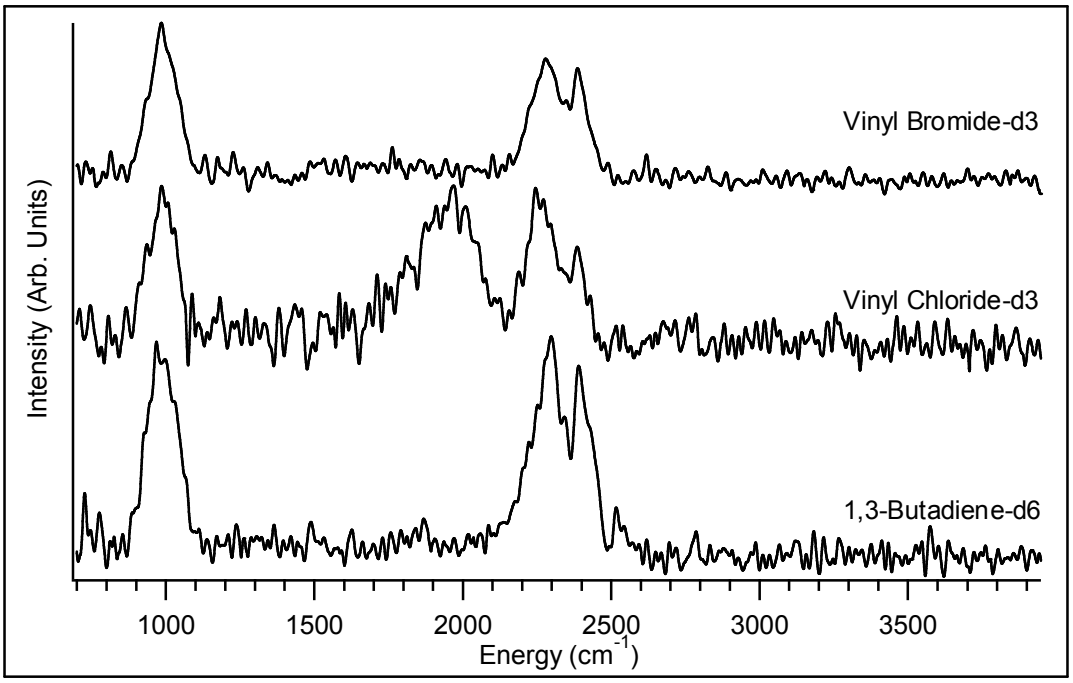

common reaction product other than vinyl that appears to emit in the IR is acetylene-d_2 with its $\nu_4 + \nu_5$ combination band at 1042 cm^{-1} and the ν_3 CD stretch at 2439 cm^{-1}. At longer detection times, typically 10 μs and longer, rotational structure can be seen in both emission features. Partially resolved rotational lines are observed for DBr and DCl between 1500 and 2100 cm^{-1} for the photolysis of VBr-d_3 and VCl-d_3, respectively. Intensities for the DBr and DCl bands are less than those seen for HBr and HCl as expected due to the increase in mass. No other strong emission features are observed.

The temporal behavior of the isotopically substituted molecules behaves analogously to the non-deuterated molecules. Longer peaking time and decay constants are observed for the acetylene-d_2 emission when compared with the vinyl-d_3 bands. There is again an extra feature in the 1000 cm^{-1} band in the 13BD-d_6 spectra that peaks and decays faster than the rest of the intensity, which, can thus be attributed to arising from another emitter. This emission shares a similar fast time decay when compared to the same vibrational modes, accounting for isotopic shift, in the non-isotopically substituted 1,3-butadiene.

The remaining features, three weak bands at ~725, 825, and 1050 cm^{-1}, which are common to all three spectra, seen in Figure 3.3, can be attributed to vinyl-d_3. There are fewer emission bands present in the isotopically substituted spectra than in the vinyl-h_3 case because some of the bands which involve Deuterium atoms shift to lower frequency and out of the detection range. Once again, 2DCSC described below will aid in determining the exact frequency more accurately.

3.3.3 The effect of filtering IR emission by room-temperature acetylene

The room temperature acetylene cell placed in between the photolysis region and the FTIR should filter out the emission in resonance with the absorption transitions of room temperature acetylene. The filtered out transitions include the fundamental transition of ν_3 and ν_5 as well as the $\nu_4 + \nu_5$ combination band in all the spectra.

The filtering of the IR emission is achievable within the bandwidth of the fundamental rovibrational lines. There are two main contributions to the bandwidth. At the low filter pressures of ~10 Torr, collisional broadening contributes approximately 0.003 cm^{-1}. At higher pressures up to 100 Torr, used in some of the filtering experiments with strong IR emission from the photolysis, the pressure broadening becomes comparable to the Doppler width of 0.007 cm^{-1}. Higher vibrational transitions that do not overlap with the fundamental transitions are not filtered by the room temperature cell. Rotational bands generated by acetylene molecules with a high rotational temperature will also pass through the cell unaltered.

The IR filtering result is shown in Figure 3.4. The series of spectra shown here represent several time slices, 1, 2, 4, 10, 15, 20, and 25 μs following the photolysis pulse. Also shown is the cold acetylene absorption spectrum at the bottom. Absorption and emission spectra are scaled independently. The effect of the acetylene gas filter is clear for the ν_5 mode at 730 cm^{-1}, the $\nu_4 + \nu_5$ mode, at 1328 cm^{-1}, and the ν_3 mode at 3289 cm^{-1}. At later time, the two main features (ν_3 and $\nu_4 + \nu_5$) in the emission spectra are almost completely filtered out. The effect of acetylene absorption of emission is also clear when the filtered spectra in Figure 3.4 are compared to the unfiltered spectra in Figure 3.2. At early time, the filter removes emission intensity from the blue side of the anharmonically

Figure 3.4. IR emission spectra, obtained with the acetylene IR filter for times following the photolysis of vinyl bromide. Seven time slices are shown corresponding to 1, 2, 5, 10, 15, 20, and 25 μs following photolysis. The absorption spectrum of room temperature acetylene is shown in the lower graph. The emission curves are normalized to the total emission signal. The absorption spectrum is normalized independently.

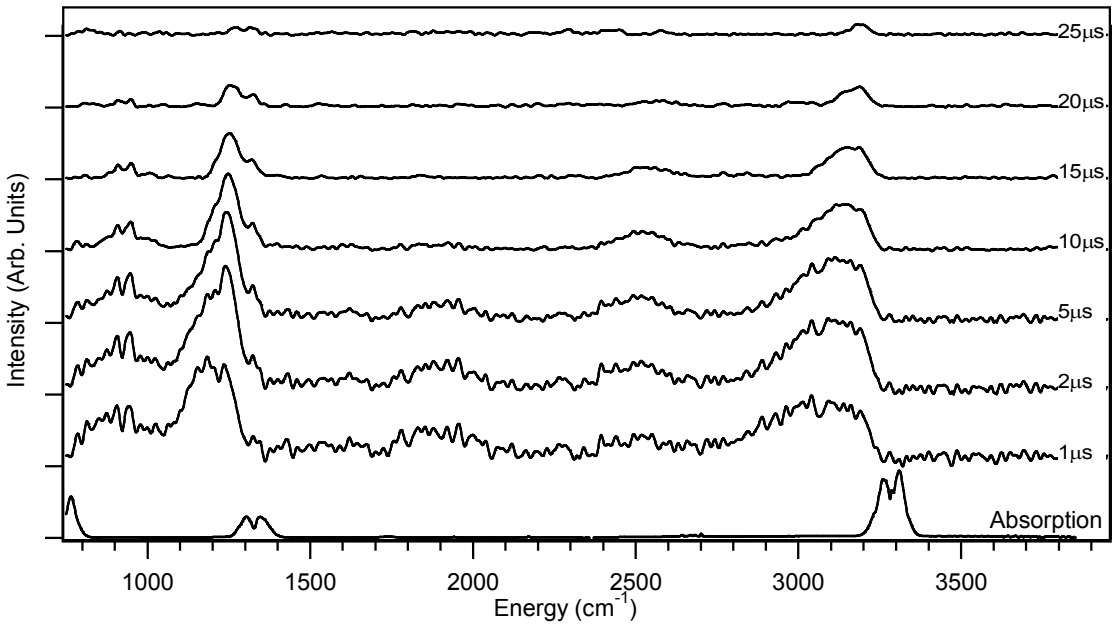

shifted $\nu_4 + \nu_5$ and ν_3 modes. Artificial peaks are generated at 1325 and 3300 cm^{-1} which lie between the rotational bands of the $\nu_4 + \nu_5$ and ν_3 modes, respectively. This is due to the acetylene gas filter acting as a band pass filter and selectively filtering the emission signal within the room temperature rotational band.

3.4 2D-cross spectral correlation analysis

The emission bands assigned to vinyl-h_3 and vinyl-d_3 are weak and fast decaying, thus making definitive assignments difficult, even with the aid of multiple precursors. They can in principle be identified to arise from a common source through a correlation analysis. A common transient source of emission will show similar temporal behavior in intensity and frequency even when generated through different reaction pathways or from different precursors entirely. These emission features from a common source, displaying similar time-dependence, can be expressed with similar phase functions in a Fourier analysis. A correlation analysis can then be employed to identify these phase-matched features and enhance the signal to noise ratio in the spectra.

The 2DCSC analysis was developed[56], based on the general 2-dimensional correlation analysis, for deciphering correlations among spectral features from two different spectra. Briefly, the time-dependent intensity at each frequency in each spectrum is subjected to Fourier analysis and represented by a set of phase-coded sinusoidal functions. The phase correlation among the two spectra generates two 2-dimensional maps –the synchronous and asynchronous maps. The synchronous map is generated by the positive overlap of the phase information for common features. The diagonal of the synchronous correlation map can be extracted to display enhanced S/N

ratio for the correlated features in the spectra. The asynchronous map represents features with different phase information anti-correlated on the off-diagonal points. Features from a common source will show a correlated behavior on these off-diagonal points.

The cross correlation takes advantage of different precursor molecules producing the same radical of interest. Uncorrelated features including random and non-random noise are subsequently reduced. A 5-10 times enhancement of the S/N ratio has been found utilizing the 2DCSC analysis.[56,67] The correlation diagonals from different possible pairs are extracted from their synchronous maps to display the common emission features with enhanced S/N: the correlated spectral peaks appear with enhanced intensity while the noise as uncorrelated intensity is suppressed. We can further enhance the S/N by combining the different correlation diagonals from different pairs of precursors producing a spectra that is representative of common emission features from five different sources.

3.4.1 Analysis of spectra containing vinyl-h_3 emission

The main source of spectral information is found in the synchronous map generated from the 2DCSC analysis. A sample map for the VBr and 13BD unfiltered emission experiments is shown in Figure 3.5. Strong correlations involving the two main features at 1100 - 1400 and 3000 - 3300 cm^{-1}, corresponding to emission from the $\nu_4 + \nu_5$ and ν_3 modes of acetylene respectively, are evident. In addition, there are less intense correlation features near 1900 and 2500 cm^{-1}. The 2500 cm^{-1}feature may arise from HBr emission and possibly weak overtones of acetylene, $2\nu_4 + 2\nu_5$ at 2260 and and $\nu_2 + \nu_5$ 2703 cm^{-1}. The 1900 cm^{-1} emission may arise from the combination $2\nu_4 + \nu_5$ acetylene

Figure 3.5. 2DCSC synchronous map for the VBr-13BD correlation pair. The color scheme for the relative magnitude is shown on the right.

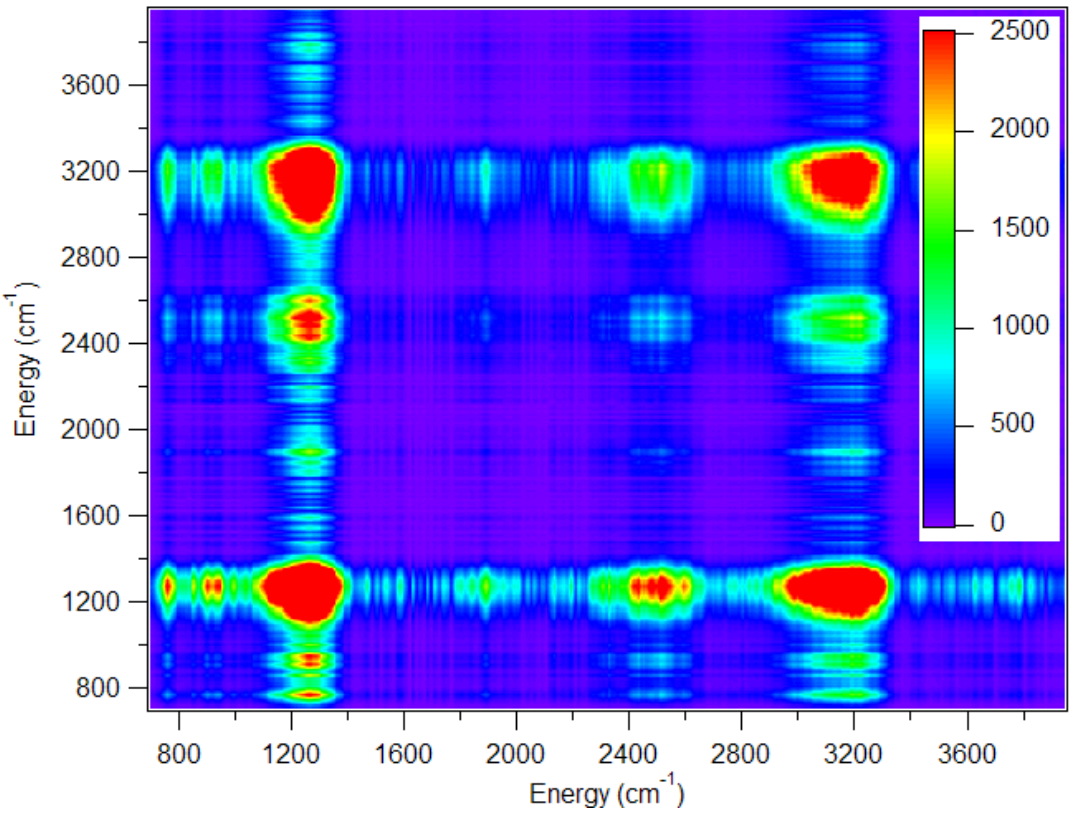

mode at 1941 cm^{-1}. The two main emission features at 1100 - 1400 and 3000 - 3300 cm^{-1} are so strong that they generate off-diagonal correlation features with all other observed emission. In the low frequency bending region from 700 – 1700 cm^{-1}, there are off diagonal components at 765, 855, 895, 945, 1000, 1040, 1065, 1410, 1475, 1540, and 1590 cm^{-1}, in addition to the main feature that stretches from 1100 – 1400 cm^{-1}. Only some of these features correspond to vinyl emission.

One way to utilize the correlation diagram to efficiently view the positive correlation between the two correlated spectra is the diagonal of the synchronous map.[56] The diagonal displays the peaks that commonly exist in both spectra and its magnitude corresponds to the strength of the correlation. The vinyl radical's five precursor molecules allow a total of 10 independent 2DCSC diagonals to be generated. All 10 synchronous diagonal spectra are shown in Figure 3.6. The correlation diagonals are generated from unfiltered emission spectra. The correlation diagonals are obtained using all (~500) of the observable emission spectra in the typical time span from 0 - 50 μs. Emission features with varying intensity are identified in 5 distinct regions in the correlations, as labeled in the figure.

In region 1, there is some low intensity bending mode emission that is detectable down to the detector cut-off at ~700 cm^{-1}. The most prominent peak at around 1275 cm^{-1} in the spectra occurs in region 2 with several weak, close lying but visibly independent emission bands to the red and blue of this main feature. These other bands show a faster decay rate when compared with the main feature. There are some small features that lie just to the blue of region 2, one of which is common to all the spectra, but most just being

Figure 3.6. 2DCSC synchronous diagonals of the 10 correlation pairs from the five precursors. The spectra are grouped into five regions, labeled 1-5, for discussion. Each curve is normalized independently and shown on the same scale. The correlation diagonals are generated from unfiltered spectra. The complete emission signal, typically from 0 – 50 μs, is included in the correlations.

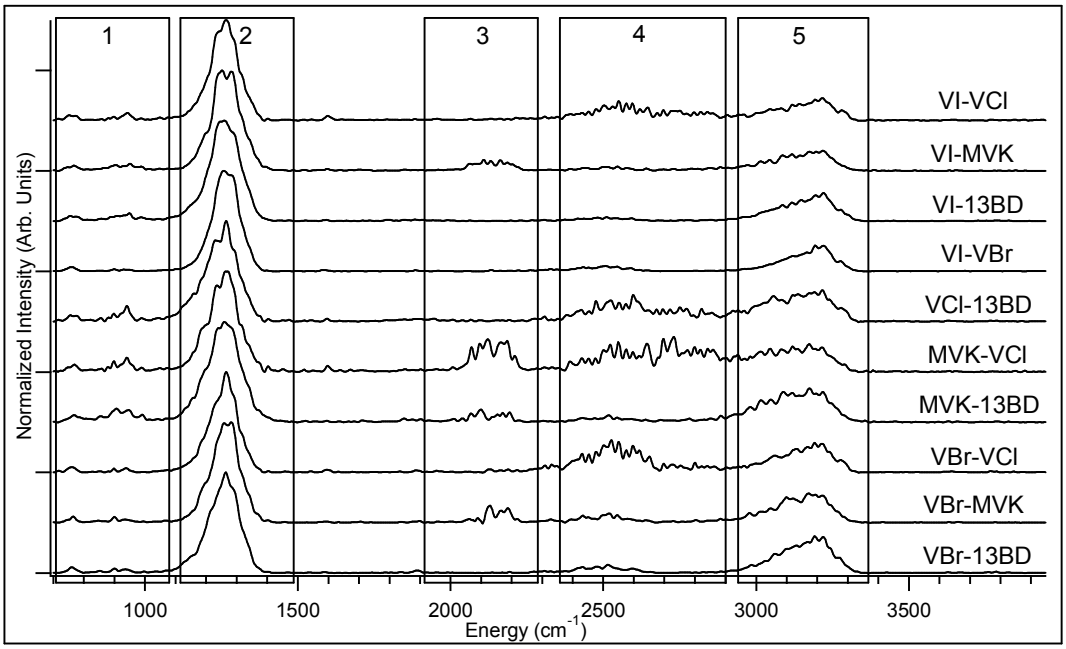

noise. Region 3 contains a feature that can be attributed to the very intense CO stretching mode at 2145 cm^{-1} produced in the photodissociation of methyl vinyl ketone. Even though the other precursors do not produce CO, the intensity of the CO emission in the MVK spectra, being several orders of magnitude higher than any other emission in all precursor spectra, spills over into the correlation diagonal. This feature does not appear in the correlations without MVK. Region 4 contains HBr and HCl emission, located between 2300 and 3100 cm^{-1}, generated from VBr and VCl photolysis. There is also an unresolvable feature in the spectra from VI, MVK, and 13BD, where no HBr or HCl is generated. This weak feature has no discernable structure, nor any detectable anharmonic shift. Though this feature lies close to the $\Delta\upsilon=2$ transition for the combination $\nu_4 + \nu_5$ mode of acetylene and the strength of the combination band suggests that this overtone band, though weak, can be observed, the true origin of this feature remain undetermined. All CH stretching is observed in region 5 as an unresolved feature. The ν_3 CH stretch of acetylene at 3289 cm^{-1} appears at the blue side of the region. The large irresolvable emission observed in region 5 prohibits further analysis even with the aid of the 2DCSC technique. We expect the three stretching modes of vinyl to be much weaker compared to the bending modes assigned below.[54] This feature can be assigned to the ν_3 emission from acetylene based on modeling of the rotational contour, anharmonic shift, and intensity[57]. There may be a small amount of emission on the red end of the feature assignable to vinyl. A lack of corresponding features found in the deuterated results as well as the weak nature of these features, however, prohibits a definitive assignment here.

Each of the 10 diagonals obtained from 2DCSC represents a correlated spectrum between the two sets of time resolved emission spectra. Comparing the correlation pairs

shown in Figure 3.6, one notices that not all pairs have the same intensity ratios between the spectral peaks. For example, the relative intensity of the two vinyl emission features at 897 and 944 cm^{-1} varies between the different correlation pairs. This is likely due to several reasons. Vinyl radicals are generated with different amounts of internal energy depending on the precursor used. Thus vinyl emission may exhibit slightly different temporal decay/frequency shift characteristics. In addition, there are other factors influencing the correlation intensity, including emission from other sources, systematic and random noise, and pressure fluctuations (~5%) during the experiments. Because of these experimental artifacts on the correlations, the correlation diagonals are used only for frequency determination. The correlation spectra are particularly useful for vinyl as the vinyl radical is produced with low amounts of internal energy and the vinyl peaks are not expected to display much shift with time.[45] (See discussion on the energetics of the photolysis reactions below). Spectral intensities reported are determined directly from the experimentally observed spectra.

The product of all correlation diagonals provides a presentation of the common spectral features in all correlated spectra with much enhanced S/N for identifying where the spectral peaks are located. The magnitude of the points along the diagonal of each pair of spectra is numerically proportional to the product of the spectral intensities. The apparent intensity ratios of the features in the product of the 10 diagonals are approximately proportional to the 20^{th} power of the original vales.[56] The features that appear in all of the spectra are greatly enhanced in magnitude whereas the noise, uncommon to all spectra, is dramatically suppressed. While the 'intensity' in the product spectra is greatly altered from the actual strength, the spectral frequency remains accurate

throughout the analysis for peaks that show little anharmonic shift with time.[67] The overall correlation of all emission spectra can be approximately represented by the 20th root of the product of the 10 diagonals. The resulting spectrum is referred to as the geometric mean (GM) correlation shown in Figure 3.7. The magnitude of the GM correlation is directly in proportion to the relative spectral intensity.

The result shown here is from the correlation diagonals of unfiltered emission spectra. The two main features, 1100 - 1400 and 2900 – 3300 cm^{-1}, correspond to hotbands of the $\nu_4 + \nu_5$ and ν_3 modes of acetylene. There are several features in the low energy region which will be discussed shortly. There is also some intensity between 2000 and 2700 cm^{-1}, which may arise from other emission products HBr, HCl, and CO. There is, however, some emission from other combination bands of acetylene, namely, $\nu_2 + \nu_5$ at 2703 cm^{-1}, $2\nu_4 + 2\nu_5$, near 2660 cm^{-1}, $3\nu_5$ at 2170 cm^{-1}, and $2\nu_4 + \nu_5$ at 1941 cm^{-1}. Assignments of these bands are difficult due to their low intensity and overlap with other emission features.

The inset in Figure 3.7 represents a 10x magnification of the GM correlation spectrum at 700 – 1700 cm^{-1}, which shows several features in the low energy bending region. Feature A coincides with the unfiltered portion of the R-branch of the ν_5 mode of acetylene, though it decays faster than other acetylene peaks. The remainder of this emission feature is cut off due to the detectivity fall-off of the detector. Features B and C are assigned to the out of plane modes, ν_9 and ν_8, respectively, of the vinyl radical. Agreement with theoretical calculations and rotational band contour fitting, discussed below, support this assignment. Peaks D and E are assigned to vinyl even though they are in close proximity to the most intense acetylene feature. These features can not be

Figure 3.7. The geometric mean (GM) of the square root of each of the 2DCSC diagonals in Figure 3.5 in the region from 700 - 3500 cm^{-1}. The inset curve represents 10 times magnification in the region 700-1700 cm^{-1}. Labeled peaks (A-F) are discussed in the text. The * represent rotational bands of the two oop bending modes of vinyl. The curve is generated from the correlation diagonals of unfiltered emission spectra from Figure 3.6.

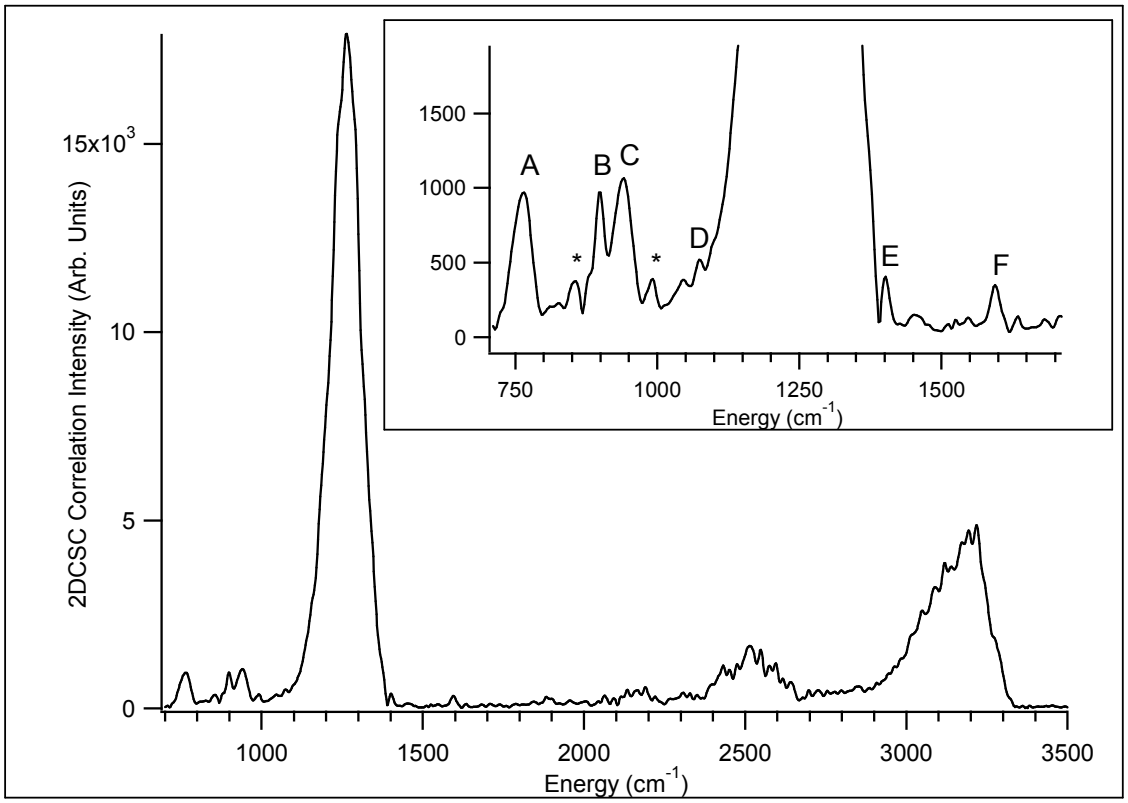

from acetylene: peak D lies too far to the red to be from highly vibrationally excited acetylene, while peak E lies over 70 cm^{-1} to the blue of the acetylene $\nu_4 + \nu_5$ band. Peak F can be assigned to the C=C stretch of vinyl. Its fast time decay profile matches the other features attributed to vinyl. This feature should not arise from the secondary reaction product 13BD because the low precursor pressure used in our experiment greatly reduces secondary reactions. In addition, emission from 13BD has only been observed in higher pressure experiments and at much later time.[1,62]

The band centers of the assigned features correlate well to those harmonic frequencies reported by Sattelmeyer and Schaefer.[54] The accuracy of the harmonic frequencies generated by EOMIP-CCSD/cc-pVQZ has been stated to be within 100 cm^{-1} of experimental frequencies without anharmonic corrections.[68,69] However, linear correlations between experimental anharmonic results and harmonic calculations have yielded corrections of ~0.95-0.96[55,70-72] depending on the molecule and level of theory used. Nonetheless, we expect the frequency correction to be small because of the low frequencies of modes in the bending region. In addition, the low frequency vibrations do not exhibit a detectable shift in frequency as seen in Figure 3.2 even with 30-80 kcal/mole (see Table 3.2) of internal energy.

All assigned low energy vibrational modes are listed in Table 3.1 together with the calculated vibrational frequencies for comparison. All reported experimental frequencies are obtained from band contour fitting. Rotational fits were used for ν_8 and ν_9, while Gaussian profiles were used for the remaining features. During the entire data

TABLE 3.2. Major products and exothermicities of 193 nm photolysis of the five precursor molecules. Only those channels generating vibrationally excited products that are detectable through IR emission are listed. VCl, VBr, and VI enthalpies are taken from [79] while MVK and 13BD are from [1]. The * indicates electronic excitation.

Precursor Molecule	Photolysis Product	ΔH (kcal/mole)
C_2H_3Cl	$C_2H_3 + Cl$	-58
	$C_2H_2 + HCl$	-123.7
C_2H_3Br	$C_2H_3 + Br/Br^*$	-69/-59
	$C_2H_2 + HBr$	-123
C_2H_3I	$C_2H_3 + I/I^*$	-86/-79
	$C_2H_2 + HI$	-122
$CH_3COC_2H_3$	$CH_3 + C_2H_3 + CO$	-46.4
	$CH_3 + C_2H_2 + H + CO$	-9.1
C_4H_6	$C_2H_3 + C_2H_3$	-31
	$C_2H_4 + C_2H_2$	-108

collection time period following the photolysis of the precursor molecule, many species are emitting IR signal with different time behavior. These species include primary photolysis and secondary reaction products. In the overall 2DCSC, correlations appear for all pairs of emission features and render the diagram complex for interpretation. This complexity may be reduced if the duration of time period for correlation examination is restricted to a shorter duration. For example, if the correlation is restricted to the initial time period, the emission features from the primary reaction products are dominant while the contributions from the secondary products are reduced. This practice of correlation with reduced time duration is hereafter termed "pseudo-time correlation".

Figure 3.8 shows four GM pseudo-time correlations taken 2 μs apart with 20 time slices included in each correlation. The first four pseudo-time correlations, corresponding to the observation time 0 – 8 μs are shown. The pseudo-time correlations are taken from unfiltered spectral data. The labeling of the peaks is the same as in Figure 3.7. The 5 vinyl features, peaks B – F, reach maximum intensity at 1-2 μs and decrease with little vibrational shift indicating low vibrational energy content after photolysis. This is in marked contrast to the acetylene features which show much larger anharmonic shift in the ν_3 CH stretch at 3000-3300 cm^{-1} and the $\nu_4 + \nu_5$ combination band at 1100-1400 cm^{-1}. In addition, the lifetimes of the acetylene features are significantly longer than those of the vinyl features. Emission near the fundamental transitions of acetylene has been measured to be longer than the diffusion-limited 60 μs.

Because of the reduced number of time slices included in the correlation, the pseudo-time correlated spectra may contain unintended effects such as increase in noise,

Figure 3.8. The GM pseudo-time correlations of the 10 diagonal psedo-time correlations pairs during the first 8 μs after the precursor photolysis from 700 – 3500 cm^{-1}. Each time correlation encompasses 2 μs duration. The four correlation spectra are presented with lighter to darker shades as time progresses. The labeled peaks are the same ones identified as in Figure 3.7 and discussed in the text. The * represent rotational sidebands for the two oop vibrations of the vinyl radical. The correlations are generated from unfiltered emission spectra. The inset is a 5x magnification of the 700 – 1700 cm^{-1} region.

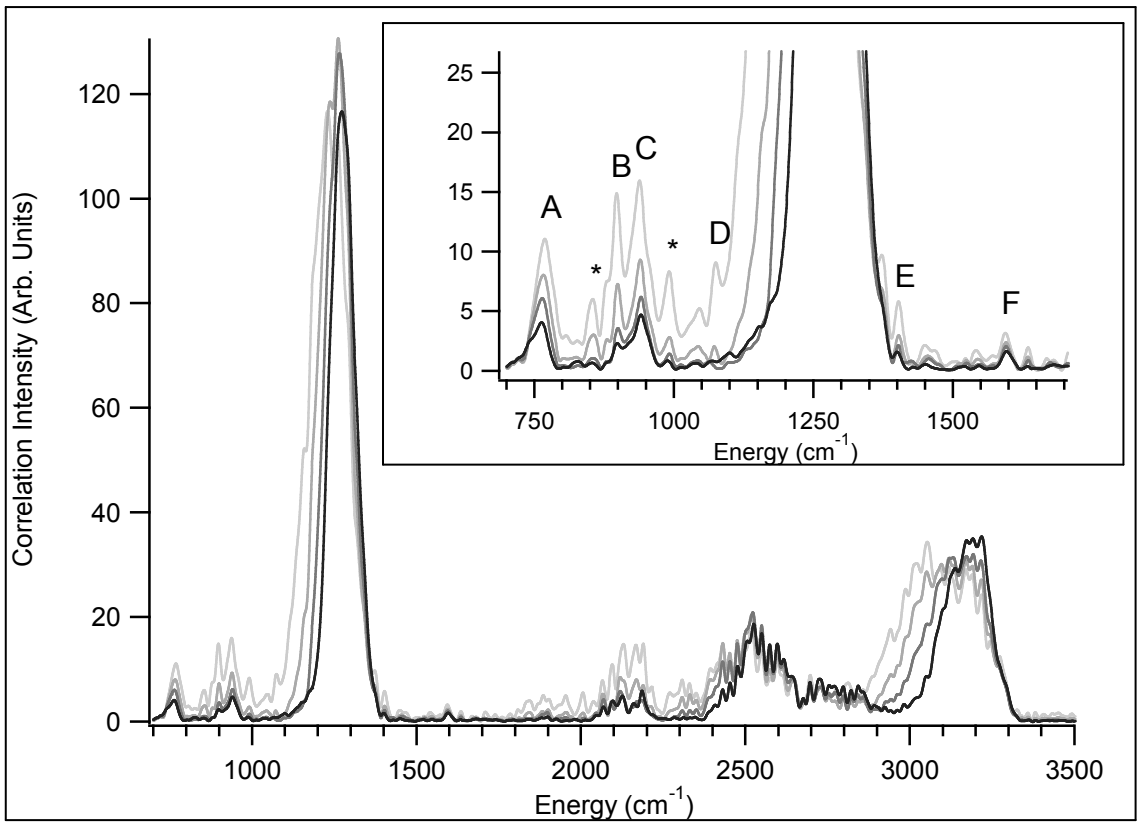

as seen in congested low frequency region in Figure 3.8, and less accurate intensity representation for the spectral peaks. As the time evolution of the system is truncated and the integration windows are smaller in the pseudo-time correlations, the relative spectral intensity may appear different in different set of correlations using different time-windows. This is observed in the pseudo-time correlation in Figure 3.8, where peaks C, B, D, E, and F, which are all assigned to vinyl, appear with decreasing intensity, C>B>D>E>F. The overall correlation in Figure 3.7, however, shows the intensities of peaks B and C are approximately equal, and the intensities of peaks D, E, and F are weaker with the trend D>E>F. Because of these discrepancies, the intensities are determined directly from experimentally measured, unprocessed spectra.

One of the two out-of-plane bending modes has been previously determined at 897 cm^{-1} by high resolution techniques.[33-35] Recent *ab initio* calculations have placed the two out-of-plane modes at 850 and 965 cm^{-1}.[49,54,73,74] The rotational band contour of the two C-type transitions are modeled here using asymmetric rotor calculation (XASYROT)[75] with rotational constants either measured by Kanamori[33] or calculated by Gaussian 03.[76,77] The rotational band contour fits were performed on the 2DCSC diagonal spectra. One such correlation diagonal spectrum and its rotational contour fit for both the 897 and 944 cm^{-1} bands are shown in Figure 3.9. The rotational contour fitting of the correlation diagonal of MVK and 13BD is shown. The correlation diagonal is generated from unfiltered emission spectra. Note that in fitting the 2DCSC diagonal spectrum the intensity of the rovibrational transitions is squared. In the rotational band contour calculation, a Watson asymmetric top Hamiltonian with A-reduction[75,78] was used to generate rotational states for the lower and upper vibrational levels

Figure 3.9. Band contour fitting (in black) of the features in the 800 – 1000 cm^{-1} region. The rotational fitting of the MVK-13BD pair is shown. The two out-of-plane vibrations (ν_8 in triangle points, ν_9 in circle points) of the vinyl radical contribute to the emission features. The MVK-13BD correlation pair is generated from unfiltered emission spectra.

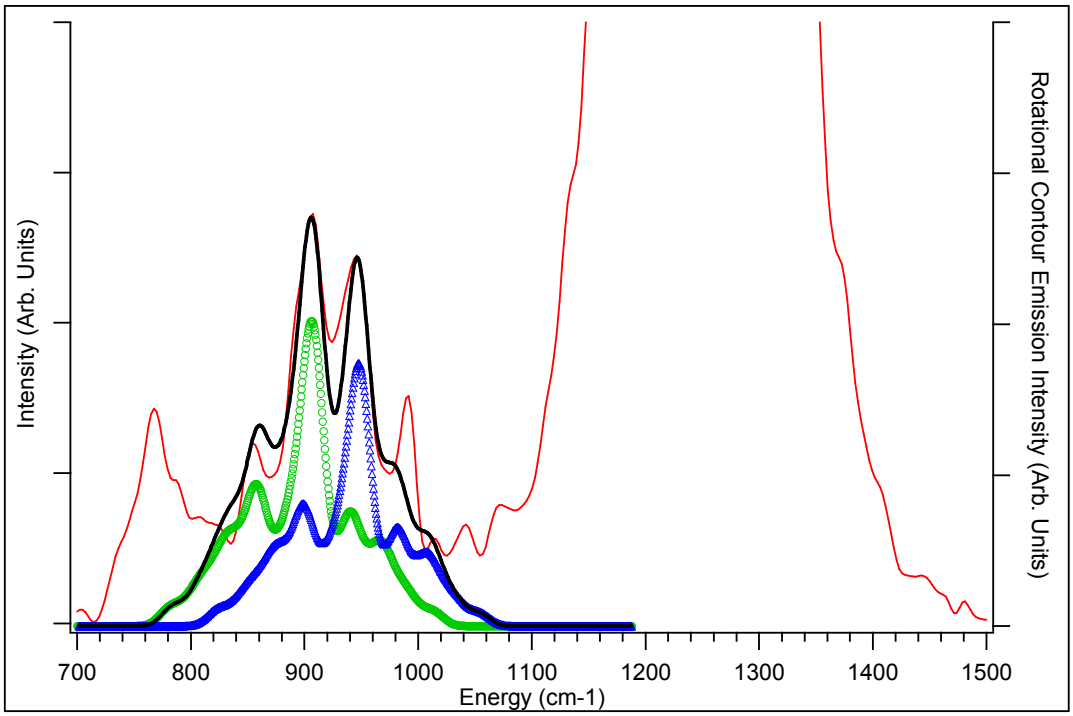

independently. Molecular constants, transition types, and nuclear spin statistics for the vinyl modes have been previously established.[33] To diagonalize the Hamiltonian matrix for the near-prolate symmetric rotor (A>B~C), representation I^r was utilized to define the inertial axes. The emission transitions are from a rotational population defined by a temperature. Only first order transitions with $\Delta K=0, \pm 1$ are included. A least-squares fit was performed to yield two band centers at 897 and 944 cm^{-1} respectively with a rotational temperature of 350 K. This temperature is justifiable: Vinyl molecules may be generated with a high degree of rotational energy, however, several hundred collisions with the buffer gas would have cooled the rotational temperature. The bandwidth resolution of 12 cm^{-1} was imposed in the calculation. It is found that the temperature is weakly correlated with the resolution width.

3.4.2 Analysis of spectra containing vinyl-d_3 emission

Isotopic substitution of the three vinyl radical precursors, VBr-d_3, VCl-d_3, and 13BD-d_6 has the distinct advantage of providing deuterated vinyl, C_2D_3, which affords the opportunity to test the C_2H_3 assignments through the isotope effect. It is anticipated that the frequency of the vibrational mode will change according to the change of the normal mode mass while the intensity remains relatively unchanged with respect to the unsubstituted molecule. Through complete deuteration of the molecules, each vibrational mode containing H/D motion in the vinyl molecule will display a vibrational frequency shift ~ 1.3 from the deuterated to the hydrogenated molecule, Table 3.1. The only exception to this is the ν_4 C=C stretch whose mass contains very limited contribution from the H/D atoms and thus shows a very small isotopic shift of 1.06. The isotopic

Figure 3.10. The GM of the set of 2DCSC diagonals of the correlation pairs from the three deuterated precursors in the region 700 – 3500 cm^{-1}. The inset represents a 1.5x magnification of the 700 – 1200 cm^{-1} region. The labeled peaks have the same assignment as the vinyl-h_3 radical seen in Figure 3.7. Some rotational bands appear near peak C which are labeled with an *. The deuterated result shown here contains correlations of unfiltered emission spectra.

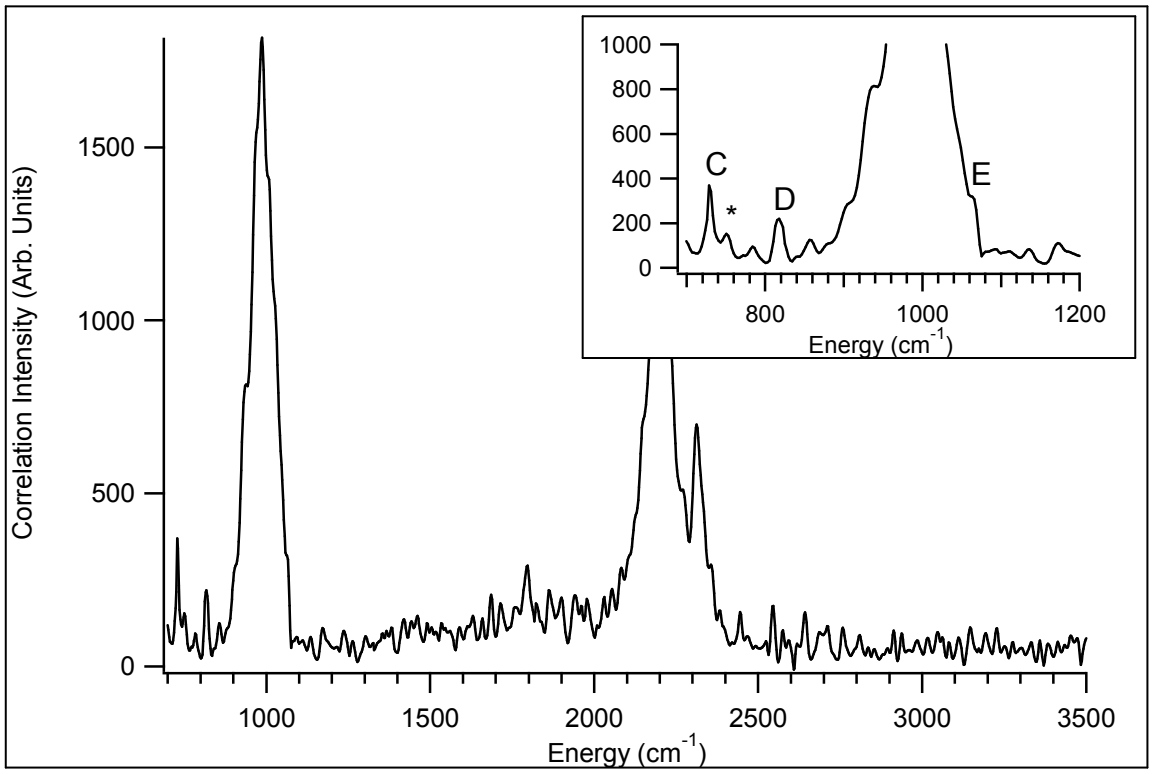

ratios of the vibrational frequencies in Table 3.1 were calculated through Gaussian 03[76,77] DFT calculations utilizing 6-311+G(d,p) basis set.

Spectra taken from deuterated precursor photolysis show emission from vinyl-d_3 as well as acetylene-d_2. Figure 3.10 displays the GM correlation spectrum of the 3 correlation diagonals obtained from the three precursors. The result is based on the unfiltered deuterated emission spectra. The lower quality of the GM correlation is due to the decrease in the number of possible correlation pairs as compared to the non-deuterated result. Only three bending modes of vinyl-d_3 could be identified primarily because of the detector cut-off at ~700 cm^{-1}. Features C, at 728 cm^{-1}, with some rotational structure displayed on the blue side, and D, at 820 cm^{-1}, are clearly visible and correlate well with the corresponding vinyl-h_3 peaks in both frequency and intensity. Feature C has a H:D ratio of 1.30 compared to the calculated value of 1.27. Feature D has a ratio of 1.31 compared to 1.29 determined from the calculation. The combination band of acetylene once again dominates the low energy region, however there is another feature, E, that appears as a shoulder on the strong acetylene band. Feature E is assigned to the ν_5 bending mode of the vinyl-d_3 radical based on pseudo-time correlation analysis, to be presented in Figure 3.11, which allows this shoulder to be separated from the main peak. Feature E displays a 1.32 H:D frequency ratio compared with the calculated value of 1.38. This slightly larger difference between the experimental and theoretical values may have been caused by the uncertainty in the determination of the band centers because of the close proximity to the strong acetylene band. The only other feature in the deuterated correlation diagonal is the CD stretch of acetylene-d_2 between 2000 and 2400 cm^{-1}.

Figure 3.11. Four GM pseudo-time correlations, each 2 μs duration, for the first 8 μs after the photolysis of the deuterated precursors in the range of 700 – 3500 cm^{-1}. The inset is a 2.5x magnification of the 700 – 1550 cm^{-1} region. They are presented with lighter to darker shades as time progresses. Labeled peaks share the same assignment as in Figure 3.7. Some rotational bands appear near peak C and are labeled with an *. The correlations are generated from unfiltered emission spectra.

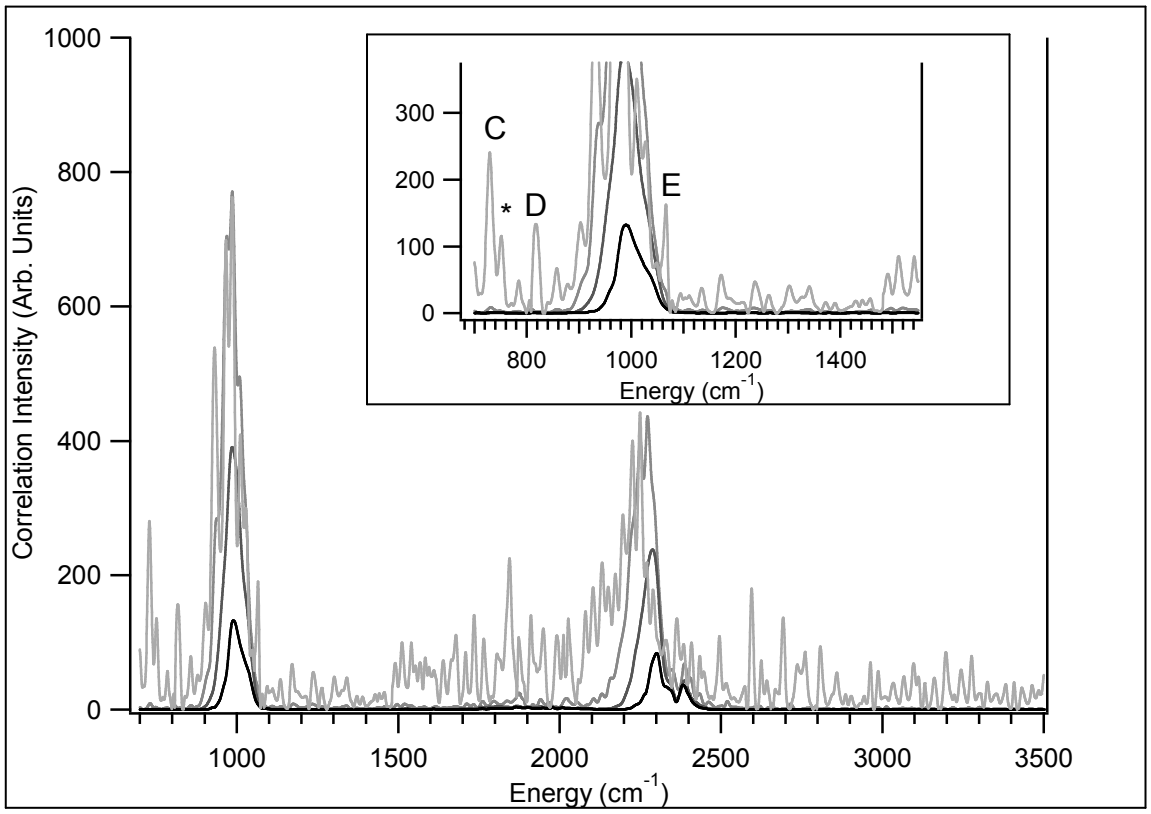

The GM pseudo-time correlation spectra of the deuterated molecules are shown in Figure 3.11 in the range of 700 – 3500 cm^{-1}. The inset is a 2.5x magnification of the 700 – 1550 cm^{-1} region. These correlations are generated from unfiltered deuterated emission spectra. Four GM pseudo-time correlations are shown. Each correlation contains 2μs of emission spectra (20 spectra). The acetylene-d_2 $\nu_4 + \nu_5$ combination and ν_3 CD stretching band at 985 and 2100 – 2400 cm^{-1} show significant anharmonic shifts, while the vinyl-d_3 bands, as expected, do not confirming the vinyl assignment. The three vinyl bands assigned in Figure 3.10, peaks C, D, and E, are observed in the pseudo-time correlations in Figure 3.11. The deuterated precursor pseudo-time correlation seen in Figure 3.11 can also be compared with the pseudo-time correlation for vinyl-h_3 shown in Figure 3.8. Assignments for features C and D in Figure 3.10 are analogous to assignments made from Figure 3.8. In comparison with the overall correlation spectrum, Feature E in the earliest time pseudo-correlation appears as an isolated peak, as opposed to a shoulder in Figure 3.10. Features C, D, and E decay immediately, with time constants of $\tau \sim 0.5\ \mu s^{-1}$, which are similar to the time constants recorded for vinyl-h_3 features. In contrast, acetylene-d_2 displays a later peak time, has a longer decay time, and shows more anharmonic shift in frequency.

3.5 Discussion

3.5.1 Precursor photolysis

The main products of vinyl halides following 193 nm photolysis include vinyl + halogen radicals from the atomic channel and acetylene + hydrogen halide from the molecular channel. The atomic/molecular elimination channel ratio increases with the

halide atom size (0.48, 0.56, >0.8 for VCl, VBr, and VI).[79] This trend can be understood from a combination of their respective carbon-halogen bond energies (95.0, 78.8, and 61.9 kcal/mole) and the relatively unchanged molecular elimination channel heats of reactions (27.1, 26.6, and 25.9 kcal/mole for VCl, VBr, and VI respectively).[17,79] Subsequently it is understandable that there is a lack of emission from HI after photolysis of VI while there is significant amount of HCl and HBr emission from their respective precursors.

Molecular elimination channels producing HCl and HBr with acetylene from vinyl bromide and vinyl chloride have been extensively studied.[19,62,63] HCl emission up to υ=7 and HBr emission up to υ=6 have been recorded as early as 1 μs after the 193 nm photolysis pulse. The HCl/C_2H_2 emission channel has been determined to have a bimodal rotational distribution for HCl of 500 K and 9500 K. The branching ratio between the two matches the ratio of the reaction channels of 0.81:0.19 for 3-center, high-*J* to 4-center, low-*J* rotational distribution. Vinylidene is generated with an internal energy of 35 kcal/mole and its isomerization to acetylene produces a nascent energy of 76 kcal/mole.[80] The HBr/C_2H_2 emission channel has been determined to primarily arise from a three center elimination yielding HBr with a vibrational and rotational temperature of 8690 K and 7000 K respectively and vinylidene with 24 kcal/mole of internal energy.[63] Fast isomerization from vinylidene to acetylene leaves 64 kcal/mole of internal energy in the stable product.

The lack of HI emission after the photolysis of VI is due to the lower yield of the molecular elimination channel. But still vibrationally hot acetylene is observed. We attribute the vibrationally excited acetylene as from the secondary dissociation of

vibrationally excited vinyl. As has been previously determined[13], the energy required to dissociate the vinyl radical into acetylene is 33 kcal/mole, leaving up to 53 kcal/mole available, after the sequential bond breaking of VI, for acetylene and atomic hydrogen and iodine.

The atomic elimination channel produces vinyl + halogen radicals with 53.5, 69.7, and 86.6 kcal/mole of energy following photolysis of VCl, VBr, and VI respectively. Those photolysis exothermicities are significantly less than their corresponding molecular elimination channels (121.4, 121.9, and 122.6 kcal/mole for VCl, VBr, and VI).[79] This offers a possible thermodynamic explanation for why the emission signal obtained from vinyl is not significantly anharmonically shifted as opposed to what is observed with the features from highly vibrationally excited acetylene.

The photodissociation of 13BD is dominated by emission from acetylene. No emission from vibrationally hot ethylene, the reaction co-product, however, is detected. The acetylene emission shows a strong anharmonic shift at early time, indicating acetylene production with a large amount of vibrational energy. The vinyl peaks, however, do not show a strong red shift indicating production with little vibrational excitation. This observation is consistent with exothemicity values of -31 and -108 kcal/mole for vinyl and acetylene dissociation pathways respectively.

Sequential dissociation of methyl vinyl ketone allows for a sufficient amount of internal energy to be partitioned into the vibrational modes of vinyl; however production of vibrationally hot acetylene has not been detected prior to this work. Based on the dissociation of acetone, the methyl radical exits the reaction with 8.4 kcal/mole of internal energy leaving 37.8 kcal/mole of internal energy in the vinyl and CO co-

products. Vinyl radicals therefore have a small amount of internal energy available and thus do not exhibit a large shift in frequency observed for highly energetic molecules such as acetylene. Vinyl dissociation to ground state acetylene requires 33 kcal/mole. It is therefore unlikely that there is any acetylene emission produced from this channel. Another mechanism must exist for the production of hot acetylene. One possibility for the production of the acetylene emission features observed in the photolysis of MVK is a concerted three center elimination with the products being vinylidene and acetaldehyde. This concerted channel involving two bond-breaking and two bond-forming should be more exothermic, leaving a larger amount of energy in the acetylene molecule.

3.5.2 Comparison with noble gas matrix studies

A recent absorption study on vinyl radicals trapped in solid Ne matrices at 4 K has reported 7 of the 9 vibrational modes of vinyl.[41] The symmetric CH_2 stretching mode, reported as 2911 cm^{-1} in solid Ne, is close to the 2901 cm^{-1} value reported by a recent high resolution gas phase study,[55] though they are both substantially lower in energy than the highest level theoretical calculation predictions of 3042 cm^{-1} [41] or 3118 cm^{-1}.[54] This comparison indicates that the matrix has limited influence on the frequency of the vibrational motion, particularly the ones with smaller amplitude of motion. The large blue shift of the theoretical calculation could be due to a significant anharmonic correction needed for the typically anharmonic CH stretching motions.

In comparing the vibrational modes identified here with the matrix results we have found generally good agreement, as shown in Table 3.1. The ν_5, ν_8, and ν_9 modes at 1401 cm^{-1}, 944 cm^{-1}, and 897 cm^{-1} assigned here lie 40-50 cm^{-1} higher in energy than the

matrix results. This is understandable as interaction with the matrix may generate as much as 5% deviation from the non-perturbed value. The ν_4 and ν_6 modes were not detected in the matrix experiment and thus can only be compared with theoretical results in the next section.

There is one remaining low energy mode detected in the Ne matrix study,[41] the ν_7 in plane bend, found at 677 cm^{-1} which has also been observed at 674 cm^{-1} in the action spectra of vinyl.[13] This mode is close to the frequency of peak A in Figure 3.7, observed at 765 cm^{-1}, which was obtained without using the acetylene filter. However the feature is filtered out by the acetylene cell shown in Figure 3.4. This observation dictates that peak A should be assigned to an acetylene fundamental transition. The low frequency ν_5 bending mode of acetylene has its fundamental transition centered at 730 cm^{-1}. As the fundamental transition of this mode is very close to the detector cut-off at 700 cm^{-1}, the red side of this emission feature may have been clipped. Based on this speculation, we assign this peak as a part of the R-rotational branch of the ν_5 transition. Our modeling suggests[57] that this acetylene mode with sufficient vibrational excitation and high rotational temperature shows strong emission to the blue of the fundamental transition, supporting the assignment. The time profile of this feature, on the other hand, appears to have a fast decay similar to those of the vinyl peaks, as seen in Figure 3.8. The temporal behavior, however, does not contradict assigning peak A to acetylene. It is likely that the rotational transitions in this feature are associated with higher rotational levels which can be quenched faster than the lower energy levels and therefore have faster decays.

3.5.3 Comparison with theoretically calculated normal mode frequencies

Compared with recent theoretical work utilizing the EOMIP-CCSD/cc-pVQZ to generate the harmonic vibrational frequencies and intensities for the vinyl radical,[54] our assigned features agree well with calculated frequencies as seen in Table 3.1. For all the modes, except the ν_9 oop bending mode, the experimental anharmonic frequencies are red shifted (94, 18, 3, and 21 cm^{-1} for ν_4, ν_5, ν_6, and ν_8 respectively) from the calculated harmonic frequencies. These discrepancies can be explained by the need of an anharmonic correction for the calculated harmonic frequency in comparison with the fundamental transition frequency since the largest discrepancy appears in the stretch mode (ν_4). A simplistic DFT theory calculation utilizing the 6-311+G(d,p) basis set is performed to estimate the anharmonic correction for the ν_4 mode as 0.981, which corresponds to an anharmonic shift of 31 cm^{-1} and improves the match with the experimentally observed value.

The intensities determined from our study, 3.3:4.2:6.9:100 for ν_4:ν_5:ν_6:ν_8, also agree quite well with the calculated results of 1.4:10.6:12.5:100. The only mode where the intensity is significantly different is again the ν_9 mode. The calculated intensity is 13.7, while the measured intensity is 64.9.

There is some deviation between theoretical calculations and the experimentally determined frequencies for the C=C stretch, assigned at 1595 cm^{-1} but theoretically predicted to lie at 1689 cm^{-1}. This may be due to a larger anharmonic shift when compared to the bending modes. The weak mode was not observed in the deuterated experiments because the mode assigned is the weakest out of all the observed vinyl modes and was only completely resolvable once the five precursor 2D correlations were

combined. With this enhanced S/N ratio obtained from the correlation analysis, there were no observable features around the theoretically predicted value of 1689 cm^{-1}.

3.5.4 Comparison to previously assigned vinyl vibrational modes

In this work five of the nine vinyl (C_2H_3) modes are presented. The absence of assignment for the ν_7 mode is due to the low frequency cut off of the detector, as well as interference from the relatively strong emission from the ν_5 mode of acetylene. With respect to the ν_1, ν_2, and ν_3 stretching modes, the irresolvable feature which contains emission from the ν_3 emission from acetylene prevents accurate determination of their positions and therefore assignment. An accurate assignment of these modes will require production of vinyl in the absence of vibrationally hot acetylene or via high resolution studies, of which the ν_2 mode has recently been observed.[81]

For the remaining five vibrational modes there are two primary improvements in comparison with our first report[1]. The strong 1275 cm^{-1} band that appeared in emission spectra following the photolysis of all precursors and was assigned to the ν_5 mode has now been assigned to an unexpectedly strong combination band emission from hot acetylene. The ν_5 mode has now been identified and assigned at 1401 cm^{-1} with frequency and intensity consistent with theoretical calculations. In addition, the ν_4 mode has been identified and assigned at 1595 cm^{-1}. This mode is the weakest and subsequently only appears very briefly in the emission spectra following photolysis. The application of the 2DCSC technique enables the peak position to be better determined in the average correlation diagonal curves. The remaining modes ν_6, ν_8, and ν_9 along with the ν_6 and ν_8 modes from the deuterated vinyl are consistent with the previous report.

3.5.5 Vinyl-d_3 and the isotope effect

The deuteration of the vinyl radical precursors has allowed the detection of three vibrational modes, ν_5, ν_6, and ν_8, of vinyl-d_3. Their experimentally determined values of 1060, 820, and 728 cm^{-1}, compare with the theoretical values of 1028, 834, and 759 cm^{-1} which are calculated from the theoretical frequencies for hydrogenated vinyl and the isotopic ratios from the DFT calculation. The intensities of these transitions (7.2:9.4:100) agree well with both the theoretical (10.6:12.5:100) and experimental (4.2:6.9:100) values for the vinyl-h_3 molecule. The ν_5 and ν_8 bands of the deuterated molecule also compare well with the vinyl-d_3 in solid Ne work[41] with the ν_5 and ν_8 modes deviating higher by 6% and 3% respectively. The ν_6 mode was not detected in the matrix experiment even though it was predicted to be as intense as the ν_5 mode in this work. In addition, the solid matrix absorption work observed CH (and CD) stretches that have been predicted[54] to be less intense than this unobserved mode. A possible reason for this missing feature in the matrix work could be that the ethylene precursor ν_7 mode absorbing at 950 cm^{-1} overshadows the ν_6 vinyl band.

3.5.6 Emission from highly vibrationally excited acetylene

The 2DCSC analysis and the isotope-substituted vinyl study enabled five of the six low energy vibrational modes of vinyl to be assigned. The assignments are consistent with previous experimental measurements and theoretical calculations.[41,54] A consequence of the identification of these lower frequency modes is that the most intense emission feature at 1300 cm^{-1} does not come from vinyl. There have been speculations on the origin of this intense peak observed in emission spectra detected from all

precursors. One hypothesis proposed by Sattelmeyer and Schaeffer[54] is that this peak belongs to a vibrational motion in the electronic excited state. The width and temporal shift of this feature indicates a large anharmonicity that is consistent with an emitting species with a significant amount of rotation-vibration energy in the emitter. This implies that the emitter is likely not electronically excited as the excitation energy is not large enough to leave substantial rotation-vibration energy in electronically excited products.

Another possible source for this emission is the combination band of acetylene which band center lies at 1328 cm^{-1}.[82] Assigning this feature to a combination band would be unexpected as IR combination bands are usually much weaker than the allowed fundamental transition. The strength of the combination band intensity, on the other hand, scales approximately with the product of the vibrational quantum numbers of the two modes involved and, thus, increases sharply with vibrational energy. In the experiments where a room-temperature acetylene filter is not used, it is observed that the intensity at 1328 cm^{-1} has a much later peak time and slower decay constant, as shown in Figure 3.2, when compared to the vinyl bands and the emissions assignable to highly vibrationally excited acetylene. The anharmonic shift of the feature toward the fundamental transition indicates that this peak arises from the $\nu_4 + \nu_5$ combination band of acetylene. This assignment is further shown by the removal of the fundamental emission of acetylene on the blue side of the $\nu_4 + \nu_5$ and ν_3 features when the acetylene filter is used in Figure 3.4. In the next Chapter, IR emission modeling of the combination band at 1300 cm^{-1} and the CH bands at 3000-3300 cm^{-1} confirms the assignment to vibrationally hot acetylene. Details of this modeling will be reported in the following Chapters. This discovery has also put some restrictions on the assignments of the three CH stretching modes of the

vinyl radical. The three CH stretching modes reported previously lie within the ν_3 mode of vibrationally hot acetylene. Though there is emission intensity detected to the red of this broad ν_3 emission feature that may be assignable to vinyl, the intensity is too weak and with too much interference to be accurately assigned even after the 2DCSC analysis. The stretching modes can not be assigned in the deuterated experiment either due to the overlap of deuterated acetylene emission. This is understandable due to the fact that the frequencies of the deuterated stretching modes are shifted closer together and their intensity is still clustered with emission from the ν_3 mode of vibrationally hot acetylene-d_2. Assignment of the CH stretching modes by this technique may only be obtained in the absence of vibrationally hot acetylene.

From prior studies of precursor photolysis, the production of abundant vibrationally hot acetylene is apparent. All precursor molecules except methyl vinyl ketone have been shown to produce acetylene directly, but with varying amounts of internal energy.[17-21] In addition to direct dissociation channels, vinyl radical generated from precursor dissociation may have sufficient energy for dissociation resulting in significant quantities of highly vibrationally excited acetylene and/or vinylidene which rapidly isomerizes to ground state acetylene. Furthermore, the nacent vinyl from precursor dissociation may absorb another 193 nm photon and dissociate, producing vibrationally hot acetylene.[14,15,53] This channel, though, is considered unlikely under the present experimental conditions. There are currently no absorption cross section measurements of the vinyl radical near 193 nm. A strong $\pi^*(2a'') \leftarrow \pi(1a'')$ band, however, has been observed from 225 – 238 nm with a maximum absorption cross section of ~1×10^{-17} cm^2 molecule^{-1}.[7] The absorption cross section of the vinyl radical at

193 nm is likely to be more than one order of magnitude weaker. The laser fluxes used were typically 30 mJ/cm^2. At this photon flux level, the vinyl generated during the photolysis pulse would in average have a dissociation probability of <1%.

3.6 Conclusion

Photolysis at 193 nm of five precursor molecules, three of them with deuterated isotopomers, has been used to produce vibrationally excited vinyl C_2H_3 and vinyl-d_3 C_2D_3. IR emission from the vibrationally excited molecules, predominantly vinyl and acetylene, is recorded by time-resolved Fourier Transform emission spectroscopy. The emission spectra were analyzed using 2-dimensional cross spectra correlation Analysis for the identification of the bands from the same emitting species. A room temperature acetylene cell is used to eliminate the bands associated with the fundamental transitions of acetylene which appears in abundance as a photolysis product. Emission bands are identified to be associated with vinyl and vinyl-d_3. Comparison with the anticipated isotope shift of the vibrational frequencies, which can be calculated from ab-initio methods, confirms the assignment of the vibrational modes. Altogether four low energy bending modes: ν_5 at 1401 cm^{-1}; ν_6 at 1074 cm^{-1}; ν_8 at 944 cm^{-1}; and ν_9 at 897 cm^{-1} and one stretching mode, ν_4 at 1595 cm^{-1} of the vinyl-h_3 radical have been assigned. Three bending modes: ν_5 at 1060 cm^{-1}; ν_6 at 820 cm^{-1}; and ν_8 at 728 cm^{-1} of vinyl-d_3 have also been determined. Theoretical calculations are in good agreement, except for the ν_9 mode which was found slightly higher in energy and more intense than calculations predict. Calculated isotopic ratios agree with frequency shifts while sharing the same intensity ratio between vibrational modes. The experimental results here reinforce the low

frequency vinyl-h_3 and vinyl-d_3 results found in absorption measurements in low temperature noble gas matrices.

The strongest emission feature near 1300 cm^{-1} appearing in each of the five precursor molecules spectra is not assigned to vinyl. This feature arises from vibrationally hot acetylene which will be discussed in the next Chapter. Vibrationally hot acetylene was produced from the photolysis of VBr, VCl, and 13BD, as expected. It was also observed following dissociation of MVK and VI, which was not previously observed as a primary reaction product. In these cases, it is likely that the vibrationally excited acetylene is produced through another mechanism or secondary dissociation reaction of the vinyl radical and thus warrants further study.

References:

(1) Letendre, L.; Liu, D.-K.; Pibel, C. D.; Halpern, J. B.; Dai, H.-L. *J. Chem. Phys.* **2000**, *112*, 9209.

(2) Okabe, H. *Photochemistry of Small Molecules*; Wiley: New York, 1978.

(3) Fahr, A.; Laufer, A. H.; Klein, R.; Braun, W. *J. Phys. Chem.* **1991**, *95*, 3218.

(4) Donaldson, D. J.; Okuda, I. V.; Sloan, J. *J. Chem. Phys.* **1995**, *193*, 37.

(5) Hunziker, H. E.; Kneppe, H.; McLean, A. D.; Siegbahn, P.; Wendt, H. R. *Can. J. Chem.* **1983**, *61*, 993.

(6) Blush, J. A.; Chen, P. *J. Phys. Chem.* **1992**, *96*, 4138.

(7) Fahr, A.; Hassanzadeh, P.; Atkinson, D. B. *Chem. Phys.* **1998**, *236*, 43.

(8) Pibel, C. D.; McIlroy, A.; Taatjes, C. A.; Alfred, S.; Patrick, K.; Halpern, J. B. *J. Chem. Phys.* **1999**, *110*, 1841.

(9) Ahmed, M.; Peterka, D. S.; Suits, A. G. *J. Chem. Phys.* **1999**, *110*, 4248.

(10) Xu, K.; Zhang, J. *J. Chem. Phys.* **1999**, *111*, 3783.

(11) Tonokura, K.; Marui, S.; Koshi, M. *Chem. Phys. Lett.* **1999**, *313*, 771.

(12) Osborn, D. L.; Frank, J. H. *Chem. Phys. Lett.* **2001**, *349*, 43.

(13) Pusharsky, M. B.; Mann, A. M.; Yeston, J. S.; Moore, C. B. *J. Chem. Phys.* **2001**, *115*, 10738.

(14) Shahu, M.; Yang, C.-H.; Pibel, C. D.; McIlroy, A.; Taatjes, C. A.; Halpern, J. B. *J. Chem. Phys.* **2002**, *116*, 8343.

(15) Mann, A. M.; Chen, X.; Lozovsky, V. A.; Moore, C. B. *J. Chem. Phys.* **2003**, *118*, 4452.

(16) Wodtke, A. M.; Hintsa, E. J.; Somorjai, J.; Lee, Y. T. *Isr. J. Chem.* **1989**, *29*, 383.

(17) Cao, J. R.; Zhang, J. M.; Zhong, X.; Huang, Y. H.; Fang, W. Q.; Wu, X. J.; Zhu, Q. H. *Chem. Phys.* **1989**, *138*, 377.

(18) Fahr, A.; Braun, W.; Laufer, A. H. *J. Phys. Chem.* **1993**, *97*, 1502.

(19) Blank, D. A.; Sun, W.; Suits, A. G.; Lee, Y. T.; North, S. W.; Hall, G. E. *J. Chem. Phys.* **1998**, *108*, 5414.

(20) Katayanagi, H.; Yonekuira, N.; Suzuki, T. *Chem. Phys.* **1998**, *231*, 345.

(21) Robinson, J. C.; Harris, S. A.; Sun, W.; Sveum, N. E.; Neumark, D. M. *J. Am. Chem. Soc.* **2002**, *124*, 10211.

(22) Robinson, J. C.; Sveum, N. E.; Neumark, D. M. *J. Chem. Phys.* **2003**, *119*, 5311.

(23) Mu, X.; Lu, I.-C.; Lee, S.-H.; Wang, X.; Yang, X. *J. Phys. Chem. A* **2004**, *108*, 11470.

(24) Lee, S.-H.; Chen, W.-K.; Chaudhuri, C.; Huang, W.-J.; Lee, Y. T. *J. Chem. Phys.* **2006**, *125*, 144315/1.

(25) Berkowitz, J.; Mayhew, C. A.; Ruscic, B. *J. Chem. Phys.* **1988**, *88*, 7396.

(26) Riehl, J. F.; Morokuma, K. *J. Chem. Phys.* **1994**, *100*, 8176.

(27) Abrash, S. A.; Zehner, R. W.; Mains, G. J.; Raff, L. M. *J. Phys. Chem.* **1995**, *99*, 2959.

(28) Mains, G. J.; Raff, L. M.; Abrash, S. A. *J. Phys. Chem.* **1995**, *99*, 3532.

(29) Cho, S. H.; Park, W.-H.; Kim, S. K.; Choi, Y. S. *J. Phys. Chem. A* **2000**, *104*, 10482.

(30) Tu, J.; Lin, J. J.; Lee, Y. T.; Yang, X. *J. Chem. Phys.* **2002**, *116*, 6982.

(31) Chang, J.-L. *J. Chem. Phys.* **2005**, *122*, 194321/1.

(32) DeSain, J. D.; Jusinski, L. E.; Taatjes, C. A. *Phys. Chem. Chem. Phys* **2006**, *8*, 2240.

(33) Kanamori, H.; Endo, Y.; Hirota, E. *J. Chem. Phys.* **1990**, *92*, 197.

(34) Kim, E.; Yamamoto, S. *J. Chem. Phys.* **2002**, *116*, 10713.

(35) Tanaka, K.; Toshimitsu, M.; Harada, K.; Tanaka, T. *J. Chem. Phys.* **2004**, *120*, 3604.

(36) Shepherd, R. A.; Doyle, T. J.; Graham, W. R. *J. Chem. Phys.* **1988**, *89*, 2738.

(37) Tanskanen, H.; Khriachtchev, L.; Rasanen, M.; Feldman, V. I.; Sukhov, F. F.; Orlov, A. Y.; Tyurin, D., A. *J. Chem. Phys.* **2005**, *123*, 064318/1.

(38) Paolucci, D. M.; Gunkelman, K.; McMahon, M. T.; McHugh, J.; Abrash, S. A. *J. Phys. Chem.* **1995**, *99*, 10506.

(39) Forney, J.; Jacox, M. E.; Thompson, W. E. *J. Mol. Spec.* **1995**, *170*, 178.

(40) *Note: There have been numerous errors in the labeling of the vibrational modes of the vinyl radical. The correct labeling follows the common notation of highest symmetry modes labeled highest frequency to lowest frequency, followed by the next highest symmetry and so on.*

(41) Wu, Y.-J.; Lin, M.-Y.; Cheng, B.-M.; Chen, H.-F.; Lee, Y.-P. *J. Chem. Phys.* **2008**, *128*, 204509.

(42) Hartland, G. V.; Xie, W.; Dai, H.-L.; Simon, A.; Anderson, M. J. *Rev. Sci. Instr.* **1992**, *63*, 3261.

(43) Hartland, G. V.; Qin, D.; Dai, H.-L. *J. Chem. Phys.* **1993**, *98*, 6906.

(44) Hartland, G. V.; Qin, D.; Dai, H.-L. *J. Chem. Phys.* **1997**, *107*, 2890.

(45) Qin, D.; Hartland, G. V.; Dai, H.-L. *J. Phys. Chem. A* **2000**, *104*, 10460.

(46) Letendre, L.; Dai, H.-L. *J. Phys. Chem. A* **2002**, *106*, 12035.

(47) Wilhelm, M. J.; McNavage, W.; Groller, R.; Dai, H.-L. *J. Chem. Phys.* **2008**, *128*, 064313/1.

(48) McNavage, W.; Dailey, W.; Dai, H.-L. *Can. J. Chem.* **2004**, *82*, 925.

(49) Dupuis, M.; Wendoloski, J. J. *J. Chem. Phys.* **1984**, *80*, 5696.

(50) Stanton, J. F.; Bartlett, R. J. *J. Chem. Phys.* **1993**, *98*, 7029.

(51) Stanton, J. F. *Chem. Phys. Lett.* **1995**, *237*, 20.

(52) Wang, J.-H.; Chang, H.-C.; Chen, Y.-T. *Chem. Phys.* **1995**, *206*, 43.

(53) Mebel, A. M.; Chen, Y.-T.; Lin, S.-H. *Chem. Phys. Lett.* **1997**, *275*, 19.

(54) Sattelmeyer, K. W.; Schaefer, H. F., III. *J. Chem. Phys.* **2002**, *117*, 7914.

(55) Dong, F.; Roberts, M.; Nesbitt, D. J. *J. Chem. Phys.* **2007**, *128*.

(56) McNavage, W.; Dai, H.-L. *J. Chem. Phys.* **2005**, *123*, 184104/1.

(57) Nikow, M.; Wilhelm, M. J.; Smith, J. M.; Dai, H.-L. **to be published.**

(58) Orr, B. J. *Int. Rev. Phys. Chem.* **2006**, *25*, 655.

(59) Herman, M. *Mol. Phys.* **2007**, *105*, 2217.

(60) Yamanouchi, K.; Miyawaki, J.; Tsuchiya, S.; Jonas, D. M.; Field, R. W. *Laser Chem.* **1994**, *14*, 183.

(61) Temsamani, M. A.; Herman, M.; Solina, S. A. B.; O'Brien, J. P.; Field, R. W. *J. Chem. Phys.* **1996**, *105*, 11357.

(62) Carvalho, A.; Hancock, G.; Saunders, M. *Phys. Chem. Chem. Phys* **2006**, *8*, 4337.

(63) Liu, D., -Kuo; Letendre, L.; Dai, H.-L. *J. Chem. Phys.* **2001**, *115*, 1734.

(64) Abrash, S. A.; Pimentel, G. C. *J. Phys. Chem.* **1989**, *93*, 5828.

(65) Yamashita, S. *Chem. Lett.* **1975**, *9*, 967.

(66) Yamashita, S.; Noguchi, S.; Hayakawa, T. *Bull. Chem. Soc. Japan* **1972**, *45*, 659.

(67) Wilhelm, M.; Nikow, M.; Dai, H.-L. *Journal of Molecular Structure* **2008**, *883-884*, 242.

(68) Christiansen, O.; Hattig, C.; Jorgensen, P. *Spec. Acta, Part A.* **1999**, *55*, 509.

(69) Sattelmeyer, K. W.; Stanton, J. F.; Olsen, J.; Gauss, J. *Chem. Phys. Lett.* **2001**, *347*, 499.

(70) Scott, A. P.; Radom, L. *J. Phys. Chem.* **1996**, *100*, 16502.

(71) Simmonett, A. C.; Evangelista, F. A.; Allen, W. D.; III, H. F. S. *J. Chem. Phys.* **2007**, *127*.

(72) Dong, F.; Davis, S.; Nesbitt, D. J. *J. Phys. Chem. A* **2006**, *110*, 3059.

(73) Curtiss, L. A.; Pople, J. A. *J. Chem. Phys.* **1988**, *88*, 7405.

(74) Galli, C.; Guarnieri, A.; Koch, H.; Mencarelli, P.; Rappaport, Z. *J. Org. Chem.* **1997**, *62*, 4072.

(75) Birss; Ramsay. *Comp. Phys. Comm.* **1984**, *38*, 83.

(76) M. J. Frisch, G. W. T., H. B. Schlegel, G. E. Scuseria, M. A. Robb, J. R. Cheeseman, J. A. Montgomery, Jr., T. Vreven, K. N. Kudin, J. C. Burant, J. M. Millam,

S. S. Iyengar, J. Tomasi, V. Barone, B. Mennucci, M. Cossi, G. Scalmani, N. Rega, G. A. Petersson, H. Nakatsuji, M. Hada, M. Ehara, K. Toyota, R. Fukuda, J. Hasegawa, M. Ishida, T. Nakajima, Y. Honda, O. Kitao, H. Nakai, M. Klene, X. Li, J. E. Knox, H. P. Hratchian, J. B. Cross, C. Adamo, J. Jaramillo, R. Gomperts, R. E. Stratmann, O. Yazyev, A. J. Austin, R. Cammi, C. Pomelli, J. W. Ochterski, P. Y. Ayala, K. Morokuma, G. A. Voth, P. Salvador, J. J. Dannenberg, V. G. Zakrzewski, S. Dapprich, A. D. Daniels, M. C. Strain, O. Farkas, D. K. Malick, A. D. Rabuck, K. Raghavachari, J. B. Foresman, J. V. Ortiz, Q. Cui, A. G. Baboul, S. Clifford, J. Cioslowski, B. B. Stefanov, G. Liu, A. Liashenko, P. Piskorz, I. Komaromi, R. L. Martin, D. J. Fox, T. Keith, M. A. Al-Laham, C. Y. Peng, A. Nanayakkara, M. Challacombe, P. M. W. Gill, B. Johnson, W. Chen, M. W. Wong, C. Gonzalez, and J. A. Pople. Gaussian 03, Revision 6.0; Gaussian, Inc.: Pittsburgh, PA, 2003.

(77) The advances presented for the first time in Gaussian 03 are the work of M. J. Frisch, G. W. T., H. B. Schlegel, G. E. Scuseria, M. A. Robb, J. R. Cheeseman, J. A. Montgomery, Jr., T. Vreven, K. N. Kudin, J. C. Burant, J. M. Millam, S. S. Iyengar, J. Tomasi, V. Barone, B. Mennucci, M. Cossi, G. Scalmani, N. Rega, G. A. Petersson, H. Nakatsuji, M. Hada, M. Ehara, K. Toyota, R. Fukuda, J. Hasegawa, M. Ishida, T. Nakajima, Y. Honda, O. Kitao, H. Nakai, M. Klene, X. Li, J. E. Knox, H. P. Hratchian, J. B. Cross, C. Adamo, J. Jaramillo, R. Gomperts, R. E. Stratmann, O. Yazyev, A. J. Austin, R. Cammi, C. Pomelli, J. W. Ochterski, P. Y. Ayala, K. Morokuma, G. A. Voth, P. Salvador, J. J. Dannenberg, V. G. Zakrzewski, A. D. Daniels, O. Farkas, A. D. Rabuck, K. Raghavachari and J. V. Ortiz.

(78) Watson, J. K. G. *J. Chem. Phys.* **1967**, *46*, 1935.

(79) Zou, P.; Strecker, K. E.; Ramirez-Serrano, J.; Jusinski, L. E.; Taatjes, C. A.; Osborn, D. L. *Phys. Chem. Chem. Phys* **2007**, *10*, 713.

(80) Lin, S.-R.; Lin, S.-C.; Lee, Y.-C.; Chou, Y.-C.; Chen, I.-C.; Lee, Y.-P. *J. Chem. Phys.* **2001**, *114*, 160.

(81) Dong, F.; Roberts, M.; Nesbitt, D. J. *J. Chem. Phys.* **2008**, *128*, 044305.

(82) Herman, M.; Campargue, A.; ElIdrissi, M. I.; Auwera, J. V. *J. Phys. Chem. Ref. Data* **2003**, *32*, 921.

Chapter 4

Strong combination-band IR emission from highly vibrationally excited acetylene

4.1 Introduction

Despite the relative weakness of combination bands in the absorption spectrum, the $\nu_4 + \nu_5$ combination band has been identified with exceptionally high intensity in the IR emission spectra from highly vibrationally excited acetylene, which is produced with ~71 kcal mol^{-1} of vibrational energy from the 193 nm photolysis of vinyl bromide. The 'fundamental' transition of this combination band, from the $(0,0,0,1^1,1^{-1})$ level to the zero point, occurs at 1,328 cm^{-1}. Utilizing the general IR emission modeling procedure from Chapter 2, the intensity and frequency of this band as well as the ν_3 and ν_5 bands, IR active but with lower emission intensity, as a function of the acetylene energy can be modeled accurately using the normal mode harmonic oscillator model with frequency anharmonicity corrections. Good fitting results are achieved even though the normal mode quantum numbers are no longer good for levels in the high energy region and the combination band is forbidden in the harmonic oscillator model. The identification of this intense combination band in emission, compared to its weak intensity in the absorption spectrum, highlights the necessity to include in consideration the combination bands for assignment of emission spectra in general and in particular emission from vibrationally hot acetylene which is ample in combustion, atmospheric, and interstellar environments.

Acetylene is one of the most important and subsequently well studied hydrocarbons.[1] Its importance ranges from the interstellar, where it was recently discovered by high resolution IR in large abundance in the comets Hyakutake and Hale-Bopp,[2] to the planetary where its significance is evident in origins of life studies,[3,4] to the environmental,[5,6] and to numerous other energy and chemical applications. In spectroscopic studies, acetylene has in general been well characterized. Recent studies have focused more on the highly vibrationally excited levels in the electronic ground state.

There has been a substantial amount of spectroscopic works using the techniques of double resonance[7-9] (IR-UV and Raman-UV), stimulated emission pumping,[10] laser induced fluorescence[7,11] and dispersed fluorescence[12] to probe vibrationally excited acetylene. In addition to a wealth of information obtained on inter- and intra-molecular vibrational relaxation,[1] the vibrational manifold has been well documented to near 20,000 cm^{-1}.[13,14] The rovibrational manifold has been found to rapidly become complex even at low quanta vibrational states. At high vibrational energies, perturbations to the normal mode coordinates become pronounced and disrupt the normal mode progression.[1] The anharmonic resonances, Coriolis couplings, and *l*-type resonances eventually destroy the 7 vibrational quantum numbers in the normal mode progression. Instead, a three quantum number $\{N_s, N_r, k\}$ poly-ad system emerges to provide a better zero-order description. Though the normal mode quantum numbers begin to become discernibly less effective starting at ~7,000 cm^{-1}, a significant number of eigenstates still retain their original normal mode character.[15] In addition, one would expect the normal mode states to be conserved, at least where the molecule retains a similar structure.

Recent unpublished theoretical work, performed by Prof. Andrew Rappe, Dr. Sara Mason, and Steve Young,[16] have used direct dynamics simulations to study highly vibrationally excited molecules. Temperature dependent, first-principle direct dynamics simulations on acetylene and vinyl were performed and their IR spectra extracted. Initial analysis of the IR spectra indicates that the normal mode picture is still valid as the spectra exhibit predictable features similar to those found in room temperature absorption measurements. Further temperature dependent analysis of the IR spectra extracted from the simulations shows a strong band near 1300 cm^{-1}, which has been determined to arise from the $\nu_4 + \nu_5$ combination band vibrational motion. The combination band gains intensity as the temperature is increased, going from an intensity of 3% at 50 K to 64% at 1000 K, relative to the ν_5 bend mode, following a similar behavior observed in the IR emission spectra recorded here.

IR emission from vibrationally excited molecules is particularly effective in representing the normal mode characters of the vibrational levels since the strongest emission is through $\Delta\upsilon=1$ transitions of IR active normal modes. The IR emission, when recorded with frequency resolution, can be used to determine the energy of the emitting molecules because the frequencies of the transitions change with excitation energy due to anharmonic shift. In principle, the IR emission spectra can be used for the examination of the appropriateness of the normal mode representation of the vibrational levels as a function of the excitation energy. In such an experiment, generating vibrationally excited acetylene with high but well defined energy is essential.

One approach to produce vibrationally excited acetylene in large quantity, so its IR emission is detectable, is through the photolysis of a precursor which results in vibrationally excited acetylene as a product. In the previous Chapter on detecting IR

emission from the vinyl radical,[17] a similar approach has been employed to produce large quantities of vibrationally excited vinyl. The 193 nm photolysis of all these vinyl precursors in fact also results in the production of acetylene through one of the several available dissociation channels. Subsequently, IR emission spectra taken with time-resolution, using the Time-Resolved Fourier Transform IR Emission Spectroscopy approach[18,19] described in Chapter 1, following the photolysis of the precursors,[17] consist of emission bands from vibrationally excited acetylene.

In this Chapter, several emission features in these IR emission spectra can be identified to originate from highly vibrationally excited acetylene, produced through photolysis of the precursor molecule vinyl bromide. The surprising observation is that the emission bands not only arise from the $\Delta\upsilon=1$ transitions from the IR active modes, namely the ν_3 and ν_5 normal modes of acetylene, but the strongest emission band actually comes from the $\nu_4 + \nu_5$ combination band that is forbidden in the harmonic oscillator selection rules. This unexpectedly strong combination band emission from highly vibrationally excited acetylene provides new perspectives for interpreting IR emission in combustion, atmospheric, and astrophysical studies.

4.2 Experimental

The experimental set up for detecting IR emission with frequency and time resolution through Time-Resolved Fourier Transform IR Emission Spectroscopy has been discussed previously in Chapters 1 and 3. The time-resolved emission spectra were obtained in an identical fashion to the experiments performed in Chapter 3. Only the experimental pressures were changed. Vinyl bromide (VBr) (Aldrich, >98%) was used without further purification. He (Airgas, 99.999%), Ne (Airgas, 99.999%), Ar (Airgas,

99.999%), and Kr (Airgas, 99.999%) were used as buffer gases. Typical experiments were performed with 5-25 mTorr VBr and 2-6 Torr of the noble gas.

4.3 Results and analysis

4.3.1 IR emission

Several IR emission time slices following the 193 nm photolysis of 5 mTorr vinyl bromide in 2 Torr Ar are shown in Figure 4.1. There are two main dissociation channels following the 193 nm photolysis of vinyl bromide: (1) products C_2H_2 + HBr with ΔH = -123 kcal mol^{-1}, and (2) C_2H_3 + Br/Br*, ΔH = -69/59 kcal mol^{-1}.[17,20] All of the reaction products have been detected experimentally.[21-24] Since the exothermicities are high, the molecular fragments can be vibrationally excited and emit in the IR region. HBr emission, shown in Figure 4.1 between 2000 and 2750 cm^{-1}, has been observed to as high as v=7 vibrational excitation.[22,23] Several of the low frequency modes of the vinyl radical and emission from Br* have been identified through isotopic substitution, utilization of numerous precursors, 2-dimensional cross-spectral correlation analysis, and cold-chemical IR filters.[17] The intensity of these features in Figure 4.1 is relatively low due to the low precursor pressures used here.[22,23,25]

Two main features, at ~1,250 and in between 3,000-3,300 cm^{-1}, in the emission spectra in Figure 4.1 are not assigned to vinyl and hypothesized to originate from vibrationally excited acetylene.[17] In the region below 2,000 cm^{-1} all the lower frequency modes of the vinyl radical have been assigned,[17,21,26] and acetylene is the only other possible reaction product that may emit in the regions of the two unassigned bands.[24] The previous study on identifying normal modes of the vinyl radical[17] utilized five different

Figure 4.1. Time resolved IR emission following photodissociation of vinyl bromide at 193 nm. Each spectrum is the average of 10 spectra taken at 100 ns intervals. The spectra at 1, 2, 5, 15, 35, and 55 μs are shown.

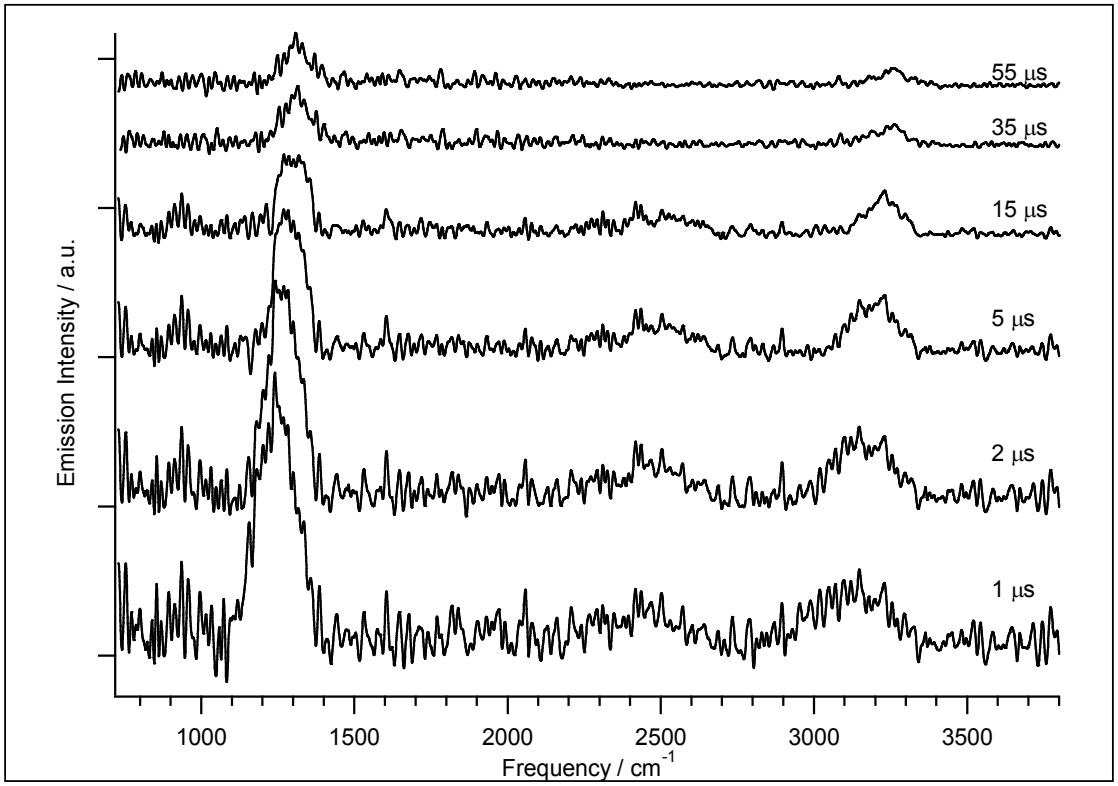

precursor molecules, all yielding similar features at ~1,250 and 3,000-3,300 cm^{-1}. The only common reaction product other than vinyl following photolysis of the five precursor molecules was acetylene and it is logical to assume that the two features arise from vibrationally excited acetylene.

Based on the comparison of the emission spectra bands with the absorption bands of acetylene, the 1,250 cm^{-1} feature is assigned to the $\nu_4+\nu_5$ combination band while the broad emission feature from 3,000-3,300 cm^{-1} arises from the ν_3 CH stretch. The temporal response of the two features is much slower than the fast decay observed for the emission bands assigned to the vinyl radical. The acetylene emission bands may appear in the spectrum as far as 100 μs after photolysis. The decay of the emission intensity may be affected by diffusion out of the finite detection region (~±5 cm from the center of the chamber where photolysis occurs) before the vibrationally excited molecules are collisionally quenched. This highlights the importance of properly adjusting the collider gas pressure in the experiments. To observe the true collisional quenching rate of the excited molecules, the collider gas pressure must be sufficiently high to deactivate the vibrationally excited population before their diffusion out of the observation zone.

The two features also display a strong frequency shift and change in relative intensity with time. The $\nu_4 + \nu_5$ band is significantly stronger than the ν_3 band at early times, but becomes equally intense at late times. As the model calculation below shows, this change in relative intensity is due to the harmonic oscillator scaling factors. The ν_3 CH stretch band shows a strong red shift, particularly in the early times, indicating that the emitting acetylene molecules contain a large amount of vibrational energy. This observation is consistent with the exothermicity of reaction (1), that 123 kcal mol^{-1} is left in the products acetylene and HBr.

For comparison, the absorption spectra of acetylene taken at a partial pressure of 20 Torr with 400 Torr N_2 is shown in Figure 4.2. The strongest band is the ν_5 mode centered at 730 cm^{-1}. This perpendicular band in the spectrum presented here is clipped by the sharp drop in the detector sensitivity at 750 cm^{-1}. Only the R-branch of this band is observed. The next strongest band in the absorption spectra is the ν_3 CH stretch, a parallel band centered at 3,294 cm^{-1} whose fundamental is in resonance with the $\nu_2 + \nu_4 + \nu_5$ band. We also identify a parallel band at 1,328 cm^{-1}, where no fundamental transition is expected. This band has long been understood as an unusually strong $\nu_4 + \nu_5$ combination band.[27] Though combination bands are not allowed within the harmonic oscillator approximation, anharmonicities may cause them to appear with varying intensities.

Combination bands are typically much weaker than their normal mode counterparts. There are, however, exceptions, as in the case of acetylene, where strong anharmonicities exist. The linear acetylene molecule has 7 vibrational modes, with 3 IR active: the ν_3 asymmetric stretch and the doubly degenerate ν_5 cis-bend. The IR inactive modes are the ν_1 symmetric stretch, the ν_2 CC stretch, and the doubly degenerate ν_4 trans-bend. The $\nu_4 + \nu_5$ combination band is quite strong in that its intensity is about one eighth of that of the ν_5 band. There are other weak overtone and combination bands that are observed in the absorption spectra shown in the inset in Figure 4.2: the rotationally resolved $\nu_2 + \nu_5$ combination band at 2,703 cm^{-1}, $3\nu_5$ overtone band at 2,170 cm^{-1}, and $2\nu_4 + \nu_5$ combination band at 1,941 cm^{-1}. The intensity of these bands is weaker by more than two orders of magnitude than that of the ν_5 band.

Figure 4.2. IR absorption spectrum of 20 Torr acetylene in 400 Torr N_2. The inset in 1800-2800 cm^{-1} shows minor vibrational modes of acetylene. All peaks are assignable to acetylene except the one at 1650 cm^{-1} which arises from the acetone impurity in the acetylene sample.

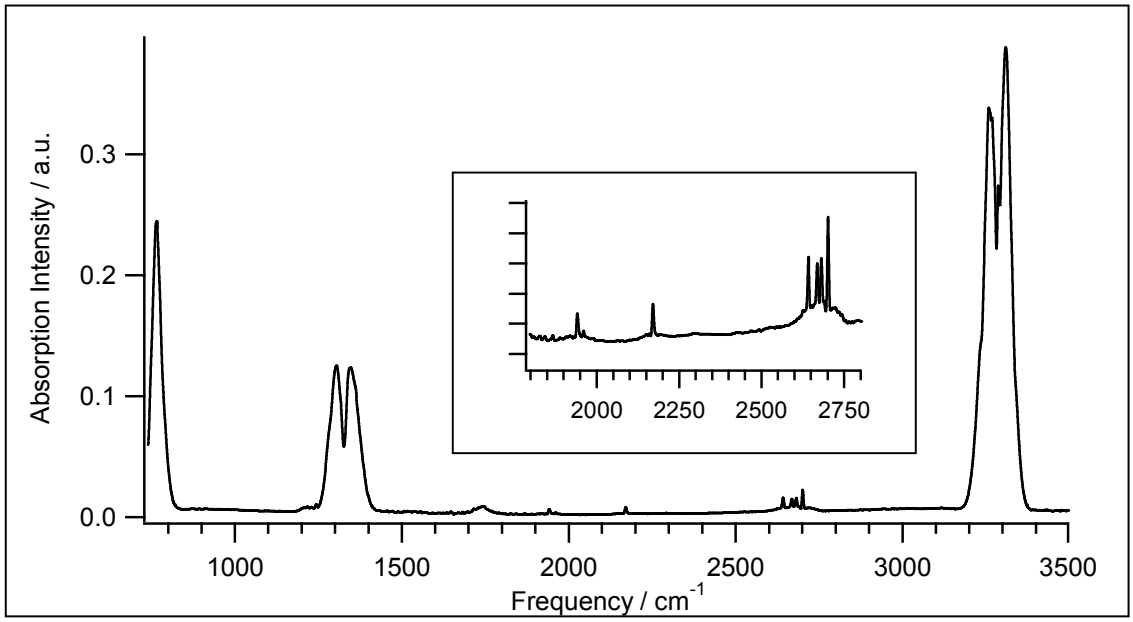

4.3.2 Modeling the acetylene emission bands

Here we model the frequency and intensity of the $\nu_4 + \nu_5$ combination band emission from vibrationally excited acetylene based on the harmonic oscillator model using normal mode quantum numbers. First, the energy of the excited vibrational levels is calculated by using the best available, experimentally determined constants in the normal mode basis. It is assumed that acetylene molecules residing in one of the excited normal mode levels would emit through one-quantum-change downward transitions of the IR active modes and the combination band transition with two-quantum change. The intensity scales with the vibrational quantum numbers according to the harmonic oscillator selection rules and the experimentally measured absorption band intensity.

All vibrational levels up to 30,000 cm^{-1} were first calculated using experimentally determined harmonic frequencies, first order anharmonic constants, and rotational constants according to the set of zero-order normal mode vibrational and the vibrational angular momentum quantum numbers.[1,14] All possible ν_3, ν_5, and $\nu_4 + \nu_5$ downward transitions with $\Delta l = 0, \pm 1$, from the *i*th vibrational level $(\upsilon_1, \upsilon_2, \upsilon_3, \upsilon_4^l, \upsilon_5^l)_i$ defined by its set of normal mode quantum numbers were then accounted and sorted in terms of energy using the spectral emission functions, $S_3^i(\nu)$, $S_5^i(\nu)$, and $S_{4+5}^i(\nu)$:

$$S_3^i(\nu) = A_3 D(\nu) I_3^i \left(\nu_3^i / \nu_3^0\right)^3 \exp\left\{-\left(\nu - \nu_3^i\right)^2 / 2\sigma_V^2\right\}, \tag{4.1a}$$

$$S_5^i(\nu) = A_5 D(\nu) I_5^i \left(\nu_5^i / \nu_5^0\right)^3 \exp\left\{-\left(\nu - \nu_5^i\right)^2 / 2\sigma_V^2\right\}, \tag{4.1b}$$

$$S_{4+5}^i(\nu) = A_{45} D(\nu) I_{45}^i \left(\left(\nu_4 + \nu_5\right)^i / \left(\nu_4 + \nu_5\right)^0\right)^3 \times \exp\left\{-\left(\nu - \left(\nu_4 + \nu_5\right)^i\right)^2 / 2\sigma_V^2\right\} \tag{4.1c}$$

where A_3, A_5, and A_{45}, are the Einstein coefficients for spontaneous emission which can be related to experimentally measured absorption intensity as[28-30]

$$A_3 = 976\times10^{10}\left(\nu_3^0\right)^3 (cm^{-1}s^{-1}) \tag{4.2a}$$

$$A_5 = 2410\times10^{10}\left(\nu_5^0\right)^3 (cm^{-1}s^{-1}) \tag{4.2b}$$

$$A_{45} = 302\times10^{10}\left(\nu_4^0+\nu_5^0\right)^3 (cm^{-1}s^{-1}) \tag{4.2c}$$

The experimental response function $D(\nu)$ was determined to be predominantly associated with the detector response function which was supplied by the manufacturer. The emission frequencies $\nu_3^0, \nu_5^0,$ and $\left(\nu_4+\nu_5\right)^0$ correspond to the centers of the fundamental emission bands of the modes while ν_3^i, ν_5^i, and $\left(\nu_4+\nu_5\right)^i$ represent the anharmonicity-corrected *i*th level emission frequency. The emission band shape was assumed to be Gaussian with a bandwidth σ_V, which was determined from room temperature absorption bands as σ_V = 30 cm^{-1}. The intensity scaling factors I_3^i, I_5^i, and I_{45}^i, in the harmonic oscillator model, derived based on a previous model for HCN absorption hot bands,[31] are:

$$I_3^i = \upsilon_3^i \tag{4.3a}$$

$$I_5^i = \frac{\upsilon_5^i \pm l_5^i + 2}{2g_5^i} \tag{4.3b}$$

$$I_{45}^i = \left(\frac{\upsilon_4^i \pm l_4^i + 2}{2g_4^i}\right)\left(\frac{\upsilon_5^i \pm l_5^i + 2}{2g_5^i}\right) \tag{4.3c}$$

Here l_4^i, and l_5^i are the angular momentum quantum numbers for the degenerate ν_4, and ν_5 modes. The sign in Eqns. 4.3b and 4.3c is positive when $\Delta l = l' - l''$ is positive and negative when $\Delta l < 0$. The g_4^i and g_5^i terms are the degeneracy factor for ν_4 and ν_5, which take the value of unity if either angular momentum is zero, or 2 if both angular momenta are

nonzero. If either state angular momentum is zero, there exists only a Q or RP branch(es). If, however, both are non-zero, Q, R, and P branches exist. The g_ν term accounts for this intensity discrepancy.

The Gaussian profile used here for representing the band shape should be sufficient without the need for rotational modeling because of the significant overlap among emission bands from nearby states. Furthermore, a constant width is adequate for modeling latter time spectra as rotational temperature remains relatively constant. Nascent, vibrationally hot acetylene may have a relatively high rotational temperature; however, after several hundred collisions with bath gas molecules, high rotational excitation would be quenched.

The observed IR emission can be modeled for an ensemble of molecules with a particular population distribution over the zero-order normal states, P^i, such that the emission intensity is described by

$$S(\nu) = \sum_i P^i \left(S_3^i(\nu) + S_5^i(\nu) + S_{4+5}^i(\nu) \right) \tag{4.4}$$

The use of a quantum-state specific population distribution would be unrealistic for this calculation where the density of states is very high. We therefore group the quantum states into emission "bins" [32-36] each with a width of 1,000 cm^{-1}, and calculate the emission spectrum of each bin as accumulated sum of all states in the bin but normalized by the total number of states (N_j in bin j with energy E_j). The states within each bin are assumed to contribute equally to the overall emission spectra. The emission spectrum for the j^{th} bin is then

$$\overline{S}^j(\nu) = (1/N_j) \sum_k \left(S_3^k(\nu) + S_5^k(\nu) + S_{4+5}^k(\nu) \right) \tag{4.5}$$

and the total emission spectra of all bins with a population distribution $\overline{P}^j$ over E_j as

$$S(\nu) = \sum_j \overline{P}^j \overline{S}^j \tag{4.6}$$

The emission spectra from bins containing emission from 1,000-2,000, 3,000-4,000, 7,000-8,000, and 14,000-15,000 cm^{-1} energy, are shown in Figure 4.3. The emission bin spectra shown do not include the detector response function, $D(\nu)$, to illustrate the intensity dependence on internal energy without experimental bias. The response function will be included for the calculation of the model spectra from the experimental emission spectra. The detector response function was used only on the model spectra instead of correcting the experimental result so that the experimental spectra presented are shown as they are detected without bias in S/N.

Of particular interest in Figure 4.3 is the relative increase in intensity of the combination band at 1,200-1,300 cm^{-1}. In the absorption spectrum, this band is ~12% of the ν_5 mode in intensity. Because of the harmonic scaling factor and emission coefficient, the combination band becomes just as intense as the ν_5 mode at only 2,000 cm^{-1} of internal energy and ~5 times more intense at 15,000 cm^{-1}! The ν_3 mode, which has ~40% of the intensity of the ν_5 mode in absorption spectra, is absent from the 2,000 cm^{-1} emission spectra as the energy is not sufficient to cause emission from the ν_3 mode at 3,294 cm^{-1}. This band, which first appears in the 4,000 cm^{-1} emission bin, is slightly more intense than the combination band and remains more intense than the combination band, due to the quadratic power scaling with frequency in the Einstein coefficient for spontaneous emission. This mode remains the dominant emission mode until ~10,000 cm^{-1}, above which the combination band becomes the dominant feature. There is also a strong anharmonic shift apparent in the ν_3 CH stretch, which does not appear in the

Figure 4.3. Four emission curves for the energy bins with energy E_j=1,000 – 2,000, 3,000 – 4,000, 7,000 – 8,000, and 14,000 – 15,000 cm^{-1}. Intensities are offset but on the same scale.

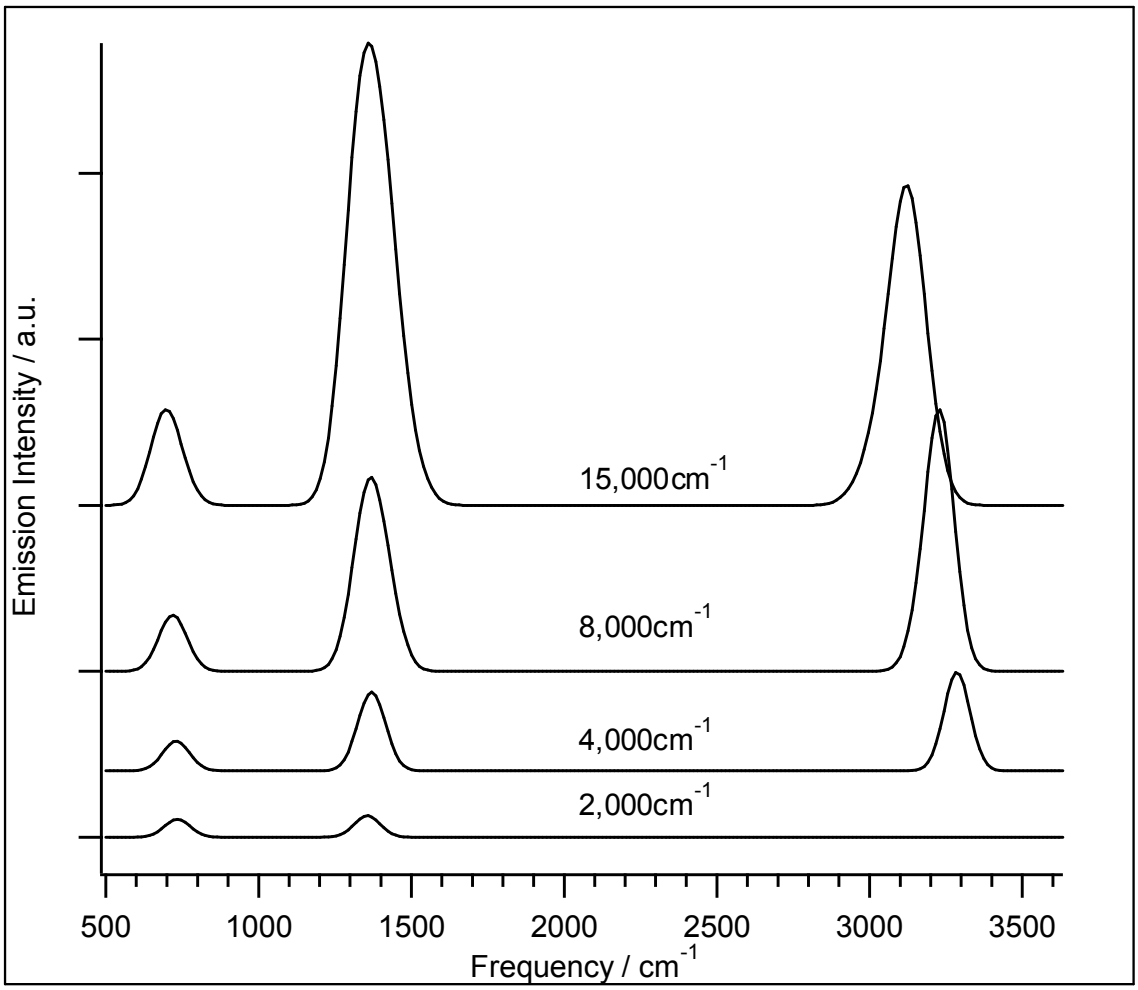

bending modes. This anharmonic shift is the dominant characteristic in the modeling of the emission spectra.

The overall population distribution as a function of energy can be obtained from a nonlinear least squares fit of the experimentally detected emission spectra. In the fitting, a bimodal distribution with two Gaussian functions was assumed for the overall population: a high energy Gaussian representing the nascent acetylene that decays through collision energy transfer and a low energy Gaussian centered at E_j=0 as the thermal sink. The population, as a function of energy in the jth bin with E_j, is described as

$$\begin{aligned} \overline{P}^{\,j} &= a \times \exp\left(-\overline{E}_j^{\,2} / 2\sigma_1^2\right) / \sqrt{2\pi}\sigma_1 + \\ &\quad (1-a) \times \exp\left(-\left(\overline{E}_j - \langle E \rangle\right)^2 / 2\sigma_2^2\right) / \sqrt{2\pi}\sigma_2 \end{aligned} \tag{4.7}$$

Here the a parameter depicts the ratio of the two distributions, σ_1 and σ_2 are the Gaussian widths, and $\langle E \rangle$ is the average vibrational energy of the high energy distribution.

The population distribution, Eq. 4.7, is based on two evolving systems, (1) a high energy nascent vibrational population formed with significant width following the photolysis of vinyl bromide, and (2) a thermal sink population generated from highly efficient vibrational-vibrational energy transfer between hot acetylene and precursor molecules or between acetylene molecules.

The broad population distribution of (1) is based on the HBr counterfragment observed rovibrationally hot following the 193 nm photolysis of vinyl bromide.[22,37] A wide range, over 10,000 cm^{-1}, of internal energy in HBr is observed. There is a exponential distribution in the vibrational energy of HBr following photolysis, with the majority of the population in v=1. This would correspond to a similar exponential distribution in acetylene. However, collisional deactivation would cool this population

into a broad distribution, thus justifying the use of a Gaussian distribution for the high energy population.

The sink population (2) represents the lowly excited acetylene generated via vibrational energy transfer from an excited species. The most probable cause of this excitation is from vibrationally hot acetylene. In addition, collisions between highly excited acetylene and cold precursor molecules may also be efficient at removing energy from acetylene leaving a low energy population. The low energy population is necessary for the accurate fitting of the spectra shown in Figure 4.4.

Time-resolved IR emission spectra recorded following photolysis of vinyl bromide in 4 Torr of Ar are shown in Figure 4.4. Emission spectra corresponding to 5, 10, and 20, and 40 μs after the photolysis pulse are shown in grey with the best fit spectra overlaid in black. The average internal energies, $\langle E \rangle$, of the excited acetylene extracted from the fittings are 12100, 9500, 7200, and 6300 cm^{-1}, for the 5, 10, 20, and 40 μs spectra respectively. The vibrational energy distribution defined by the two Gaussian profiles is shown as a function of time in Figure 4.5. Both the thermal and the high energy components are apparent during the entire time of interests. The collision frequency of the excited acetylene in the 4 Torr Ar gas is approximately 40 per μs, providing a sufficient energy transfer rate to cool the vibrational population before the excited molecules diffusing out of the observation zone of the gas cell.

The average vibrational energy, $\langle E \rangle$, of the excited acetylene molecule, extracted from each time slice, is shown as triangle marker in Figure 4.6. The error bar represents the FWHM of the higher energy distribution. The data was fit to a double exponential decay, $I(t) = y_0 + A_1 e^{-k_1 t} + A_2 e^{-k_2 t}$, as the simplest function which accurately fits the data.

Figure 4.4 Four time-resolved emission spectra at 5, 10, 20, and 40 μs after the photolysis of vinyl bromide in the presence of 4 Torr Ar, are shown in grey. The model fitting is overlaid, shown in black.

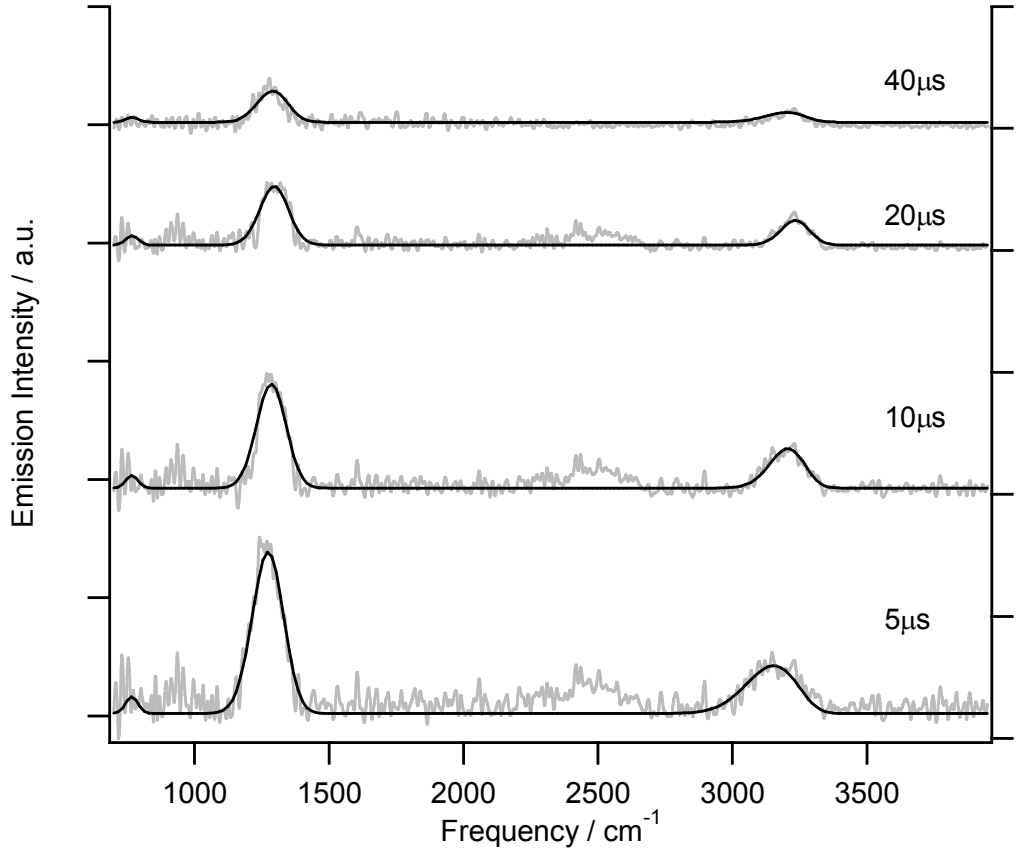

Figure 4.5. The vibrational energy population distribution of acetylene following photolysis of 10 mTorr VBr in 4 Torr Ar as extracted from model calculation.

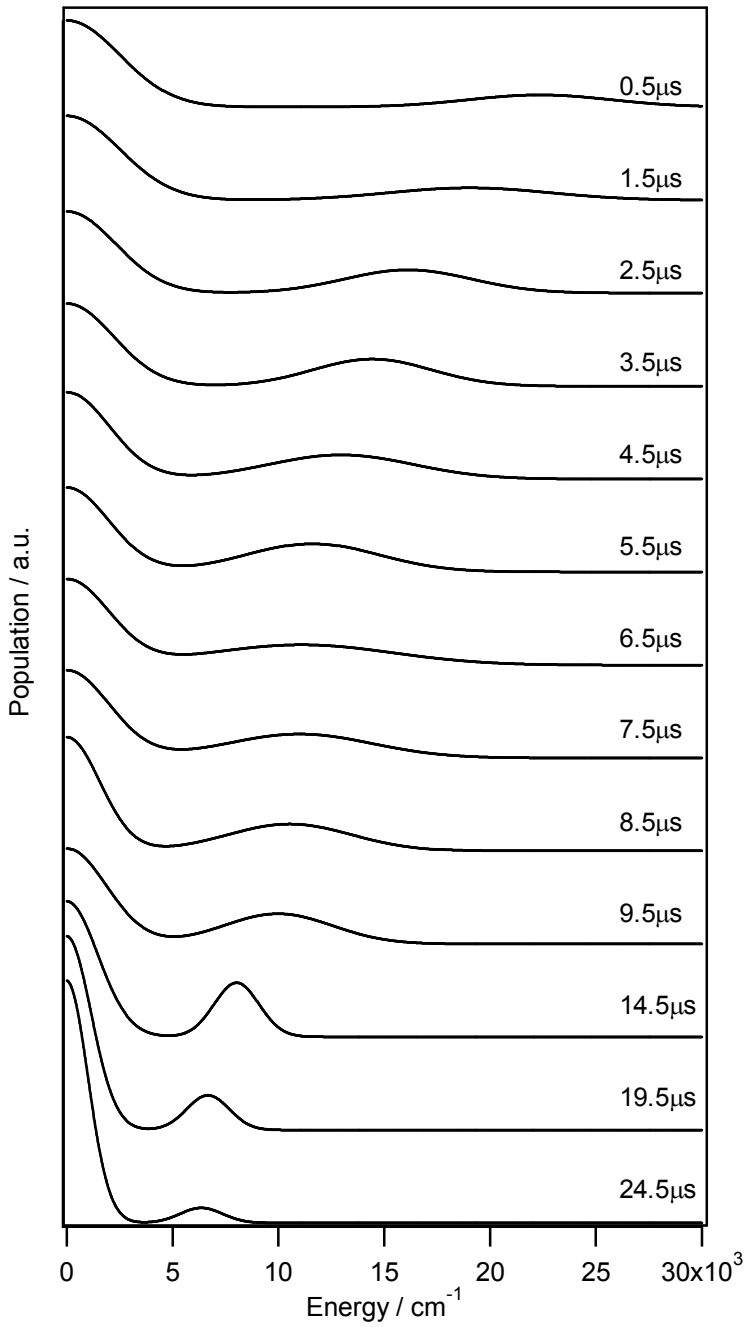

Figure 4.6. $\langle E \rangle$ of the highly vibrationally excited acetylene as a function of time, triangular points, following photolysis of 10 mTorr VBr in 4 Torr Ar. The solid line is the fit to a double exponential decay.

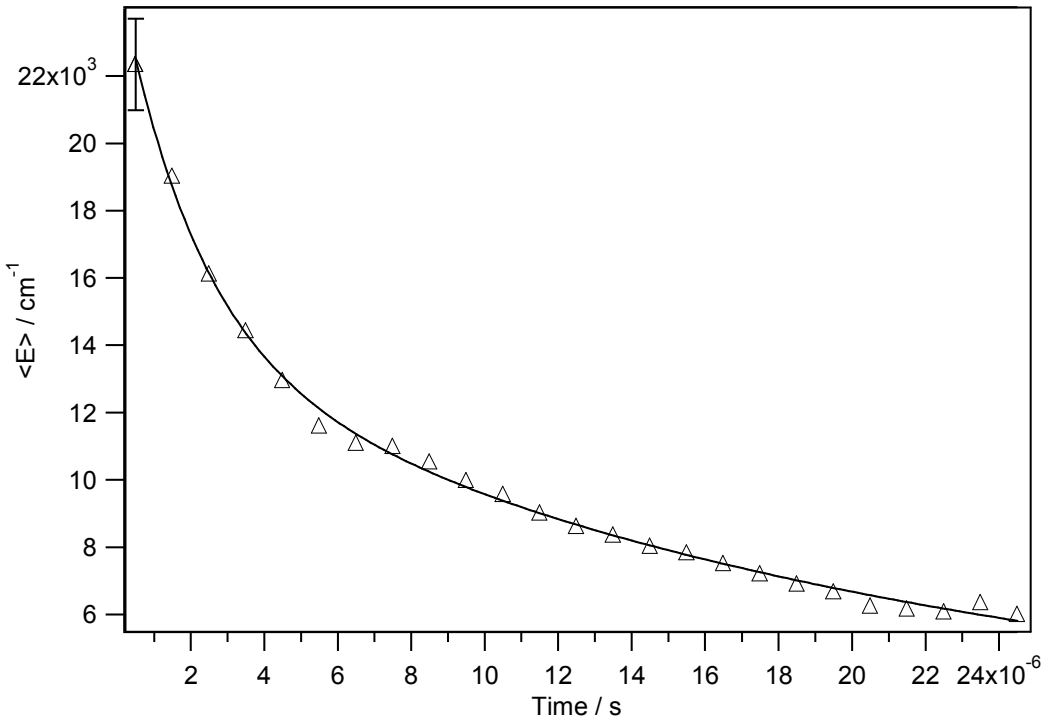

Fittings using a single exponential decay could not represent the temporal dependence of the average internal energy, particularly the faster energy decay at higher internal energies in the early time part of the energy decay curve. The two-exponential fit was found to be accurate for all four different noble gas colliders used, as well as for data obtained with other acetylene precursors. Fittings of results from several experiments utilizing different colliding partners yielded an average energy for nascent acetylene at time zero as $\langle E \rangle_0$ =24,769 cm^{-1} with a width of σ=1,185 cm^{-1}.

4.3.3 IR emission modeling of vinyl chloride

IR emission modeling of the three IR bands of acetylene, following the procedure outlined previously in this Chapter and Chapter 2, was performed for the photolysis of vinyl chloride. IR emission spectra and the fitting results are shown in Figure 4.7. The emission spectra is in grey, with the fitting result overlaid in black 3, 6, and 12 μs following the photolysis pulse. The broad feature with several sharp bands contained within arises from rovibrationally hot HCl. Vibrational excitation of HCl up to v=6 has been observed.[37,38] The intense $\nu_4 + \nu_5$ combination and ν_3 stretch bands of acetylene are well described by the fitting. The ν_5 bend at low energy is masked by the noise of the spectra, the sharp drop in the detector spectral response at 750 cm^{-1} and emission from the vinyl radical features at 897 and 944 cm^{-1}.

The average vibrational energy is plotted as a function of time in Figure 4.8. The population distribution is constrained to the two Gaussian distribution shown in Eq. 4.7. The energy $\langle E \rangle$ is extracted from the fitting results of all available time slices. The vibrational emission observed following the photolysis of vinyl chloride is shorter

Figure 4.7. Three IR emission time slices, 3, 6, and 12 μs are shown in grey following the 193 nm photolysis of 25 mTorr vinyl chloride in 4 Torr Ar. The IR emission model fitting result is overlaid in black. IR emission features are discussed in the text.

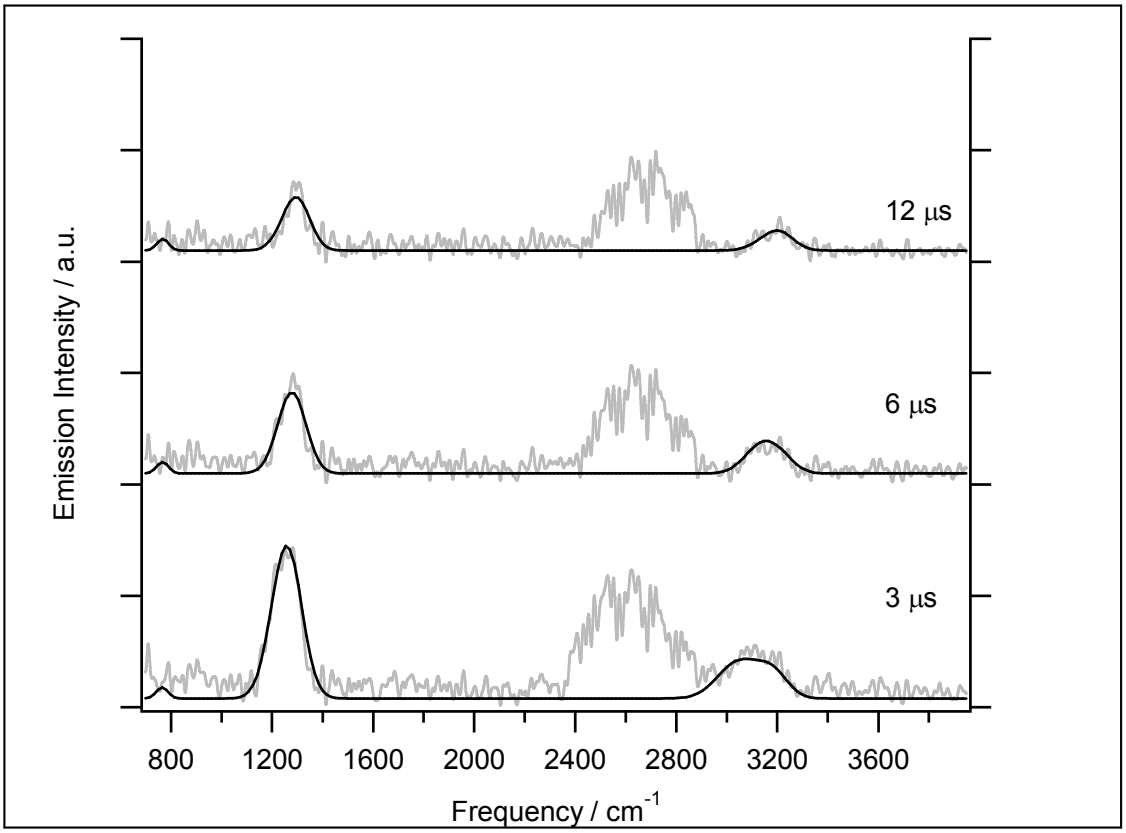

Figure 4.8. The average vibrational energy, $\langle E \rangle$, is shown as open circles. The $\langle E \rangle$ is determined from each time slice in Figure 4.7. The $\langle E \rangle$ are then fit to a single exponential decay function.

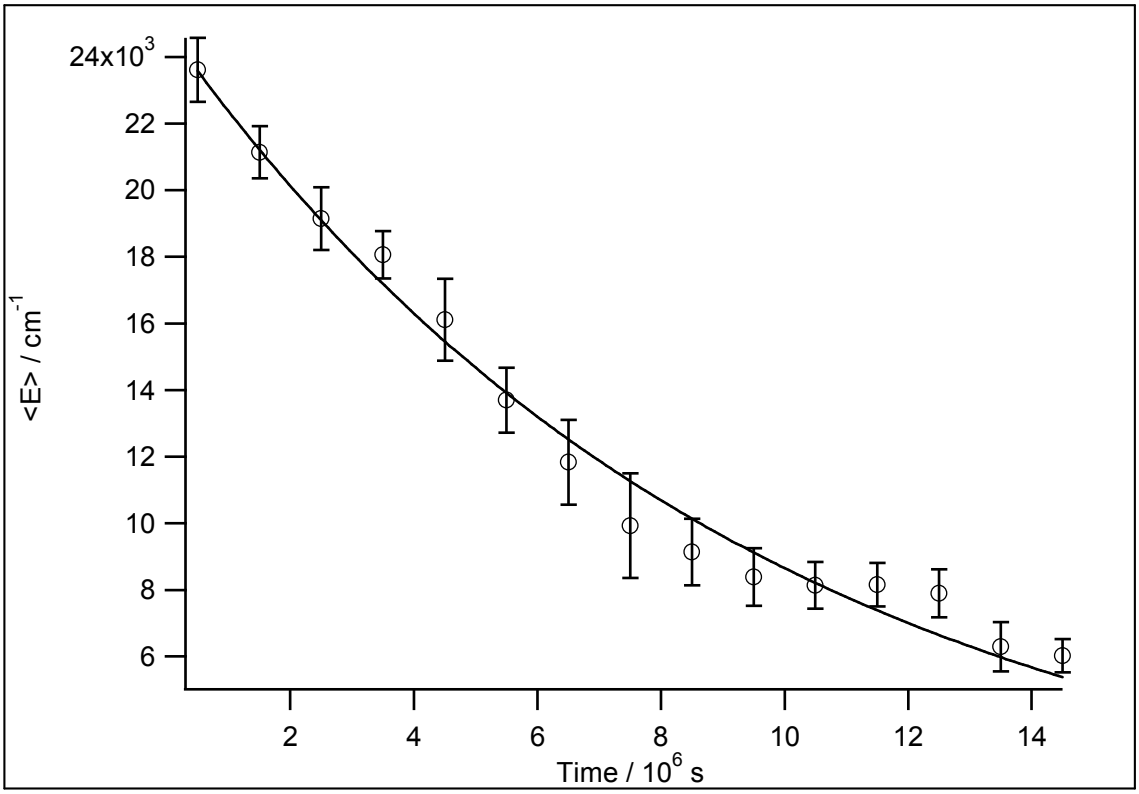

compared to the observed emission following photolysis of vinyl bromide. This is due to the higher precursor and collider gas pressures used, 25-50 mTorr and 4-6 Torr, respectively, in the experiments with vinyl chloride. These pressures were necessary to generate the signal needed to observe vibrationally hot acetylene. Consequently, due to the high pressures, less than 20 μs of IR emission is observed from acetylene. This is observed in Figure 4.8 and precludes the observation of acetylene near its fundamental emission. The high pressures used also permit the average vibrational energy, $\langle E \rangle$, vs. time data to be fit by a single exponential function, as opposed to the two exponential function used to fit the $\langle E \rangle$ vs. time data for vinyl bromide. The nascent vibrational energy of acetylene has been determined from this fitting to be 25,600 ± 2400 cm^{-1}. The large error bar on the nascent vibrational energy of acetylene is directly related to not observing and subsequently fitting acetylene bands at late times. The fitting is therefore only performed on the beginning of the vibrational relaxation process. Nonetheless, the nascent vibrational energy of acetylene compares quite favorably to the exothermicities determined for the 193 nm photolysis of vinyl chloride. The 193 nm photon should leave approximately 124 kcal/mol of energy into the acetylene and HCl photolysis products.[39] HCl is formed vibrationally hot with approximately 25 kcal/mol of vibrational energy, along with translational energies of 15-20 kcal/mol from similar PTS studies.[25,40,41] Acetylene is therefore expected to contain less than 78 kcal/mol of internal energy which compares very well to the 74 kcal/mol vibrational energy observed here.

4.3.4 IR emission modeling of vinyl iodide

IR emission modeling for the vibrational bands of acetylene has been performed following the 193 nm photolysis of vinyl iodide. The 193 nm photolysis of vinyl iodide

shows strong pressure dependent emission features, shown in Figure 4.9. At low precursor pressures, only a small amount of vibrationally hot acetylene in observed, with emission from electronic transitions of atomic iodine dominating the spectra. Atomic iodine emission is observed as a series of sharp features at 1350, 2050, 2500, 2525, 2575, 2900, and several features between 3000 and 3500 cm^{-1}.[42] The features are rapidly quenched at high precursor pressures. At 50 mTorr vinyl iodide, there is very little atomic iodine emission, however the intense combination and CH stretching bands of acetylene now become apparent. The emission of highly excited acetylene is only apparent at high precursor pressures due to the low absorption cross section of vinyl iodide at 193 nm compared to that of vinyl bromide and vinyl chloride.

The time resolved IR emission result for several time slices following photolysis of vinyl iodide is shown in Figure 4.10. IR emission from vibrationally hot acetylene is observed through the $\nu_4 + \nu_5$ combination, ν_5 bend, and ν_3 stretch modes at 775, 1275, and near 3000 cm^{-1}, respectively. Only ~10 μs of emission is observed primarily due to the high precursor pressures used which rapidly quench the vibrationally excited acetylene population. The average vibrational energy of acetylene, $\langle E \rangle$, plotted as a function of time is shown in Figure 4.11. The open circles and the $\langle E \rangle$ values extracted from the fitting result. The population and derivation of the vibrationally excited acetylene molecules is performed in a similar manor as was done to vinyl bromide. A single exponential function was used to fit the vibrational energy decay. The nascent vibrational energy of acetylene formed via the photolysis of vinyl iodide is 25,200 ± 1,600 cm^{-1}.

Figure 4.9. IR emission results approximately 2 μs after photolysis of varying pressures of vinyl iodide in 4 Torr of Ar. Features are discussed in the text.

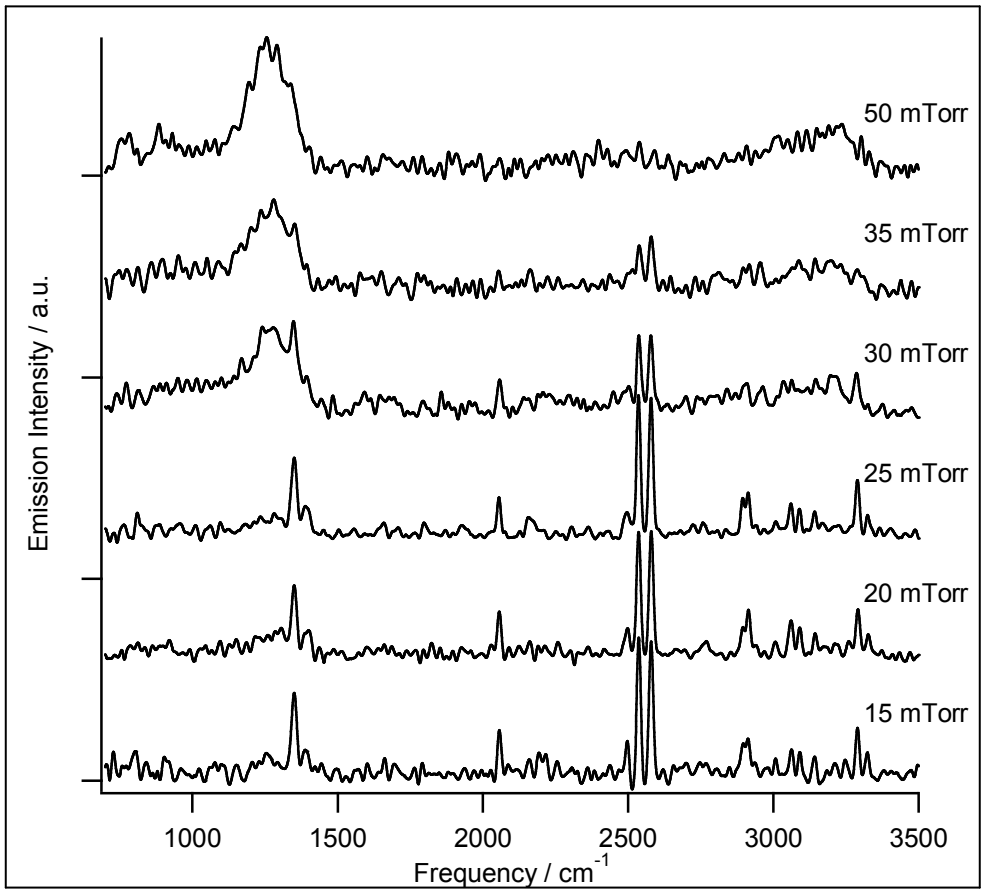

Figure 4.10. IR emission time slices following the 193 nm photolysis of 50 mTorr vinyl iodide in 4 Torr Ar. Raw spectra are shown in grey. IR emission fitting results are overlaid in black.

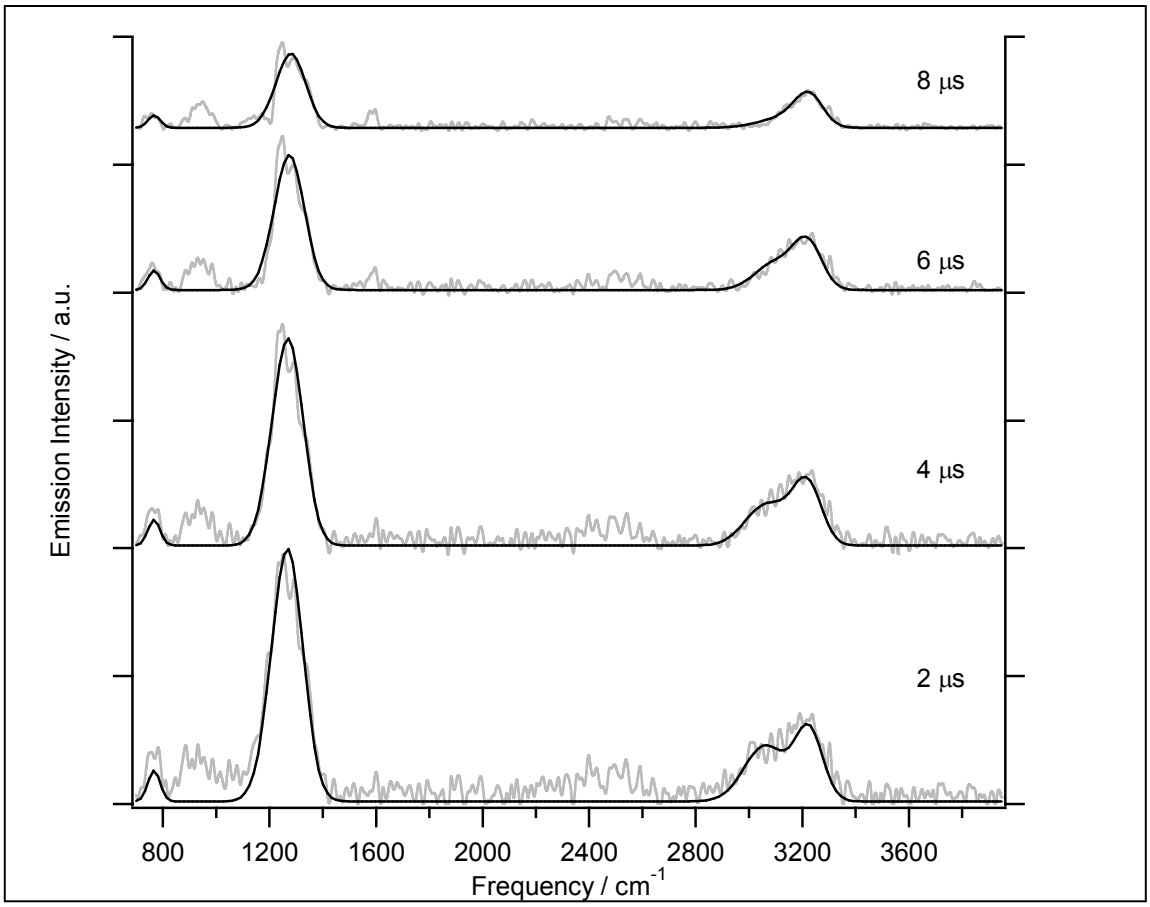

Figure 4.11. The average vibrational energy of acetylene, $\langle E \rangle$, is plotted as a function of time. The open circles are the individual $\langle E \rangle$ determined directly from the fitting procedure. The line is a fit to a single exponential decay function.

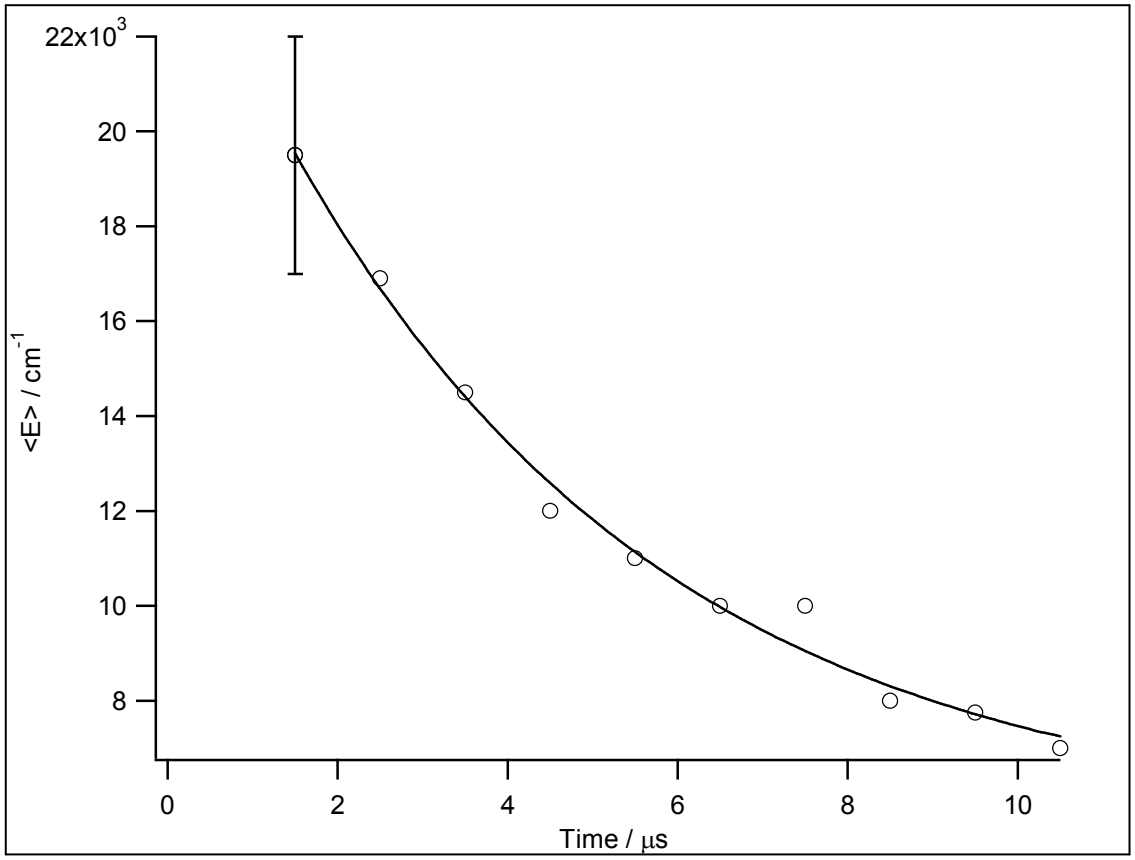

4.3.5 IR emission modeling of 1,3-butadiene

IR emission following the 193 nm dissociation of 1,3-butadiene generates predominantly vibrationally hot acetylene. Time-resolved IR emission results for several time slices are shown in Figure 4.12. The raw IR emission spectra are shown in grey. The IR emission model fitting of the acetylene features is overlaid in black. The dominant features present in the IR emission result arise from the $\nu_4 + \nu_5$ combination, ν_5 bend, and ν_3 stretch modes, located at 775, 1275, and 3000-3300 cm^{-1}, respectively, as seen in the spectra. The two low energy bending and combination bands are adequately modeled using the method described previously, however the CH stretching band is inadequately modeled at early times. This may be due to the three CH stretches of the vinyl radical. Recent spectroscopic studies of the vinyl radical indicate that the asymmetric CH stretch mode lies around 2900 cm^{-1},[43] well below theoretical estimates which place the band between 3000 and 3100 cm^{-1}.[44,45] The three CH modes of the vinyl radical, all theoretically determined within 200 cm^{-1} of each other may contribute to this feature, however can not be resolved because of the overlap.

There are four other emission features observed at early time, centered at 900, 1800, and 2500 cm^{-1} and a feature which appears as a shoulder to the intense 1275 cm^{-1} combination band of acetylene, located at 1100cm^{-1}. The first grouping of features at 900 and 1100 cm^{-1} is assigned to the two out of plane mode of the vinyl radical at 897 and 944 cm^{-1} and the in plane bending mode at 1074 cm^{-1}, as described in Chapter 3. The feature at 2500 cm^{-1} may arise from a weak overtone/combination band of vibrationally hot acetylene. The exact identification of this peak will be discussed in Chapter 6. The feature at 1800 cm^{-1} is rotationally unresolvable and an accurate assignment could not be

Figure 4.12. Time-resolved IR emission results following the 193 nm photolysis of 20 mTorr 1,3-butadiene in 4 Torr Ar. Three time slices are shown in grey. Acetylene IR emission modeling results are overlaid in black for each spectra.

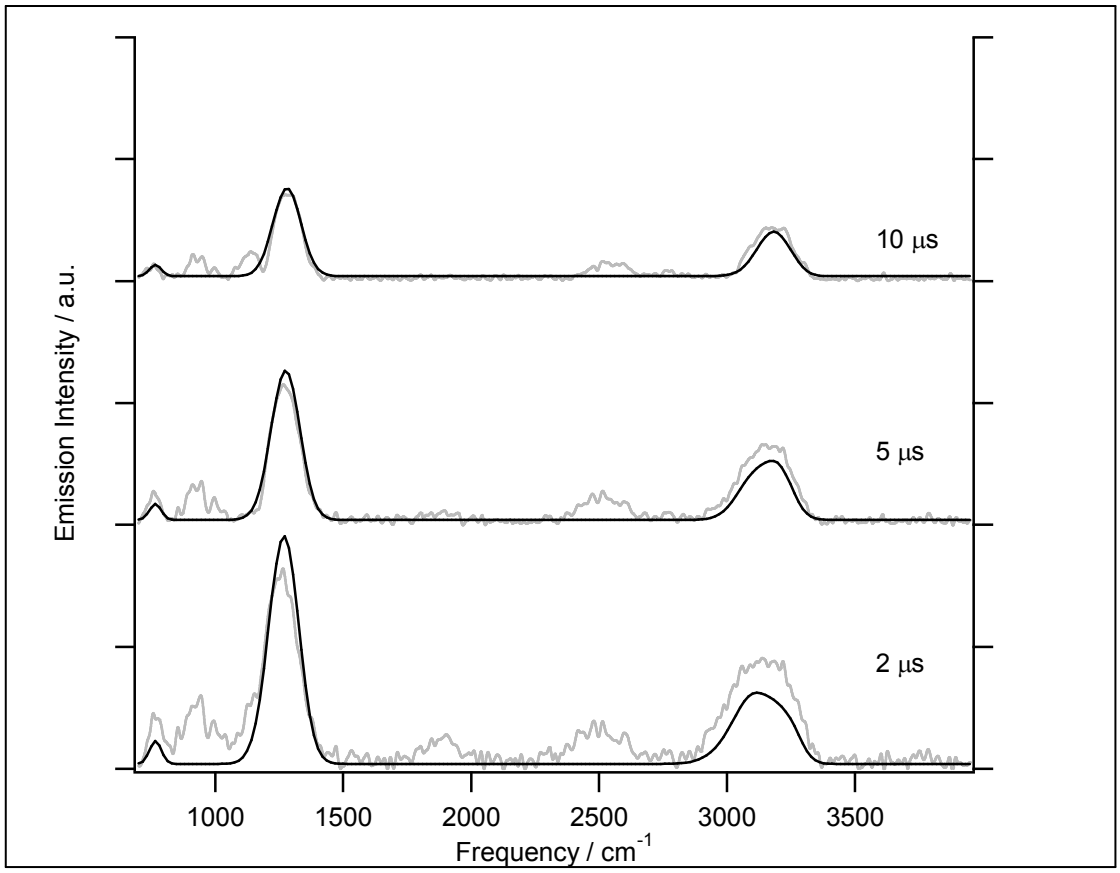

made due to the large number of dissociation pathways for 1,3-butadiene generating several vibrationally excited polyatomic species.[46] There is one feature that appears at late time near 1100 cm^{-1}. This is attributed to a secondary reaction forming vibrationally excited 1,3-butadiene. In addition, another feature appears at 1600 cm^{-1} which is also attributed to 1,3-butadiene. Both of these features gain intensity as the precursor pressure is increased.[42]

The average vibrational energy of acetylene is plotted vs. time following the photolysis of 1,3-butadiene in Figure 4.13. The vibrational energy $\langle E \rangle$ is extracted from the vibrational emission modeling results for each time slice. The energy $\langle E \rangle$ is fit to a single exponential decay with a nascent vibrational energy of 24,800 ± 12,800 cm^{-1}. The large error bar is due to the limited number of vibrational energies extracted from the time resolved spectra. This is a direct result of a high precursor pressure used to generate a sufficient amount of vibrationally excited acetylene.

4.3.6 IR emission modeling of methyl vinyl ketone

The IR emission of acetylene following the 193 nm photolysis of methyl vinyl ketone is more complicated than that performed on the previous molecules. Emission from vibrationally hot acetylene is observed via the $\nu_4 + \nu_5$ combination, ν_5 bend, and ν_3 stretch modes at 775, 1275, and near 3000 cm^{-1}, respectively. This is shown in Figure 4.14. IR emission modeling of the acetylene features is less accurate at early times where there appears to be additional emitters present. The modeling is more accurate at late time when it appears that the only vibrationally hot acetylene is emitting.

Figure 4.13. The average vibrational energy of acetylene, $\langle E \rangle$, is plotted as a function of time following the photolysis of 1,3-butadiene. The individual energy values are extracted from the IR emission model fitting results. A single exponential function is fit to the $\langle E \rangle$ vs. time data.

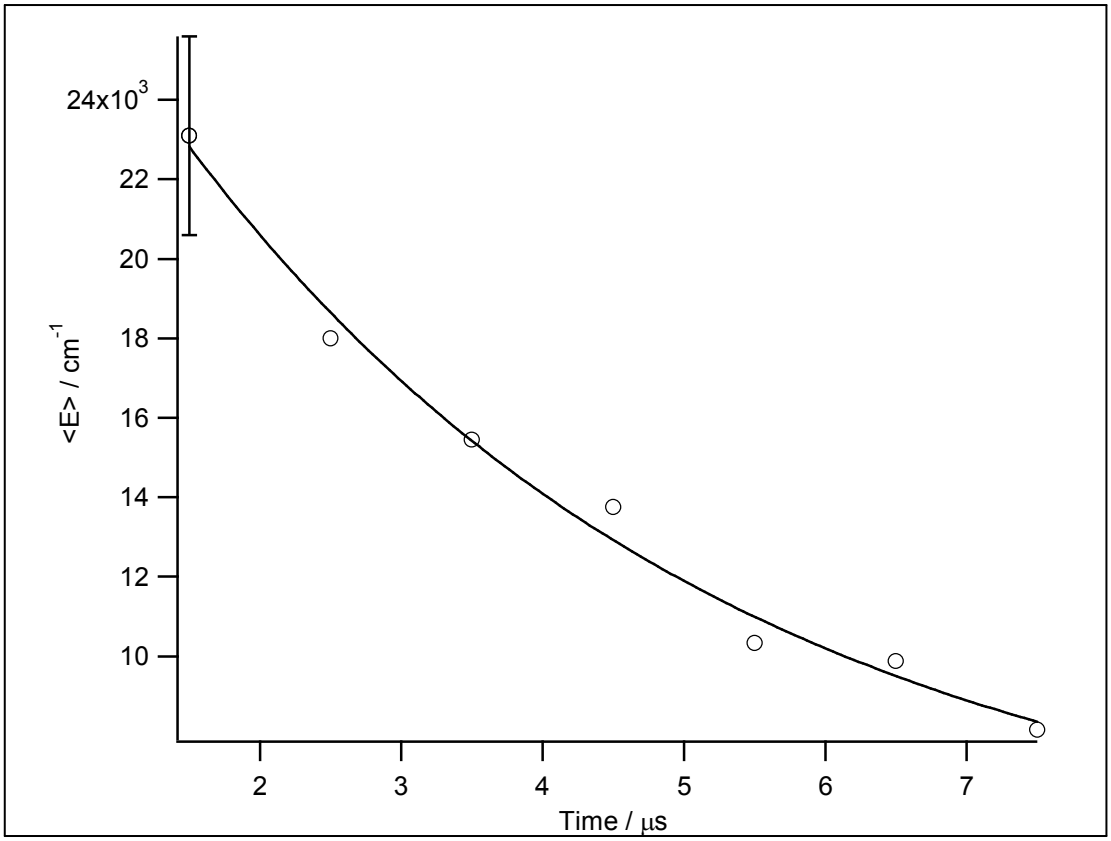

Figure 4.14. Four IR emission spectra time slices following the 193 nm photolysis of 25 mTorr methyl vinyl ketone in 4 Torr Ar is shown in grey. The IR emission fitting result for acetylene is overlaid in black.

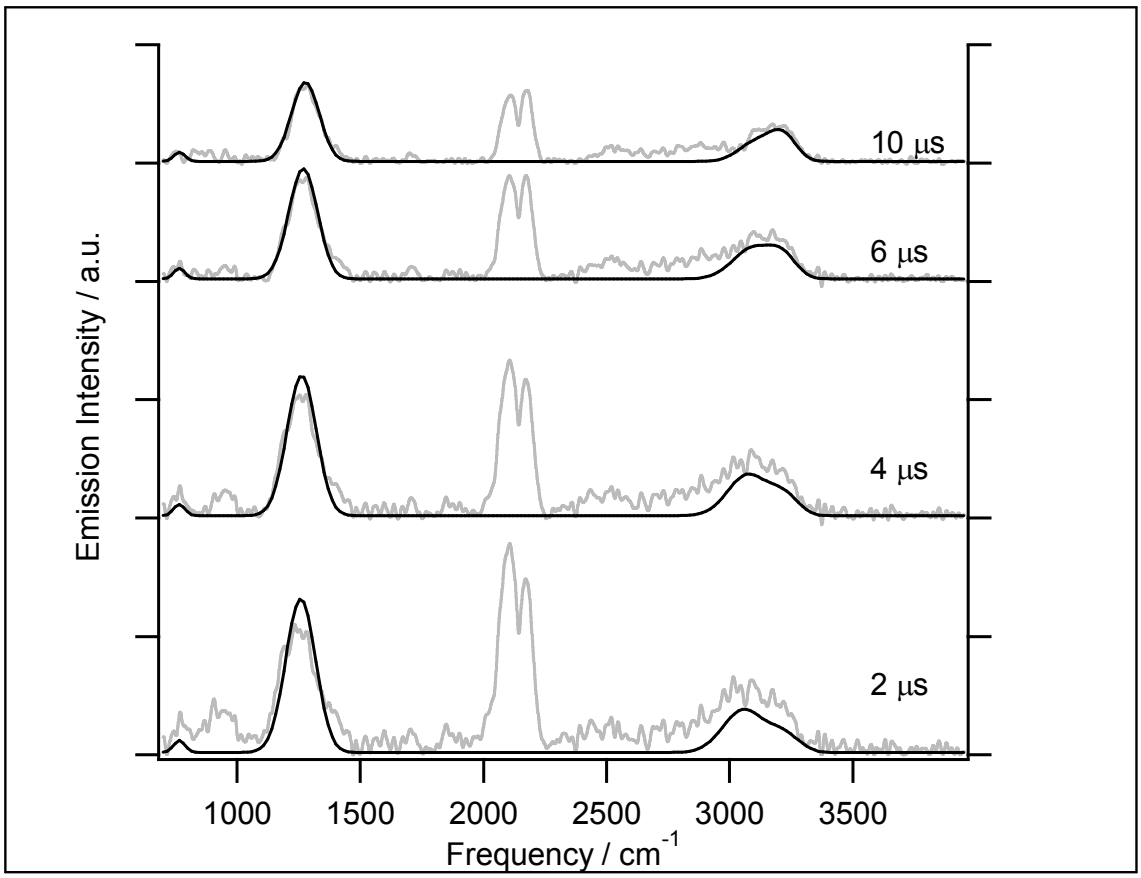

In addition to emission from acetylene, strong CO emission is observed near 2150 cm^{-1}, predominantly from v=1→v=0. In addition, at early time, shown as 2 μs in Figure 4.14, there is a substantial emission near 900, 1400, 2500, and 2800 - 3000 cm^{-1} which can not be assigned to acetylene. The 900 and 1400 cm^{-1} features are assigned to the vinyl radical as described in Chapter 3. The 2500 cm^{-1} feature may arise from weak overtone and combination bands of acetylene. This feature will be discussed more in Chapter 6 where positive identification of the band can be made and subsequently modeled. The broad feature from 2800-3000 cm^{-1}, which can not be accurately fit using the acetylene IR emission model, may arise from the vinyl radical as well. As in the case of 1,3-butadiene, the three CH vinyl stretching modes can not be extracted from the IR emission at early times due to the overlap with the CH stretching mode of vibrationally excited acetylene.

The average vibrational energy, $\langle E \rangle$, is plotted as a function of time in Figure 4.15. The open circles are the $\langle E \rangle$ values extracted from the vibrational emission model fitting results. A single exponential function was used to fit the $\langle E \rangle$ vs. time data based on the accurate fitting results of the previous systems and the expected exponential decay rate for vibrational cooling.[47-49] The nascent vibrational energy of acetylene was found from the single exponential fit to be 27,200 ± 13,500 cm^{-1}. The large error bar is due to the limited number of data points in the fitting. Based on the qualitative comparison between the $\langle E \rangle$ and the fitting result, we expect this value to be more accurate than the error bar predicts.

Figure 4.15. The average vibrational energy, $\langle E \rangle$, is plotted as a function of time for the photolysis of methyl vinyl ketone. The open circles represent $\langle E \rangle$ extracted from the vibrational emission model fitting result. The error bar on the first $\langle E \rangle$ represents the FWHM of the distribution. The line represents the best fit single exponential.

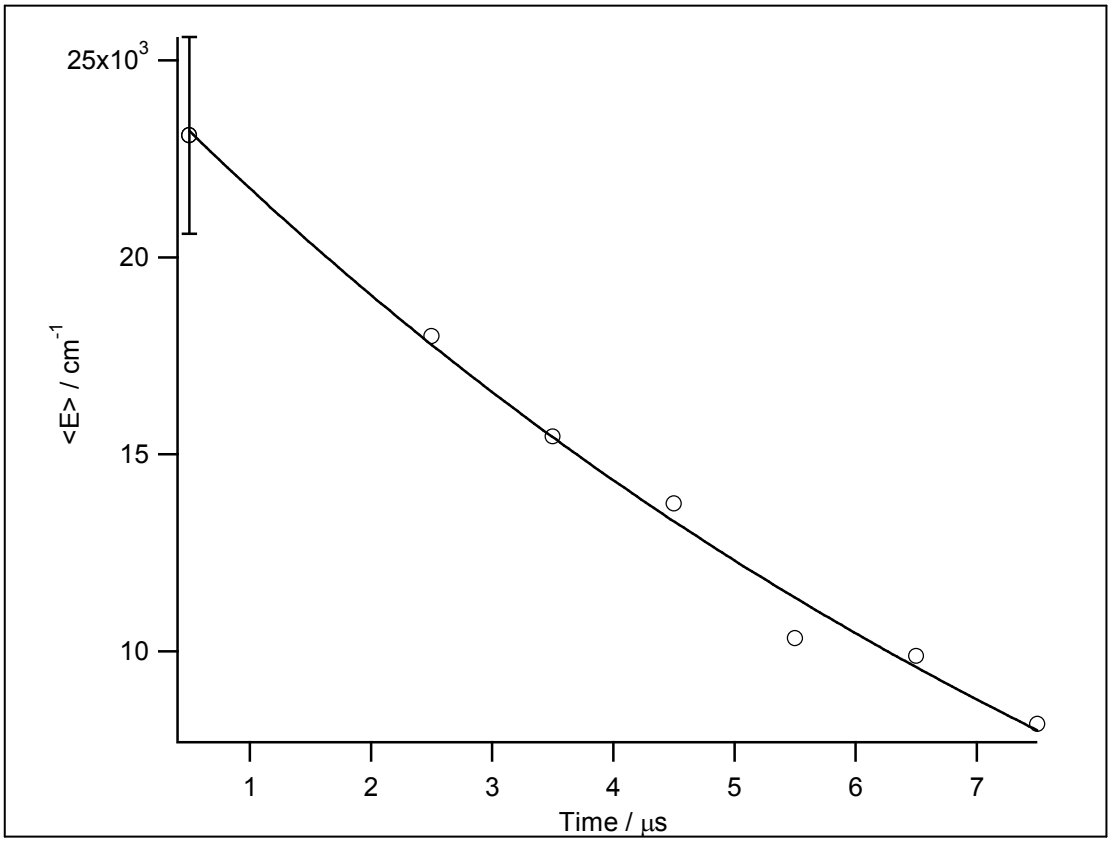

4.4 Discussion

4.4.1 Combination-band intensity

The intensity of the $\nu_4 + \nu_5$ combination band from highly vibrationally excited acetylene is unexpectedly strong relative to the $\Delta\upsilon$=1 transitions of other modes despite that combination bands are forbidden in harmonic oscillator selection rules and that in the absorption spectrum this combination band is relatively weak. The primary factor that can be used to account for the high intensity of this combination band is the harmonic oscillator scaling term with respect to the normal mode quantum numbers. Its effect is elaborated here.

This harmonic scaling factor for combination bands has been proposed in several theoretical papers.[50,51] The term has been used to account for absorption hot bands of HCN.[31] The complete derivation of the harmonic oscillator scaling factor is given in Chapter 2. Here, we will only discuss the terms relevant in identifying the origin of this factor in the combination band emission intensity. We first relate the intensity of a vibrational transition between two states, υ' and υ", to the electric dipole operator μ and normal mode coordinates Q's as:

$$\sqrt{I} \propto \langle \psi_{\upsilon'} | \mu | \psi_{\upsilon''} \rangle = \sum_{k=1} \frac{\partial \mu}{\partial Q_k} \langle \psi_{\upsilon'} | Q_k | \psi_{\upsilon''} \rangle + \sum_{k=1} \sum_{l=1} \frac{\partial^2 \mu}{\partial Q_k \partial Q_l} \langle \psi_{\upsilon'} | Q_k Q_l | \psi_{\upsilon''} \rangle + \ldots \quad (4.8)$$

Expressing normal mode wavefunctions as $\psi_\upsilon = \psi(Q_1)\psi(Q_2)\ldots\psi(Q_{3N-6})$, we obtain the overtone ($k = l$) and combination ($k \neq l$) band intensity from the second term along Q_k and Q_l as

$$\sqrt{I} \propto \sum_{k=1} \sum_{l=1} \frac{\partial^2 \mu}{\partial Q_k \partial Q_l} \langle \psi_{\upsilon'}(Q_k) | Q_k | \psi_{\upsilon''}(Q_k) \rangle \langle \psi_{\upsilon'}(Q_l) | Q_l | \psi_{\upsilon''}(Q_l) \rangle + \ldots \quad (4.9)$$

Upon solving Eq. 4.8 with the normal mode wavefunctions expressed in the Hermite polynomial of degree υ_k, it is found that for the transitions involving multiple modes becomes

$$I \propto \prod_k \left[\left(\upsilon_k + \Delta\upsilon_k \right)! / \left(\Delta\upsilon_k ! \upsilon_k ! \right) \right] \tag{4.10}$$

Here υ_k is the lower state quantum number. Eq. 4.10 is generally applicable to all multiple mode transitions including overtone bands where $\Delta\upsilon_k$>1. For a single quanta emission transitions to the lower state υ_k, Eq. 4.10 further simplifies to

$$I \propto \prod_k \left(\upsilon_k + 1 \right) \tag{4.11}$$

The above equation is applicable for non-degenerate modes. For degenerate modes such as modes ν_4 and ν_5 of acetylene, degenerate harmonic oscillator wavefunctions, such as those by Pauling and Wilson[52] in the doubly degenerate case, will have to be used. Similar to results by Maki *et al.*,[31] we obtain for the simplified case of $\Delta l = \pm 1$ (l = $0, \pm 2, \pm 4, ..., \pm \upsilon$ if υ is even and $\pm 1, \pm 3, ..., \pm \upsilon$ if υ is odd):

$$I \propto \frac{\left(\upsilon \pm l + 2 \right)}{2 g_\upsilon} \tag{4.12}$$

where g_υ is equal to 1 when either l' or $l'' = 0$, or 2 when l' and $l'' \neq 0$. The g_υ term originates from the restriction of having one of the angular momentum states equal to zero, thus restricting rotational branches to P and R, or Q, but not all three when l' and $l'' \neq 0$. Since we are assuming a constant rovibrational envelope function, independent of internal energy and rotational structure, this term only affects the overall intensity of the rovibrational transition. If we consider two or more independent, doubly degenerate modes, Eq. 4.12 can be generalized to:

$$I \propto \prod_k \frac{(\upsilon_k \pm l_k + 2)}{2g_{\upsilon_k}} \tag{4.13}$$

for all doubly degenerate bands with $|\Delta\upsilon_k|=1$ and $\sum_k \nu_k > 1$.

The accurate modeling of the IR emission bands from highly vibrationally excited acetylene using the normal mode basis is somewhat surprising and indicates that the description of vibrationally excited molecules depends on the observables. In the high energy region where the eigenstates are no longer properly described in the normal mode basis, for observables such as IR transitions involving low quantum number changes, $\Delta\upsilon$ = 1 or 2, normal mode descriptions remain an effective means of characterizing vibrational energy. When transitions occur through electronic motion or multiple changes in vibrational quanta the local mode picture of acetylene may be utilized accurately. In the experiment discussed here, the observation window is suited for only low quantum number jumps and normal mode states.

4.4.2 Energetics of the Photolysis Reaction

The $\langle E \rangle_0$ determined in Section 4.3 is in agreement with previous experiments on the 193 nm photolysis of vinyl bromide. A photofragment translational energy study found the center of mass translational energy content, $\langle E_t \rangle$ ~18 kcal mol^{-1}.[25,40] From work done on the vibrational emission of photolysis exothermicity of 121.5 kcal mol^{-1}, the nascent acetylene would have at most 79 kcal mol^{-1} of vibrational energy,[41] as compared to the 71 kcal mol^{-1} of vibrational energy determined from the IR emission modeling. The remaining energy unaccounted for, ~8 kcal mol^{-1}, may be explained by the rotational energy of acetylene in the model.

One concern over the accuracy of the fitting result may arise from the seemingly arbitrary choice of a Gaussian vibrational population distribution for the nascent acetylene emission. The use of a Gaussian distribution stems from the initially generated vibrationally and rotationally hot acetylene molecule produced through a concerted dissociation mechanism from vinyl bromide with HBr as a counterfragment. HBr is formed vibrationally and rotationally hot with an exponential vibrational population with the majority excited in v=1.[22,37] This population would correspond to a similar vibrational population distribution in acetylene, however collisional deactivation by the noble gas colliders would blur this distribution into something more broad and undefined. Therefore we utilize a variable width Gaussian function as a semi-quantitative model distribution.

The $\langle E \rangle$ vs. time and $\langle E \rangle_0$ suggest acetylene is formed in the vibrational ground state directly following dissociation. Recent work on the counter fragment of acetylene, HBr, revealed the dominance of a three center elimination pathway following the 193 nm absorption.[22,25] The three center elimination channel forms a vibrationally and rotationally hot HBr fragment plus a vinylidene molecule, as opposed to the four center elimination channel producing HBr and acetylene. Vinylidene is a high energy isomer of acetylene located approximately 15,000 cm^{-1} of energy above the acetylene ZPE.[53] The vinylidene molecule is thought to be very short lived with lifetimes of τ~0.04 – 0.2 ps at the zero-point level.[53] It is expected that vinylidene produced with high internal excitation will rapidly isomerizes and appear as acetylene with dominating probability since the density of vibrational states of acetylene is much higher than that of vinylidne. Accordingly, no spectroscopic assignments of vinylidene are made here.

4.4.3 Implications of strong combination bands in IR emission from highly vibrationally excited molecules

There is a significant interest in the IR emission signature of molecules in many areas of science. We briefly discuss the role of acetylene IR emission in combustion and environmental chemistry and in spectroscopy of interstellar and extraterrestrial systems. In particular, we focus on the potential application of the unexpectedly strong combination band emission of vibrationally excited acetylene.

Acetylene is well known in combustion chemistry as a fuel source as well as an unreacted product usually found in stack gas emissions. Acetylene is even more prevalent in the production of coke, which is used in the production of steel. A recent work monitored the production of acetylene molecules at the stacks of a steel mill.[54] The analytical method consisted of an open-path Fourier transform spectrometer mounted on top of the production building. The open-path absorption method allowed for a long absorption path length, 109 m, maximizing spectral intensity. Nine coke oven gases (COG's) were monitored. The production of these gases was found to vary depending on what step of the coke production was performed. Little is known about the production of the COG's. Utilizing the highly temperature dependent coke production dynamic information can be obtained from IR emission. IR emission and subsequent modeling of acetylene and the 8 other COG's may yield information about the role of these molecules in the coke production process and COG exhaust. In addition, the unexpectedly strong $\nu_4 + \nu_5$ combination band may be used as a marker for identification of (vibrationally hot) acetylene.

Emission from acetylene has been found in large quantities in the atmosphere of Jupiter[55] and the carbon asymptotic giant branch star IRC +10216.[56] Spatially resolved

IR emission of Jupiter was detected via the Composite Infrared Spectrometer on the Cassini spacecraft. Acetylene is thought to exist primarily in the upper atmosphere of Jupiter where photochemical processes dominate producing many highly excited molecules and radicals. Most of these processes are only generally known and hypothesized to occur in the planetary atmosphere. Since all of the spectra are recorded through emission, and the possibility of the production of highly excited species is expected from the photochemistry, an accurate picture of emission from these excited species is necessary. On July 20th, 2009, the planet Jupiter was struck by a passing object.[57,58] The impact left a visibly dark spot in the atmosphere of Jupiter. The impact also caused a large plume of hot gases to erupt from the atmosphere which was observed through NASA's Infrared Telescope Facility. Since acetylene has been observed to be present in the atmosphere of Jupiter,[55] the possible observation of the intense combination band may yield a substantial amount of information about the static and dynamic environment of Jupiter's atmosphere.

Acetylene has been observed in a slightly different environment, the IRC +10216 star and surrounding gas and dust cloud.[56] The IR signature of the star was detected at the NASA Infrared Telescope Facility in the spectral range of 720 – 864 cm^{-1} with very high sensitivity and resolution. Acetylene and hydrogen cyanide were found among several hundred bands observed. The authors have identified a majority of these rovibrational features; however, there are still many other unassigned modes which may arise from higher vibrational excitation. Modeling of IR emission of several low lying bands has yielded vibrational, rotational, and kinetic temperatures in different areas of the star. It is quite evident however, that a clearer view of emission from high vibrational

states is needed. The strong combination bands may provide for the easiest detection of emission of acetylene and may account for other unassigned bands.

4.4.4 Recent observations of IR emission from highly vibrationally excited acetylene

Several recent spectroscopic studies on the photolysis of vinyl halides have made mention of the presence of acetylene in their recorded spectra, while some have not observed acetylene emission where one would expect some emission signal to be observed.

Low resolution FTIR emission results from Lin *et al.*[37] reveal the presence of the ν_3 band of highly vibrationally excited acetylene at early times following the 193 nm photolysis of vinyl chloride. The excited population quickly cools to the fundamental transition by 47 μs. Only a brief mention of this feature is given, even though it is in direct overlap with several of the R branches (1-0, 2-1, 3-2) of HCl rovibrational emission bands. A similar study by Carvalho *et al.*[23] on vinyl chloride revealed highly excited acetylene emission from the $\nu_4 + \nu_5$ and ν_3 bands at late time, ~30 μs, following photolysis. The high precursor pressures used in this study may account for the large population of highly excited acetylene observed late following photolysis. The accurate modeling of these features would aid greatly in understanding the spectroscopic assignement and dynamics of these two modes.

Highly excited acetylene has also been observed in studies analogous to the one performed here on vinyl bromide. Liu *et al.*[22], Lin *et al.*[25], and Carvalho *et al.*[23] analyzed the HBr elimination channels following the 193 nm photolysis of vinyl bromide. All three studies acknowledged the existance of highly excited acetylene, however no

spectroscopic or thermodynamic data was extracted. Further, the exceptionally strong combination band of acetylene was not noted.

In addition to vinyl bromide, Lin *et al.*[25] analyzed the emission following the photodissociation of vinyl fluoride. The energetics and dissociation of vinyl fluoride is similar to that of the other vinyl halides, however no emission from the ν_3 mode of acetylene is observed even though the mode is in overlap with many rovibrational bands of HF, which are observed in the region between 3000 and 3300 cm^{-1}. Two possible explanations for the absence of this feature are: (1) the high precursor pressure (180 mTorr) rapidly quench the emission from acetylene via efficient vibrational to vibrational energy transfer, and (2) the low S/N ratio prohibiting the observation of vibrationally hot acetylene.

The photolysis of vinyl iodide by Zou *et al.*[39] reveals a marked departure from the other vinyl halides. The authors state that no acetylene emission is observed following photolysis between 193 and 266 nm. The emission observed near 3000-3300 cm^{-1} is assigned to the three CH stretching modes of the vinyl radical. In addition, no HI is observed. They justify their observations by discussing the photodissociation dynamics of the vinyl halide series from vinyl fluoride, where dissodiation is dominated by internal conversion to the ground state, to vinyl iodide, where dissociation occurs predominantly on the excited state surface.

This observation of Zou *et al.*[39] is in contrast to a previous study in our laboratory on the assignment of the nomal modes of the vinyl radical.[17] In that study, vibrationally hot acetylene is observed from vinyl chloride, vinyl bromide, and vinyl iodide. One explanation may arise from the fact that the vinyl radical is produced vibrationally hot and may dissociate. It may be that the noble gas used by Zou *et al.*,[39]He, may be more

efficient, than Ar, used in our previous study, at cooling vibrationally excited vinyl radicals before they dissociate.

We will make one final note on two molecules, methyl vinyl ketone and 1,3-butadiene, that have also been observed to generate vibrationally hot acetylene following photolysis. Both molecules, following photolysis, generate a significant amount of vibrationally excited acetylene.[17] In the case of 1,3-butadiene, this is expected, as photofragment translational spectroscopy results indicate that this is a major reaction channel.[46] The observation of acetylene following the 193 nm photolysis of methyl vinyl ketone, however, is unexpected. Spectroscopic and chromatographic results by Fahr *et al.*,[59] indicate a near unity quantum yield for the formation of methyl and vinyl radicals following the 193 nm photolysis of methyl vinyl ketone. No acetylene is observed in their study. The observation of emission assignable to acetylene in our previous study[17] indicates that there may be another mechanism, possibly concerted, forming vibrationally hot acetylene. Even more unexpected is the fact that emission from acetylene is similar in intensity in all five photolysis results. This discrepancy therefore warrants further study.

4.5 Conclusion

The $\nu_4 + \nu_5$ combination band in emission from highly vibrationally excited acetylene has been observed with unexpected strong intensity following the dissociation of vinyl bromide, vinyl chloride, vinyl iodide, 1,3-butadiene, and methyl vinyl ketone. This combination band, though relatively weak in comparison to the IR active fundamental bands in the room temperature absorption spectrum, has grown to more than one order of magnitude stronger than the other emission bands at the vibrational energies

of 50 – 70 kcal mol^{-1}. Although the emission is from energy regions where normal mode quantum numbers are no longer good, the combination band intensity can be justified by its proportionality to the product of the vibrational quanta in the ν_4 and ν_5 modes. The emission spectra in the mid-IR region can be quantitatively described by a normal mode model that incorporates anharmonicity for the energy levels, experimentally measured absorption spectral intensity, and intensity scaling according to normal mode quantum numbers. A nonlinear least-squares fit of the three IR emission bands of acetylene, ν_5, $\nu_4 + \nu_5$, and ν_3 yields an initial average vibrational energy for acetylene as 71 kcal mol^{-1} following the 193 nm photolysis of vinyl bromide which agrees with previous IR emission spectroscopy and fragment translational energy mass spectrometry measurements.

References:

(1) Orr, B. J. *Int. Rev. Phys. Chem.* **2006**, *25*, 655.

(2) Hiraoka, K.; Sato, T.; Takayama, T. *Science* **2001**, *292*, 869.

(3) Ziurys, L. M. *Proc. Nat. Acad. Sci.* **2006**, *103*, 12274.

(4) Kaiser, R. I. *Eur. Space Agen. Sp. Pub.* **2001**, *SP-496*, 145.

(5) Bartlett, K. B.; Sachse, G. W.; Slate, T.; Harward, C.; Blake, D. R. *J. Geophys. Res.* **2003**, *108*, GTE28/1.

(6) Moreira, A.; Penkett, S.; Reeves, C. *Proc. Air & Waste Manag. Ann. Conf.* **2001**, 2516.

(7) Chadwick, B. L.; King, D. A.; Berzins, L.; Orr, B. J. *J. Chem. Phys.* **1989**, *91*, 7994.

(8) Frost, M. J.; Smith, I. W. M. *Chem. Phys. Lett.* **1992**, *191*, 574.

(9) Chadwick, B. L.; Milce, A. P.; Orr, B. J. *Can. J. Chem.* **1994**, *72*, 939.

(10) Chen, Y.; Jonas, D. M.; Kinsey, J. L.; Field, R. W. *J. Chem. Phys.* **1989**, *91*, 3976.

(11) Tobiason, J. D.; Utz, A. L.; Crimm, F. F. *J. Chem. Phys.* **1994**, *101*, 1108.

(12) Jacobson, M. P.; Field, R. W. *J. Phys. Chem. A* **2000**, *104*, 3073.

(13) Herman, M.; Lievin, J.; Auwera, J. V.; Campargue, A. *Adv. Chem. Phys.* **1999**, *108*, 1.

(14) Herman, M.; Campargue, A.; ElIdrissi, M. I.; Auwera, J. V. *J. Phys. Chem. Ref. Data* **2003**, *32*, 921.

(15) El Idrissi, M. I.; Lievin, J.; Campargue, A.; Herman, M. *J. Chem. Phys.* **1999**, *110*, 2074.

(16) Young, S. M.; Mason, S. E.; Rappe, A. M. *Unpublished work* **2007**.

(17) Nikow, M.; Wilhelm, M. J.; Dai, H.-L. *J. Phys. Chem. A* **2009**, *113*, 8857.

(18) Hartland, G. V.; Xie, W.; Dai, H.-L.; Simon, A.; Anderson, M. J. *Rev. Sci. Instr.* **1992**, *63*, 3261.

(19) Letendre, L.; Dai, H.-L.; McLaren, I.; Johnson, T. J. *Rev. Sci. Instr.* **1999**, *70*, 18.

(20) Zou, P.; Strecker, K. E.; Ramirez-Serrano, J.; Jusinski, L. E.; Taatjes, C. A.; Osborn, D. L. *Phys. Chem. Chem. Phys* **2007**, *10*, 713.

(21) Kanamori, H.; Endo, Y.; Hirota, E. *J. Chem. Phys.* **1990**, *92*, 197.

(22) Liu, D., -Kuo; Letendre, L.; Dai, H.-L. *J. Chem. Phys.* **2001**, *115*, 1734.

(23) Carvalho, A.; Hancock, G.; Saunders, M. *Phys. Chem. Chem. Phys* **2006**, *8*, 4337.

(24) Wodtke, A. M.; Hintsa, E. J.; Somorjai, J.; Lee, Y. T. *Isr. J. Chem.* **1989**, *29*, 383.

(25) Lin, S.-R.; Lin, S.-C.; Lee, Y.-C.; Chou, Y.-C.; Chen, I.-C.; Lee, Y.-P. *J. Chem. Phys.* **2001**, *114*, 7396.

(26) Pusharsky, M. B.; Mann, A. M.; Yeston, J. S.; Moore, C. B. *J. Chem. Phys.* **2001**, *115*, 10738.

(27) Herzberg, G. *Molecular Spectra and Molecular Structure*; Van Nostrand: New York, 1950; Vol. II Infrared and Raman Spectra of Polyatomic Molecules.

(28) Kelly, R. L.; Rolefson, R.; Schurin, B. S. *J. Chem. Phys.* **1951**, *19*, 1595.

(29) *Infra-Red Spectroscopy and Molecular Structure*; Fahrenfort, J.; Davis, M., Eds. NY, 1963.

(30) Mandin, J. Y.; Jacquemart, D.; Dana, V.; Regalia-Jarlot, L.; Barbe, A. *J. Quant. Spectrosc. Radiat. Transfer* **2005**, *92*, 239.

(31) Maki, A.; Quapp, W.; Klee, S. *J. Mol. Spec.* **1995**, *171*, 420.

(32) Hartland, G. V.; Qin, D.; Dai, H.-L. *J. Chem. Phys.* **1994**, *100*, 7832.

(33) Hartland, G. V.; Qin, D.; Dai, H.-L. *J. Chem. Phys.* **1994**, *101*, 8554.

(34) Hartland, G. V.; Qin, D.; Dai, H.-L. *J. Chem. Phys.* **1997**, *107*, 2890.

(35) Pibel, C. D.; Sirota, E.; Brenner, J.; Dai, H.-L. *J. Chem. Phys.* **1998**, *108*, 1297.

(36) Qin, D.; Hartland, G. V.; Dai, H.-L. *J. Phys. Chem. A* **2000**, *104*, 10460.

(37) Lin, S.-R.; Lin, S.-C.; Lee, Y.-C.; Chou, Y.-C.; Chen, I.-C.; Lee, Y.-P. *J. Chem. Phys.* **2001**, *114*, 160.

(38) Bahou, M.; Lee, Y.-P. *Aust. J. Chem* **2004**, *57*.

(39) Zou, P.; Strecker, K. E.; Ramirez-Serrano, J.; Jusinski, L. E.; Taatjes, C. A.; Osborn, D. L. *Phys. Chem. Chem. Phys* **2008**, *10*, 713.

(40) Blank, D. A.; Sun, W.; Suits, A. G.; Lee, Y. T.; North, S. W.; Hall, G. E. *J. Chem. Phys.* **1998**, *108*, 5414.

(41) Letendre, L.; Liu, D.-K.; Pibel, C. D.; Halpern, J. B.; Dai, H.-L. *J. Chem. Phys.* **2000**, *112*, 9209.

(42) *Infrared Spectra*; Linstrom, P. J.; Mallard, W. G., Eds.; NIST Chemistry WebBook: Gaithersburg, MD 20899.

(43) Dong, F.; Roberts, M.; Nesbitt, D. J. *J. Chem. Phys.* **2008**, *128*, 044305.

(44) Sattelmeyer, K. W.; Schaefer, H. F., III. *J. Chem. Phys.* **2002**, *117*, 7914.

(45) Wu, Y.-J.; Lin, M.-Y.; Cheng, B.-M.; Chen, H.-F.; Lee, Y.-P. *J. Chem. Phys.* **2008**, *128*, 204509.

(46) Robinson, J. C.; Harris, S. A.; Sun, W.; Sveum, N. E.; Neumark, D. M. *J. Am. Chem. Soc.* **2002**, *124*, 10211.

(47) Lambert, J. D. *Vibrational and Rotational Relaxation in Gases*; Clarendon Press: Oxford, 1977.

(48) Yardley, J. T. *Introduction to Molecular Energy Transfer*; Academic Press: New York, 1980.

(49) Baer, T.; Hase, W. L. *Unimolecular Reaction Dynamics: Theory and Experiment*; Oxford University Press: New York, 1996.

(50) Legay-Sommaire, N.; Legay, F. *J. Mol. Spec.* **1962**, *8*, 1.

(51) Tipping, R. H. *J. Mol. Spec.* **1976**, *61*, 272.

(52) Pauling, L.; Wilson Jr., E. B. *Introduction to Quantum Mechanics*; Dover: New York, 1935.

(53) Ervin, K. M.; Ho, J.; Lineberger, W. C. *J. Chem. Phys.* **1989**, *91*, 5974.

(54) Lin, C.; Liou, N.; Chang, P.-E.; Yang, J.-C.; Sun, E. *J. Air Waste Mang. Assc.* **2007**, *57*, 472.

(55) Kunde, V. G.; Flasar, F. M.; Jennings, D. E.; Bezard, B.; Strobel, D. F.; Conrath, B. J.; Nixon, C. A.; Bjoraker, G. L.; Romani, P. N.; Achterberg, R. K.; Simon-Miller, A. A.; Irwin, P.; Brasunas, J. C.; Pearl, J. C.; Smith, M. D.; Orton, G. S.; Gierasch, P. J.; Spilker, L. J.; Carlson, R. C.; Mamoutkine, A. A.; Calcutt, S. B.; Read, P. L.; Taylor, F. W.; Fouchet, T.; Parrish, P.; Barucci, A.; Courtin, R.; Coustenis, A.; Gautier, D.; Lellouch, E.; Marten, A.; Prange, R.; Biraud, Y.; Ferrari, C.; Owen, T. C.; Abbas, M. M.; Samuelson, R. E.; Raulin, F.; Ade, P.; Cesarsky, C. J.; Grossman, K. U.; Coradini, A. *Science* **2004**, *305*, 1582.

(56) Fonfria, J. P.; Cernicharo, J.; Richter, M. J.; Lacy, J. H. *Astrophys. J.* **2008**, *673*, 445.

(57) NASA; JPL. New NASA Images Indicate Object Hits Jupiter; NASA, <http://www.jpl.nasa.gov/news/news.cfm?release=2009-112>: Jet Propulsion Lab, Pasadena, CA, 2009.

(58) NASA; ESA; Hammel, H.; Institute, S. S.; Team, J. I.; NASA: <http://hubblesite.org/newscenter/archive/releases/2009/23/full/>, 2009.

(59) Fahr, A.; Braun, W.; Laufer, A. H. *J. Phys. Chem.* **1993**, *97*, 1502.

Chapter 5

The effect of intramolecular large amplitude motion in collision energy transfer from highly vibrationally excited molecules: the case of acetylene - vinylidene

5.1 Introduction

5.1.1 A brief summary

Collisional relaxation of highly vibrationally excited acetylene, produced from the photolysis reaction of vinyl bromide, by noble gas colliders has been studied via sub-microsecond time resolved FTIR emission spectroscopy. Three IR emission bands in association with the acetylene (ν_5, $\nu_4 + \nu_5$, and ν_3) were identified in the time resolved spectra and were modeled for the extraction of vibrational energy content of the emitting acetylene molecules as described in Chapters 2 and 4. The average internal energy, $\langle E \rangle$, as a function of time, which can be related to the number of collisions the nascent acetylene suffered, was determined. The average energy lost per collision, $\langle \Delta E \rangle$, was deduced as described in Chapter 4. It is observed in the $\langle \Delta E \rangle$ vs. $\langle E \rangle$ curve, $\langle \Delta E \rangle$ displays a sharp increase when the acetylene excitation is above 15,000 cm^{-1}.

It is shown that the increase observed in the energy transfer rate in the "high $\langle \Delta E \rangle$" region arises because of the existence of the isomer vinylidene for the highly vibrationally excited acetylene. The onset of the increase corresponds energetically to the onset of acetylene-vinylidene isomerization which occurs approximately 14,000 cm^{-1} above the acetylene ground state zero point energy. The significant enhancement of the energy transfer rate is a result of the much more efficient energy transfer from vinylidene than acetylene.

The collision energy transfer rates of acetylene and vinylidene are compared theoretically by using both an analytical model and semiclassical trajectory calculations. The Schwartz, Slawsky, and Herzfield (SSH)[1,2] theory was originally developed for describing collision energy relaxation of diatomic molecules excited in low energy region and was later extended for polyatomic systems by Tanczos,[3] the SSHT model. This model was based on the repulsive interaction of the LJ potential between the colliders and has been proven effective in semi-quantitative description of V-T relaxation of molecules excited at *low* vibrational levels over decades of comparison with experiments.[4] The model used here has been adapted, a collective effort of several members in the Dai group, Min Zhang, Jianqiang Ma, Michael Wilhelm, Jonathan Smith and myself, for the *high* vibrational excitation region where the energy gap is smaller and level density much higher. The model depicts that highly excited vinylidene, primarily because of its lower frequency vibrational modes, is much more efficient in V-T transfer than acetylene with the same energy. Similar relative magnitude of the V-T rates from vinylidene and acetylene is also obtained using quasiclassical trajectory calculations though the absolute magnitude of the amount of energy transferred is less accurate.

This work shows that existence of structural isomers greatly influences collision energy transfer from highly vibrationally excited molecules. In this case, our observation and interpretation of the collision energy transfer results are consistent with the prediction of the existence of vinylidene and the energy barrier of the acetylene isomerization.

5.1.2 Collision energy transfer from excited molecules

The rates of chemical reactions are dependent on the energy content of the reactants. Energy is needed to overcome barriers to promote the reaction rate. This

energy is typically supplied or removed through collisions between the reactants and the surrounding bath molecules in a macrocanonical system. In a microcanonical system where the energy is well defined the reaction of the molecule is in competition with collision energy relaxation. To describe the reaction rate for an energized molecule, it is critical that collision energy transfer is characterized.

The process of collision induced intermolecular energy transfer is of fundamental importance in chemistry. Through collisions, energy may be transferred in between the various degrees of freedom of the excited molecule and the collider. Energy may be transferred to the internal degrees of freedom of a molecule to promote its chemical reaction or the excited molecule can be quenched through energy transfer out of its internal degrees of freedom to the colliders. The quenching mechanism decreases the reaction rate of the excited molecule.

Characterizing collision energy transfer from vibrationally excited molecules aids in the quantitative analysis of macroscopic molecular (and/or radical) reactions. The ideal understanding of collision energy transfer is a state specific study over a wide range of internal energies. However, due to experimental difficulties this has only been performed, to limited extent, on a few diatomic molecules.[4-6] For larger molecules excited in high energies, the vibrational manifold becomes extremely congested with significant vibrational mode coupling.[7] The high state density and IVR severely hinder state resolved spectroscopic measurements at chemically relevant energies. For example, in a small polyatomic molecule such as cyclopropane, at 35,000 cm^{-1} the level density is ~10^6 states / cm^{-1}.[8]

A good understanding of energy transfer at low vibrational excitation of small molecules has been established from studies on many different systems.[4,9] It is well

anticipated, however, that energy transfer rates of lower and highly vibrationally excited molecular systems differ significantly.[6,10] The study of collision induced energy transfer involving highly excited polyatomic molecules is significantly more difficult due to the increase in vibrational density of states. Even when an accurate vibrational manifold for the polyatomic molecule can be generated, probing these highly dense states with state specificity is quite difficult. Due to the increasing complexity as the collisional deactivation process proceeds, average properties of the ensemble of molecules is typically pursued instead of single state resolved properties.[7]

The technique of time resolved IR emission spectroscopy allows the detection of the vibrational emission from a molecule with nanosecond time resolution as discussed in detail in Chapter 1. Molecules typically have IR emission lifetimes on the order of ~10^{-3} s. These highly excited molecules can be deactivated at a much faster rate through collision with an excess amount of a bath gas. After energy is transferred from the excited molecule it is left with less vibrational energy which can be discerned from the IR emission spectra. Work within the Dai group has explored energy transfer of several highly excited molecules including NO_2,[11] SO_2,[12] CS_2,[13] HCN/HNC[14] and others.[15] The energy distribution of the excited molecules as well as average energy transfer rates have been determined. It was found that long range interactions mediated through transition dipoles are mainly responsible for energy transfer from these highly vibrationally excited molecules.

It is generally well known that the structure of a molecule greatly affects its chemical properties. The structure of a molecule determines the potential energy surface on which the reaction takes place. The PES dictates the preferential reaction paths and products. For example, in the case of UV photodissociation of the three vinyl halides

(vinyl fluoride, vinyl chloride, and vinyl bromide) the formation of vinylidene and the corresponding hydrogen halide via a three centered elimination was found to be highly favored over the four centered elimination forming acetylene and hydrogen halide based on the HBr rovibrational emission observed.[16-18]

Molecular structure has just as an important role in affecting bimolecular reactions. Using acetylene as an example: Its structural isomer vinylidene, which was theoretically predicted to exist as an isomer at approximately 14,000 cm^{-1} above the acetylene ground state zero-point energy, is proposed to be an important reaction intermediate in organic chemistry because of its reactivity while acetylene is known to be less reactive.[19] It is reasonable to anticipate that the structure of the molecule also has serious influence on the energy transfer properties. Again, in the case of acetylene-vinylidene isomer pair, when the excitation energy of acetylene exceeds the isomerization barrier, the excited acetylene appears with finite probability as vinylidene. The presence of vinylidene may have several effects on collision energy transfer: The radical nature of the molecule may bring about very different interaction between the excited acetylene and the collider. The existence of the isomer may greatly increase the vibrational level density in the energy region of interest. And, the vibrational mode structure of vinylidene, been very different from acetylene, may affect the exact quantity of energy that can be transferred. In short, the presence of the isomer may have significant bearing on the mechanism and rate of collision energy transfer from the vibrationally excited molecule.

In this Chapter, we characterize the collision energy transfer properties of acetylene excited in energy regions above and below the predicted isomerization barrier. The vibrationally hot acetylene was generated by a UV photolysis of a suitable acetylene producing precursor in a similar manner to that presented in Chapters 3 and 4.[20] The

energetics of the dissociation of vinyl bromide, producing vibrationally hot acetylene, have been discussed in Chapter 4 and the literature.[21] V-T energy transfer from acetylene to He, Ne, Ar, and Kr noble gases is studied.

5.2 Experimental

The time resolved IR emission experiment has been detailed in the previous chapters and only the relevant details to the current study will be addressed here. Precursor pressures were typically between 2 and 10 mTorr, while the collider gas pressures were 1-5 Torr. The S/N recorded in these experiments was worse than previous experiments due to the desired low precursor pressures to prevent secondary reactions and/or collisional deactivation with the parent molecules. In addition, the low precursor pressures, ~3 orders of magnitude lower than the collider gas pressures, afford the opportunity to study the pure V-T energy transfer dynamics of acetylene with the noble gas atoms.

5.3 Results

5.3.1 IR emission spectra

The UV photolysis of vinyl bromide proceeds via two main reaction channels, radical and molecular dissociations, and is described in detail in Chapter 4. Acetylene emission will be described briefly as it pertains to the energy transfer dynamics discussed in this chapter. The radical channel produces vinyl and Br/Br*, where the * indicates electronic excitation. This channel leaves up to 69 kcal/mol of energy in the products following 193 nm photodissociation. The molecular channel produces acetylene and HBr, with up to 123 kcal/mol internal energy available to the products.[22,23] The effect of having

a large difference in exothermicities appears in the emission spectra. Acetylene emission appears more intense and with a significant anharmonicity frequency shift, while vinyl emission is less intense and lying closer to the previously determined fundamental mode frequencies. Anharmonicity shifts and intensity enhancement are effects of higher vibrational excitation.[21,24] These effects will be described in more detail below.

Time-resolved IR emission recorded following the 193 nm dissociation of 3 mTorr vinyl bromide in 2 Torr He is shown in Figure 5.1. The two most prominent peaks, at ~1250 cm^{-1} and 3000-3300 cm^{-1}, are vibrational progressions of the $\nu_4+\nu_5$ combination band and ν_3 CH stretch mode of acetylene. The assignments of these two bands, as well as that of the less intense ν_5 bending mode at 730 cm^{-1}, have been established in previous Chapters.[20,21] During the first several μs after photolysis, there is a lot of emission below 1500 cm^{-1}. This short lived emission is from the ν_5, ν_6, ν_8, and ν_9 bending modes of the vinyl radical whose fundamentals have been observed at 1401, 1074, 944, and 897 cm^{-1}, (see Chapter 3).[20] The lowest frequency emission observed in our experiments, at ~750 cm^{-1}, corresponds to the ν_5 emission convoluted with a sharp decline in the detector spectral response. The experimental results shown here are not corrected by the spectral response function of the detector. The response function is, however, accounted for in the calculation of the emission bands.[21]

The dominant feature, observed at 1250 cm^{-1}, has been determined to arise from emission through the acetylene $\nu_4 + \nu_5$ combination band. The intensity in the emission spectra for this combination band is much higher than that in the absorption spectra. The origin of the strong emission intensity has been explained in Chapter 4.[21]

Figure 5.1. IR emission following the photolysis of 3 mTorr vinyl bromide in 2 Torr He taken at 12 cm^{-1} resolution. Spectra recorded at 1, 5, 10, 15 and 30 μs following the photolysis pulse are shown.

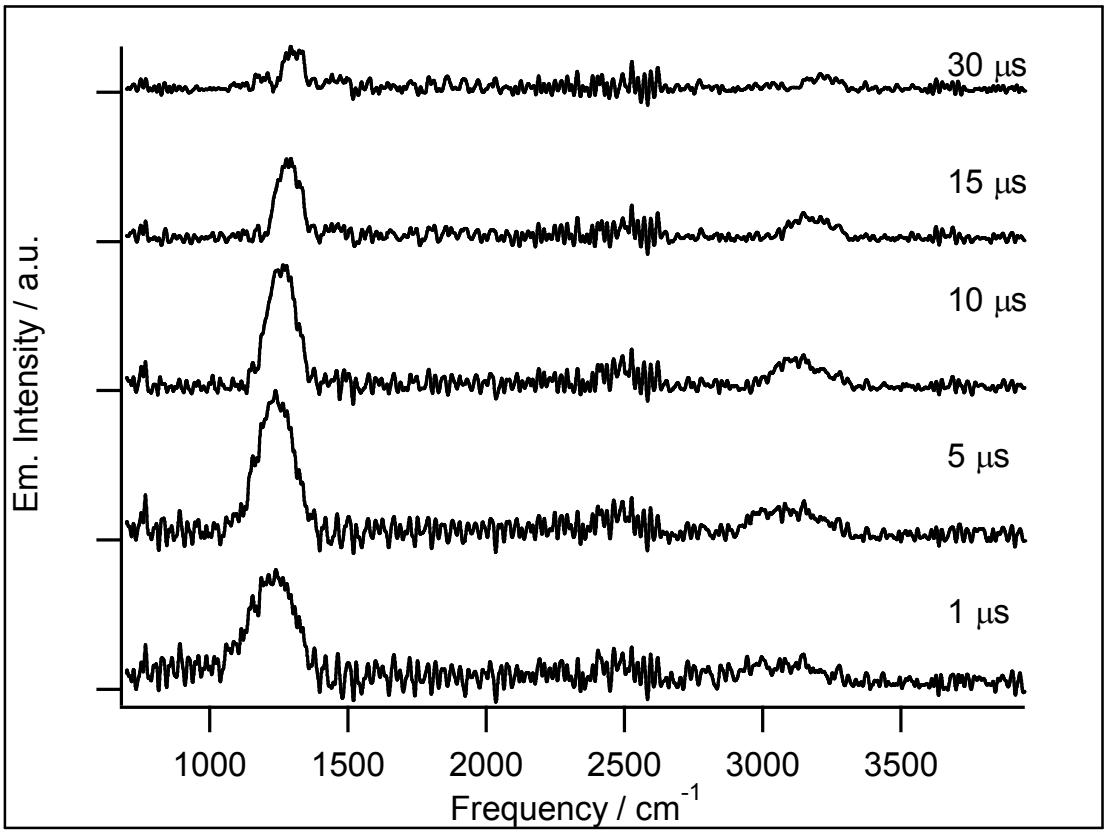

Rovibrational transitions from HBr are observed around 2500 cm^{-1} that last for several tens of μs depending on the colliding partner. Modeling of these emission features has been performed in several laboratories.[16,25,26]

The broad peak that stretches from 2800-3300 cm^{-1} at early times and remains broad for several tens of μs is from the strongly anharmonic ν_3 CH stretch of acetylene. The large shift of this feature is due to the large anharmonicity associated with the CH stretching motion. No other emission features are apparent in our spectra.

5.3.2 Modeling the acetylene IR emission bands

The modeling of the IR emission from highly vibrationally excited acetylene was performed in a manner similar to that described in Chapters 2 and 4. Only a brief overview will be presented here, as it pertains to the energy transfer result. The IR emission spectra from the energy "bins" are used for fitting the overall emission spectrum based on the energy distribution of the emitting molecules which is described by a bimodal population distribution. One distribution is right above $\langle E \rangle = 0$ and corresponds to a thermal population of acetylene. This population arises from hot acetylene undergoing V-V energy transfer to cold acetylene, populating low vibrationally excited states. Cold acetylene, with up to 10 kcal/mol of internal energy, may be formed from the dissociation of vinyl radicals also formed in the photolysis cell.[16,22] By using low precursor pressures, we reduce the amount of cold acetylene in the reaction chamber which populates these low vibrational energies of acetylene. The other population distribution is centered at $\langle E \rangle_t$ and represents the nascent vibrational population of

acetylene following the photolysis of vinyl bromide. This distribution is described by a Gaussian profile for the evolving and cooling vibrational population.

The fitting of four experimental results, at 5, 10, 15, and 20 μs following the dissociation of 3 mTorr VBr in 2 Torr Ar is shown in Figure 5.2. The emission is well described by our fitting parameters, with only the ν_5 symmetric bend mode showing some deviation. This is to be expected as the detector response function has a sharp cut off around 750 cm^{-1}. The other features have been identified in previous chapters as well as in the literature.[16,20,21,26] The average internal energy, $\langle E \rangle$, vs. time (and correspondingly the number of collisions) is shown in Figure 5.3 for collisions with the four noble gases. Collisional frequencies were determined through calculations utilizing Lennard-Jones cross-sections. The error bar on the first $\langle E \rangle$ data point represents the full width at half max of the first Gaussian energy distribution. The first time slice has the largest breadth, falling steadily till reaching the "bin" size limit at late times (typically > 50 μs). The solid line shown is the simplest functional form, a double exponential decay, which accurately describes the decay of the energy as a function of time. The fitting yielded an $\langle E \rangle_0$ =24,800 cm^{-1} (70.9 kcal/mol) corresponding to the average vibrational energy in nascent acetylene, with a σ=1200 cm^{-1} (3.4 kcal/mol).

A recent photofragment translational spectroscopy (PTS) study conducted on 193 nm dissociation of vinyl bromide determined the center of mass translational energy of the two products to be $\langle E_t \rangle$~18 kcal/mol.[18,25] Vibrational emission modeling of HBr following photolysis has yielded an initial vibrational and rotational energy, $\langle E_{V,R} \rangle$=25 kcal/mol.[16,18] By adding the total translational energy, the HBr internal energy and the

Figure 5.2. Four selected time slices, 5, 10, 15, and 20 μs, following the 193 nm dissociation of 3 mTorr vinyl bromide in 2 Torr of Ar. The fitting results are shown overlaid in black.

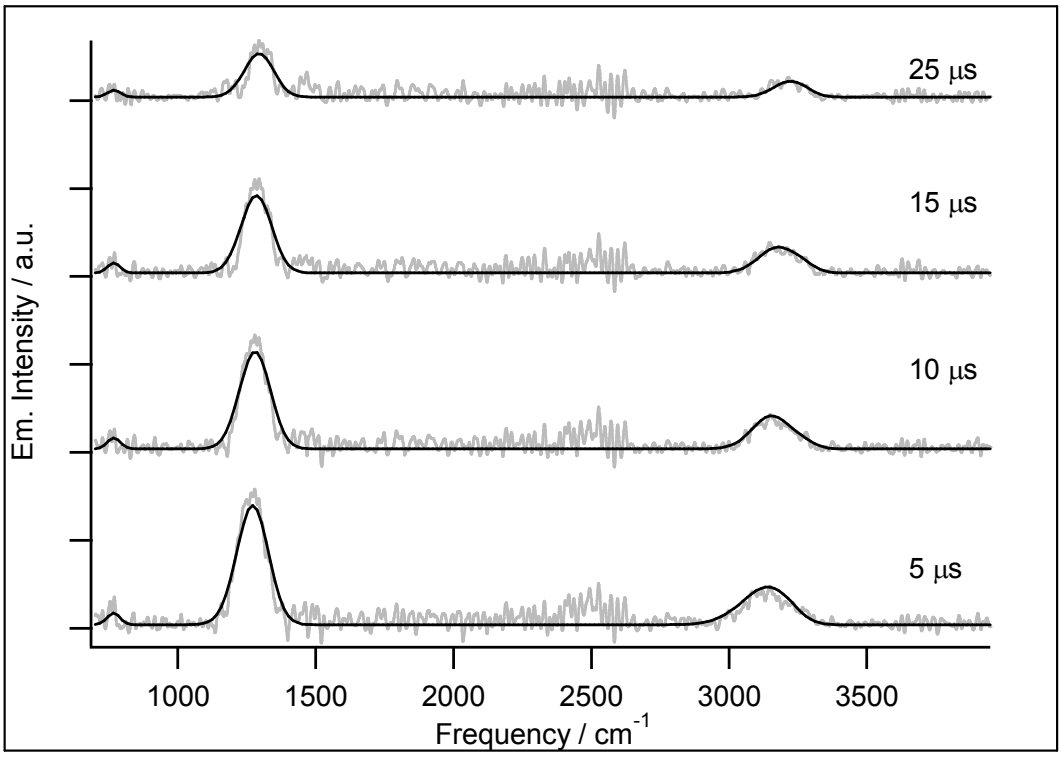

Figure 5.3. The $\langle E \rangle$ as a function of time following photolysis of 5 mTorr vinyl bromide in 2 Torr He, Ne, Ar, and Kr are shown in panels A, B, C, and D, respectively. The error bar for the initial $\langle E \rangle$ in the Ar results corresponds to the full width at half max of the fitted energy distribution. The fit is a double exponential as discussed in the text. The number of Lennard-Jones collisions between C_2H_2 and the noble gases are shown on the top horizontal axes.

A. Collisions with He

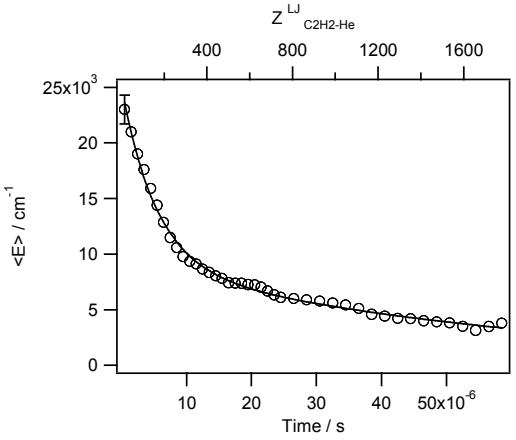

B. Collisions with Ne

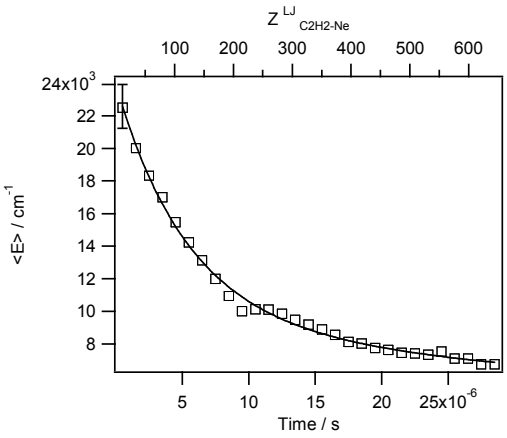

C. Collisions with Ar

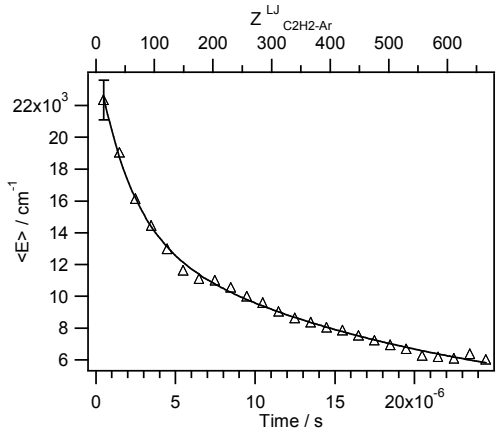

D. Collisions with Kr

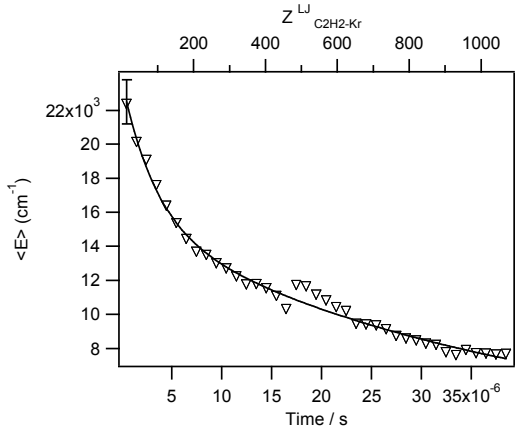

acetylene nascent vibrational energy together we obtain 114 kcal/mol. This number is consistent with the exothermicity of the reaction 122 kcal/mol. The discrepancy can be explained by not including the rotational energy in acetylene as well as the ~4 kcal/mol uncertainty in our vibrational emission modeling result.

5.3.3 Collision energy transfer

The energy transfer rate is obtained by taking the derivative of the average vibrational energy, $\langle E \rangle$, with respect to time:

$$d\langle E \rangle / dt = \sum_m Z_{LJ}(m) p_m \langle \Delta E \rangle_m \tag{5.1}$$

where the time is related to the number of collisions calculated as Z_{LJ}*p_m, the LJ collisional frequency multiplied by the partial pressure of species m, which is shown on the top axis in Figure 5.3(a-d). The total energy transfer rate is dependent on all kinds of possible collisions involving acetylene. The collisional quenching is dominated by acetylene-noble gas collisions, but acetylene-acetylene and acetylene-vinyl bromide collisions do occur. The rate of these collisions is however much slower because the precursor pressure used was three orders of magnitude lower than the inert gas pressure. ($p_m \sim 10^3 p_{C_2H_3Br}$, *m*=He, Ne, Ar, Kr) It is therefore assumed here that the quenching rate measured here is dominated by the inert gas collisions. This assumption will be discussed later based on a study probing the acetylene self quenching rates.[27] The result, which was conducted at high vibrational energies probing the overtone ν_3 CH stretching bands concluded that the acetylene self quenching rate was approximately double that of the acetylene - noble gas rate collisional deactivation rage.[27]

The energy transferred per collision, $\langle \Delta E \rangle$ is calculated according to Eq. 5.1. The derivative of the $\langle E \rangle$ vs. time data was determined from the double exponential fitting of the data. The energy transfer per collision, $\langle \Delta E \rangle$, is plotted as a function of the average internal energy, $\langle E \rangle$, of the energy donor molecule, shown in Figure 5.4, for the four noble gas colliders. To assess the uncertainty in the amount of energy transferred, we must include the error, in addition to the one of the $\langle E \rangle$ determined, associated with fitting the $\langle E \rangle$ vs. time curve. The fitting error can be determined from the range of $\langle E \rangle$ used. The accuracy in $\langle \Delta E \rangle$ is taken as $\pm 1\sigma$ of the decay rate from the $\langle E \rangle$ vs. time fitting. They are then converted into the energy transferred by utilizing Eq. 5.1. The overall uncertainty is plotted in Figure 5.4. These error bars are largest for high energy features, and decrease substantially as the vibrational population cools.

5.4 Theoretical calculations

5.4.1 The SSH model

A model for describing the inelastic collisions between an excited molecule with an atom/molecule was established as an 1D collinear case by Schwartz, Slawsky, and Herzfeld[1] (SSH) in 1952. This theory was expanded to the three-dimensional case for diatomic collisions by Schwartz and Herzfeld[2] in 1954 and further expanded to include polyatomics with large energy spacing in 1956 by Tanczos.[3] This theory of energy transfer is known as the SSHT theory.

The SSHT theory is an approximate quantum mechanical treatment which has had much success describing vibrational energy transfer in collisions involving diatomic

Figure 5.4. $\langle \Delta E \rangle$, the amount of energy transferred per L-J collision between excited acetylene and an inert gas collider, plotted as a function of the acetylene energy $\langle E \rangle$. The inert gas collider He is in red, Ne green, Ar blue, and Kr purple.

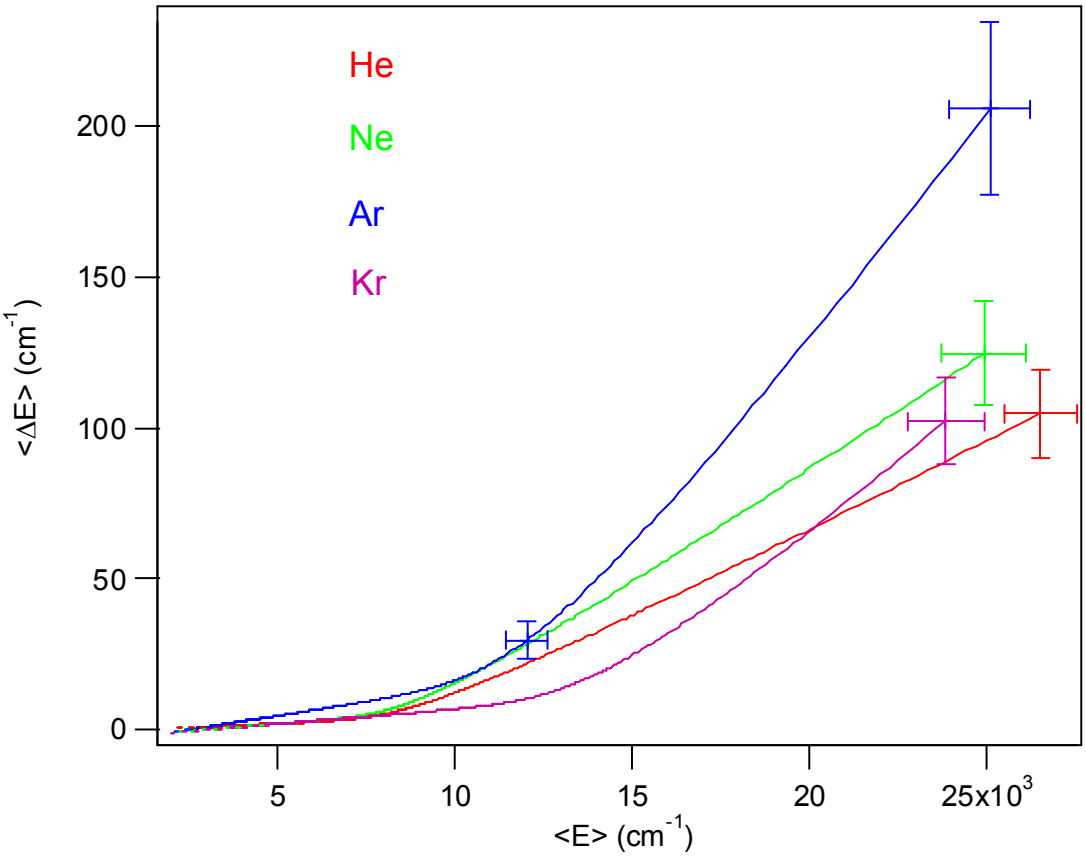

molecules with other diatomic or monatomic colliders at low energies.[6,28,29] It grows in part from the Landau-Teller theory.[4 29 30 31] The SSHT theory applied to polyatomic case in this study is meant to form a qualitative basis for understanding the experimental results.

The basis of the SSHT theory is rooted in the commonly accepted notion that energy transfer is a result of momentum transfer during a collision and thus the action takes place along the repulsive part of the potential energy surface[4,5]. Landau and Teller[32] developed an elementary theory based purely on the repulsive collision, expressed as a simple exponential, to calculate energy transfer probabilities. Landau and Teller calculated the vibrational relaxation probability from states $1 \rightarrow 0$ by semi-classical time-dependent perturbation theory. In this model the transition probability is proportional to the square of the Fourier component of the force at the frequency of oscillation. The model states that the probability is proportional to $\exp(-4\pi^2\nu/\alpha\mathbf{v})$, where ν is the vibrational frequency, α is the steepness of the exponential repulsive surface, and $\mathbf{v}$ is the velocity. The velocities are described in thermal distribution, with the proportion of molecules with a minimum velocity v to induce a transition equal to $\exp(-mv^2/2kT)$. Integrating over the range of probabilities and velocities above the minimum velocity yields $P_{10} = \exp[-3(2\pi^4\mu\nu^2/\alpha^2 kT)]^{1/3}$. This is the famous Landau-Teller equation and is commonly plotted as $\log(P_{10})$ vs $T^{1/3}$.

The theory devised by Schwartz, Slawsky, and Herzfeld (SSH) improves upon the Landau-Teller model by incorporating a quantum mechanical treatment of the system: The collider translational motion is described by a de Broglie wave, interacting with a stationary molecule. Furthermore, the effect of attractive part of the potential in the collision is included as added energy for the relative translational energy between the two

colliders. In the SSH treatment, the vibrational energy transfer process is described by a Hamiltonian comprised of the harmonic oscillator and exponential repulsive terms. The repulsive term is typically expressed along one of the vibrational or normal mode coordinates. The Born approximation is used since the effect of the perturbation to the harmonic oscillator is small. The harmonic oscillator approximation is used for the molecular vibration for calculating the matrix elements.[33]

The SSH model was adapted to handle polyatomic molecules by Tanczos by incorporating a "breathing sphere" approach.[3] In the SSHT theory, an average polyatomic orientation is assumed and the lowest frequency modes generally contribute the most to the energy transfer rate.[3-6,29] The SSHT theory has been used to successfully model numerous molecular collisions at low vibrational energies, primarily the $1 \rightarrow 0$ transitions.[4,5] The application of the SSHT theory to highly vibrationally excited species has been performed for NO[34,35], I_2[36], HF[37], O_2[38], and other diatomic systems.[6] There have been few prior applications to collisions involving highly vibrationally excited polyatomic molecules, perhaps partly because only until recently experimental measurements on highly vibrationally excited states are avaiable.[6]

A recent work by Barker investigated the collisional process between highly vibrationally excited cyclopropane and He and compared energy transfer rates with those calculated from the SSH theory.[39] Barker used the SSH model for calculations at high energies though details of the model was not provided. Good agreement between experimental and calculated results was found to internal energies > 20,000 cm^{-1} with state densities of ~1000 states / cm^{-1}. Kable and Knight investigated a variety of conjugated ring molecules, benzene, p-difluorobenzene, aniline, and pyrazine, in collisions with several different bath molecules and modeled the results using a

simplified SSHT model.[40] Good agreement was found up to 10,000 cm^{-1} and state densities of 500 states / cm^{-1}. Tang and Parmenter used a simplified SSHT model to explain the state to field energy transfer rate coefficient in benzene with a wide variety of collisional partners.[41] In addition, work within the Dai group has successfully compared SSH energy transfer rates with those collisional processes involving highly vibrationally excited molecules. Calculations for molecules NO_2, SO_2, HCN, and HNC have all yielded good comparisons with experimental observations such as mass dependence and structural changes.[14,15]

In the below, we apply the SSHT theory, with modifications designed for polyatomic molecules excited with high vibrational energy, to calculate the absolute quantities of energy transfer as a function of excitation energy for the various atomic colliders and to examine the trends in energy transfer rates as a function of collider mass and excitation energy.

5.4.1.1 The SSHT theory for polyatomic molecules

The probability of a collision induced vibrational relaxation, $P_{k-l(b)}^{i-j(a)}$, between molecule *a* initially in state *i* and molecule *b*, initially in state *k* is described in the SSH model. Molecule *a* can gain or lose energy transitioning to state *j*, while molecule *b* loses or gains that same energy transitioning to state *l*.

$$P_{k-l(b)}^{i-j(a)} = P_0(a)P_0(b)\left[V^{ij}(a)\right]^2\left[V^{kl}(b)\right]^2\left(\frac{4\mu}{kT}\right)\exp\left(\frac{-\varepsilon}{kT}\right)\left(\frac{8\pi^3\mu\Delta E}{h^2}\right)^2\int_0^\infty f(\bar{u})d\bar{u} \quad (5.5)$$

where

$$f(\bar{u}) = \frac{\bar{u}}{\alpha^4}\left(\frac{r_c}{\sigma}\right)^2\exp\left(\frac{-\mu\bar{u}}{2kT}\right)\left\{\frac{\exp[L-L']}{(1-\exp[L-L'])^2}\right\},$$

$$L = \frac{4\pi^2 \mu}{\alpha h} \times \bar{u}\,, \qquad \text{and} \qquad L' = \frac{4\pi^2 \mu}{\alpha h} \times \bar{v}$$

The P_0 terms define the steric interactions, [V], the vibrational matrix elements, μ, the reduced mass, T, the temperature, ε, the attractive well depth, ΔE, the energy gap, α, the repulsive potential slope, r_c, the classical turning point, σ, the Lennar-Jones distance, $\bar{u}$ and $\bar{v}$, the average relative speed before and after the collision.

Tanczos has analytically solved the integral in Eq 5.5 for polyatomic systems with large energy gaps.[1,3] In addition, the initial relative velocity, $\bar{u}$ and final relative velocity $\bar{v}$ are integrated over and subsequently do not appear in the final equation. The SSHT equation

$$P_{k-l(b)}^{i-j(a)} = P_0(a)P_0(b)\left(\frac{r_c^*}{\sigma}\right)^2 \left[V^{ij}(a)\right]^2 \left[V^{kl}(b)\right]^2 * 8\left(\frac{\pi}{3}\right)^{1/2} \tag{5.6}$$

$$* \left(\frac{8\pi^3 \mu \Delta E}{\alpha^{*2}}\right)^2 \zeta^{1/2} \exp\left(-3\zeta + \frac{\Delta E}{kT} + \frac{\varepsilon}{kT}\right)$$

expresses the probability of a collision inducing a change in molecule a, from state i-j, and in molecule b, from state k-l. Eq. 5.6 contains four main components. The P_0 terms are the steric factors which account for the anisotropic nature of the collision of a polyatomic molecules vibrational mode. This term was derived based on the difference between a collinear atom-diatom collision, as in the original SSH theory, and a collision with a polyatomic molecule, as in the SSHT theory. The collisional cross reference factor, $\left(r_c^*/\sigma\right)$ relates the classical turning point distance, r_c* to the Lennard-Jones distance, σ. The terms [$V^{ij}(a)$] and [$V^{kl}(b)$] are the transition matrix elements for molecules a and b, between states i-j and k-l, respectively. They are related to the matrix

elements of the harmonic oscillator solution[5] and the repulsive L-J potential and are expressed as the unitless quantities for zero, single, and double quantum jumps:

$$\left[V^{i-i}\right]^2 = 1 \tag{5.7a}$$

$$\left[V^{(i+1)-i}\right]^2 = \left[V^{i-(i+1)}\right]^2 = \alpha^2\left(\overline{A}^2\right)\frac{(i+1)}{2\gamma} \tag{5.7b}$$

$$\left[V^{(i+2)-i}\right]^2 = \left[V^{i-(i+2)}\right]^2 = \alpha^4\left(\overline{A}^4\right)\frac{(i+1)(i+2)}{16\gamma^2} \tag{5.7c}$$

where $\gamma = \frac{2\pi\nu_L}{\hbar}$. Noticing that the vibrational frequency, ν_L, is in the denominator of the above expressions, and α and $\overline{A}^2$ are generally <<1, it is easily seen that single quantum number jumps are highly favored in the vibrational matrix element. We can then simplify Eqs. 5.7 into $[V]^2$, the vibrational matrix element for a single quanta jump in a non-degenerate mode,

$$\left[V\right]^2 = \frac{\hbar\alpha^2\upsilon\left(\overline{A}^2\right)}{4\pi\nu_L} \tag{5.8}$$

where υ is the vibrational quanta in the upper state, $\overline{A}^2$ is the vibrational amplitude coefficient, ν_L is the frequency of the lowest energy mode, and α is the repulsive part of the L-J potential. The $\overline{A}^2$ term plays a crucial role in the energy transfer rate as this is projection of the normal mode motion onto the intermolecular coordinate. $\overline{A}^2$ values have been previously published for the individual vibrational modes.[42] For diatomic molecules, the vibrational amplitude coefficient is simply related to the masses of the two atoms.[5] For polyatomic molecules, however, the coefficient must be determined via normal coordinate analysis of the molecular vibrations.[43]

The last term includes the remainder of Eq. 5.6 and involves the kinetic energy of the collision, with μ, the reduced mass of the collision pair, ΔE, the amount of vibrational energy transferred in the collision, α^*, the repulsive component of the L-J potential at the classical turning point (K.E. = P.E.), ε, the attractive well depth of the L-J potential, and ζ, defined as:

$$\zeta = \frac{\pi\bar{\mu}^2}{2kT} = \left(\frac{\Delta E^2 \mu \pi^2}{2\alpha^{*2} \hbar^2 kT} \right)^{1/3} \tag{5.9}$$

The kinetic term is dependent on the attractive well depth and the repulsive potential. Increasing the attractive potential increases the collisional energy transfer probability exponentially. The opposite is true for the repulsive part; increasing the repulsive potential by making the repulsive wall steeper decreases the energy transfer probability.

Some general statements can be made about the SSHT equations, Eq. 5.6 and 5.9. It has been observed that decreasing the energy gap will enhance the energy transfer probability. This is due to the -3ζ term dominating the exponent. This trend has been shown in numerous systems.[4,5] It is therefore in agreement with the longstanding idea that polyatomic molecules decay with a single decay constant related to the lowest frequency mode. In addition, Ewing has shown that vibrational energy transfer is dominated by low vibrational, rotational, and translational quantum number changes,[44] and the vibrational predissociation rate, τ^{-1}, is approximately, $\tau^{-1} \approx 10^{13} \exp\left[-\pi\left(\Delta\upsilon_t + \Delta\upsilon_r + \Delta\upsilon_v\right)\right] = 10^{13} \exp\left[-\pi\Delta\upsilon_T\right]$, where $\Delta\upsilon_t$, $\Delta\upsilon_r$, $\Delta\upsilon_v$, and $\Delta\upsilon_T$, are the changes in the translational, rotational, vibrational, and overall quantum numbers during the collision. Therefore we calculate only $|\Delta\upsilon|=1$ changes to the vibrational quantum number.

It is also found that in pure SSH (purely repulsive collisions) a decrease in the reduced mass increases the probability as well, due to the same term in the exponent. So collisions with He would be more efficient than heavier collider partners. This effect, however, is balanced by the increase in the attractive potential as larger and more massive collider gases are used. As will be seen in the following figures, the mass dependent energy transfer rate is highly dependent on this attractive potential depth.

5.4.1.2 SSHT modified for highly vibrationally excited molecules

For acetylene-noble gas collisions, energy can only be transferred with the noble gas is through its translational energy. Eq. 5.7 thus simplifies to $P^{i\text{-}j}(C_2H_2\text{-}m)$, where the noble gas is limited to only changes in kinetic energy.

The L-J parameters for collisions between ground state acetylene and the four noble gases has been determined through viscosity[45-47] and microwave studies.[48-53] The interaction energy between acetylene and the noble gas atoms are slightly anisotropic. However, since the experiment probes the ensemble averaged energy transfer rates, the interaction here will be treated isotropically. The generally accepted method of determining the L-J distance and interaction energy between different atoms from their respective L-J values are $\sigma_{ab}=(\sigma_a + \sigma_b)/2$ and $\varepsilon_{ab} =(\varepsilon_a * \varepsilon_b)^{1/2}$, respectively. We can therefore use an average value for the interaction energy. L-J ε values of 10.22, 35, 124, 190, and 188 K for He, Ne, Ar, Kr, and C_2H_2, respectively, were used, with the L-J σ values set at 2.576, 2.858, 3.465, 3.61, and 4.221 Å correspondingly.[45]

SSHT probabilities are calculated from Eq. 5.6 for all $\Delta v = -1$ transitions arising from the normal mode description of acetylene with anharmonicities included. The probabilities are binned into 1000 cm^{-1} energy bins. The probabilities are normalized to

Figure 5.5. The SSHT energy transfer rates, $\langle \Delta E \rangle$ vs. $\langle E \rangle$ curves, for acetylene with four noble gas colliders with He in red, Ne in green, Ar in blue, and Kr in purple.

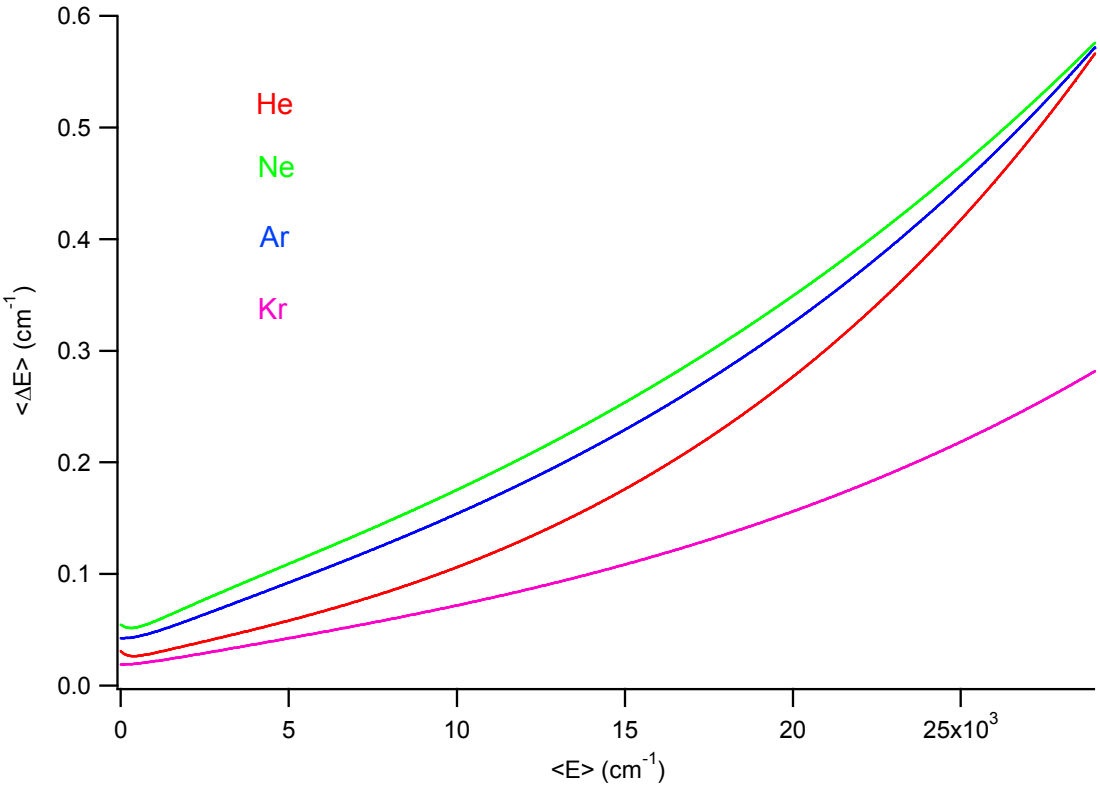

arising from a single molecule by dividing through by all the vibrational states within that energy bin. The probabilities calculated from Eq. 5.6 are converted into $\langle \Delta E \rangle$ values so we can compare them directly to the experimental $\langle \Delta E \rangle$ vs. $\langle E \rangle$ results by,

$$\langle \Delta E \rangle = \sum_{i,j} P^{i-j} * \Delta E^{i-j} \tag{5.10}$$

where P^{i-j} are the transition probabilities from state i - j with energy gap ΔE^{i-j}. The calculated energy transfer rate for acetylene as a function of internal energy is shown in Figure 5.5. The solid lines represent the SSHT energy transfer rate for collisions with He, Ne, Ar, and Kr, are shown in red, green, blue, and pink, respectively.

The SSHT calculated $\langle \Delta E \rangle$ values for He collisions at acetylene energies of 5000, 15000, and 25000 cm^{-1} are 0.06, 0.18, and 0.40 cm^{-1} respectively. These values are much smaller than the experimentally determined $\langle \Delta E \rangle$ values of 2.1 ±4, 38 ±12, and 96 ±31 cm^{-1} at the same acetylene energies. At low vibrational energies the experimental error precludes determining how accurately the SSHT calculation reproduces the experimental result. However, the rate of increase as a function of excitation energy is of interests here. The change in the energy transfer rate depicted in the SSHT calculation is much slower than the experimentally measured. The SSHT shows approximately 7 times increase in the energy transfer rate, while the experimental result shows a 45 times increase.

The SSHT energy transfer rates for collisions with Ne, Ar, and Kr show a similar behavior to He. SSHT energy transfer quantities of 0.10 and 0.46 cm^{-1} at energies of 5000 and 25000 cm^{-1} were calculated for collisions with Ne. The experimental values are 2 and 125 cm^{-1} at the same energies, respectively. The calculated increase is smaller in

comparison with the observed, 4.6 times (calculated) vs. 63 times (experimental). For Ar the calculated are 0.09 and 0.45 cm^{-1} at 5000 and 25000 cm^{-1}. The experimental values are 4.8 and 206 cm^{-1}. The calculated enhancement vs. observed are 5 times (calculated) vs. 45 times (experimental). For Kr the calculated values are 0.04 and 0.19 cm^{-1} at 5000 and 23000 cm^{-1} vs. experimental values of 2 and 103 cm^{-1}, respectively. The ratios of increase are 4 times(calculated) vs. 52 times (experimental). For all cases, the experimental energy transfer curves in Figure 5.4 increase by approximately 50 times from low to high energies, while the SSHT energy transfer rate calculated for acetylene in Figure 5.5 increases by a factor of 5 - 10 with no clear bend or enhanced high energy behavior.

The experimental error bars at low energies prevent comparison to the SSHT calculated rate. Even though we can not compare the individual mass dependent energy transfer rates, at low energies, the SSHT energy transfer rates show some similarities to the experimental rates. Both the SSHT and experimentally determined rates show a gradual increase in the rates as a function of vibrational energy. At higher energies, > 15,000 cm^{-1}, the increase in the SSHT rate with energy, however, does not keep up to the ones determined experimentally. This indicates that there are factors not included in the model which is affecting the experimental observation. The inclusion of other possible channels for vibrational relaxation should be considered.

5.4.1.3 SSHT calculation of energy transfer for vinylidene-NG collisions

The existence of vinylidene on the acetylene potential energy surface may greatly affect the overall energy transfer rate based on an increase in the vibrational level density and the vibrational mode structure affecting the amount of energy transferred per

collision. Based on these contributions to the energy transfer mechanism, the energy transfer rate of vinylidene should be calculated.

For the calculation of the energy transfer rate of vinylidene, the structural information of vinylidene needed is less definitively known. Concerning intermolecular interactions there has been no published work on vinylidene-atom/molecule potential energy surfaces. The vinylidene L-J ε value was estimated to be approximately 300 K, based on similar molecules, e.g. acetylene, ethylene, and some polar hydrocarbons.[45] Vinylidene - He, Ne, Ar, and Kr L-J ε values of 55, 105, 190, and 240 K, respectively, were utilized. The values used here are larger than those for collisions with acetylene, as expected, due to the inclusion of a dipole-induce dipole interaction present in the vinylidene case. While approximating the interaction energy based on similar molecules may be quite crude, it is not the goal of this study to determine the exact interaction energy. Instead, we wish to use this estimated value to approximate an energy transfer rate to achieve a semi-quantitative understanding. It turns out that adjusting the interaction energy by as much as 20-30% does not change the magnitude or the mass dependence of the energy transfer rates significantly.

Knowledge of the low frequency modes of a molecule is necessary for the SSHT model calculation of its energy transfer rate as the lowest frequency modes dominate the relaxation rates. Only a few of the vibrational modes of vinylidene have been experimentally determined.[19] The lowest frequency mode, ν_6, has not been detected experimentally, however the overtone has been observed. This band located at 450 cm^{-1}, was assigned to the 0 $\rightarrow$ 2 transition for the ν_6 CH_2 rocking mode.[19] Ervin et al., estimated the fundamental transition to have a frequency of 320 cm^{-1} based on results from the singlet and triplet states frequency shifts from the ground state and the estimated

anion frequencies.[19] Theoretical work has calculated this mode to range from 263 – 472 cm^{-1}.[54-56] It is clear that there is a great deal of uncertainty with this low frequency mode and further work is necessary to accurately determine the fundamental frequency. We use a harmonic frequency of 300 cm^{-1} for the ν_6 mode in the calculation of the SSHT energy transfer rate. The remaining modes have been previously observed, the ν_1 CH symmetric stretch, 3025 cm^{-1}, the ν_2 CC stretch at 1635 cm^{-1}, and the ν_3 CH_2 scissor at 1165 cm^{-1}.[19] Two other modes, the ν_4 CH_2 wag and the ν_5 CH asymmetric stretch, are predicted to lie between 716 – 775 cm^{-1} and 3065 – 3240 cm^{-1}, respectively, based on AIMD and coupled cluster calculations.[54-56] We will use these harmonic values to generate the normal mode vibrational states.

The SSHT energy transfer probabilities for vinylidene-noble gas collisions are calculated for the normal mode vibrational states from zero to 30,000 cm^{-1} of vibrational energy according to Eq. 5.6. The probabilities from each state are binned into 1000 cm^{-1} vibrational energy bins and then averaged over all the states in the bin. Probabilities are converted to $\langle \Delta E \rangle$ values according to Eq. 5.10.

The SSHT energy transfer rates expressed as $\langle \Delta E \rangle$ per L-J collision for the four vinylidene-noble gas collisions are shown in Figure 5.6 as a function of the vinylidene energy. Energy transfer rates for vinylidene-He, Ne, Ar, and Kr are shown in red, green, blue, and purple, respectively. Note the x-axis energy scale here starts at the vinylidene ZPE, which lies approximately 15000 cm^{-1} above the acetylene ZPE.[19,56] The energy transfer rate for vinylidene is at least 1-2 orders of magnitude larger than that for acetylene throughout the energy region primarily due to the lowest frequency mode of

Figure 5.6. The SSHT energy transfer rates, $\langle \Delta E \rangle$ vs. $\langle E \rangle$ curves, for vinylidene with four noble gas colliders with He in red, Ne in green, Ar in blue, and Kr in purple, relative to the vinylidene ZPE.

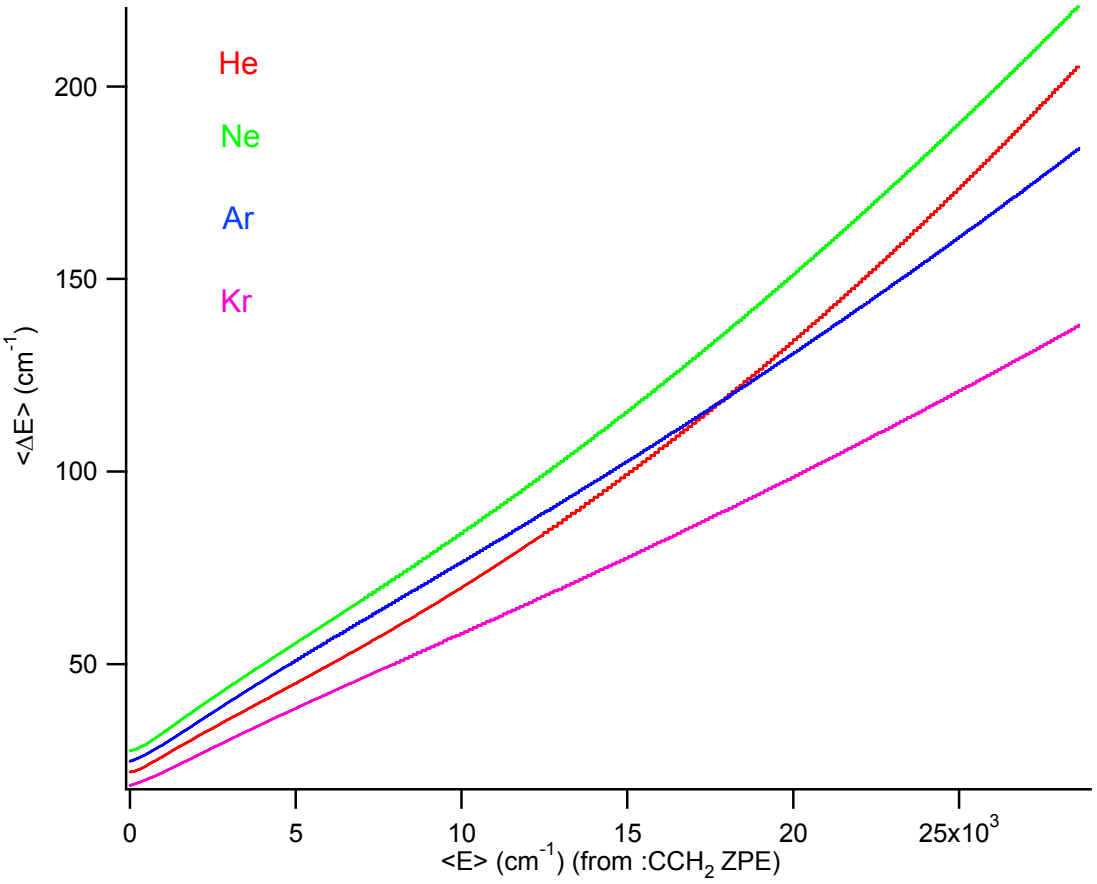

vinylidene displaying high energy transfer efficiency. This will be discussed further in Section 5.5.

The SSHT calculated energy transfer rates for acetylene-He, Ne, Ar, and Kr collisions at 25000 cm^{-1}, are 0.4, 0.46, 0.45, and ~0.21 (extrapolated from the data) cm^{-1}, respectively. The vinylidene-He, Ne, Ar, and Kr collisions at the same energy, 25000cm^{-1} (10,000 cm^{-1} relative to the vinylidene ZPE) yield calculated rates of 70, 83, 77, and 58 cm^{-1}. The more efficient vinylidene collisions more accurately depict the energy transfer rate enhancement observed experimentally at high energies. The contribution of vinylidene energy transfer to the experimental measurements will be discussed in Section 5.5.

5.4.2 Classical trajectory calculations

5.4.2.1 General Description

Classical trajectory calculations have been used to characterize collisional energy transfer events.[57-60,61-71] Because these trajectory calculations only rely on classical equations of motion, the energy content of the molecules, and the force constants of the molecules, large molecules may be modeled with good success.[61-63] Trajectory calculations have been performed on small molecules such as CS_2,[64] H_2O,[65] and propane[66] involved in collisions with a variety of noble gases, to larger molecules such as pyrazine,[10] benzene, and other conjugated ring molecules.[67]

Briefly, in the classical trajectory calculations, each molecule is treated as a collection of harmonic oscillators and the intermolecular potential between the colliding molecules are described by pairwise Lennard-Jones potentials. That is, each atom of the molecule has a set of inter-atomic potentials onto which the collision may take place.

The normal mode coordinates and momenta are initially sampled based on the vibrational energy input. After the trajectories are started, the vibrational motion is treated classically and the vibrational degrees of freedom can gain or lose any amount of energy. The output of the program calculates the energy in the vibrational, rotational, and translational degrees of freedom of the products. This information can then be used to calculate the amount of energy transferred and through which pathway (V-T, V-R, T-V, or T-R).

Each trajectory therefore yields information about one particular set of initial conditions. To get an ensemble averaged result, hundreds to thousands of trajectories are run in order to adequately sample the intermolecular potential energy surface as well as the initial translational, rotational, and vibrational energy distributions. Further details about the simulations will be provided in the next section.

The calculations are limited by the determination of accurate potential energy surfaces, the lack of quantum mechanical selection rules, and that fundamentally the collisions are actually treated classically.[61,63,68] Nonetheless, the calculations offers comparative insight for understanding energy transfer through bimolecular collisions.

5.4.2.2 Classical trajectory calculation

Classical trajectory calculations involving acetylene and vinylidene collisions with He, Ne, Ar, and Kr were performed using VENUS96.[69,70] The molecules were represented by harmonic and Morse stretch potentials, harmonic bends, and harmonic wag motions. Force constants were determined initially through *ab initio* calculations, using the coupled cluster [CCSD(T)] method and Dunning's correlation-consistent polarized valence triple ζ basis sets (cc-pVTV) with counterpoise correction and compared favorably with experimental and theoretical vibrational frequencies for

acetylene[71] and vinylidene.[19,56] The interaction potentials for acetylene – noble gases was described by an isotropic average L-J potential,[45,53] even though it is known to have an angular dependent global minimum.[49,51,72-74] The intermolecular potential parameters for the four acetylene-noble gas interactions are listed in Table 5.1. The VENUS96 program can utilize these isotropic potentials, however to improve the accuracy of the calculation, the individual atom-atom interactions may be used. Using the equilibrium geometries, the collision can take place on the atom-atom potential surface, as opposed to an isotropic molecule-atom potential surface. The SIGMON[75] program was used to generate these pairwise L-J potentials from the isotropic potentials. The SIGMON program has been shown to generate pairwise potentials for many small molecule systems. The potentials used in the trajectory calculations produced results in good agreement with experiments.[62,63,67] The pairwise interaction energies and distances are listed in Table 5.1 as well. More complete intermolecular potentials for the acetylene-noble gas interaction are available but are not utilized due to the computing power and programming requirements needed.[76] It is acknowledged that the atom-atom L-J PES does not precisely describe the short range repulsion and long range attraction forces to the same degree as the more complex potential function. It remains an interesting problem to precisely determine the correct interaction potentials, however beyond the computing power currently available in the laboratory. We utilize the L-J potential because of its straightforward interpretation and easy comparison to a wide variety of other interactions.

Intermolecular potentials for vinylidene-noble gas collisions were calculated *ab initio* using the coupled cluster [CCSD(T)] method and Dunning's correlation-consistent polarized valence triple ζ basis sets (cc-pVTV) with counterpoise correction. A coarse

Table 5.1 The intermolecular potential parameters used in the classical trajectory calculations for collisions between acetylene and vinylidene with He, Ne, Ar, and Kr. Values are given for the molecule - NG potential as well as the atom – NG potential determined from the SIGMON program.

Intermolecular Potential Parameters

		$V = (4\varepsilon\sigma^{12}r^{-12}) - (4\varepsilon\sigma^{6}r^{-6})$	
	L-J Pair	$4\varepsilon\sigma^{12}$ (kcal mol^{-1} Å^{12})	$4\varepsilon\sigma^{6}$ (kcal mol^{-1} Å^{6})
HCCH	HCCH - He[a]	8.3×10^{5}	5.4×10^{2}
	H - He	2.7×10^{4}	5.0×10^{1}
	C - He	9.1×10^{4}	5.0×10^{1}
	HCCH - Ne[a]	2.5×10^{6}	1.3×10^{3}
	H - Ne	8.1×10^{4}	5.0×10^{1}
	C - Ne	2.7×10^{5}	5.0×10^{1}
	HCCH - Ar[a]	1.3×10^{7}	3.9×10^{3}
	H - Ar	6.1×10^{5}	5.0×10^{1}
	C - Ar	1.5×10^{6}	5.0×10^{1}
	HCCH - Kr[a]	2.0×10^{7}	5.4×10^{3}
	H - Kr	1.1×10^{6}	5.0×10^{1}
	C - Kr	2.5×10^{6}	5.0×10^{1}
$:CCH_2$	$:CCH_2$ - He	1.0×10^{6}	6.7×10^{2}
	H - He	6.7×10^{4}	7.7×10^{1}
	C - He	2.1×10^{5}	1.8×10^{2}
	$:CCH_2$ - Ne	3.0×10^{6}	1.6×10^{3}
	H - Ne	1.7×10^{5}	1.6×10^{2}
	C - Ne	5.8×10^{5}	4.1×10^{2}
	$:CCH_2$ - Ar	1.5×10^{7}	4.9×10^{3}
	H - Ar	1.2×10^{6}	6.5×10^{2}
	C - Ar	2.8×10^{6}	1.1×10^{3}
	$:CCH_2$ - Kr	2.4×10^{7}	6.7×10^{3}
	H - Ar	2.1×10^{6}	9.7×10^{2}
	C - Ar	4.6×10^{6}	1.6×10^{3}

[a] Reference 40.

surface scan was performed with approximately 64 points each using Gaussian 03 D.03. An optimized vinylidene geometry was determined from the coupled cluster calculations.[56] Two fine PES, with ~360 points of vinylidene with He and Ne at the MP2 level of theory are shown in Figure 5.7. Once again the interaction energies and distances were calculated for each interaction pair. There are no previous theoretical studies on the intermolecular potential of vinylidene. The isotropic potentials were computed and the SIGMON program was used to determine the pairwise potentials.

Trajectory calculations were run at varying amounts of vibrational energy with 10,000 trajectories run at each energy, for each colliding pair. While the initial vibrational energies were fixed, the rotational and translational energies were randomly sampled from a thermal distribution at 300 K. The initial separation of the colliders was 15.0 Å, with the trajectory running for 5,000 steps of 0.02 fs each. The trajectories were stopped when the exit distance between the colliders was 15.0 Å. Each trajectory was given a particular impact parameter, β, randomly sampled from zero to a maximum impact parameter, $\beta_{\max}$. The maximum impact parameter was chosen such that all collisions contributing to the energy transfer rate are counted in reference to a predetermined β_{ref},

$$\langle \Delta E \rangle = \langle \Delta E \rangle_{trj} \frac{\beta_{\max}^2}{\beta_{ref}^2} \tag{5.11}$$

where $\beta_{ref} = \sqrt{\sigma_{LJ}^2 \Omega^{(2,2)*}}$, $\langle \Delta E \rangle_{trj} = \left(\sum_{i=1}^{N} \Delta E_i \right) \Big/ N_{trj}$, β_{max} is the maximum β value used in the trajectory calculation, σ_{LJ}, the L-J collisional cross section, $\Omega^{(2,2)*}$, the collisional integral[45,58], ΔE_i, the energy transferred in a single trajectory, and N_{trj}, the total number of trajectories. The energy transfer rates for a particular trajectory are normalized to the

Figure 5.7. The PES of vinylidene-He and vinylidene-Ne calculated in the plane of the molecule at the MP2/6-311+G(d,p) level of theory. The top PES is for He, the bottom for Ne. The x- and y- scales are in Å, while the contours are expressed in cm^{-1} units. The vinylidene molecule is added for clarity.

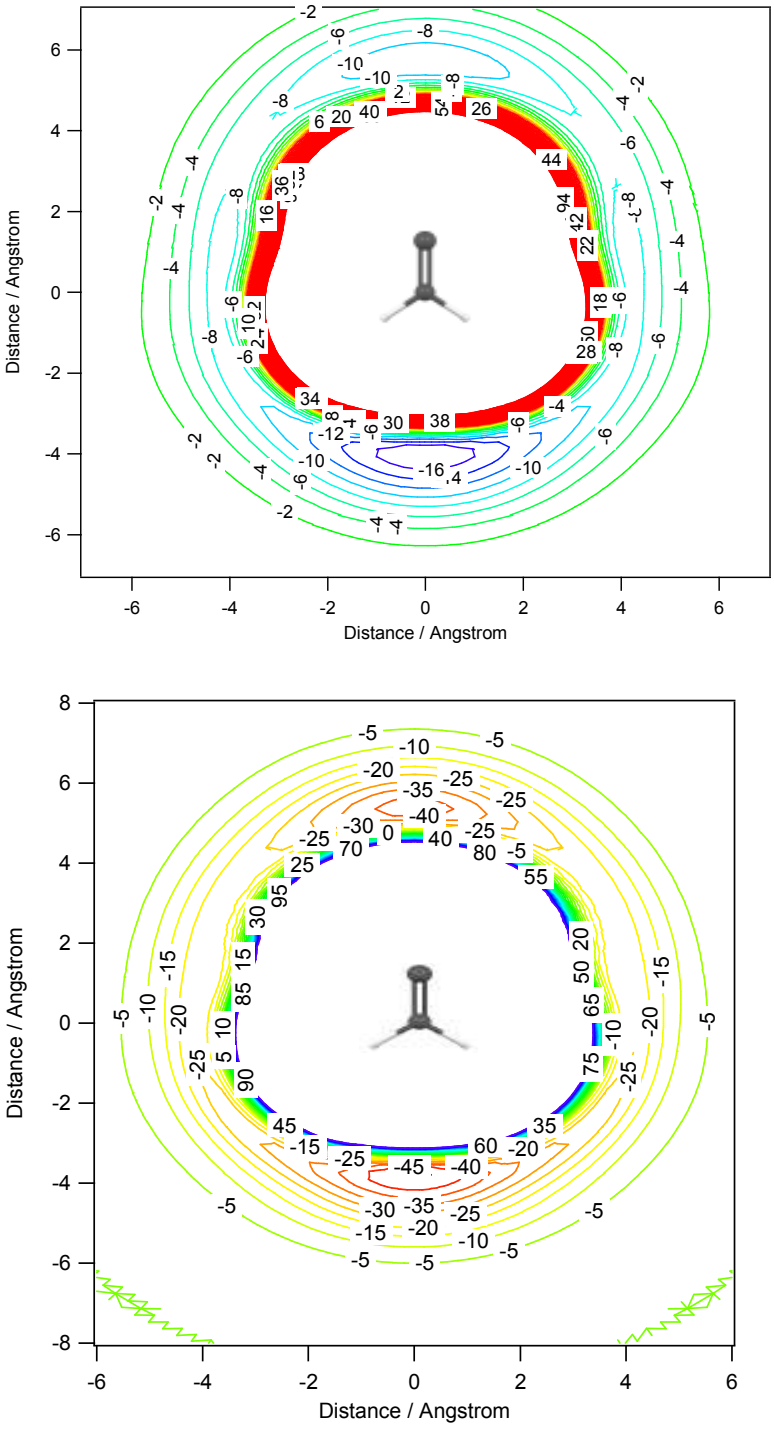

impact parameter, which carries a square dependence. The average vibrational, rotational, and translational energy changes were tracked for each set of trajectories.

5.4.2.3 Classical trajectory results for acetylene and vinylidene

The vibrational energy transfer as a function of impact parameter for each trajectory between vibrationally hot acetylene (E_{vib} = 40 kcal/mol) and a Ne atom is shown in Figure 5.8. Impact parameters were randomly sampled from 0 to 8 Å. The number of collisions inducing a change in the vibrational energy generally decreases with increasing impact parameters. This is consistent with an impulsive mechanism driving energy transfer.[77-79] The vast majority of significant collisions between acetylene and Ne occur with impact parameters between 0 and 6 Å. Above 6 Å, the collisions transfer much less energy and are considered "glancing" collisions, only involving the attractive potential well.[10] It should be noted that there exist a number of collisions where the energy transfer rate is significant (>3000 cm^{-1}). In general these "super collisions" occur within the Lennard - Jones collision radius for acetylene and Ne of ~3.5 Å ($\sigma_{acetylene}$ = 4.221 Å and σ_{Ne} = 2.858 Å). There are however a significant number of collisions with impact parameters above the L-J radius that transfer a large amount of vibrational energy. Li *et al.*[10] have suggested that these collisions involve a strong intermolecular attraction and/or highly excited vibrational modes along a particular coordinate. Clark *et al.*[80] have found through computational studies that the bath gas may interact with several atoms of the molecule over the course of a collision. The overall goal of the trajectory study is to determine an average energy transfer rate per collision without overestimating the efficiency by oversampling small impact parameters or underestimating the rate by including too large impact parameters. These factors will be discussed below. Utilizing Eq. 5.11, we are able to determine an average energy transfer rate per collision. Varying

Figure 5.8. The vibrational energy transfer between acetylene (E_{vib} = 40 kcal/mol) and Ne atoms at 300K. The amount of energy transfer is plotted according to the impact parameter, β, used for the trajectory. A positive energy transfer rate indicates a loss of vibrational energy.

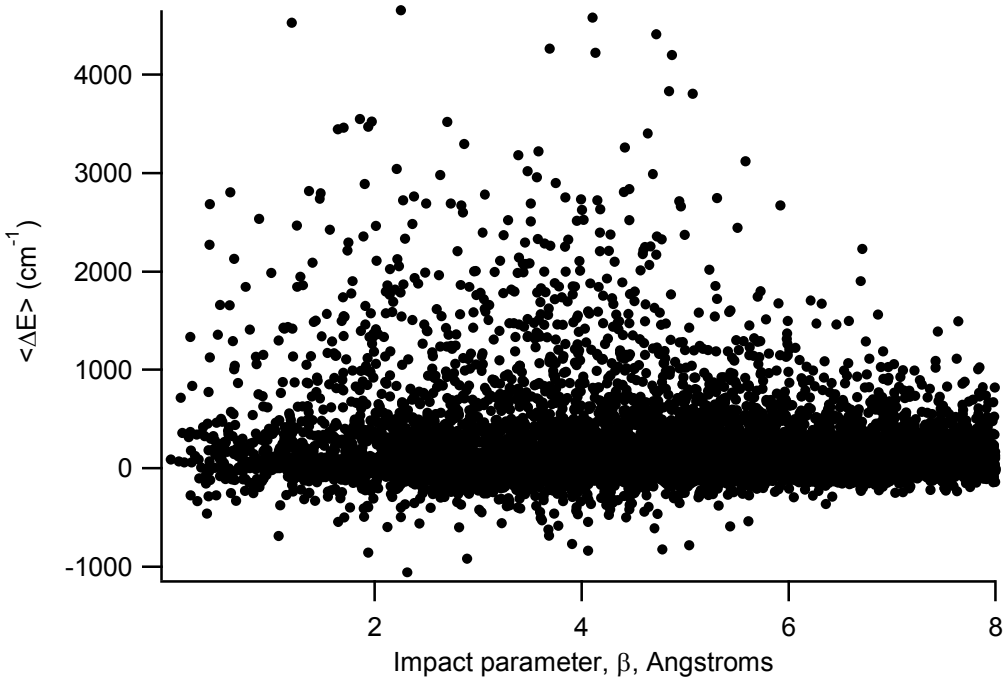

the maximum impact parameter, β_{max}, between 5.5 and 6.0 Å yielded similar $\langle \Delta E \rangle$ results when calculated using Eq. 5.11.

A histogram of the number of collisions through which the specific amount of energy is transferred per collision is plotted on semi-log scale in Figure 5.9. The vibrational excitation energy of acetylene is 20 kcal/mol for Figure 5.9. It is observed that the energy transfer rate is dominated (at this vibrational energy) by collisions transferring between +1000 and -200 cm^{-1} of energy. We have adopted the notation that positive energy transfer amounts indicate that the energy is being transferred from the vibrational modes of acetylene to the noble gas collider and negative energy transfer corresponds to that acetylene is gaining vibrational energy from the collision.

The classical trajectory calculation results for acetylene and vinylidene are shown in Figure 5.10. The amount of energy transfer per collision for acetylene were averaged for 10 000 trajectories at 7 000, 14 000, 21 000, and 28 000 cm^{-1} of vibrational energy. Vinylidene energy transfer rates were averaged over 10 000 trajectories at 19 000 and 26 000 cm^{-1} of vibrational energy above the acetylene ZPE.

The trajectory calculations fail to show a nearly two orders of magnitude increase in $\langle \Delta E \rangle$ at high excitations for acetylene. The theoretical results show a very linear behavior throughout the energy region shown in Figure 5.10, ranging from $\langle \Delta E \rangle$ ~50 cm^{-1} at $\langle E \rangle$ = 7 000 cm^{-1} to $\langle \Delta E \rangle$ ~ 120 cm^{-1} at $\langle E \rangle$ = 28 000 cm^{-1}. In addition, the energy transfer rate for collisions between acetylene and the four different noble gas atoms show a very similar dependence.

Figure 5.9. A histogram of the vibrational energy transfer between acetylene (excited at E_{vib} = 20 kcal/mol) and the Ne atom at 300K. The population of the energy transfer event is shown as a function of magnitude of the event, in 100 cm^{-1} bins. The positive sign for $\langle \Delta E \rangle$ indicates a loss of vibrational energy.

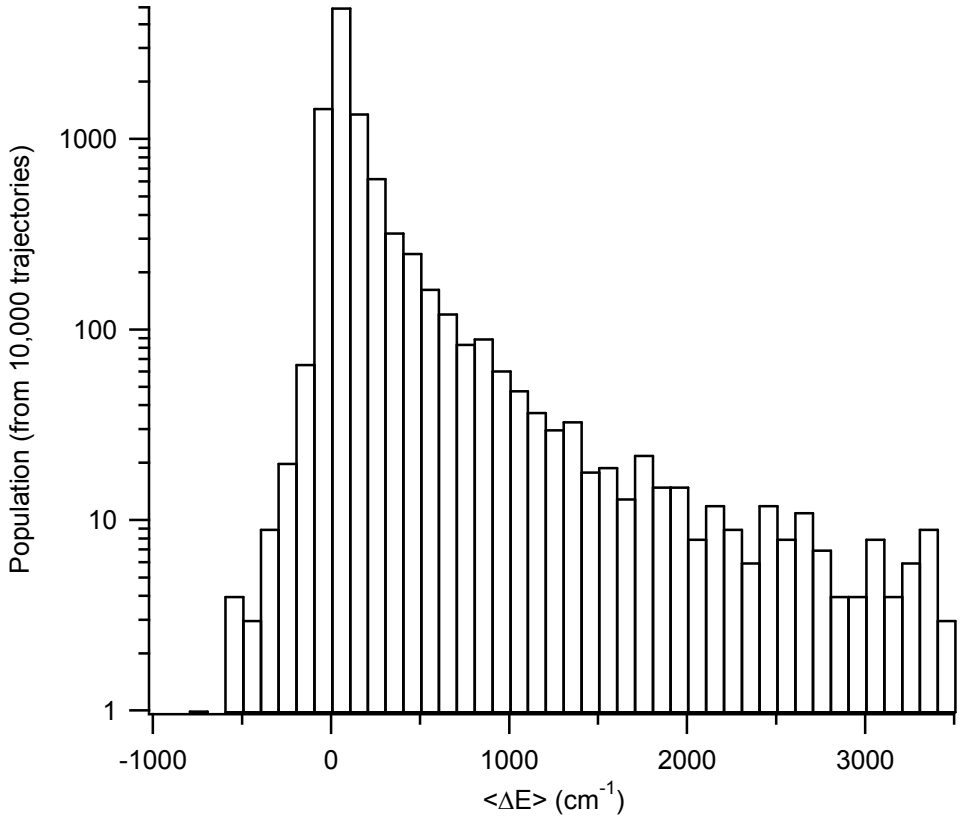

Figure 5.10. $\langle \Delta E \rangle$ vs. $\langle E \rangle$, obtained through trajectory calculations for acetylene and vinylidene with four noble gas colliders: He in red, Ne green, Ar blue, and Kr purple. Lines are drawn between the points to aid viewing.

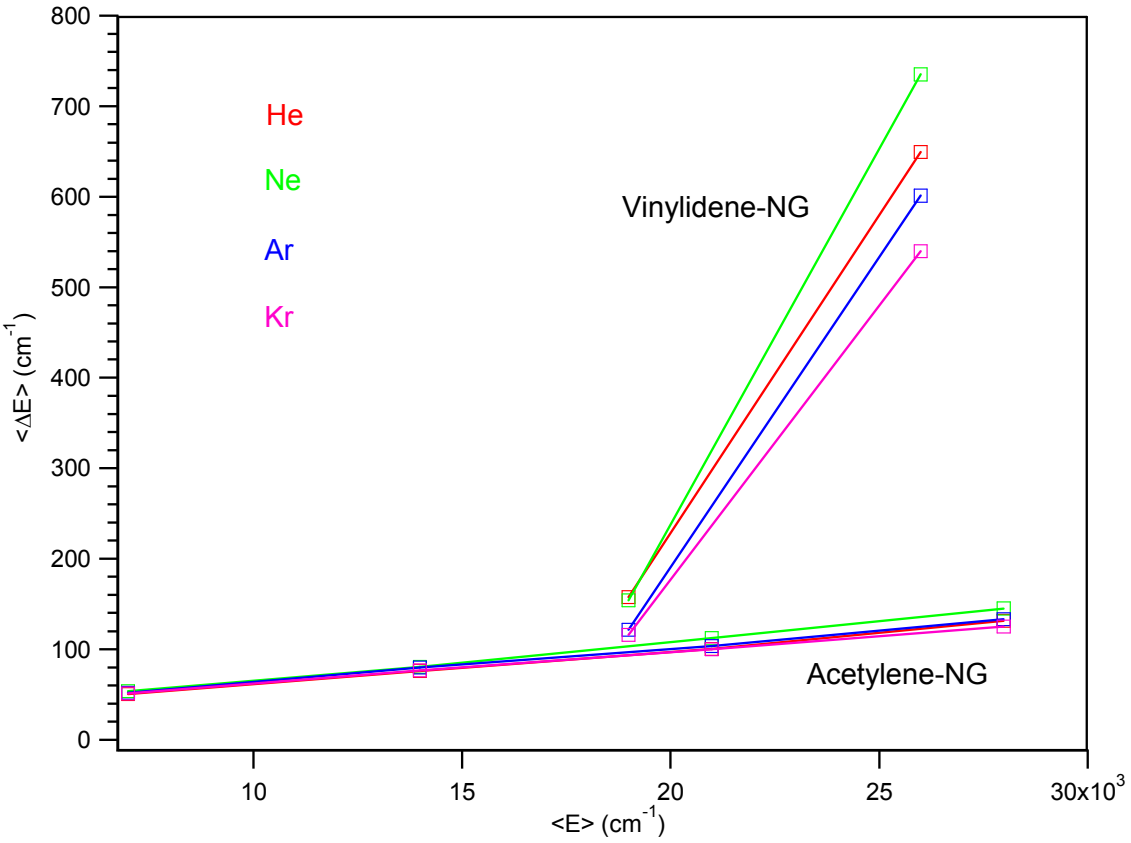

The trajectory results for excited vinylidene show a much larger energy transfer rate starting at $\langle E \rangle$ = 19 000 cm^{-1} above the acetylene ZPE than those for excited acetylene. The energy transfer rate increases from $\langle \Delta E \rangle$ = 100 - 200 cm^{-1} to $\langle \Delta E \rangle$ = 525 - 750 cm^{-1} at $\langle E \rangle$ = 26 000 cm^{-1} above the acetylene ZPE. The mass dependence appears as $\langle \Delta E \rangle_{Ne} > \langle \Delta E \rangle_{He} > \langle \Delta E \rangle_{Ar} > \langle \Delta E \rangle_{Kr}$.

The trajectory calculations notably produce much larger energy transfer amounts than the experimental observations. This has been noted previously for several small hydrocarbons and conjugated systems.[64,66,81,82] This is likely due to several factors including the inaccurate description of the inter- and intra-molecular potentials and a lack of good quantum mechanical selection rules. One other possibility is the over sampling of low impact parameter collisions.

Oversampling of the low impact collisions is possible if the maximum impact parameter is chosen too close to the L-J distance. Utilizing Eq. 5.11 alleviates some of these oversampling problems by normalizing to a reference impact parameter. It was calculated that decreasing the impact parameter by 1A for collisions between acetylene and He increases the energy transfer rate approximately 10%. Since we calculate the energy transfer rates using the same parameters, we will focus on the relative magnitudes of energy transfer from acetylene and vinylidene to the inert gases.

5.5 Discussion

The experimentally determined energy transfer curves in Figure 5.4 show several important features. The first is the magnitude of the energy transfer rate at low internal energies. The energy transfer amount is generally < 10 cm^{-1} per collision, which is

consistent with previous studies of the vibrational relaxation of low lying modes. These studies will be discussed in Section 5.5.1. The energy transfer rates at low energy lie within the error bars precluding us from determing a mass dependent efficiency.

The observed rates at high energies are of orders of magnitude larger than that observed at low energies. The increase is much faster after 15000 cm^{-1}. In addition, at high energies a mass dependence, $\langle \Delta E \rangle_{Ar} > \langle \Delta E \rangle_{Ne} > \langle \Delta E \rangle_{He} \sim \langle \Delta E \rangle_{Kr}$ is observed. This general mass dependence has been found in numerous systems of highly vibrationally excited molecules, including azulene, toluene, NO_2, SO_2, and CS_2.[13,83-85] In these cases there was generally an increasing efficiency with increasing collider mass (i.e. $\langle \Delta E \rangle_{Ne} > \langle \Delta E \rangle_{He}$), up until a certain mass, where the efficiency would "turn-around" and start to decrease with increasing mass (i.e. $\langle \Delta E \rangle_{Kr} < \langle \Delta E \rangle_{Ar} < \langle \Delta E \rangle_{Ne}$). At what mass the "turn-around" occurs seems to be system dependent.

The bend observed in the experimentally determined $\langle \Delta E \rangle$ vs. $\langle E \rangle$ curves, Figure 5.4, at approximately 10 000 – 15 000 cm^{-1} of internal energy, can not be explained by only considering the vibrational relaxation of acetylene, based on comparisons with theoretical calculations.

Above the isomerization barrier, both acetylene and vinylidene structures may exist, and subsequently both may contribute to the energy relaxation of the system. The differences in the relaxation rate for acetylene and vinylidene collisions are quite apparent from the SSHT model. For polyatomic molecules the vibrational relaxation rate is almost completely due to the lowest frequency vibrational mode of the molecule.[5] The mode with fastest collision relaxation for acetylene is the doubly degenerate ν_4 mode of 612 cm^{-1} with a small contribution from the doubly degenerate ν_5 mode at 730 cm^{-1}.[4] This is

compared with the energy transfer probability for vinylidene, occurring with the highest probability via the ν_6 mode, which has been experimentally determined to have an overtone, $\Delta\upsilon=2$, at 450 cm^{-1}.[19] The fundamental transition for the ν_6 mode has been calculated to lie between 263 and 472 cm^{-1}.[54-56,86] In the SSHT theory prediction the vinylidene energy transfer rate is much larger than acetylene with the same excitation as its lowest vibrational frequency is much lower than that of acetylene.

Quasiclassical trajectory calculations of the acetylene and vinylidene collisions with the four noble gas atoms reveal a similar dependence in the energy transfer rates above the isomerization barrier. Acetylene by itself shows a near linear energy transfer dependence with increasing energy, while the inclusion of a contribution from vinylidene may account for the dramatic increase in the energy transfer efficiency above the barrier.

Since the first reported observation of vinylidene by Burnett and coworkers,[87] there has been a great debate on the stability of this isomer of acetylene. A direct observation of vinylidene is not made here. Vinylidene has been proposed, however, to contribute to the vibrational relaxation and energy transfer rate of highly excited acetylene. The SSHT and trajectory calculated energy transfer rates for acetylene alone can not explain the experimental result. But when we include the energy transfer rates of vinylidene, we could understand the experimental results.

5.5.1 Comparison to previous work

Before discussing the results shown in this Chapter, previous state resolved energy transfer experiments on acetylene are reviewed and compared here.

The earliest work on the vibrational relaxation of acetylene involved acoustic measurements of ultrasonic waves to determine the vibrational relaxation times of pure gases.[88,89] A single relaxation process was found with a collisional probability of 3.5 x

10^{-3}, corresponding to an energy transfer rate based on the lowest frequency mode, ν_4, of 2 cm^{-1} per collision.

The first somewhat state specific work on the vibrational energy transfer of acetylene was conducted by Hager, *et al.*,[90] where laser-induced fluorescence measurements were made from the ν_2 and ν_5 modes following excitation of the ν_3 mode (which is Fermi resonant with the $\nu_2 + \nu_4 + \nu_5$ mode). Relaxation rates between acetylene and different noble gases were found to be on the order of 10^{-14} cm^3 s^{-1} $molecule^{-1}$, while self relaxation was an order of magnitude faster. No discernable mass dependence was found for relaxation from either the ν_2 or ν_5 modes, however an energy "bottleneck" exists in the ν_2 mode reducing the energy transfer rate. Even though it is commonly accepted that IVR is rapid and there are several close lying vibrational states within a kT of energy, the process is slowed because a large change in the vibrational quantum numbers is needed to relax the molecule. In addition, the character of the ν_2 mode, CC stretching, is quite different from the close lying modes, combination and overtones of the bending modes. This shows the effect of a momentum gap limiting vibrational relaxation. This "bottleneck" was also observed by Zinth, *et al.*[91] in their study of the picosecond vibrational relaxation of acetylene in solution.

A later work by Smith, *et al.*,[92] performed using the same vibrational excitation and broadband emission detection, found relaxation rates on the order of 10^{-13} cm^3 s^{-1} $molecule^{-1}$, with a clear mass dependence, $P_{He} > P_{Ne} > P_{Ar} > P_{Kr} > P_{Xe}$. The mass dependence is consistent with energy transfer processes at low vibrational energy which state the energy transfer probability will decrease with increasing reduced mass of the

collision. Assuming relaxation takes place along the ν_4 mode, we can approximate magnitude of the energy transfer rate to $\langle \Delta E \rangle$ ~ 0.25 – 1.5 cm^{-1} per collision.

Rotationally resolved energy transfer was first reported by Chadwick and Orr[93] by IR-UV double resonance. The $\nu_4 + \nu_5$ combination band of deuterated acetylene was found to vibrationally relax through the ν_4 or ν_5 mode with a rate constant of 1.6×10^{-13} cm^3 s^{-1} $molecule^{-1}$. Faster "quasi-elastic" collisions to close lying states were determined to be much faster, however with less energy transferred as the states were in close resonance with the initially prepared $\nu_4 + \nu_5$ level, even though the number of quantum jumps is larger.

Transient absorption measurements were made on acetylene in the 3 μm region, focusing on the $\nu_2 + \nu_3 - \nu_2$ and $2\nu_2 + \nu_3 - 2\nu_2$ bands by Murray *et al.*[94] These measurements were made following the 193 nm photolysis of vinyl bromide in a buffer gas, identical to the experiment performed here, but at much higher pressures, P_{VBr} = 400 mTorr and P_{He} = 20-30 Torr. At these high pressures (compared to P_{VBr} = 1-10 mTorr and P_{NG} = 2-4 Torr used here) the vibrational relaxation of highly excited states is rapid and only low vibrational states remain populated during the relatively long (10 – 100 μs) signal acquisition time. Nevertheless, rate constants of 1.5×10^{-14} and 2.1×10^{-14} cm^3 s^{-1} $molecule^{-1}$ were found for the ν_2 and $2\nu_2$ modes. Once again, the "bottleneck" effect is found with a slower relaxation rate for the ν_2 (and $2\nu_2$) mode. No other rates were determined, as the high pressures and temporal response of the experiment limited their observation.

The first study on the energy transfer of highly vibrationally excited acetylene was conducted by vibrational overtone excitation of the ν_3 CH stretch of acetylene, followed

by a UV laser probe to examine the population by laser-induce fluorescence.[27] A self-relaxation rate constant was determined to be ~9 x 10^{-10} cm^3 s^{-1} $molecule^{-1}$ with collisions between acetylene and noble gases approximately half as fast. Because only the depletion of the fluorescence of a state was measured, the amount of energy transferred per collision can not be determined. No discernable mass dependence was found when the collisional rates of He, Ar, and Xe were used.

Several other studies focus on the energy transfer efficiency of relatively low lying vibrational states, probing resonances and energy transfer rates from highly efficient pathways using a variety of monatomic and diatomic colliders.[95-99] The qualitative and quantitative vibrational relaxation rates for self-collisions and collisions with monatomic and diatomic gases agree well with the experimental result at low vibrational energies, $\langle \Delta E \rangle < 10$ cm^{-1}. The large magnitude energy transfer rates found at high energies has not been observed previously.

5.5.2 Lack of IR emission from vinylidene

Before we consider the contribution of vinylidene to the energy transfer behavior of acetylene, we comment first on why vinylidene does not appear in the IR emission from highly vibrationally excited acetylene.

The reason IR emission from vinylidene is not observed is primarily due to the low density of vinylidene states compared to acetylene. The calculated RRKM equilibrium constant, based on direct counting of the acetylene levels, and the Whitten-Rabinovitch semi-classical expression for the sum and density of states of vinylidene, lies far toward acetylene at energies near the isomerization barrier. However, the equilibrium shifts towards vinylidene as the vibrational energy is increased because of the rapid build

up of the low frequency ν_6 mode of vinylidene. The density of states and isomerization rates will be discussed in the next sections.

At high energies, there may be a sufficient population of vinylidene, especially right after photolysis which forms predominantly vinylidene.[16] IR emission from vinylidene must therefore be considered. Four IR emission modes of vinylidene have been observed previously.[19] The four modes determined experimentally are the ν_1 CH symmetric stretch, 3025 cm^{-1}, the ν_2 CC stretch at 1635 cm^{-1}, the ν_3 CH_2 scissor at 1165 cm^{-1}, and the ν_6 CH_2 rock, observed at 450 cm^{-1}. The ν_6 mode observed is thought to be the $2 \leftarrow 0$ transition as opposed to the fundamental. Two other modes, the ν_4 CH_2 wag and the ν_5 CH asymmetric stretch, are predicted to lie between 716 – 775 cm^{-1} and 3065 – 3240 cm^{-1}, respectively, based on AIMD and coupled cluster calculations.[54-56] IR intensities have not been listed in these cases, with the experimental intensities observed in the PES study mostly indicative of the nuclear wavefunction overlap. We would expect these two unobserved modes to have a similar intensity to those previously observed, with the exception of the ν_6 CH_2 rock, which should be significantly weaker. There are several factors, in addition to the low molecule density discussed previously, which would limit the observation of the IR active modes of vinylidene.

The first factor limiting the detection of the IR modes of vinylidene is the frequency overlap with vibrational modes of acetylene. The ν_1 and ν_5 modes of vinylidene overlap with the anharmonically shifted ν_3 mode of acetylene. In addition, the ν_3 and ν_4 modes of vinylidene overlap the $\nu_4 + \nu_5$ and ν_5 modes of acetylene, respectively. The ν_6 mode of vinylidene falls below the detection region of the detector

in use here and the ν_2 mode is thought to be rather weak, when compared to the same nuclear movement (CC stretch) of similar molecules.

The intensity of the modes of vinylidene would also be much weaker than those of acetylene due to the harmonic oscillator scaling factors, described in the previous Chapter, further reducing their influence on the spectra. Because of the low intensity of these modes and the frequency overlap with acetylene, detection of these modes in the IR would be quite difficult at present sensitivity of the IR detectors used.

5.5.3 Contribution of vinylidene to the overall energy transfer

Above the isomerization barrier, the acetylene molecule appears with a finite probability as vinylidene. This probability can be estimated from the ratio of the zeroth-order vibrational level densities of acetylene vs vinylidene, assuming rapid intramolecular relaxation. Using a purely statistical model by taking the ratio of the density of states of acetylene and vinylidene, the probability of the molecule in the acetylene form as a function of energy E, $b(E)$, is

$$b(E) = \frac{\rho_a}{\rho_a + \rho_v} \tag{5.17}$$

where ρ_a and ρ_v are the densities of states for acetylene and vinylidene respectively.

It is possible to count in the contribution of the vinylidene isomer with a simple assumption that the contribution to the relaxation rate is linearly proportional to the probability of existence of the isomer. Based on this assumption, the amount of energy transferred per collision can be expressed as

$$\langle \Delta E(E) \rangle = b(E) \langle \Delta E_a(E) \rangle + (1 - b(E)) \langle \Delta E_v(E) \rangle \tag{5.18}$$

where $\langle \Delta E_a(E) \rangle$ and $\langle \Delta E_v(E) \rangle$ are the energy dependent energy transfer rates for acetylene and vinylidene, respectively derived from Eq. 5.1, and $b(E)$ is the energy dependent contribution of acetylene to the overall energy transfer rate. The balance comes from vinylidene.

The overall energy transfer rate, calculated from Eq. 5.18, is shown in Figure 5.11 shows several similarities to the experimentally derived energy transfer rate in Figure 5.4. The most notable similarity is the presence of a bend in the energy transfer rate and enhancement of the rate at high internal energies. The calculated result shown in Figure 5.11 shows approximately 10 - 20x enhancement of the energy transfer rate at high energies.

Discrepancies about the location of the bend and magnitude of the energy transfer rate still need resolution. Several factors may affect the contribution of vinylidene in the overall energy transfer rate. These including large amplitude bending modes yielding a more vinylidene like structure which has been observed at energies below the isomerization barrier, strong anharmonicities within the vinylidene structure leading to a more dramatic increase in the state density, strong coupling between vibrational states of vinylidene and acetylene leading to rapid isomerization,[100-104] and possible memory effects from forming ~80% vinylidene following photolysis of vinyl bromide. Until all of these contributions (and others including tunneling effects, other coupling mechanisms, and accurate PES's) are determined, a quantitatively accurate description of the energy transfer of highly vibrationally excited acetylene will remain elusive.

Figure 5.11. The combined SSHT energy transfer rate for acetylene and vinylidene. The rate is calculated based on the relative state densities of acetylene and vinylidene.

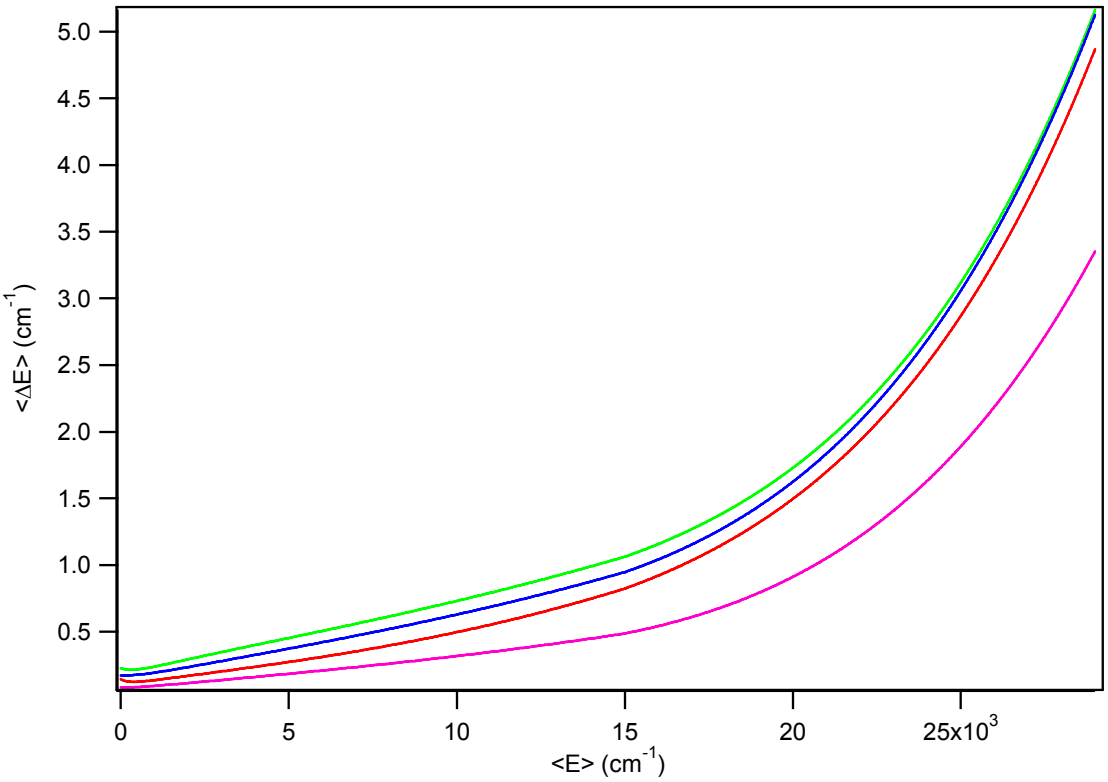

5.5.4 Classical trajectory energy transfer rate

The trajectory simulations show an analogous result to the SSHT calculation. Vinylidene shows a more efficient energy transfer rate when compared to the acetylene energy transfer rate at similar energies relative to the acetylene ZPE. The appearance of this significantly different energy transfer rate indicates that structural isomers behave quite differently even when intermolecular interactions and intramolecular force constants are quite similar. The overall vibrational energy dependent energy transfer rate for acetylene and vinylidene determined from the trajectory simulations must take into affect some vibrational level density factor which would weight the contribution from acetylene much more than that from vinylidene. The result is shown in Figure 5.12. The trajectory result is very similar to the SSHT result, with a smaller "bend" above the acetylene – vinylidene isomerization barrier. The classical trajectory calculations show a much better quantitative comparison at energies above 15,000 cm^{-1}, while the SSHT calculation shows a better quantitative agreement with experimental results below 10,000 cm^{-1}.

Two issues arise from the trajectory simulations which have already been mentioned: (1) Vinylidene – Ar collisions are less efficient than vinylidene – He and vinylidene – Ne in the trajectory results, while more efficient in the experimental result, and (2) The absolute value of the energy transfer rates are too large, even when only considering acetylene – NG collisions. These affects have been observed in past trajectory results on other systems involving polyatomic collisions with noble gas atoms.[64,66,81,82] These two discrepancies can be attributed to different intermolecular potentials affecting the collisional energy transfer rate. Bruehl and Schatz[64] have shown that changing different parameters of the potentials including interaction distance and well depth results in minor changes in the energy transfer rate. However, they show that

Figure 5.12. The combined classical trajectory calculated energy transfer rate for acetylene and vinylidene. The rate is calculated based on the relative state densities of acetylene and vinylidene.

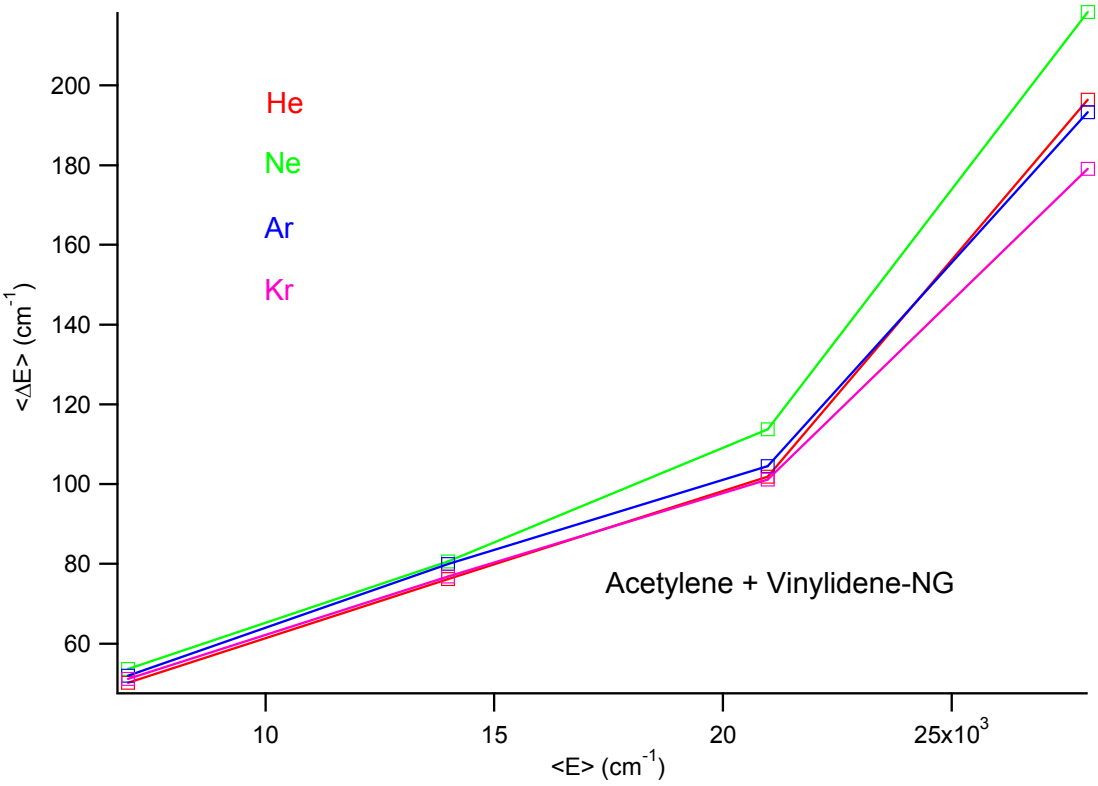

changing the steepness of the repulsive wall shows a marked change in the energy transfer rates. Other studies by Lim and coworkers[66,81] have shown large differences in the energy transfer rates when utilizing different potential models (i.e. Buckingham 6-exp, L-J 6-12, etc.) in accord with the study by Bruehl and Schatz. Their results still show good qualitative agreement, especially when utilizing the trajectories for comparisons between similar molecular species.[82]

The trajectory calculations are only meant to be used as a guide for further study into the energy transfer rate of highly vibrationally excited acetylene, with the inclusion of a significant population of vinylidene contributing to the overall rate. We can not determine the contribution of vinylidene to the energy transfer rate from the trajectory due to the discrepancies mentioned in the previous paragraph. The goal of using the quasi-classical trajectory simulations was to provide a classical interpretation of the energy transfer rate; the isomeric vinylidene structure shows a much enhanced energy transfer rate compared to acetylene.

5.6 Conclusion

The observed IR emission from highly vibrationally excited acetylene generated from the 193 nm photolysis of vinyl bromide was detected and fit to a normal mode vibrational emission model. Collisional deactivation by four noble gas colliders, He, Ne, Ar, and Kr, were studied and energy transfer as a function of excitation energy was characterized. Two distinct energy behaviors in the energy transfer rate were observed: a "low $\langle \Delta E \rangle$" corresponds to $\langle E \rangle$ < 10,000 cm^{-1} where energy transfer rates were less than 20 cm^{-1} and a "high $\langle \Delta E \rangle$" corresponding to $\langle E \rangle$ > 15,000 cm^{-1} where energy transfer rates were much larger, on the order of 100s of cm^{-1}.

SSHT and classical trajectory calculations were performed on acetylene-NG collisions. Neither the SSHT nor the trajectory calculations on acetylene reproduced this enhanced high energy behavior. Both theories underestimated the enhancement of the energy transfer rate observed in the experimental result.

The same calculations were then performed on vinylidene-NG collisions. Both the SSHT and classical trajectory calculations produced a vinylidene energy transfer rate 1-2 orders of magnitude larger than the corresponding calculations for acetylene. When the energy transfer rate from a statistical amount of vinylidene was factored into the acetylene energy transfer rate, a better qualitative agreement between the theories and experimental result were found. While neither theory quantitatively verified the experimental result, both calculations showed that by including the vinylidene isomer to describe collisional energy transfer of acetylene can reproduce an enhancement to the energy transfer rate.

References:

(1) Schwartz, R. N.; Slawsky, Z. I.; Herzfeld, K. F. *J. Chem. Phys.* **1952**, *20*, 1591.

(2) Schwartz, R. N.; Herzfeld, K. F. *J. Chem. Phys.* **1954**, *22*, 767.

(3) Tanczos, F. I. *J. Chem. Phys.* **1956**, *25*, 439.

(4) Yardley, J. T. *Introduction to Molecular Energy Transfer*; Academic Press: New York, 1980.

(5) Lambert, J. D. *Vibrational and Rotational Relaxation in Gases*; Clarendon Press: Oxford, 1977.

(6) Flynn, G. W.; Parmenter, C. S.; Wodtke, A. M. *J. Phys. Chem.* **1996**, *100*, 12817.

(7) Oref, I.; Tardy, D. C. *Chem. Rev.* **1990**, *90*, 1407.

(8) Steinfeld, J. I.; Francisco, J. S.; Hase, W. L. *Chemical Kinetics and Dynamics*, 2nd. ed.; Prentice-Hall, Inc.: NJ, 1999.

(9) *Chemical and Biochemical Applications of Lasers*; Moore, C. B., Ed.; Academic Press: New York, 1974.

(10) Li, Z.; Sansom, R.; Bonella, S.; Coker, D. F.; Mullin, A. S. *J. Phys. Chem. A* **2005**, *109*, 7657.

(11) Hartland, G. V.; Qin, D.; Dai, H.-L. *J. Chem. Phys.* **1997**, *107*, 2890.

(12) Qin, D.; Hartland, G. V.; Dai, H.-L. *J. Phys. Chem. A* **2000**, *104*, 10460.

(13) Hartland, G. V.; Qin, D.; Dai, H.-L. *J. Chem. Phys.* **1995**, *102*, 8677.

(14) Wilhelm, M. J. *PhD Thesis* **2009**.

(15) Qin, D. *PhD Thesis* **2000**.

(16) Liu, D., -Kuo; Letendre, L.; Dai, H.-L. *J. Chem. Phys.* **2001**, *115*, 1734.

(17) Lin, S.-R.; Lin, S.-C.; Lee, Y.-C.; Chou, Y.-C.; Chen, I.-C.; Lee, Y.-P. *J. Chem. Phys.* **2001**, *114*, 160.

(18) Lin, S.-R.; Lin, S.-C.; Lee, Y.-C.; Chou, Y.-C.; Chen, I.-C.; Lee, Y.-P. *J. Chem. Phys.* **2001**, *114*, 7396.

(19) Ervin, K. M.; Ho, J.; Lineberger, W. C. *J. Chem. Phys.* **1989**, *91*, 5974.

(20) Nikow, M.; Wilhelm, M. J.; Dai, H.-L. *J. Phys. Chem. A* **2009**, *113*, 8857.

(21) Nikow, M.; Wilhelm, M. J.; Smith, J. M.; Dai, H.-L. **to be published.**

(22) Letendre, L.; Liu, D.-K.; Pibel, C. D.; Halpern, J. B.; Dai, H.-L. *J. Chem. Phys.* **2000**, *112*, 9209.

(23) Zou, P.; Strecker, K. E.; Ramirez-Serrano, J.; Jusinski, L. E.; Taatjes, C. A.; Osborn, D. L. *Phys. Chem. Chem. Phys* **2007**, *10*, 713.

(24) Maki, A.; Quapp, W.; Klee, S. *J. Mol. Spec.* **1995**, *171*, 420.

(25) Blank, D. A.; Sun, W.; Suits, A. G.; Lee, Y. T.; North, S. W.; Hall, G. E. *J. Chem. Phys.* **1998**, *108*, 5414.

(26) Carvalho, A.; Hancock, G.; Saunders, M. *Phys. Chem. Chem. Phys* **2006**, *8*, 4337.

(27) Utz, A. L.; Tobiason, J. D.; Carrasquillo M., E.; Fritz, M. D.; Crimm, F. F. *J. Chem. Phys.* **1992**, *97*, 389.

(28) Yang, X.; Price, J. M.; Mack, J. A.; Morgan, C. G.; Rogaski, C. A.; McGuire, D.; Kim, E. H.; Wodtke, A. M. *J. Phys. Chem.* **1993**, *97*, 3944.

(29) Nikitin, E. E.; Troe, J. *Phys. Chem. Chem. Phys* **2008**, *10*, 1483.

(30) Nikitin, E. E.; Pitaevskii, L. P. *Phys. Rev. A* **1994**, *49*, 695.
(31) Dashveskaya, E. I.; Litvin, I.; Nikitin, E. E.; Troe, J. *J. Chem. Phys.* **2006**, *125*, 154315.
(32) Landau, L.; Teller, E. *Phys. Z. Sowj. Un.* **1936**, *10*, 34.
(33) Rapp, D.; Sharp, T. E. *J. Chem. Phys.* **1963**, *38*, 2641.
(34) Yang, X.; Wodtke, A. M. *Int. Rev. Phys. Chem.* **1993**, *12*, 123.
(35) Hancock, G.; Morrison, M.; Saunders, M. *Phys. Chem. Chem. Phys* **2009**, *11*, 8507.
(36) Nowlin, M. L.; Heaven, M. C. *J. Chem. Phys.* **1993**, *99*, 5654.
(37); Douglas, D. J.; Moore, C. B.; In Kompa, K. L.; Smiths, S. D., Eds.; Springer-Verlag: Edinberg, UK, 1979, pp 336.
(38) Drabbels, M.; Morgan, C. G.; McGuire, D. S.; Wodtke, A. M. *J. Chem. Phys.* **1995**, *102*, 611.
(39) Barker, J. R. *ACS Symposium Series* **1997**, *678(Highly Excited Molecules)*, 220.
(40) Kable, S. H.; Knight, A. E. W. *J. Phys. Chem. A* **2003**, *107*, 10813.
(41) Tang, K. Y.; Parmenter, C. S. *J. Chem. Phys.* **1983**, *78*, 3922.
(42) Stretton, J. L. *Faraday Soc.* **1965**, *35*, 1053.
(43) Wilson Jr., E. B.; Decius, J. C.; Cross, P. C. *Molecular Vibrations: The Theory of Infrared and Raman Vibrational Spectra*; Dover: New York, 1955.
(44) Ewing, G. E. *J. Phys. Chem.* **1987**, *91*, 4662.
(45) Hirschfelder, J. O.; Curtiss, C. F.; Bird, R. B. *Molecular Theory of Gases and Liquids*; John Wiley & Sons: New York, 1954.
(46) Johnston, H. L.; Grilly, E. R. *J. Phys. Chem.* **1942**, *46*, 938.
(47) Titani, T. *Bull. Chem. Soc. Japan* **1930**, *5*, 98.
(48) Reddy, C. P. K.; Sarkar, K. L.; Pandey, L. *J. Mag. Resonance* **1983**, *55*, 177.
(49) Moszynski, R.; Wormer, P. E. S.; van der Avooird, A. *J. Chem. Phys.* **1995**, *102*, 8385.
(50) Yang, M.; Alexander, M. H.; Werner, H.-J.; Bemish, R. J. *J. Chem. Phys.* **1996**, *105*, 10462.
(51) Bemish, R. J.; Oudejans, L.; Miller, R. E.; Moszynski, R.; Heijmen, T. G. A.; Korona, T.; Wormer, P. E. S.; Van der Avoird, A. *J. Chem. Phys.* **1998**, *109*, 8968.
(52) Munteanu, C. R.; Fernandez, B. *J. Chem. Phys.* **2005**, *123*, 014309.
(53) Cappelletti, D.; Bartolomei, M.; Carmona-Novillo, E.; Pirani, F.; Blanquet, G.; Thibault, F. *J. Chem. Phys.* **2007**, *126*, 064311.
(54) Chang, N.-Y.; Shen, M.-Y.; Yu, C.-H. *J. Chem. Phys.* **1997**, *106*, 3237.
(55) Stanton, J. F.; Gauss, J. *J. Chem. Phys.* **1999**, *110*, 6079.
(56) Hayes, R. L.; Fattal, E.; Govind, N.; Carter, E. A. *J. Am. Chem. Soc.* **2001**, *123*, 641.
(57) Bunker, D. L. *J. Chem. Phys.* **1962**, *37*, 393.
(58) Porter, R. N.; Raff, L. M. *Dynamics of Molecular Collisions*; Plenum: New York, 1976.
(59) Bunker, D. L.; Hase, W. L. *J. Chem. Phys.* **1973**, *54*.
(60) Bunker, D. L.; Pattengill, M. *J. Chem. Phys.* **1968**, *48*, 772.
(61) Miller, L. A.; Barker, J. R. *J. Chem. Phys.* **1996**, *105*, 1383.
(62) Yoder, L. M.; Barker, J. R. *J. Phys. Chem. A* **2000**, *104*, 10184.

(63) Lenzer, T.; Luther, K. *J. Chem. Phys.* **1996**, *105*, 10944.
(64) Bruehl, M.; Schatz, G. C. *J. Phys. Chem.* **1988**, *92*, 7223.
(65) Bustos-Marun, R. A.; Coronado, E. A.; Ferrero, J. C. *J. Chem. Phys.* **2007**, *127*, 154305.
(66) Linhananta, A.; Lim, K. F. *Phys. Chem. Chem. Phys* **2000**, *2*, 1385.
(67) Bernshtein, V.; Oref, I. *J. Phys. Chem. A* **2006**, *110*, 1541.
(68) Troya, D. *J. Phys. Chem. A* **2005**, *109*, 5814.
(69) Hase, W. L.; Duchovic, R. J.; Hu, X.; Komornicki, A.; Lim, K. F.; Lu, D.-H.; Peslherbe, G. H.; Swamy, K. N.; VandeLinde, S. R.; Varandas, A.; Wang, H.; Wolf, R. J. *J. Quantum Chem. Program Exchange Bull.* **1996**, *16*, 43 [QCPE Program 671].
(70) Hase, W. L.; Duchovic, R. J.; Hu, X.; Komornicki, A.; Lim, K. F.; Lu, D.-H.; Peslherbe, G. H.; Swamy, K. N.; Vande Linde, S. R.; Varandas, A.; Wang, H.; Wolf, R. J. VENUS96, A general chemical dynamics computer program; Texas Tech University, Department of Chemistry and Biochemistry: Lubbock, 1996.
(71) Herzberg, G. *Molecular Spectra and Molecular Structure*; Van Nostrand: New York, 1950; Vol. II Infrared and Raman Spectra of Polyatomic Molecules.
(72) Heijmen, T. G. A.; Moszynski, R.; Wormer, P. E. S.; Van der Avoird, A.; Buck, U.; Ettisher, I.; Krohne, R. *J. Chem. Phys.* **1997**, *107*, 7260.
(73) Liu, Y.; Jager, W. *Phys. Chem. Chem. Phys* **2003**, *5*, 1744.
(74) Cappelletti, D.; Bartolomei, M.; Sabido, M.; Pirani, F.; Blanquet, G.; Walrand, J.; Bouanich, J.-P.; Thibault, F. *J. Phys. Chem. A* **2005**, *109*, 8471.
(75) Lim, K. F. Program SIGMON: An aid for the semi-empirical fitting of the intermolecular potential. Available from K.F. Lim; Deakin University, School of Life and Environmental Sciences: Geelong, Vic 3217, 1992.
(76) Pirani, F.; Alberti, M.; Castro, A.; Moix Teixidor, M.; Cappelletti, D. *Chem. Phys. Lett.* **2004**, *394*, 37.
(77) Mullin, A. S.; Michaels, C. A.; Flynn, G. W. *J. Chem. Phys.* **1995**, *102*, 6032.
(78) Wall, M. C.; Mullin, A. S. *J. Chem. Phys.* **1998**, *108*, 9658.
(79) Wall, M. C.; Lemoff, A. E.; Mullin, A. S. *J. Chem. Phys.* **1999**, *111*, 7373.
(80) Clark, D. C.; Oref, I.; Gilbert, R. G.; Lim, K. F. *J. Chem. Phys.* **1992**, *96*, 5983.
(81) Lim, K. F. *J. Chem. Phys.* **1994**, *100*, 7385.
(82) Lenzer, T.; Luther, K.; Troe, J.; Gilbert, R. G.; Lim, K. F. *J. Chem. Phys.* **1995**, *103*, 626.
(83) Hippler, H.; Troe, J.; Wendelken, H. J. *J. Chem. Phys.* **1983**, *78*, 6709.
(84) Rossi, M. J.; Pladziewicz, J. R.; Barker, J. R. *J. Chem. Phys.* **1983**, *78*, 6695.
(85) Hartland, G. V.; Qin, D.; Dai, H.-L. *J. Chem. Phys.* **1993**, *98*, 6906.
(86) Schork, R.; Koppel, H. *Chem. Phys. Lett.* **2000**, *326*, 277.
(87) Burnett, S. M.; Stevens, A. E.; Feigerle, C. S.; Lineberger, W. C. *Chem. Phys. Lett.* **1983**, *100*, 124.
(88) Lambert, J. D.; Salter, R. *Proc. Roy. Soc. A* **1959**, *253*, 277.
(89) Lambert, J. D. *J. Chem. Soc. Far. Trans. 2* **1972**, *68*, 364.
(90) Hager, J.; Krieger, W.; Rueff, T.; Walther, H. *J. Chem. Phys.* **1980**, *72*, 4286.

(91) Zinth, W.; Kolmeder, C.; Benna, B.; Irgens-Defregger, A.; Fischer, S. F.; Kaiser, W. *J. Chem. Phys.* **1983**, *78*, 3916.
(92) Smith, I. W. M.; Warr, J. F. *Chem. Phys. Lett.* **1990**, *173*, 70.
(93) Chadwick, B. L.; Orr, B. J. *J. Chem. Phys.* **1991**, *95*, 5476.
(94) Murray, K. K.; Morter, C. L.; Curl, R. F. *J. Chem. Phys.* **1992**, *96*, 5047.
(95) Milce, A. P.; Barth, H.-D.; Orr, B. J. *J. Chem. Phys.* **1994**, *100*, 2398.
(96) Tobiason, J. D.; Utz, A. L.; Crimm, F. F. *J. Chem. Phys.* **1994**, *101*, 1108.
(97) Frost, M. J.; Smith, I. W. M. *J. Phys. Chem.* **1995**, *99*, 1094.
(98) Henton, S.; Islam, M.; Smith, I. W. M. *J. Chem. Soc., Faraday Trans.* **1998**, *94*, 3207.
(99) Henton, S.; Islam, M.; Gatenby, S.; Smith, I. W. M. *J. Chem. Soc., Faraday Trans.* **1998**, *98*, 3219.
(100) Jacobson, M. P.; Obrien, J. P.; Silbey, R. J.; Field, R. W. *J. Chem. Phys.* **1998**, *109*, 121.
(101) Jacobson, M. P.; Silbey, R. J.; Field, R. W. *J. Chem. Phys.* **1999**, *110*, 845.
(102) Jacobson, M. P.; Jung, C.; Taylor, H. S.; Field, R. W. *J. Chem. Phys.* **1999**, *111*, 600.
(103) Jacobson, M. P.; Field, R. W. *J. Phys. Chem. A* **2000**, *104*, 3073.
(104) Srivastava, H. K.; Conjusteau, A.; Mabuchi, H.; Callegari, A.; Lehmann, K. K.; Scoles, G.; Silva, M. L.; Field, R. W. *J. Chem. Phys.* **2000**, *113*, 7376.

Chapter 6

Collision energy transfer through reaction complex formation: Acetylene + hot H atom

6.1 Introduction

6.1.1 Summary

The mechanistic study of collisions between hot hydrogen atoms and ambient acetylene molecules producing vibrationally hot acetylene is presented. Kinetically hot hydrogen atoms are produced from a UV laser dissociation of precursor molecules. The collision between these atoms and room temperature acetylene molecules generates vibrationally excited acetylene with a bimodal energy distribution. A mechanism consisting of the generation of a highly vibrationally excited vinyl intermediate during the collision is proposed for the generation of higher excited acetylene and confirmed by isotopic substitution of the acetylene precursor. The short lived vinyl intermediate formed by a hot H atom and a room temperature acetylene molecule dissociates into a vibrationally hot acetylene molecule and a kinetically slower hydrogen atom. The existence of this mechanism is confirmed by isotope substitution experiments: in the H + C_2D_2 experiments vibrationally excited C_2D_2 and C_2HD have been detected with a ratio of approximately 1:2. The average vibrational energy in acetylene was compared to a combined statistical-impulsive dissociation model with favorable comparison for the isotopic studies performed.

6.1.2 H + acetylene reaction

Bimolecular reaction is one of the fundamental elementary reaction types in chemistry. One of the simplest bimolecular reactions involves the hydrogen atom. The role of the hydrogen atom in chemistry is extensive, ranging from environmental, combustion, atmospheric, interstellar, and other systems. Hot hydrogen atoms have been found in several environmental systems including landfill environments, where high heat and reactive gases are present,[1] and coal fuel pyrolysis.[2] Their presence in interstellar and planetary environments is even more evident: in the spatial region around Uranus,[3] in Pluto's[4] and Venus's[5] atmosphere, and in the Jovian aurora.[6] Hydrogen atoms are also observed in very cold environments such as dense interstellar clouds where they are believed to play a crucial role in the chemistry in the medium due to their size and mobility.[7] In addition, the reaction of hydrogen and acetylene forming vinyl has garnered more attention as a crucial rate determining step in the generation of saturated hydrocarbons in comets.[8]

Recent work by Kulatilaka *et al*.[9] probed the generation of H atoms in methane flames. The work represents a successful application of a spectroscopic method for producing and probing H atoms within a combustion environment. Interference was observed from other transient species such as OH radicals and vibrationally excited water molecules. In addition, mechanisms for the dissociation of methane radicals and acetylene molecules are postulated.

The reactions of this lightest atom are an interesting system of study. In some cases, collisions between hot hydrogen atoms act through a simple translational-rotational (T-R) or translational to vibrational (T-V) energy transfer pathway.[10] Other times, the

energy transferred shows a strong dependence on the interaction (attractive part) energy of the collision which enhances the energy transfer rate.[11,12] Still in other systems, hot hydrogen atoms may chemically react with other more reactive species to produce product molecules through an abstraction,[13,14] exchange or single displacement reaction.[15] The reactive nature of hydrogen atoms is highly dependent on the intermolecular forces between the two reactant species and the orientation of the interaction.

A general scheme for the possible reactions between a hydrogen atom and a molecule or radical includes three reaction pathways. The first is a pure T-V,R energy transfer collision, the second a displacement reaction, and the third a bimolecular addition reaction:

$$H + XY(\upsilon, J) \rightarrow XY(\upsilon', J') + H \quad (6.1)$$

$$H + XY(\upsilon, J) \rightarrow HX(\upsilon', J') + Y(\upsilon'', J'') \quad (6.2)$$

$$H + XY(\upsilon, J) \rightarrow HXY(\upsilon', J') \quad (6.3)$$

The notation X and Y may represent an atom, molecule, or radical, and consequently, the XY species may be a molecule or radical. The vibrational and rotational energies are described by υ and J, respectively. If the molecule or radical has a hydrogen atom, we can be more specific with reaction 6.2 and the exchange reaction becomes,

$$H + H'X\ (\upsilon, J) \rightarrow HX\ (\upsilon', J') + H' \quad (6.4)$$

where one H atom exchanges with H', a different hydrogen atom. This reaction is different than Reaction 6.1 in that there is an exchange of H atoms, instead of the transfer of energy in Reaction 6.1.

Energy transfer collision involving an H atom, Eq. 6.1, has been well studied for XY molecules such as NO,[11] CO,[10-12,16] CH_3F,[12] and CO_2[17-20] for varying amounts of H

atom kinetic energy. The primary focus of these studies was to determine the T-V (translation – vibrational) energy transfer rate. It was generally found that the energy transfer pathway was dominated by v=0 to v=1 energy transfer process, though most studies could not rule out higher vibrational excitations. An impulsive mechanism was used to describe many of these collisions.

The energetics of reaction 6.2 and 6.4, involving XY molecules such as HCN,[14] OCS,[21] HBr,[15] HI,[15] and CO_2[13] have also received a great deal of attention. A similar study on the reaction of hydrogen with water producing OH radicals was recently analyzed by trajectory calculations in a similar manor to those performed in the previous Chapter.[22] The focus of the work was on the energy distribution in OH following the collision. Most of these studies reveal that only a very small percentage of the initial kinetic energy of the hydrogen atom is directed into the vibrational and rotational degrees of freedom of the products. An example of Reaction 6.3 is the reactions of H + O_2 producing HO_2, which shows the addition of hydrogen atoms to reactive species.[23]

The interaction between hydrogen and acetylene has been studied via the association reaction, as well as the unimolecular dissociation reaction of the vinyl radical. Many of the recent studies on collisions of hydrogen atoms and acetylene molecules focus on the temperature dependent reaction kinetics between 193 and 1629 K.[24-28] In the H + C_2H_2 reactions, hydrogen atoms were generated by the pyrolysis of pentane[26] and ethyl iodide.[28] In studies of vinyl dissociation, the generation of the vinyl radical was achieved by pyrolysis of vinyl bromide or vinyl iodide,[26] as well as UV laser photolysis of vinyl bromide or methyl vinyl ketone.[27] Many of these studies have determined rates or activation energies that were sufficiently different from previous studies. Several of

the studies determined rate constants, but were not able to eliminate other reactions which would possibly interfere with the main $C_2H_2 + H \leftrightarrow C_2H_3$ reaction, such as precursor decomposition and collisional relaxation. In each of these cases, the precursor molecules produce vinyl radicals and have noted this as a limiting factor in determining the pure rate constant for $H + C_2H_2$. The notations for the association and dissociation reactions of the vinyl intermediate are based on the general Reaction 6.4:

$$H + C_2H_2 \rightarrow C_2H_3^* \quad (6.5a)$$

$$C_2H_3^* \rightarrow H + C_2H_2 \quad (6.5b)$$

with rate constants k_1 and k_{-1}, respectively. These notations have been utilized in previous studies[27] and will be used here for consistency.

Knyazev and Slagle[27] studied the dissociation of the vinyl radical and calculated a Rice–Ramsperger–Kassel–Marcus (RRKM) rate, which included tunneling and weak intermolecular potentials. The RRKM rates calculated were able to describe most of the previously determined experimental rates. They determined the high-pressure-limit rate constant for the association reaction, $k_1^{\infty}(H + C_2H_2 \rightarrow C_2H_3) = 6.04 \times 10^{-14}\ T^{1.09} \exp(-1328\ K/T)\ cm^3\ molecule^{-1}\ s^{-1}$ and for the dissociation reaction, $k_{-1}^{\infty}(C_2H_3 \rightarrow C_2H_2 + H) = 3.86 \times 10^{8}\ T^{1.62} \exp(-18650\ K/T)\ s^{-1}$ in the temperature and pressure range of 879 – 1058 K and 2 – 16 Torr, respectively.

In the work by Michael *et al.*,[28] a deuterium atom was used to study the exchange reaction proceeding through the vinyl radical intermediate, $D + C_2H_2 \rightarrow [HCCHD]^{\ddagger} \rightarrow HCCD + H$. Both hydrogen atom production and deuterium atom depletion were detected via shock tube atomic resonance absorption spectrometry. An Arrhenius expression was found for the rate constant for the H (or D) atom depletion, $k = (2.77 \pm 0.45) \times 10^{-10} \exp(-$

3051 ± 210 K/T) cm^3 $molecule^{-1}$ s^{-1}, which was the same for H and D atoms over the experimental temperatures and pressures, 1100 – 1630 K and 6 – 16 Torr, respectively.

The complexity and importance of these thermal reactions has led to a great deal of theoretical work on the interaction of H + C_2H_2 or the reverse dissociation reaction of C_2H_3. A lot of theoretical work has also focused on the reaction of H_2 and C_2H, which exist on the same potential energy surface.[27,29-34] The majority of the theoretical work focuses on the modeling of kinetic results near or below 1000 K. Knyazev and Slagle[27] determined the transition state barriers for both the dissociation and recombination reactions to be 37.9 kcal/mol and 4.04 kcal/mol, respectively; Miller and Klippenstein[32] have determined the values 39.0 and 4.3 kcal/mol; and Peeters *et al.*[30] 39.7 and 4.54 kcal/mol.

The results discussed thus far only deal with reaction rates near the vinyl dissociation barrier. A high energy study came from Knyazev and Slagle using the 193 nm photolysis of vinyl bromide and methyl vinyl ketone for generating the vinyl radical with up to 69 and 46 kcal/mol of available energy, respectively.[35,36] These energies correspond to approximately 34 and 11 kcal/mol above the dissociation energies, according to Knyazev and Slagle. It appears, however, that the effect of these energies are not considered in the reaction rates. The photolysis reaction is expected to produce vibrationally excited products, but they are allowed to cool to the thermal energies, 700 – 1058 K, of the reactor. The loss of vinyl radicals following photolysis is not discussed, even though it appears significant. Nonetheless, the rates determined in this study and previously were significantly below the energy available from direct dissociation via UV photolysis or collisions with hot hydrogen atoms, $\langle E_t \rangle$ ~ 50 kcal/mol and therefore not

directly comparable to the rates determined here. In all the previous studies involving Reactions 6.5a and 6.5b, the reaction rates determined were at thermal or near thermal energies of 300 – 1600 K. Even when highly vibrationally excited vinyl was formed, as in the work by Knyazev and Slagle, they were allowed to cool to the reactor temperature before rates were determined.

In this chapter, H atoms are produced, through 193 nm photolysis of H_2S and HBr, with $\langle E_t \rangle$ ~ 50 - 60 kcal/mol above the vinyl dissociation barrier. Both H_2S and HBr undergo a direct dissociation to form a kinetically hot H atom and a corresponding fragment. The kinetically hot H atoms may then collide with ambient acetylene molecules and the products observed through IR emission. Utilizing IR emission as a probe of the system affords the opportunity to observe all emission products with vibrational excitation generated from Reactions 6.1, 6.2, 6.3, and 6.4. Both energy transfer through a collision and chemical reactions are observed. This approach opens up a new energy range of kinetic study on the H + C_2H_2 reaction. To further understand the exact mechanisms of the H + C_2H_2 reaction, isotopic substitution is utilized to label the reaction channels. The isotopic substitution mechanism will be discussed in the next chapter.

6.1.3 The reaction of C_2D_2 + H

Isotopic substitution of the reactant molecules affords the opportunity to examine the mechanism of the reaction in which the substituted atom(s) is involved. For this particular reaction, the primary interest is whether the collision between hot hydrogen atoms and cold acetylene molecules results in a chemical reaction with or without intermediate species and if so, what is the nature of the intermediate.

Using the completely deuterated form of acetylene, C_2D_2, in the reaction with hot H atoms from H_2S and HBr, generates a unique set of product channels that allow for an accurate determination of the reaction mechanism following the high energy collision. There are several possible reactions which could generate vibrationally hot acetylene from the collision,

$$C_2D_2 + H\ (hot) \rightarrow H\ (cold) + C_2D_2^* \quad (6.6)$$

$$C_2D_2 + H\ (hot) \rightarrow [C_2D_2H]^{\ddagger} \rightarrow HCCD^* + D\ (cold) \quad (6.7)$$

$$C_2D_2 + H\ (hot) \rightarrow [C_2D_2H]^{\ddagger} \rightarrow DCCD^* + H\ (cold) \quad (6.8)$$

As described in the previous section, Reaction 6.6 involves an energy transfer collision between the hot H atom and cold deuterated acetylene molecule, while Reactions 6.7 and 6.8 involve a vinyl radical intermediate dissociating into vibrationally hot acetylene. Reactions 6.7 and 6.8 would participate similarly generating approximately 2/3 C_2HD and 1/3 C_2D_2 molecules based on an equal probability of breaking a C-H and C-D bond. This is clearly a dramatic assumption, however for the time being, will aid in determining the overall mechanism. The actual statistical rates of Reaction 6.7 and 6.8 are based on the calculated reactant and TS structures, which are similar in structure, but contain significant differences in vibrational frequencies. Utilizing the calculated structures and frequencies produces small differences in the dissociation rates for the different isotopomers. The RRKM rates, in light of these slightly different TS structures will be discussed in the following sections.

There is one other possible set of reaction paths exist due to the 193 nm absorption of acetylene forming the ethynyl, C_2H or C_2D radical. In the case of

deuterated acetylene, the C_2D radical is formed and can react with HX, the H atom precursor molecule, as follows,

$$C_2D + HX \rightarrow [DCCHX]^{\ddagger} \rightarrow C_2HD^* + X \quad (6.9)$$

$$C_2D + HX \rightarrow [DCCHX]^{\ddagger} \rightarrow [:CCHX]^* + D \rightarrow HCCX^* + D \quad (6.10)$$

$$C_2D + HX \rightarrow [DCCHX]^{\ddagger} \rightarrow DCCX^* + H \quad (6.11)$$

where X may be an atom or radical. In this case, the deuterated ethynyl radical abstracts a proton or X radical via the intermediate [DCCHX] and dissociates into an acetylene species, HCCD, HCCX, or DCCX and an X, D, or H radical, respectively. Each of the reactions produces a distinct product emission spectra, both in terms of molecular/radical species and internal energy content. In general, the C-X bond is significantly weaker than the C-H bond therefore Reactions 6.10 and 6.11 should not (and do not, as described in the following sections) show a significant yield.

In this Chapter, the generation of hydrogen atoms is accomplished by the UV photolysis of two precursor molecules. Collisions between kinetically hot hydrogen atoms generated from the photolysis pulse and cold acetylene molecules produce a large quantity of highly vibrationally excited acetylene. A two step reaction mechanism is postulated; the first step being the bimolecular collision forming a high energy vinyl radical intermediate followed by the unimolecular dissociation of the vinyl intermediate into vibrationally hot acetylene and cold hydrogen atoms (relative to the initially prepared atoms). Conservation of energy and momentum through a combined statistical energy and sudden impulsive model analysis of the unimolecular dissociation reaction produce vibrational energies in good agreement with experimental results. In addition, isotopic substitution of acetylene afford the opportunity to study the reactions, C_2D_2 + H and C_2D

+ HX, Reactions 6.7, 6.8 and 6.9, respectively. Reactions 6.7 and 6.8 form a mixture of mono and completely deuterated acetylene, while Reaction 6.9 only produces monodeuterated acetylene. By studying the reaction product emission features, the accurate and definitive assignment of the proper reaction channel and mechanism forming vibrationally excited acetylene is discovered.

6.2 Experimental

The nanosecond time-resolved FTIR emission spectroscopic technique has been discussed in Chapter 1 and only the relevant details of experiments on the reaction of acetylene and H are discussed. The sources for the gases are C_2H_2 (Airgas, AA acetylene, dissolved, 99.6%), C_2D_2 (Cambridge Isotopes, 98%), HBr (Sigma-Aldrich, ResearchPlus, >99%), and H_2S (Matheson, 99.5%). The acetylene gas was flowed through cold trap immersed in a dry ice/acetone slush bath to remove any acetone stabilizer. Absorption spectra measured for acetylene after the cold trap revealed only trace amounts (< 1%) of acetone following trapping. Argon gas (Airgas, ResearchPlus, 99.9999%) was used as a buffer gas (2-4 Torr) to collisionally deactivate the vibrationally excited molecules and to prevent product deposition on the chamber windows and mirrors. The gases were mixed in situ prior to entering the chamber through a showerhead nozzle. Excess Ar (up to the total pressure desired, typically 2-4 Torr) was flowed close to the UV windows to limit deposition. A typical experiment utilized 50 mTorr of acetylene and 100 mTorr of either HBr or H_2S, with 2 Torr of Ar.

6.3 Time-resolved IR emission results

The 193 nm photolysis of acetylene and HBr (or H_2S), in a bath of Ar gas can produce significant amounts of vibrationally excited products, either through direct dissociation of acetylene (forming C_2H) or through collisions. In this Section, the photolysis of the individual reactants will first be discussed, followed by the observed emission from the reactant mixtures. Two H atom precursors, HBr and H_2S, were utilized to verify that the IR emission results originate from reactions between H atoms and acetylene.

6.3.1 C_2H_2 + HBr

The dissociations of C_2H_2 and HBr respectively at 193 nm have been well studied. The dissociation of acetylene proceeds primarily through the C_2H + H channel, with a bond dissociation energy D_0(HCC-H) ~131 kcal/mol.[37] The absorption of the 193 nm photon excites acetylene to the ν_3=10 (CH bending mode) of the ^1A_u electronic excited state, with an absorption cross section of 1.34 x 10^{-19} cm^2 $molecule^{-1}$.[38] There has been controversy as to what is the primary reaction channel following the photo-excitation. It was initially determined that the production of C_2H + H has a quantum yield, Φ ~ 0.85.[39] A few later studies, however, revealed a much lower Φ ~ 0.3 for this channel.[38,40] The major channel was proposed to be, instead, the production of a metastable molecule, $C_2H_2^{**}$, proposed to be $^3B_2$ vinylidene.[40,41] Subsequent IR emission[42] and pump-probe spectroscopy[43] works on the 193 nm dissociation of acetylene have determined the C_2H + H channel to be the dominant channel, in line with the earlier work (and some work done at longer wavelengths).[44]

HBr has been used as a source through its photolysis for generating translationally hot hydrogen atoms.[10,11,14,45-47] The absorption cross section of HBr at 193 nm is 8.3 x 10^{-19} cm^2 $molecule^{-1}$.[48] The available translational energy of the H atom depends on the electronic state of the accompanying bromine atom, $^2P_{3/2}$ and $^2P_{1/2}$, ranging from 51 – 62 kcal/mol. An average translational energy was found by utilizing the branching ratio, 0.15:0.85 for $^2P_{3/2}$:$^2P_{1/2}$, determined by Lambert *et al.*, to be 61 kcal/mol.[14,45]

IR emission results of C_2H_2 and HBr in Ar are shown in Figure 6.1. Several time slices are shown following photolysis. The pressures of C_2H_2, HBr, and Ar are 50 mTorr, 50 mTorr, and 2 Torr, respectively. The experiment shown here had the optimal pressures to produce a large S/N, but low enough pressure to keep the collisional cooling of the products low enough to observe IR emission for several μs. At high acetylene pressures, the appearance of C_2H is indicated as vibrational and electronic emission from 3700 – 3900 cm^{-1}. To reduce the amount of C_2H formed and to simplify the emission spectrum and limit secondary reactions, the acetylene pressures were kept equal to or less than the HBr pressures. Since the absorption cross section of HBr is 6 times larger than that of C_2H_2, and the quantum yield of H + Br/Br* is larger than that of C_2H + H, a larger amount of H atoms will be present in the chamber following photolysis, when compared with C_2H. In addition, because the generation of excess H atoms was sought, the HBr pressure was kept higher than C_2H_2.

Several emission bands are observed in Figure 6.1. The most prominent bands at 1250 and 3000-3300 cm^{-1} are assigned to emission from the $\nu_4 + \nu_5$ and ν_3 progressions of acetylene. The ν_5 cis-bend of acetylene is observed as a low intensity band near 750

Figure 6.1. IR emission following the 193 nm photolysis of 50 mTorr C_2H_2 and 50 mTorr HBr in 2 Torr Ar. Seven time slices are shown from 250 ns to 3250 ns in 500 ns increments.

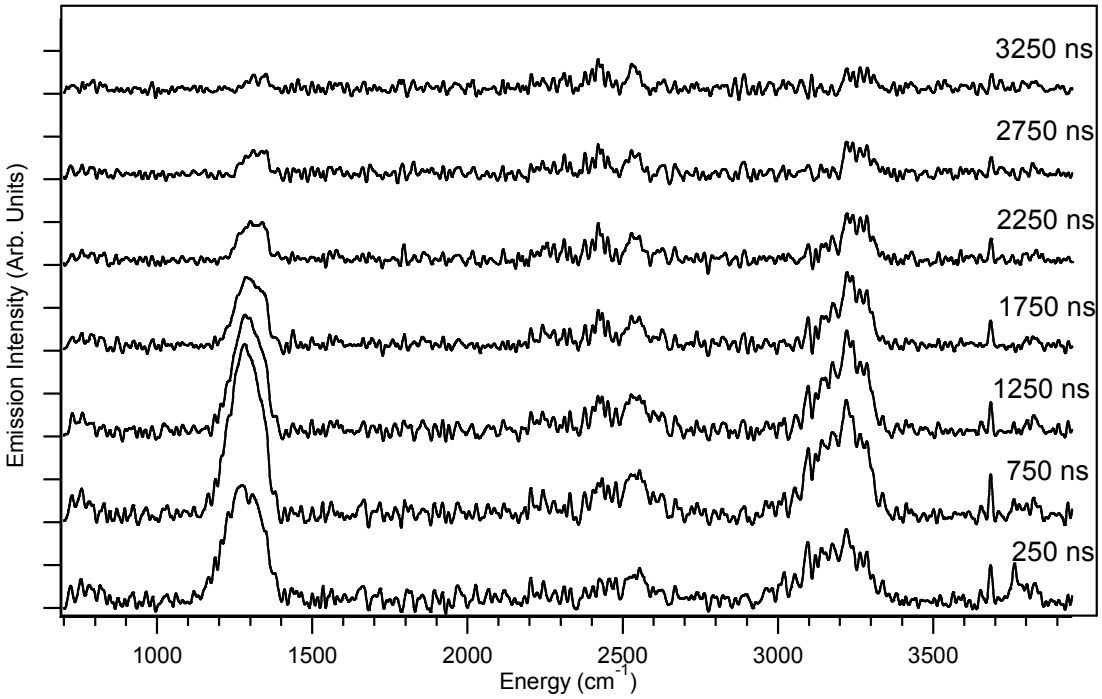

cm^{-1}. The emission is difficult to detect due to the detector cut-off which occurs between 700 and 750 cm^{-1}. Some HBr emission is observed near 2500 cm^{-1}. This emission arises from vibrationally excited HBr generated from energy transfer collisions between HBr and hot atoms or other excited molecules. Only low vibrational excitation of HBr is observed. Emission from vibrationally and electronically excited C_2H is observed in the high frequency region between 3700 and 4000 cm^{-1}. The assignment of these bands has been previously performed by Fletcher and Leone.[42] Emission observed from C_2H is identical to that observed in the photolysis of pure acetylene case and previous work on the 193 nm photolysis of C_2H_2.[42] Electronically excited bromine atoms are observed as a sharp electronic transition located near 3685 cm^{-1}.[49]

6.3.2 $C_2H_2 + H_2S$

H_2S has been used extensively as a source of hot H atoms generated via 193 nm photolysis, with an average translational energy of 53 kcal/mol.[10] The dissociation energy D_0(HS-H) has been determined to be 89.9 kcal/mol.[50] The absorption cross section of H_2S at 193 nm is 2.3 x 10^{-18} cm^2 $molecule^{-1}$. The photodissociation of H_2S at 193 nm results in the majority of HS radicals are formed vibrationally cold, i.e. primarily $\upsilon = 0$, with only a very small amount of vibrationally excited ($\upsilon > 0$) HS formed.[50-53]

Our results on the 193 nm photolysis of pure H_2S or H_2S + noble gas show no IR emission from HS (at fundamental at υ = 2711 cm^{-1}), in line with previous studies concluding HS is predominantly formed vibrationally cold.

IR emission spectra following the photolysis of 50 mTorr C_2H_2 and 100 mTorr H_2S in 2 Torr Ar are shown in Figure 6.2. Several time slices are shown. Here, pressures were also optimized for preservation of S/N while allowing sufficient collisional

Figure 6.2. IR emission following the 193 nm photolysis of C_2H_2 and H_2S in Ar. Ten time slices are shown from 200 ns to 3800 ns in 400 ns increments. The experimental IR emission is shown in black, the IR emission fitting results are shown overlaid in blue open circles for each of the time slices.

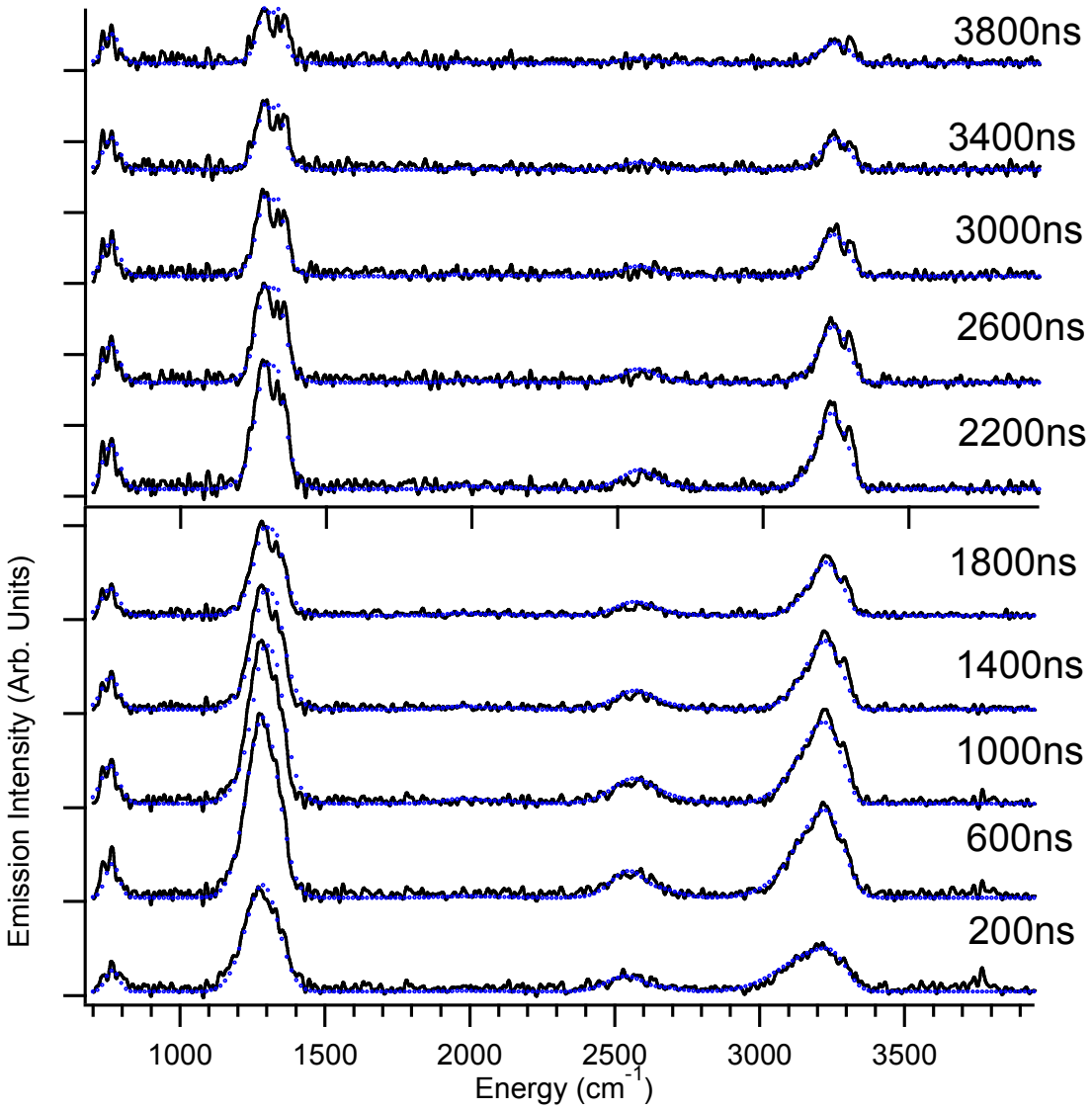

deactivation following photolysis. In order to maximize the amount of vibrationally hot acetylene, an excess of hot H atoms is desired, compared to cold acetylene molecules. Therefore, as in the case of HBr, the H_2S pressure was kept higher than the acetylene pressure. This also has the added benefit of minimizing C_2H reactions, which is formed via the photolysis of acetylene. Limiting C_2H emission and reaction is further aided by the fact that the absorption cross section of H_2S is ~17 times larger than that of C_2H_2 and that the quantum yield of H atoms from H_2S is larger than that of C_2H from C_2H_2.

The main features of the emission spectra in Figure 6.2 are the four main features, all assigned to acetylene. The features at 750, 1250, and 3000-3300 cm^{-1}, corresponding to the ν_5, $\nu_4 + \nu_5$, and ν_3 modes, are analogous to emission band progressions in Figure 6.1. Some emission from electronic transitions of C_2H are observed around 3700 cm^{-1}, as in the case of pure C_2H_2.

The broad feature seen at 2550 cm^{-1}, which shifts toward longer frequencies with time, is not assignable to modes of HS, H_2S, or any potential secondary reaction products diacetylene or HCCSH. The feature does, however, agree quite well with some low strength combination and overtone bands of acetylene. The $\nu_2 + \nu_5$ band is found at 2703 cm^{-1} in absorption measurements and is approximately 1% as intense as the ν_5 band. The discrepancy in emission frequency (2550 cm^{-1}) vs. fundamental frequency (2703 cm^{-1}) at early times is due to anharmonic effects shifting the emission frequencies to the red. The rotationally resolved IR absorption from this band is shown in Figure 4.2 in Chapter 4. It should be mentioned that this mode is not directly observed in the C_2H_2 + HBr experiment, because it is in overlap with the stronger HBr bands. HBr receives some T-V (or V-V) energy transfer from collisions with other molecules populating low

vibrational states. The HBr emission from low vibrational levels is still quite strong and masks the modes observed from experiments with H_2S.

The main observation from the two systems, C_2H_2 + HBr and C_2H_2 + H_2S, is the dominance of emission from vibrationally excited C_2H_2. No emission from vinyl is observed. In addition, only a small amount of vibrationally and electronically excited emission from C_2H is observed in both systems produced via the direct photolysis of acetylene. In the following sections, the energetics of and mechanisms which produce the vibrationally excited acetylene will be discussed.

6.3.3 C_2D_2 + H_2S

Several time resolved IR emission spectra following the 193 nm photolysis of 50 mTorr C_2D_2, 50 mTorr H_2S, and 2 Torr Ar are shown in Figure 6.3. Seven time slices, 1, 2, 3, 5, 10, 15, and 20 μs following photolysis are shown. The first observation is the relative complexity of the IR emission spectra compared to the non-deuterated case shown and described in the previous sections. This is an indication that there are multiple reaction products that are formed vibrationally hot. The features may be broken down into "early" time (1 – 5 μs) features and "late" time (5 – 20 μs) features to help clarify their contributions.

The "early" time features generally grow in quickly and are convoluted by the detector/amplifier rise time. These features decay quickly, with lifetimes ~2-5 μs. Peaks are observed at 1000, 1300, 2300, 2400, 3250, and 3750 cm^{-1}. All of these features correspond to emission from mono or completely deuterated acetylene based on their

Figure 6.3. Time resolved IR emission following the 193 nm photolysis of 50 mTorr C_2D_2 and 50 mTorr H_2S in 2 Torr Ar. Seven time slices are show corresponding to 1, 2, 3, 5, 10, 15, and 20 μs following photolysis.

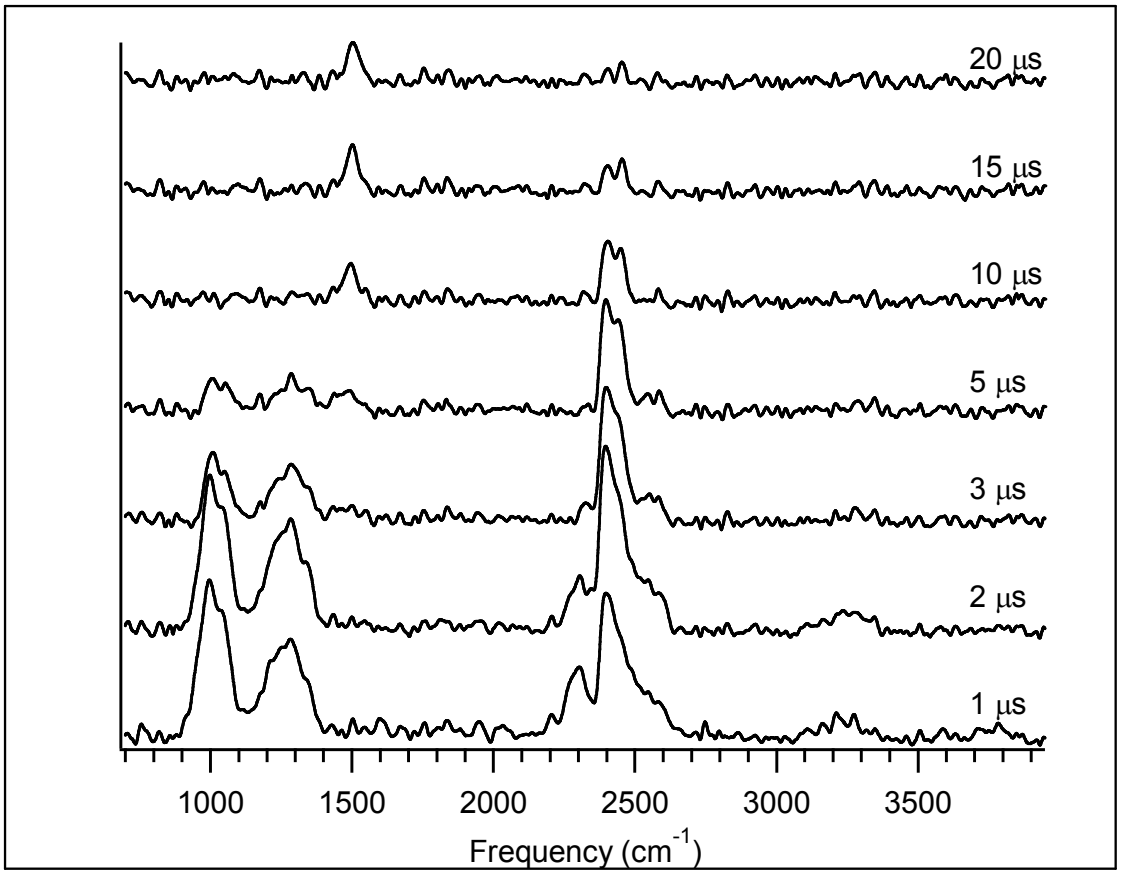

later time frequencies compared to IR absorption frequencies of C_2HD and C_2D_2. The vibrational emission modeling of those peaks will be discussed in the next section.

The quickly decaying peak at 1000 cm^{-1}, which shifts to 1050 cm^{-1} after ~5 μs, corresponds to emission from the $\nu_4 + \nu_5$ mode of vibrationally excited C_2D_2. Some rotational resolution of the P and R branches of this mode are observed in the 5 μs time slice. The intensity and width of this peak suggest vibrational excitation. Rotationally resolved IR emission from the ν_3 mode of C_2D_2 is observed near 2400 cm^{-1}, with very little shift in frequency. This feature decays slightly slower than the assigned $\nu_4 + \nu_5$ mode. The weak feature to the red of the fundamental ν_3 mode emission, near 2300 cm^{-1}, is assigned as ν_3 mode emission from highly excited C_2D_2. The feature shows a very similar decay rate to that of the combination band of C_2D_2. In addition, there are no other reasonable assignments that can be made based on the available products from the reactions above.

The intense and broad feature near 1300 cm^{-1} is assigned to the $\nu_4 + \nu_5$ and $2\nu_5$ modes of C_2HD. The feature remains broad and rotationally irresolvable even at late times when features of C_2D_2 are rotationally resolved. The feature decays with a time constant similar to that of the $\nu_4 + \nu_5$ of C_2D_2. There is a broad shoulder to the blue of the ν_3 mode of C_2D_2. This feature cannot be assigned to rotationally hot ν_3 emission from C_2D_2, as the feature lies 100-150 cm^{-1} to the blue of the fundamental mode. In addition, there is a clear rotational structure seen observed between 3 and 5 μs, which correspond well with the ν_3 mode of C_2HD. Based on the observation of the $\nu_4 + \nu_5$ and $2\nu_5$ modes, formed with significant vibrational energies, the ν_3 mode should display a strong anharmonic shift in frequency corresponding to the large vibrational energy. There is

some overlap of the anharmonically shifted ν_3 mode of C_2HD, with the fundamental ν_3 mode of C_2D_2. In addition, the feature at 3250 cm^{-1}, which shifts to 3300 cm^{-1} as the population is collisionally cooled, corresponds to the ν_1 mode of C_2HD. The feature shows a similar decay rate to the other C_2HD features. The feature cannot be rotationally resolved even at later times. Nonetheless, the emission features assigned to C_2HD and C_2D_2 indicate a significant amount of nascent vibrational excitation.

There are two "late" time features, near 1500 and 2450 cm^{-1}. The feature at 1500 cm^{-1} shows a slow growth rate, is slightly red shifted at early times, and survives past the last collected time slices > 20 μs. No definitive assignment of this feature can be made based on the emission frequency as no reaction products emit in this range. The temporal signature of this feature suggests that it arises from a secondary reaction product. One interesting hypothesis is that this feature corresponds to emission from one or more of the deuterated 1,3-butadiene molecules, which has been observed in the production of the vinyl radical at high precursor pressures, in the non-deuterated case.[54] Emission from the ν_{20} C=C stretch mode of 1,3-butadiene is a strong indicator of the formation of the butadiene molecule via a secondary reaction. The ν_{20} mode of the non-deuterated 1,3-butadiene molecule is observed at 1596 cm^{-1}. For the singly deuterated 1,3-butadiene-d_1 molecule, the mode shifts to 1580 cm^{-1}; for the triply deuterated molecule, 1,3-butadiene-d_3, the mode shifts to 1549 cm^{-1}; for 1,3-butadiene-d_4, the mode shifts to 1535 cm^{-1}; and for the completely deuterated 1,3-butadiene-d_6, the mode shifts to 1520 cm^{-1}. It is clear from this progression that there may be some different isotopes of 1,3-butadiene generated with vibrational excitation. The width of this feature, ~100 cm^{-1}, preclude the accurate determination of exact compostion of 1,3-butadiene isotopomers.

The feature at 2450 cm^{-1}, assigned as the ν_3 mode of C_2D_2, grows in quickly, but does not decay until much later time. This would indicate that there are multiple emitters in overlap in this range or multiple processes producing the same molecule in different amounts of internal energies. In addition, due to the significant overlap in vibrational emission bands in this region, there is a strong possibility of resonant or near resonant V-V energy transfer. The efficient resonant V-V energy transfer would dump energy into the most stable transitions, namely the ν_3 bands of C_2D_2 and C_2HD.

The main result from the isotopically substituted reactions is the generation of highly vibrationally excited C_2D_2 and C_2DH. In addition, there appears to be a significant amount of emission from lowly vibrationally excited C_2D_2. As in the case of the non-deuterated experiment, no vinyl is observed. In the next sections the vibrational energy of acetylene produced via collisions and reactions will be discussed as well as the mechanisms describing those collisions and reactions.

6.4 Quantitative analysis of IR emission spectra

6.4.1 C_2H_2 IR emission

Modeling of the IR emission from several molecules,[55-57] including acetylene[58,59] has been described in Chapters 2 and 4. Modeling of the acetylene features proceeds according to the previously prescribed outline with some adjustments. Particularly, in the case of C_2H_2 + HBr, only the ν_5, $\nu_4 + \nu_5$ and ν_3 modes are modeled, as was performed in Chapter 4. In the case of C_2H_2 + H_2S, the $\nu_2 + \nu_5$ band is also modeled. These additional features will be discussed shortly.

The IR emission fitting results are shown in Figure 6.2. Experimental IR emission results following the 193 nm photolysis of 50 mTorr C_2H_2 and 100 mTorr H_2S in 2 Torr Ar is shown in black. The IR emission fitting results are shown overlaid in blue. The $\nu_4 + \nu_5$ band is the most intense band observed in emission experiments, even though it has lower 'fundamental' transition strength than those of the ν_3 and ν_5 modes. In addition the $\nu_2 + \nu_5$ band now becomes apparent even though it is an extremely weak band in absorption spectra measurements.

The emission spectrum of each individual zeroth-order vibrational level within an energy range are all integrated and normalized into an energy-bin emission spectrum. The energy-bin spectra are then used as the basis set for fitting the observed emission for the determination of the population distribution in energy. Typically, transitions which originate from levels within 1000 cm^{-1} "bins" are used, which gives an 1000 cm^{-1} resolution in the population distribution determined from spectral fitting. Smaller bin sizes such as 500 cm^{-1} have been used for test and it was found that the bin size did not affect the overall fit.

The energy distribution of the emitting population is determined through a nonlinear least squares fitting procedure. The distribution used is represented by two Gaussian functions: one centered at zero average vibrational energy and the other a higher energy. The low energy distribution represents the combination of ambient and lower excited molecules. The higher energy distribution tracks the population of the highly vibrationally excited acetylene molecules generated from collision excitation. The fitted vibrational energy distributions for several time slices are shown in Figure 6.4.

Figure 6.4. The vibrational energy distributions for the reaction of C_2H_2 + H_2S in Ar. Several distributions from 200 ns to 5800 ns in 400 ns increments are shown. The bimodal vibrational energy distribution is discussed in the text.

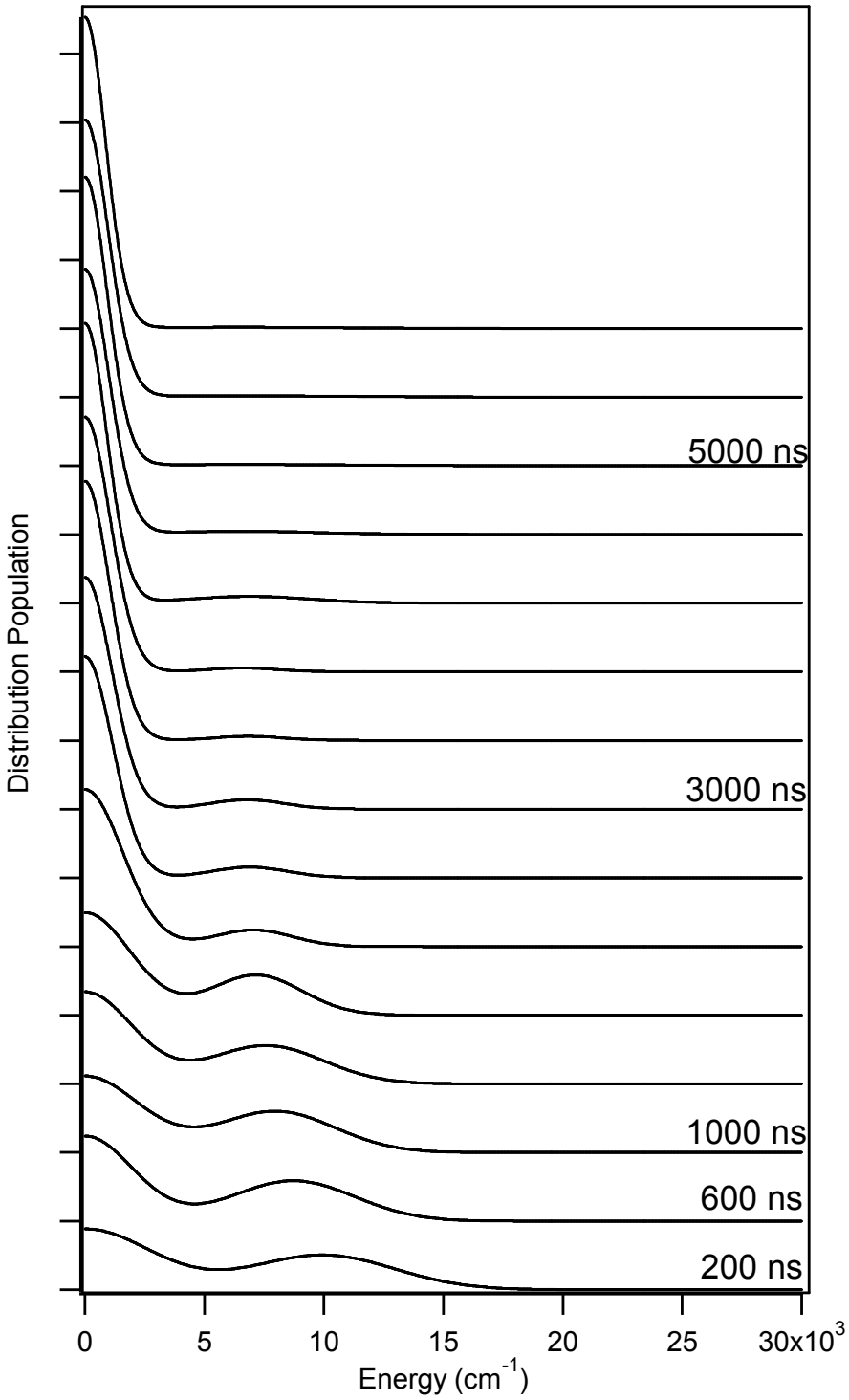

The low energy distribution is primarily from the large amount of acetylene present in the chamber during the collisional deactivation. Since we are forming vibrationally excited acetylene, in the presence of vibrationally cold acetylene, resonant or near resonant V-V energy transfer collision between the species is likely.[61,62] The resonant or near resonant collisions are highly efficient at removing vibrational energy from high vibrational states and populating low vibrational states in the cold molecules. The high $\langle E \rangle$ distribution tracks the vibrational population following the reaction pathway of interest. The high energy average vibrational energy, $\langle E \rangle$ vs. time is shown in Figure 6.5.

The average vibrational energy, $\langle E \rangle$, for the high energy distribution is shown for the photolysis of C_2H_2 + H_2S in Ar in Figure 6.5. The average vibrational energy at each time period are shown as blue circles and the solid blue line represents a single exponential fit.

The average initial vibrational energy of acetylene, $\langle E \rangle_0 = 11\ 019 \pm 195$ cm^{-1} has been determined following the photolysis of C_2H_2 + H_2S in Ar. This initial vibrational energy corresponds to the energy transferred from the kinetically hot hydrogen atom to the vibrationally cold acetylene molecule. Based on initial precursor pressures of 100 mTorr H_2S and 100 mTorr C_2H_2, $\sigma_{H2S} = 2.3 \times 10^{-18}$ cm^2 molecule^{-1}, and E_t ~ 50 kcal/mol, the collisional rate of H + C_2H_2 is on the order of 10^8 s^{-1}. A more detailed description of the collisional energy transfer rate will be given in later sections, but this gives an indication that several collisions will occur prior to the first measurement. The initial vibrational energy of acetylene represents the energy transferred through these first collisions between hot H atoms and cold acetylene.

Figure 6.5. The average vibrational energy, $\langle E \rangle$, for the high energy distribution as a function of time for the reaction of C_2H_2 + H_2S in Ar. The open blue circles represent the $\langle E \rangle$ values from fitting all of the vibrational modes seen in the absorption spectra as described in the text. The solid line is the fitting result discussed in the text.

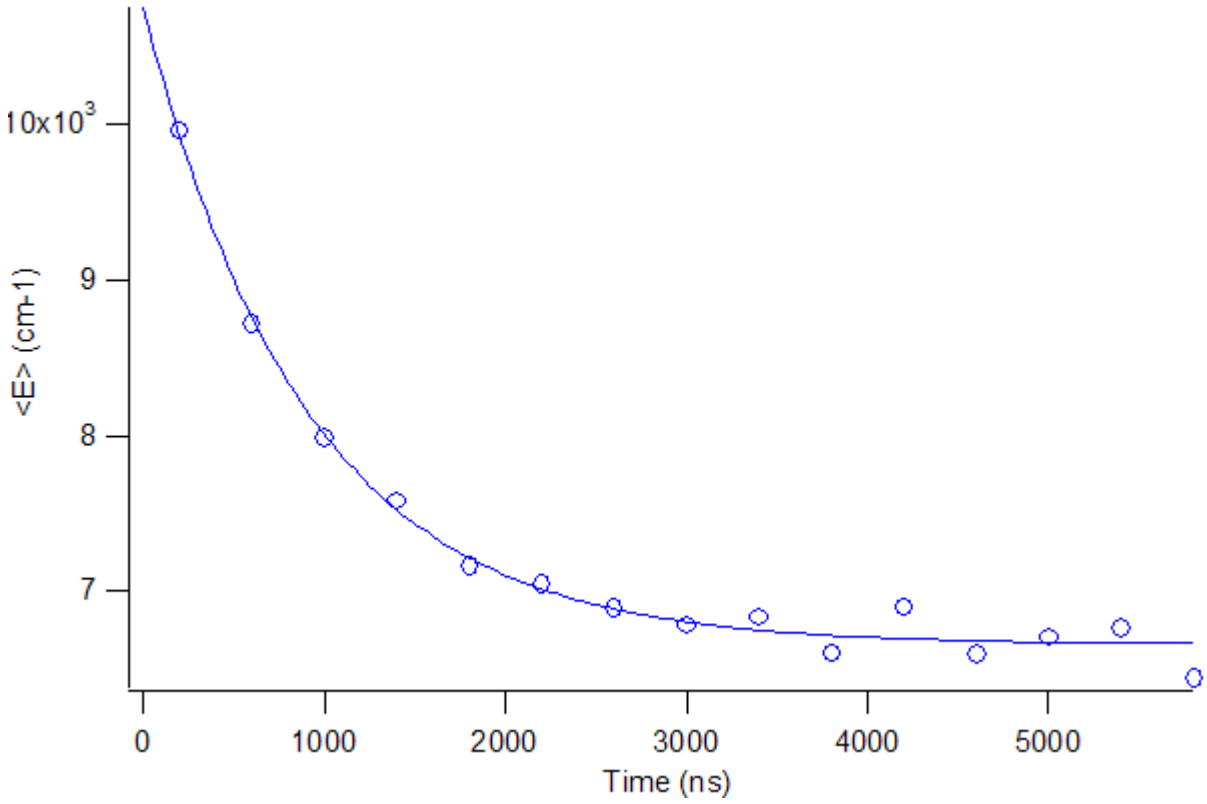

Analogous results have been obtained from the photolysis of C_2H_2 + HBr in Ar. An $\langle E \rangle_0 = 15\ 564 \pm 744$ cm^{-1} has been determined for this reaction. The single exponential decay constants for H_2S and HBr reactions are 1.11 ± 0.07 x 10^6 and 2.2 ± 0.3 x 10^6 s^{-1}, respectively. These are much faster than relaxation results seen in previous experiments due to efficient vibrational energy transfer to cold acetylene molecules as described previously.

6.4.2 IR absorption spectra of C_2D_2 and C_2DH

In order to model the IR emission from C_2D_2 and C_2DH, the strong IR active modes must first be determined from IR absorption. The two different isotopomers differ significantly due to the breaking of inversion symmetry in the monodeuterated species. The absorption spectra of C_2D_2 and C_2DH (CDN Isotopes, >98% purity) are shown in Figure 6.6. Deuterated acetylene pressure was 10 Torr in 100 Torr N_2. The spectra shown was taken in at a resolution of 8 cm^{-1}. The absorption spectrum of C_2DH was extracted from the absorption spectra of C_2D_2 as monodeuterated acetylene was not available. Monodeuterated acetylene intensities were determined using literature values relative to completely deuterated acetylene.[63,64]

There was some contaminant due to acetone in the sample, however this was removed by repeat vacuum distillation. Completely deuterated acetylene is shown in red, while monodeuterated acetylene is shown in black. The absorption of both species have been scaled according to the ν_3 CD stretching mode of each species.[63] The relative absorption frequencies for the IR active bands and their intensities are listed in Table 6.1 based on literature assignments.[65]

Figure 6.6. The IR absorption of C_2D_2 and C_2DH between 700 and 4000 cm^{-1}. Monodeuterated acetylene is shown in black. Completely deuterated acetylene is shown in red. Peaks are discussed in the text and in Table 6.1.

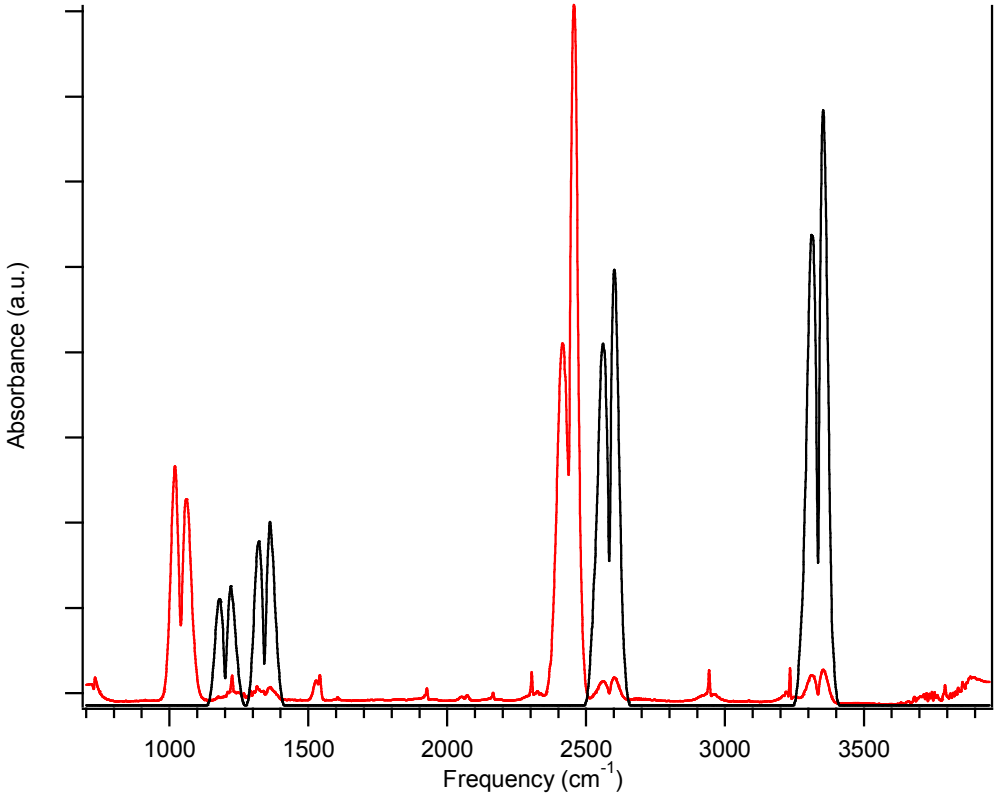

Table 6.1. The IR active modes for the three isotopomers of acetylene, C_2H_2, C_2HD, and C_2D_2. Frequencies are listed in cm^{-1} with intensities in parenthesis. Symmetry labels are shown for each mode. The first label corresponds to the HCCH and DCCD isotopomers, while the second label corresponds to the HCCD isotopomer.

Mode	Isotopomer		
	HCCH	HCCD	DCCD
ν_1 (σ_g^+ / σ^+)	-	3335 (30.1)	-
ν_2 (σ_g^+ / σ^+)	-	1854 (1.0)	-
ν_3 (σ_u^+ / σ^+)	3289 (70.4)	2584 (21.7)	2439 (21.7)
ν_4 (Π_g / π)	-	518 (20.0)	-
ν_5 (Π_u / π)	730 (177)	678 (94.3)	537 (114.8)
$\nu_4 + \nu_5$ (Σ_u^+ / Σ^+)	1328 (22.9)	1202 (6.2)	1042 (12.3)
$2\nu_5$ ($- / \Sigma^+$)	-	1342 (9.5)	-

There are only two IR active bands of C_2D_2, the ν_3 CD stretch at 2439 cm^{-1} and the $\nu_4 + \nu_5$ combination bend at 1042 cm^{-1}. The ν_5 cis bend at 537 cm^{-1} is below the low frequency cut off of the detector. There are several weaker bands in the IR region corresponding to the $\nu_2 - \nu_5$ band at 1225 cm^{-1}, the $\nu_3 - \nu_4$ band at 1927 cm^{-1}, the $\nu_1 - \nu_5$ band at 2165 cm^{-1}, the $\nu_2 + \nu_5$ band at 2304 cm^{-1}, the $\nu_3 + \nu_4$ band at 2943 cm^{-1}, and the $\nu_1 + \nu_5$ band at 3234 cm^{-1}. In addition, there is some C_2HD contamination in the C_2D_2 sample generating absorption features of the strongest bands in the C_2HD IR spectra described in the next paragraph.

The IR spectrum of C_2HD contains 5 IR active fundamental modes as well as two combination bands. The fundamental modes are the ν_1 CH stretch at 3335 cm^{-1}, the ν_2 CC stretch at 1854 cm^{-1}, the ν_3 CD stretch at 2584 cm^{-1}, the ν_4 trans bend at 518 cm^{-1}, and the ν_5 cis bend at 678 cm^{-1}, with the final two modes out of detection range. Two combination bands of C_2HD exist, the $\nu_4 + \nu_5$ at 1202 cm^{-1} and the $2\nu_5$ bend at 1342 cm^{-1}.

6.4.3 C_2D_2 + H IR emission modeling

Emission modeling calculations based on the general IR emission modeling calculation described in Chapter 2 were carried out. The three IR active modes of C_2D_2 were modeled: the ν_5 cis bend, the $\nu_4 + \nu_5$ combination bend, and the ν_3 CD stretch. Seven IR active modes of C_2DH were modeled: the ν_1 CH stretch, the ν_2 CC stretch, the ν_3 CD stretch, the ν_4 trans bend, the ν_5 cis bend, the $\nu_4 + \nu_5$ combination bend, and the $2\nu_5$ overtone bend. All harmonic and anharmonic constants used were from the literature.[66] The generation of accurate modeling spectra was performed according to

procedures in Chapters 2 and 4. In addition, fitting two emitters simultaneously affords the opportunity to find the relative concentrations of both species according to,

$$S(\nu) = a(S_{DCCD}(\nu)) + (1-a)(S_{HCCD}(\nu)) \quad (6.12)$$

where $S(\nu)$, $S_{DCCD}(\nu)$, and $S_{HCCD}(\nu)$ are the calculated IR emission spectra for the total signal, signal from C_2D_2, and signal from C_2DH, respectively, and a is the fraction of C_2D_2 in the final emission spectra.

The increase in the number of fitting parameters due to the modeling of both C_2D_2 and C_2DH simultaneously caused some problems which will be discussed in the next sections. Several early time slices along with the IR fitting results are shown in Figure 6.7. Five IR emission time slices are shown in black with the fitting of four time slices overlaid in blue. Initial inspection of Figure 6.7 reveals some positive, as well as inadequate fitting results.

The two low frequency features at 1000 and 1300 cm^{-1}, as well as the high frequency CH stretching feature at 3250 cm^{-1} are adequately represented by the fitting result. This result initially confirms the existence of highly vibrationally excited C_2D_2 and C_2DH, of which both species emit in these three features. The main problem in the fitting is centered around the ν_3 CD stretch of C_2D_2 at 2439 cm^{-1}. The intense ν_3 fundamental emission is underestimated in the modeling, while the emission from the other modes is accurately fit. Due to the significant overlap of features between 2200 and 2700 cm^{-1} and the large number of fitting parameters, successful modeling was not achieved. Utilizing the same fitting parameters from the previous sections on the modeling of emission from C_2H_2 + H yielded inadequate results.

Figure 6.7. Five time slices, 0.25, 0.75, 1.25, 1.75, and 2.25 μs following photolysis of 50 mTorr C_2D_2 and 50 mTorr H_2S in 2 Torr Ar. Experimental IR emission is shown in black with the IR emission model fit overlaid in blue.

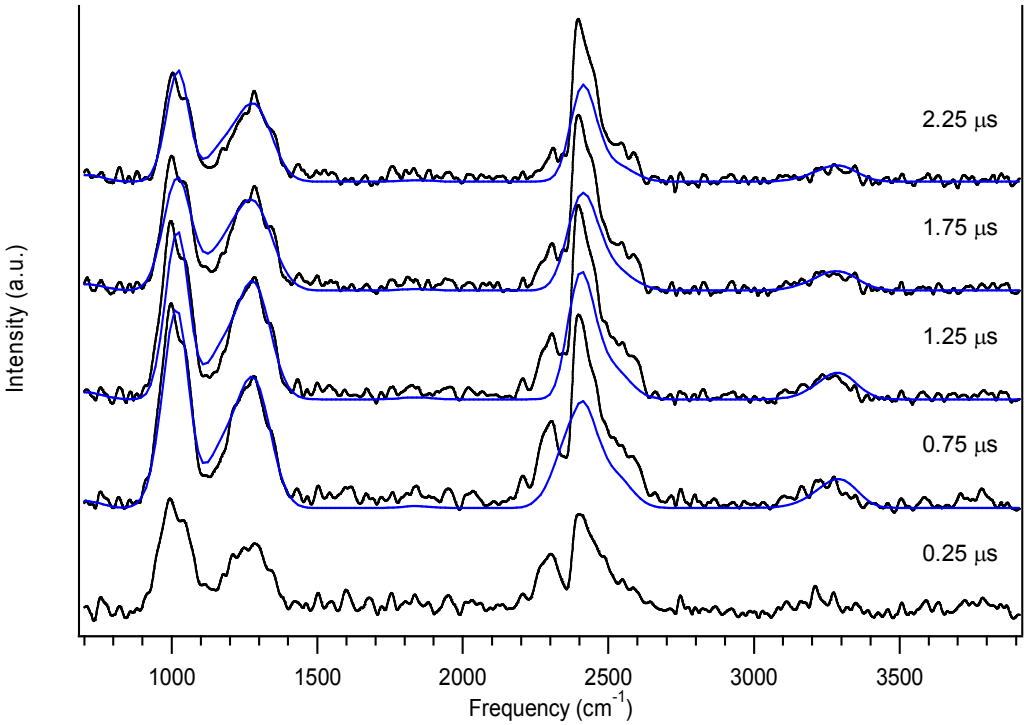

One explanation which has already been postulated in the previous sections is that resonant energy transfer between the ν_3 modes of highly vibrationally excited C_2D_2 and C_2DH molecules transfer energy to the fundamental transition of the ν_3 mode of C_2D_2. This process would populate the low lying vibrational levels in the ν_3 mode of C_2D_2 and rapidly deplete the highly excited population. The result would be a large emission signature from the fundamental ν_3 mode of C_2D_2, which is what is observed is Figure 6.7.

The IR emission fitting results can account for this highly efficient energy transfer pathway by including emission from the fundamental modes. The fitting is performed by combining the emission result from Eq. 6.12 with an emission spectra $S_{DCCD,fund}(\nu)$, which is the fundamental emission from C_2D_2. The result is shown in Figure 6.8. Five experimental time slices are shown in black. The fundamental C_2D_2 transitions are subtracted shown in red. The fitting result obtained from Eq. 12 is shown in blue.

The fit achieved in Figure 6.8 is noticeably better than that achieved in Figure 6.7. The removal of the fundamental C_2D_2 transitions allows a more accurate fitting of the experimental data. From this "corrected" fitting result, the average vibrational energy $\langle E \rangle$ can be plotted as a function of time as shown in Figure 6.9. The average vibrational energy of C_2D_2 is shown in red circles, fit to a single exponential decay, solid red line, and the average vibrational energy of C_2DH is shown as blue squares, also fit to a single exponential decay shown as a solid blue line.

The average initial vibrational energy $\langle E \rangle_0$, for C_2D_2, was determined to be 12 000 $\pm$ 390 cm^{-1}, while the $\langle E \rangle_0$ for C_2DH was determined to be 10 700 $\pm$ 610 cm^{-1}. The difference in vibrational energies suggest that there may be unique mechanisms

Figure 6.8. Five emission time slices from the same conditions as Figure 6.7. Emission results are shown in black, here with the fundamental modes of C_2D_2 added in ad hoc in red, and the IR emission fitting results in blue.

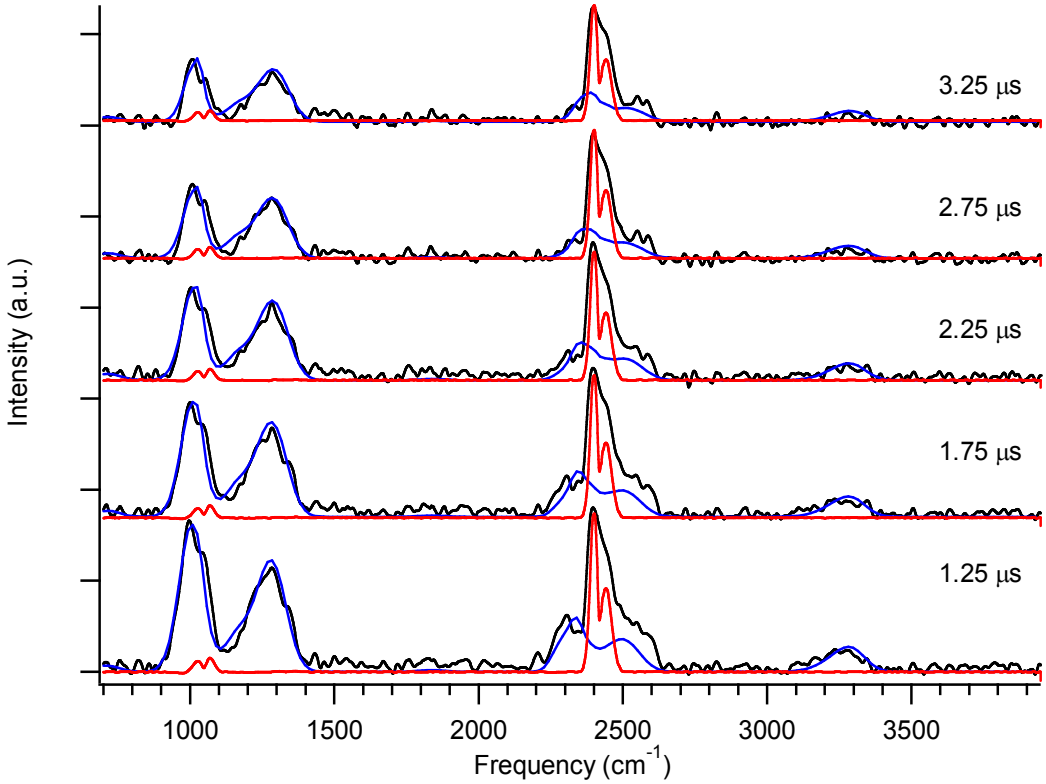

Figure 6.9. $\langle E \rangle$ vs time following the photolysis of 50 mTorr C_2D_2 and 50 mTorr H_2S in 2 Torr Ar. The average vibrational energy of C_2D_2 is shown in red circles, while the average energy of C_2DH is shown in blue squares. A single exponential fit of both is shown as the solid line in their respective colors.

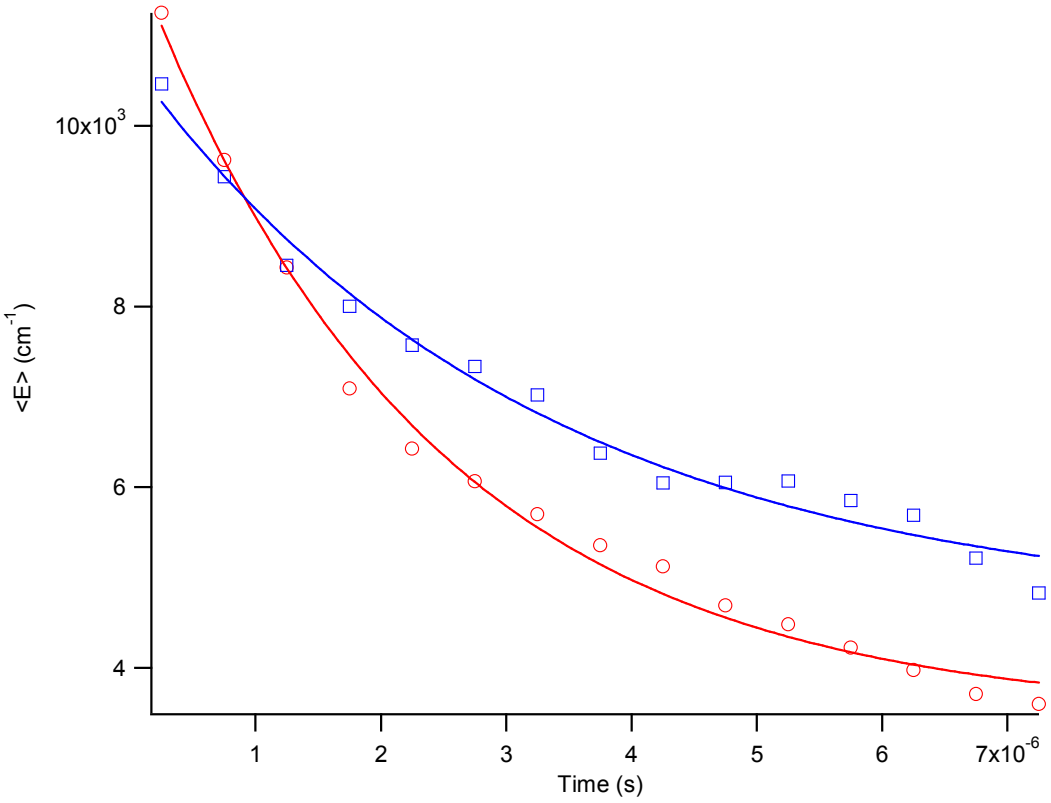

forming C_2D_2 and C_2DH. Possible mechanisms for the formation of C_2D_2 and C_2DH will be discussed in the next sections. The difference in initial vibrational energies of C_2D_2 and C_2DH may also be because of the fitting of the C_2DH feature at 2500 cm^{-1}. Since this feature, corresponding to the C-D stretch mode, shows the strongest (or equally as strong as the C-H stretch mode) anharmonic shift in frequency, the feature becomes important in determining the $\langle E \rangle$ of C_2DH. Since, however, this feature is masked by the intense ν_3 mode from C_2D_2, there is a significant amount of uncertainty in the modeling of this feature. Nonetheless, both C_2D_2 and C_2DH show a similar $\langle E \rangle_0$ when compared to the C_2H_2 + H result from the previous sections of $\langle E \rangle_0 = 11\,019 \pm 195$ cm^{-1}.

An interesting dynamical result is seen in Figure 6.9 as well. The collisional deactivation or energy transfer rate, shown as $1/\tau$ is faster for C_2D_2 than for C_2DH, in accordance with the generally accepted notion of the rate being inversely proportional to the lowest frequency mode(s) but in disagreement with studies on the energy transfer rate of lowly excited deuterated acetylene.[61,62] It has been found that C_2DH collisionally cools faster than C_2D_2 due to efficient V-R energy transfer effects. For C_2D_2, the lowest frequency mode is the ν_4 trans bend at 505 cm^{-1}, while the lowest frequency mode of C_2DH is the ν_4 mode at 518 cm^{-1}. The origins of the overall decay rates $\tau^{-1} = 4.325 \times 10^5$ s^{-1} for C_2D_2 and $\tau^{-1} = 3.126 \times 10^5$ s^{-1} for C_2DH are therefore difficult. One explanation is that the precursor pressure are quite high (50 mTorr each) and as has already been discussed, there is a significant amount of efficient V-V energy transfer between the hot species and cold C_2D_2 molecules thereby cooling C_2D_2 faster than C_2DH. The pure V-T

energy transfer rates from acetylene to the buffer gas cannot be determined due to this efficient resonant V-V energy transfer.

The relative concentrations of C_2D_2 and C_2DH have also been extracted from the model fitting based on Eq. 6.12. The value of a is shown in Figure 6.10 for each of the fitted time slices. The value attains an average value of a = 0.319 ± 0.017. The small error and seemingly random fluctuation around the average value, shown in Figure 6.10 as a horizontal bar, indicate that this value is constant. The value obtained for a from Eq. 6.12 indicates that the $[C_2DH] \sim 2x [C_2D_2]$. An attempt, based on the statistical dissociation pathways, will be made to justify this ratio.

6.5 Discussion

6.5.1 C_2H_2 + H collision mechanisms

There are three possible mechanisms producing the vibrationally hot acetylene observed experimentally. The first possible mechanism involves the production of the ethynyl radical directly from acetylene, followed by the abstraction of a H atom from HBr or H_2S. The second possible mechanism involves the formation of a vinyl radical intermediate from the reaction of acetylene with hot H atoms followed by dissociation. The third possible mechanism involves the reaction of H atoms and the ethynyl radical forming vibrationally hot acetylene.

The first mechanism is expressed in Eq. 6.13 where HX is either HBr or H_2S. In this mechanism acetylene absorbs a 193 nm photon and dissociates into ethynyl and a cold hydrogen atom. The ethynyl radical then reacts with an HX molecule to form the HCCHX radical. This substituted vinyl radical then dissociates forming vibrationally hot

Figure 6.10. The experimentally determined value of a from the fitting result of Eq. 6.12. The circles represent the individual values determined from the IR emission fittings. The line represents the average ratio, 0.319 ± 0.017.

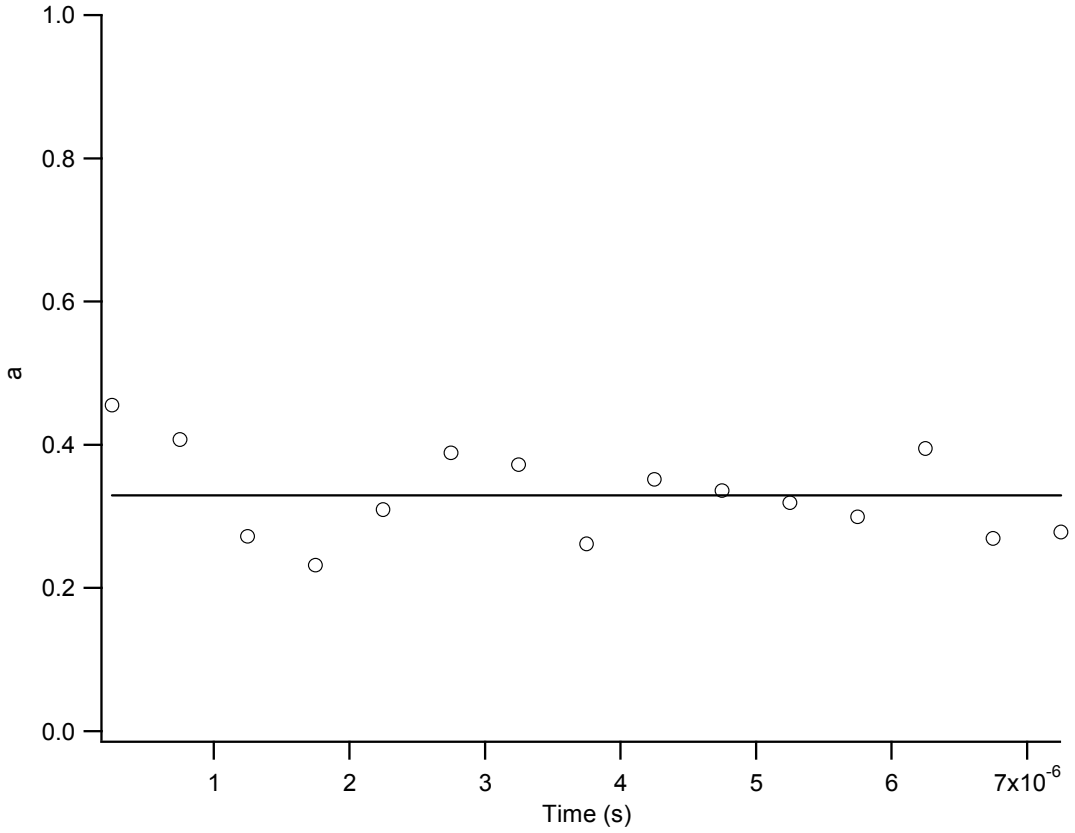

acetylene plus a cold H atom and X atom/radical. The addition reaction is of the general form seen in Reaction 6.3.

$$\begin{aligned} &C_2H_2 + HX + 193\ nm \rightarrow \\ &\quad H\ (cold) + [C_2H]^{\ddagger} + HX \rightarrow \\ &\quad H + [HXCCH]^{\ddagger} \rightarrow H + HCCH^* + X \end{aligned} \qquad (6.13)$$

The 2nd mechanism is expressed in Eq. 14 where hot H atom is produced from HX photolysis:

$$\begin{aligned} &C_2H_2 + HX + 193\ nm \rightarrow \\ &\quad C_2H_2 + H\ (hot) + X \rightarrow \\ &\quad [H_2CCH]^{\ddagger} + X \rightarrow HCCH^* + H + X \end{aligned} \qquad (6.14)$$

The HX species absorbs a 193 nm photon and dissociates forming a hot hydrogen atom and a cold X fragment. The hot hydrogen atom reacts with the cold acetylene molecule forming a high energy vinyl intermediate which dissociates to form vibrationally hot acetylene, a cold H atom and X fragment atom/radical. Reaction 6.14 is based on the general association/dissociation steps of Reactions 6.2 and 6.4. It is also shown as an equilibrium process in Reaction 6.5a and 6.5b.

Both processes should leave similar amounts of energy in the vibrational degrees of freedom of acetylene due to IVR which occurs faster than our detection system unless energy is specifically channeled into different degrees of freedoms following reaction and/or dissociation steps. Both reactions are highly dependent on the strength of the HX bond and CH bond of acetylene. The energetics of these reactions will be discussed in

the following sections. Reaction 6.14 is favored due to the larger absorption cross sections and higher partial pressures of HBr and H_2S, when compared to acetylene. It is estimated that there is a H:C_2H abundance of 12:1 and 34:1 for HBr and H_2S in our experiments. In addition to the higher abundance, the hydrogen atoms have a much higher collisional frequency due to the large amount of translational energy after dissociation, E_t ~ 50 kcal/mol. The collisional rate of C_2H with HBr, at room temperature, for pressures of 10-100 mTorr, is on the order of 10^5 - 10^6 s^{-1}. The collisional rate of hot hydrogen atoms with cold acetylene molecules is much larger, on the order of 10^7 - 10^8 s^{-1} depending on the acetylene pressure used. If this were the dominant reaction mechanism, IR emission from the emerging C_2H_2 population should be observed over the first tens of μs or longer. This is not observed. The IR emission observed peaks prior to our detector response time (500 ns) and decreases rapidly.

The third possible mechanism, the bi-radical reaction of ethynyl and hydrogen atoms must also be considered, as both radicals are created following the precursor absorption of a 193 nm photon. Thermodynamics of this reaction between two very reactive species suggest that the resulting acetylene molecule formed would contain a large amount, > 50,000 cm^{-1} of energy. Acetylene with this much internal energy is not observed in our results. The lack of a high energy feature would suggest the bi-radical reaction does not play a significant role in the production of highly vibrationally excited acetylene in this case.

The most likely mechanism for the creation of vibrationally hot acetylene following the 193 nm photolysis of HX and C_2H_2 is found to be the first mechanism where hot H atoms from HX react with cold acetylene to form a vinyl intermediate. The

high energy vinyl radical then dissociates to form vibrationally hot acetylene and a kinetically slow H atom.

6.5.2 Formation and unimolecular dissociation of the vinyl intermediate

The reaction of hydrogen atoms with other atoms, molecules, and radicals has been observed in several studies.[13-15,21] In addition, the collisional energy transfer (T-V and T-R) between "fast" hydrogen atoms and other molecules has also been well documented.[10-12,17-20] In this work, however, the hydrogen atom is believed to react with the cold acetylene molecule forming a vibrationally hot vinyl radical intermediate. The vinyl intermediate then dissociates before it can collisionally cool thus producing vibrationally hot acetylene and a "slow" H atom. The overall association/dissociation process proceeds via the normal exchange reaction, Reaction 6.4, however with a tremendous amount of energy transferred in the collision.

The reaction energetics of acetylene and a hydrogen atom has received some recent theoretical attention.[30] The vinyl intermediate is predicted to be 35.1 kcal/mol lower in energy than the dissociated species. There is a dissociation barrier of 39.6 kcal/mol with the combination/association barrier being 4.3 kcal/mol.[32] The transition state structure has been determined and is best described by a slightly bent acetylene molecule (161.4^0 and 170.2^0 HCC bond angles) with the hydrogen atom approaching at a 109.0^0 angle from the CC bond normal.

Knowledge of a statistical dissociation rate would aid greatly in determining the presence of a highly vibrationally excited vinyl intermediate. Hydrogen atoms are generated with 53 and 61 kcal/mol from H_2S and HBr, respectively, following 193 nm

photolysis, providing up to 100 kcal/mol of internal energy in the vinyl intermediate. RRKM rate constants on the order of 10^{12}-10^{13} s^{-1} have been determined using experimentally and theoretically determined frequencies for the vinyl radical and transition state, respectively, in the energy region of 90 – 100 kcal/mol above the vinyl ZPE.[27,54]

The fast unimolecular dissociation rate suggests the vinyl intermediate is short lived and not observable in our experiment due to the detector response time. The experimental observation of nascent hot acetylene with ~30 – 45 kcal/mol of vibrational energy requires the vinyl intermediate rapidly redistribute its internal energy obtained along the H + C_2H_2 reaction path. The energetic analysis following vinyl dissociation is discussed in the next section.

In addition, using the isotopic ratio of vibrationally excited C_2D_2 and C_2DH allows us to determine whether the energy is distributed in the vinyl radical following the collision or the energy is directed into specific channels. The branching ratio will be discussed in the following section.

6.5.3 Combined statistical information theoretic and sudden impulsive model

The distribution of vibrational energy in acetylene generated through the vinyl intermediate can be calculated by a combination of a sudden impulsive model[67,68] and a statistical method developed by Muckerman.[69] This method follows the unimolecular dissociation over an exit barrier similar to Mordaunt *et al.*[70] and Wilhelm *et al.*[71] Briefly, the total available energy, E^{avail}, is the excitation above the ZPE of the products. This energy may come from excitation of a reactant, or in this case, a reactant colliding with a

hot hydrogen atom. The available energy, E^{avail}, is comprised of two energy distributions, a statistical distribution, E^{stat}, and an impulsive distribution, E^{imp}. The statistical energy distribution comes from energy being partitioned through the transition state and into the products, therefore we define E^{stat} as

$$E^{stat} = E^{avail} - E^{TS} \tag{6.15}$$

where the transition state energy, E^{TS}, is calculated from the ZPE. The impulsive energy distribution originates from the notion that a bond breaking induces a sharp recoil and release of energy before the other atoms in the fragments can respond. We define the impulsive energy released by,

$$E^{imp} = E^{avail} - E^{stat} = E^{TS} \tag{6.16}$$

where the ZPE are included in the E^{TS} and E^{avail}, in relation to the product channel.

The information theoretic prior distribution function[69] was determined through the use of a continuous rigid-rotor harmonic oscillator approximation. For a given unimolecular dissociation, the energy may be partitioned into the various degrees of freedom of the atoms and molecules produced. The prior distribution function is dependent on the number of vibrational modes of the product molecules, as well as the structure of the fragment, linear or non-linear, which influences the rotational degrees of freedom. For the case of the dissociation of vinyl into the linear acetylene molecule and hydrogen atom, the probability density function, $\rho(f)$, takes into account all 7 vibrations and J(J+1) rotations (approximated as $(J+1/2)^2$. The variable f represents the fractional energy in a particular degree of freedom. The probability density function of a single vibrational degree of freedom is

$$\rho(f_1) = \frac{9!}{\Gamma(9)}(1 - f_1)^8 \tag{6.17}$$

where f_1 is the fractional vibrational component in ν_1. The fractional amount of energy in ν_1 can be represented by

$$\langle f_1 \rangle = \int_0^1 f_1 \rho(f_1) df_1 = 1/10 \tag{6.18}$$

The total vibrational energy can be found by adding all of the contributions of the individual vibrations, counting degenerate vibrations twice, or determining the probability density function for f_V, which is the sum of all the vibrational fractions.

A general approach to determining the translational, rotational and vibrational energy distributions through an impulsive model is given by Trentelman *et al*.[67] Briefly, the energy partitioned into the product degrees of freedom [dof's] is governed by the masses of the atoms involved in bond breaking, the masses of the two fragments, and the structure of the fragments. The structure of the vinyl intermediate and transition state structure have been determined from UCCSD(T)/6-311++G(d,p) calculations.[30] For vinyl dissociating into acetylene and a hydrogen atom, only acetylene may contain vibrational, rotational, and translational components, with hydrogen only leaving with kinetic energy. The energy available to the impulsive distribution is the TS energy, including ZPE's, equal to 4.3 kcal/mol.[32] The impulsive model yields the translational energy of the exiting H atoms containing the majority of the available energy, 3.97 kcal/mol, with a small amount of energy partitioned into the translational, rotational and vibrational motions, 0.15, 0.13, and 0.04 kcal/mol, respectively, of acetylene.

The small E^{TS} corresponds to a small impulsive contribution to the energy distribution. We consider the total kinetic energy of the hydrogen atoms, $\langle E_t \rangle$ = 61 kcal/mol for HBr photolysis and $\langle E_t \rangle$ = 53 kcal/mol for H_2S photolysis, being available

to the vinyl radical following the initial "fast" H + cold C_2H_2 collision. The experimental and calculated energies following the dissociation of the vinyl radical is shown in Table 6.2. The hydrogen atom kinetic energies are listed and used as the total energy available to the vinyl radical. The experimentally determined initial vibrational energies of acetylene are taken from the fitting of $\langle E \rangle$ vs. time curves. Error bars represent one standard deviation from the fitting result. The error bars may be larger, however, as the center of the Gaussian distribution is used to generate the $\langle E \rangle$ vs. time curves. The FWHM are typically on the order of 10 kcal/mol at early times, as seen in Figure 6.4. The calculated vibrational energies are determined utilizing the statistical-prior distribution above the TS energy and the sudden-impulsive distribution below the TS energy. The experimentally reported translational energies are taken as the difference between the initial H atom translational energy and the experimental initial vibrational energy. The rotational contribution is determined through the statistical-prior and impulsive models and removed from the translational energy term. The calculated translational energy is determined in a similar manor to the calculated vibrational energy above and below the TS energy.

In general, there is good agreement between the experimentally determined vibrational energies and the theoretical calculations based on the two models used. For H atoms produced from H_2S, the experimentally determined acetylene $\langle E \rangle_0$ = 31.5 kcal/mol compared to 34.2 kcal/mol determined from the calculation. For H atoms produced from the photolysis of HBr, the experimental energy 44.5 kcal/mol is close to the calculated value of 39.7 kcal/mol. It should be noted that there is a much smaller contribution from

Table 6.2. Experimental and calculated vibrational energies after the dissociation of the vinyl radical intermediate following "fast" H atom collisions with cold C_2H_2 molecules are shown. The energies listed are relative to the ZPE of the C_2H_2 + H atom products. Experimental $\langle E_v \rangle_0$ are from the fitting results of the $\langle E \rangle$ vs. time plots while experimental $\langle E_t \rangle_0$ are from the difference between $\langle E_v \rangle_0$ and $\langle E_t \rangle$ of the "fast" H atoms. All energies are in kcal/mol.

	H Atom	Product C_2H_2		Product C_2H_2 + H	
	$\langle E_t \rangle$	$\langle E_v \rangle_0$		$\langle E_t \rangle_0$	
H atom precursor		Expt.	Calc.	Expt.	Calc.
H_2S	53[a]	31.5 ± 0.6	34.2	16.5	13.8
HBr	61[b]	44.5 ± 2.1	39.7	11.0	14.8

[a] Ref. 9

[b] Ref. 13

the impulsive model as the TS energy is much smaller than the excitation energy and subsequently the energy used in the statistical model. However, there is a strong translational energy dependence in the impulsive model, and adjusting the TS energy would affect the overall distribution of energies.

The good agreement with the established statistical/impulsive model suggests that the formation of a highly vibrationally excited vinyl radical following the collision of a "fast" hydrogen atom and acetylene molecule is reasonable. Converting a large amount of the hydrogen atom kinetic energy into the vibrational (and rotational) energy of the vinyl radical which dissociates rapidly is a unique reaction which has not been observed previously. It must be stressed that the mechanism proposed is purely postulated from observed product IR emission and energies. It is entirely possible for certain reaction pathways to be dominant if they produce cold reaction species.

6.5.4 Collisional frequency estimate and trajectory calculation results

It would be very useful to determine the percent of total H and acetylene collisions that would result in a large transfer of energy. Because the experimental method uses emission and not absorption, we are not able to directly measure the absorption or collisional cross section. However, we can compare the H + acetylene emission results with the direct photolysis results from the 193 nm photolysis of vinyl bromide (VBr), vinyl chloride (VCl), and 1,3-butadiene, which generate highly vibrationally excited acetylene directly to estimate the efficiency of H + acetylene yielding hot acetylene.

There is about an order of magnitude difference in the 193 nm absorption cross sections of VBr, VCl, and 1,3-butadiene (σ~10^{-17} cm^3/molecule) and H_2S (σ~10^{-18} cm^3/molecule). Laser fluencies of 20-40 mJ/cm^2/molecule and precursor pressures of 5-10 mTorr was used for VBr, VCl, and 1.3-butadiene. To increase the yield of the H_2S reaction, a larger laser fluence (100- 200 mJ/cm^2/molecule) and higher pressures (50-100 mTorr) were used. The same experimental apparatus was used to monitor the emission from the reaction products and gave peak emission results of 200-400 mV for VBr, VCl, and 1,3-butadiene. The emission signal from H_2S + acetylene ranged from 20-50 mV. If we compare the signal (10x larger for direct photolysis vs H+acetylene) and the precursor pressures (10x larger for H+acetylene vs. direct photolysis) we can estimate a collisional efficiency of 1% for H+acetylene producing highly vibrationally excited acetylene.

Recent trajectory calculations between hot H atoms and acetylene molecules were performed by Han, Sharma, and Bowman.[72] Three collisional energies, 51.1, 53.0, and 61.6 kcal/mol were investigated. The vibrational energy of acetylene was set to the harmonic zero point energy (16.4 kcal/mol for C_2H_2 and 13.0 kcal/mol for C_2D_2) and normal mode sampling was used. The rotational energy was set at a 300K thermal distribution. Initial separation was set at 12 Å and a final separation of 25 Å concluded the trajectory run. Impact parameters of 0 to b_{max} were analyzed in 0.2 Å increments. The potential energy surface has been calculated at the RCCSD(T)/aug-cc-pVTZ level of theory and basis by Sharma et al.[73]

The results of the trajectory calculation by Han et al.[72] indicate that approximately 10% of the total vdW collisions result in a large energy transfer from hot H atoms to the vibrational dof's of acetylene. This compares favorably to the collisional estimate of ~1%

determined from emission experiments. At a collision energy of 61.6 kcal/mol, the $<\Delta E_{vib}>$ for the large energy transfer rate was determined to be ~32 kcal/mol with a FWHM of 20 kcal/mol. This compares favorably to the experimental result of 44.5 kcal/mol for the H atom generation from HBr.

The trajectory calculations also yielded information on the mechanistic origin of this large energy transfer rate. The calculation indicated that two mechanisms dominated this high energy transfer collision: (1) a reactive mechanism and (2) a complex formation but unreactive collision mechanisms. The reactive mechanism proceeds through a vinyl intermediate where the departing H atom is different from the hot H atom. The second mechanism, complex formation but unreactive collision, proceeds through a vinyl intermediate, where the hot H atom departs as a cold atom. A small portion of this high energy transfer collision proceeds through a non-reactive, non-complex forming collision.

In order to verify the existence of a vinyl intermediate instead of a high energy collision between H and acetylene, we can use the isotopic substitution results and product branching ratio. The branching ratios are compared with RRKM calculated rates in the next section.

6.5.5 Revelations from C_2D_2 + H

The observation of highly vibrationally excited C_2D_2, as well as C_2DH would indicate that a reaction forming a vinyl intermediate is probable as depicted by Reaction 6.7 and 6.8. No other reaction mechanism proposed would yield large populations of both highly vibrationally excited C_2D_2 and C_2DH. If the mechanism preceded by an

energy transfer collision from hot hydrogen atoms to the cold acetylene molecules, without going through an intermediate, as described by 6.12, no excited C_2DH would be observed. If the reaction proceeded by first ethynyl-d_1 production, from the photolysis of C_2D_2, followed by the abstraction of a hydrogen atom from H_2S, as described by Reactions 6.9, 6.10, and 6.11, the only hot species would be C_2DH, while C_2D_2 would only gain energy from collisions with hot C_2DH molecules. This is clearly not the case as there is a significant amount of vibrationally hot C_2D_2 at high internal energies, as shown in Figure 6.7.

Therefore, the only remaining mechanism involves the generation of a vinyl radical intermediate, postulated earlier in this Chapter when discussing the non-deuterated results, and described by Reactions 6.7 and 6.8. Because the bond energies of hydrogen and deuterium atoms to carbon atoms are very similar, as well as the transition states for both dissociation processes to be similar, the statistical ratio of $[C_2D_2]$:$[C_2DH]$ should be approximately 1:2, if we assume equal populations and dissociation rates of the three $[C_2D_2H]$ isotopomer structures. Differences in the dissociation rate may appear because of the isotopic substitution affecting the transition state structure and vibrational frequencies. RRKM rates based on ground state and transition state structures are used to determine the different dissociation rates for the three possible isotopomers. A DFT theory calculation with the 6-311+G(d,p) basis set was used to determine the optimized ground and transition state structure as well as their respective vibrational frequencies. The model structures for the ground state and transition state are shown in Figure 6.11 (A). The three possible isotopomers are shown in Figure 6.11 (B). The lone hydrogen is located in the alpha position in molecule (i), in the β position, in (ii), and in the γ

position, in (iii). A closer inspection of molecule (i) shows that this isotopomer can not be directly formed following the collision of the hydrogen atom with C_2D_2 since both deuterium atoms are located on the same carbon atom. To form this isotopomer, a deuterium atom in the β or γ position must isomerize through a transition state, shown in Figure 6.11 (C). The barrier for this process was calculated to be 46.9 kcal/mol.[30] In contrast, the α deuterium isomerization, which takes place between structures (ii) and (iii) crosses a much lower barrier of ~4 kcal/mol.[30]

The calculated vibrational frequencies and geometries are shown in Table 6.3. As is expected, the ground state and transition state geometries were consistent through the different isotopomers calculated. The level of calculation was sufficient for the purposes of determining the differences between dissociation rates for the three different isotopomers.

The RRKM rates calculated for the three isotopomers are based on the Whitten-Rabinovitch harmonic sum and density of states. The frequencies for the ground state and transition state determined through a DFT calculation, shown in Table 6.3 are used to generate the harmonic sum and densities of states. The transition state energy was taken from Peeters *et al.*,[30] and compared favorably to DFT calculations performed here. The vinyl → TS → acetylene + H barrier of 39.7 kcal/mol and acetylene + H → TS → vinyl barrier of 4 kcal/mol were used. RRKM rates were calculated taking into account 300K of rotational energy and tunneling across the barrier. Tunneling rates were determined using the Eckart barrier to determine the transmission coefficients. The effect of the tunneling contribution was quite minor to the overall dissociation rate. The RRKM rates

Figure 6.11. (A) The ground and transition state geometries. Angles (a) and distances (r) have been calculated through DFT level calculations. Values for the angles and distances are shown in Table 6.3. (B) The three isotopomers (i, ii, and iii) of the doubly deuterated vinyl radical. In each case the dissociation proceeds via the β atom. (C) The vinyl isomerization transition state structure forming isotopomer (i) as described in the text.

(A)

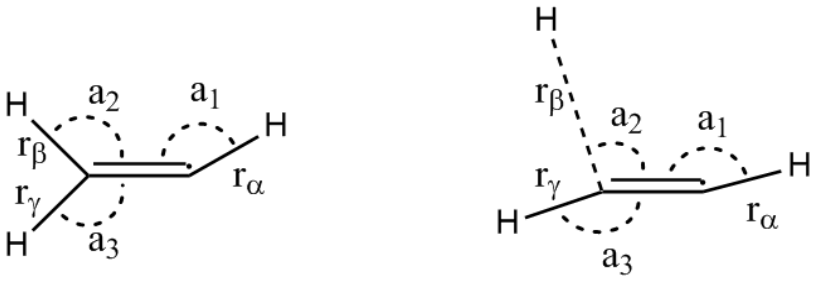

(B)

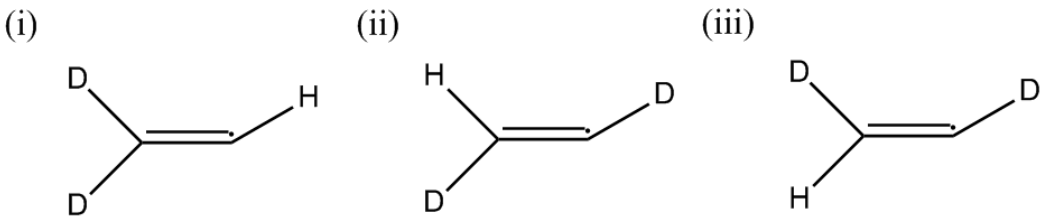

(C)

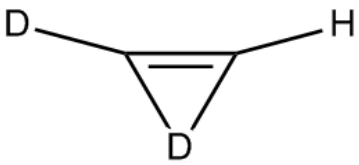

Table 6.3. (A) Values for angles and distances for structures shown in Figure 6.10. (B) Vibrational frequencies (cm^{-1}) for the three isotopomers of doubly deuterated ground state (GS) vinyl and the corresponding frequencies for the transition state (TS) structures.

(A)

	Ground State	Transition State
a_1	137.479	173.056
a_2	122.171	107.028
a_3	122.212	166.915
r_α	1.08333	1.06688
r_β	1.09589	2.07587
r_γ	1.09041	1.06735
$r_{C=C}$	1.31029	1.21274

(B)

	$HCCD_2$	HCCD-D	DCCHD	DCCH-D	DCCDH	DCCD-H
	GS	TS	GS	TS	GS	TS
ν_1 or ν_{TS}	628	402	545	407	559	514
ν_2	717	274	641	265	634	334
ν_3	789	492	849	498	815	480
ν_4	967	561	913	512	899	525
ν_5	1039	675	1283	691	1274	567
ν_6	1626	705	1611	762	1609	620
ν_7	2248	1904	2262	1901	2320	1811
ν_8	2351	2667	2431	2677	2431	2525
ν_9	3256	3492	3158	3482	3084	2797

for the three possible dissociation channels for C_2DH are shown in Figure 6.12. The three possible reactants, with the lone hydrogen atom in the α, β, and γ position, as seen in Figure 6.11 (B), dissociate with similar, but distinctively different dissociation rates. In addition, since molecule (i) in Figure 6.11 (B) can not be directly formed from a collision between C_2D_2 and H atoms, the isomerization rate, through the TS complex, shown in Figure 6.11 (C), must be calculated. The RRKM rate of this process is also shown in Figure 6.12.

It is observed that the calculated dissociation rates are significantly faster, 10 – 50x, throughout the energy region of interest, 30000 – 35000 cm^{-1}, compared to the isomerization rate. We thus conclude that isotopomer (i) from Figure 6.11 (B) would not contribute greatly to the overall dissociation pathway. The slow isomerization rate indicates that there are only two main dissociation pathways, originating from isotopomer (ii) and (iii), which form vibrationally hot C_2D_2 and C_2DH, respectively. The statistical ratio between these rates can yield some information about the relative concentrations of the two species. This is shown in Figure 6.13.

The RRKM dissociation rate forming C_2DH is calculated to be twice as fast at low energies compared to the RRKM rate forming C_2D_2 as seen in Figure 6.13. At very high energies, these two rates converge to equivalent values. In the region of interest, 30 000 – 35 000 cm^{-1}, where the intermediate vinyl radical would contain all of the energy following a collision with a hot hydrogen atom, the ratio, k_{HCCD}/k_{DCCD} is approximately 1.2. The 20% faster RRKM calculated HCCD rate compared with the DCCD rate is less than what is observed experimentally: [HCCD] ~ 2x [DCCD], as shown in Figure 6.10.

Figure 6.12. The RRKM rates of dissociation for the three possible dissociation channel of doubly deuterated vinyl [◆ molecule (i) in Figure 6.11(B), ■ molecule (ii) in Figure 6.11(B), ▲ molecule (iii) in Figure 6.11(B)] and one isomerization channel, x.

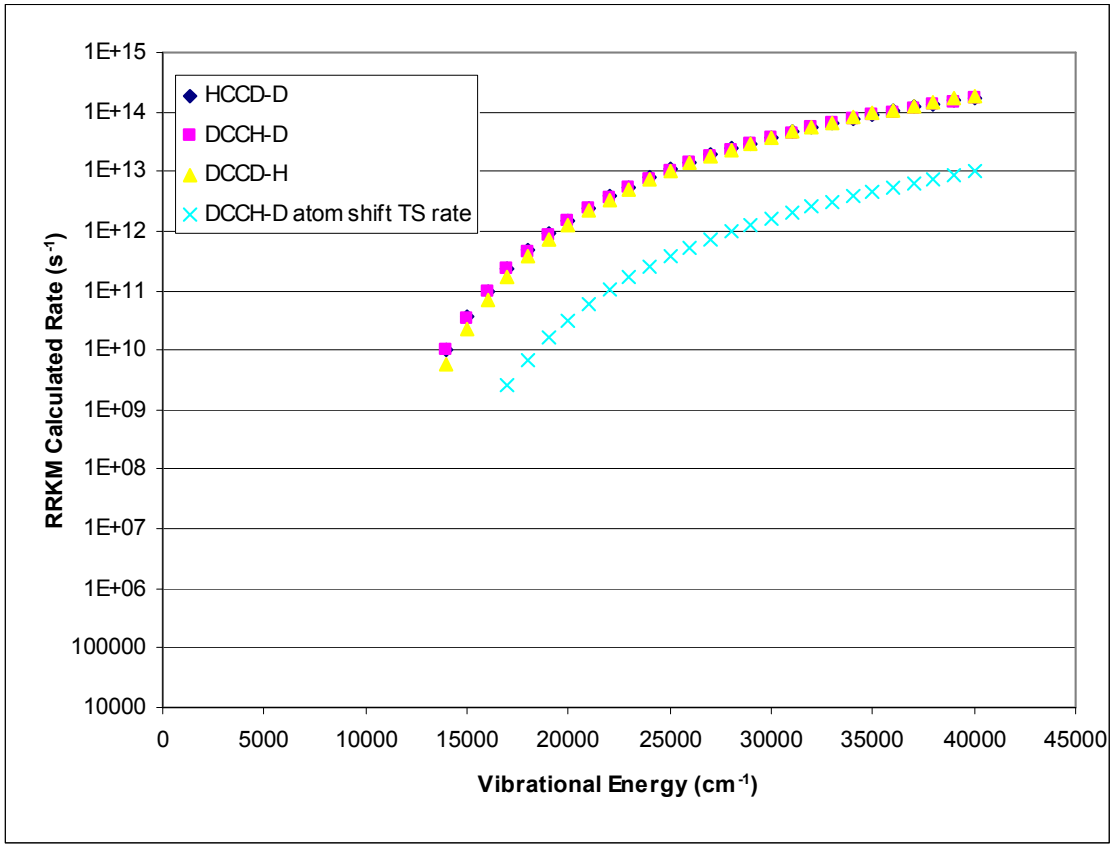

Figure 6.13. The ratio of the RRKM rates for the dissociation of molecule (iii) in Figure 6.11(B) and molecule (ii) in Figure 6.11(B) for the dissociation forming C_2DH and C_2D_2, k_{HCCD} / k_{DCCD}, respectively.

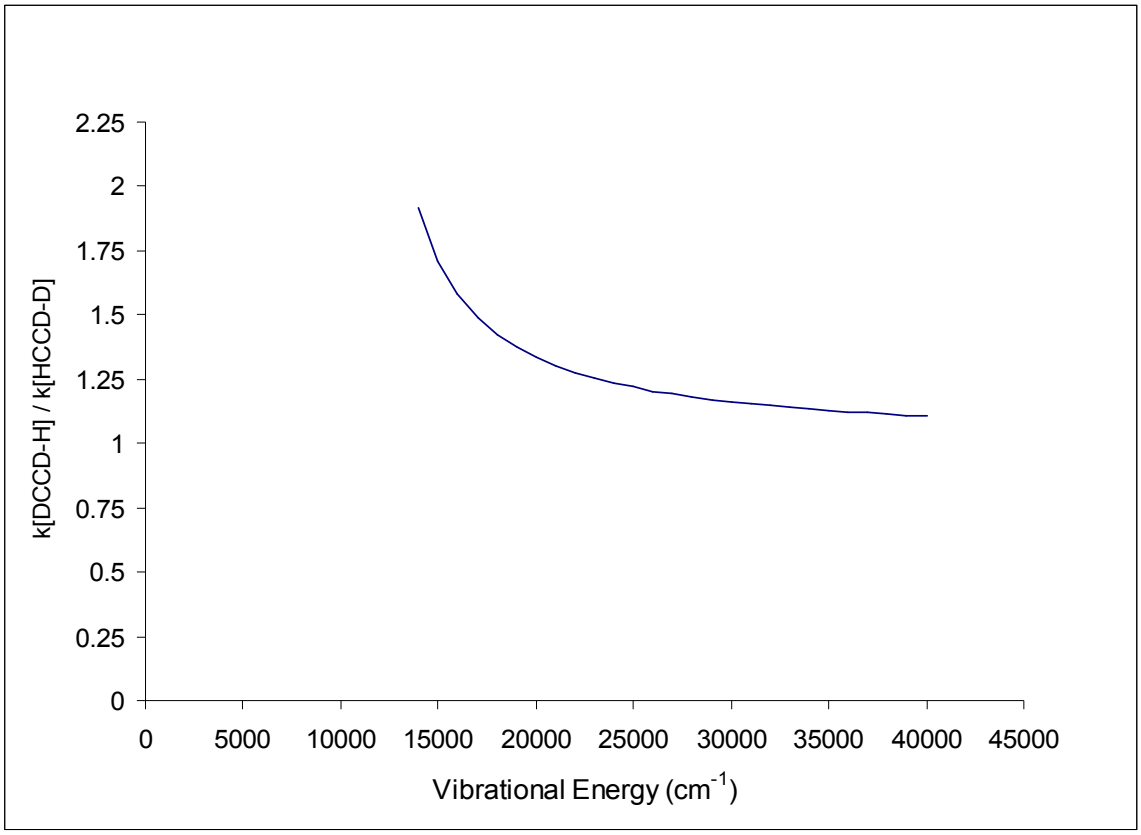

The experimental result suggests that the HCCD dissociation is even faster than that calculated through RRKM theory. It is interesting to note that even though RRKM theory underestimates the rate of C_2DH formation (or overestimates the rate of C_2D_2 formation), values consistent with the observation of [HCCD] ~ 2x [DCCD] are observed in Figure 6.10 at low vibrational energies near the dissociation barrier. This may indicate that a range of vibrationally excited vinyl is formed and can then dissociate. In our experiments, however, only one high energy population of acetylene is observed.

The static experimental isotopomer ratio seen in Figure 6.10 is also indicative of a single reaction mechanism. If more than one mechanism populated either C_2D_2 or C_2DH in a different amount of internal energy, the isotopomer ratio would change based on the energy dependent collisional quenching rate. Since only one static ratio is observed, a second source of highly vibrationally excited C_2D_2 or C_2DH is improbable.

In addition, because of the static isotopomer ratio, which is in general agreement with the RRKM rates shown in Figure 6.12 and 6.13, IVR, as typically found, is extremely rapid. The initial kinetic energy of the H atom is quickly converted to the internal degrees of freedom of the intermediate. This energy is then redistributed rapidly into the nearby vibrational states. This is confirmed by the observation of a static statistical distribution of vibrationally hot C_2D_2 and C_2DH. If IVR was not faster than the statistical RRKM dissociation rate, ~$10^{12} - 10^{13}$ s^{-1}, as discussed in the previous sections, there would be a preferential dissociation pathway forming either C_2D_2 or C_2DH in a non-statistical ratio. Since the experiment uses H atoms to collide with C_2D_2, initial vibrational excitation should be along some C-H coordinate. If C_2D_2-H dissociates before the energy can redistribute within the molecule, there will be a preferential

formation of vibrationally hot C_2D_2 over C_2DH. There is some indication that at very early times there is a little more C_2D_2 than at later times, as seen in Figure 6.10. The higher $[C_2D_2]$ may indicate that vibrational energy has not been redistributed fully when the vinyl intermediate dissociates. However, the early time $[C_2D_2]$:$[C_2DH]$ ratio fall within the range of ratios and may only deviate due to experimental error.

6.6 Conclusion

The generation of highly vibrationally excited acetylene has been found through a collision and dissociation mechanism. The proposed mechanism includes a bimolecular reaction of fast "hot" hydrogen atoms, generated by the photolysis of HBr and H_2S, and vibrationally cold acetylene molecules leading to the formation of a highly excited vinyl radical intermediate. The vinyl radical dissociates producing a vibrationally hot acetylene molecule and a "slow" H atom. The vibrational energy content of the acetylene molecule follows the statistical information theoretic prior energy distribution and trajectory calculation results. The exact mechanism following the collisions of hot H atoms with cold acetylene molecules was called into question in the reaction of $H + C_2H_2$, based on the existence of two possible reaction pathways. The two pathways, following either the vinyl or ethynyl species, were indistinguishable in the non-deuterated experiments. The use of isotopic substitution of the acetylene molecule has allowed the exact mechanism to be elucidated. Energetics of the reaction products, as well as isotopic abundance of the different products have been determined and are consistent with the vinyl radical intermediate. Vibrational energies are consistent with the non-deuterated results and further confirm the usefulness of vibrational emission modeling of highly

excited species. The confirmation of the vinyl intermediate mechanism implies that this association $H + C_2H_2 \rightarrow C_2H_3$ and dissociation, $C_2H_3 \rightarrow H + C_2H_2$, is a unique type of reaction which warrants further study. This high energy collision was estimated to occur in approximately 10% of the total vdW collisions between hot H atoms and acetylene based on recent trajectory calculation results.

References:

(1) Ikeguchi, T.; Watanabe, I. *Environmental Technology* **1991**, *12*, 947.

(2) Serio, M. A.; Hamblen, D. G.; Markham, J. R.; Solomon, P. R. *Energy & Fuels* **1987**, *1*, 138.

(3) Herbert, F.; Hall, D. T. *J. Geophys. Res.* **1996**, *101*, 10877.

(4) Krasnopolsky, V. A.; Cruikshank, D. P. *J. Geophys. Res.* **1999**, *104*, 21979.

(5) Lammer, H.; Lichtenegger, H. I. M.; Biernat, H. K.; Erkaev, N. V.; Arshukova, I. L.; Kolb, C.; Gunell, H.; Lukyanov, A.; Holmstrom, M.; Barabash, S.; Zhang, T. L.; Baumjohann, W. *Planetary and Space Science* **2006**, *54*, 1445.

(6) Bisikalo, D. V.; Shematovich, V. I.; Gerard, J.-C.; Gladstone, G. R.; Waite, J. H. J. *J. Geophys. Res.* **1996**, *101*, 21157.

(7) Hiraoka, K.; Sato, T.; Takayama, T. *Science* **2001**, *292*, 869.

(8) Hiraoka, K.; Takayama, T.; Euchi, A.; Handa, H.; Sato, T. *Astrophys. J.* **2000**, *532*, 1029.

(9) Kulatilaka, W.; Frank, J.; Patterson, B.; Settersten, T. *Appl. Phys. B: Lasers and Opt.* **2009**, *97*, 227.

(10) Wight, C. A.; Leone, S. R. *J. Chem. Phys.* **1983**, *78*, 4875.

(11) Wight, C. A.; Leone, S. R. *J. Chem. Phys.* **1983**, *79*, 4823.

(12) Datta, S.; Weston Jr., R. E.; Flynn, G. W. *J. Chem. Phys.* **1984**, *80*, 4071.

(13) Brouard, M.; Hughes, D. W.; Kalogerakis, K. S.; Simons, J. P. *J. Phys. Chem. A* **1998**, *102*, 9559.

(14) Lambert, H. M.; Carrington, T.; Filseth, S. V.; Sadowski, C. M. *J. Phys. Chem.* **1993**, *97*, 128.

(15) Aker, P. M.; Germann, G. J.; Tabor, K. D.; Valentini, J. J. *J. Chem. Phys.* **1989**, *90*, 4809.

(16) Ni, C.-K.; Flynn, G. W.; Green, S. *J. Chem. Phys.* **1994**, *101*, 9499.

(17) Khan, F. A.; Kreutz, T. G.; O'Neil, J. A.; Wang, C. X.; Flynn, G. W.; Weston Jr., R. E. *J. Chem. Phys.* **1990**, *93*, 445.

(18) Kreutz, T. G.; Flynn, G. W. *J. Chem. Phys.* **1990**, *93*, 452.

(19) Khan, F. A.; Kreutz, T. G.; Flynn, G. W.; Weston Jr., R. E. *J. Phys. Chem.* **1993**, *98*, 6183.

(20) Ni, C.-K.; Kreutz, T. G.; Flynn, G. W. *J. Phys. Chem.* **1995**, *99*, 7381.

(21) Nikolaisen, S. L.; Cartland, H. E. *J. Chem. Phys.* **1993**, *99*, 1145.

(22) Troya, D.; Lendvay, G.; Gonzalez, M.; Schatz, G. C. *Chem. Phys. Lett.* **2001**, *343*, 420.

(23) Bates, R. W.; Golden, D. M.; Hanson, R. K.; Bowman, C. T. *Phys. Chem. Chem. Phys* **2001**, *3*, 2337.

(24) Keil, D. G.; Lynch, K. P.; Cowfer, J. A.; Michael, J. V. *Int. J. Chem. Kinet.* **1976**, *8*, 825.

(25) Payne, W. A.; Stief, L. J. *J. Chem. Phys.* **1976**, *64*, 1150.

(26) Rao, V. S.; Skinner, G. B. *J. Phys. Chem.* **1988**, *92*, 6313.

(27) Knyazev, V. D.; Slagle, I. R. *J. Phys. Chem.* **1996**, *100*, 16899.

(28) Michael, J. V.; Su, M.-C.; Sutherland, J. W.; Harding, L. B.; Wagner, A. F. *J. Phys. Chem. A* **2003**, *107*, 10533.

(29) Szichman, H.; Gilibert, M.; Gonzalez, M.; Gimenez, X. *J. Chem. Phys.* **2001**, *114*, 9882.
(30) Peeters, J.; Ceursters, B.; Nguyen, H. M. T.; Nguyen, M. T. *J. Chem. Phys.* **2002**, *116*, 3700.
(31) Wang, D. *J. Chem. Phys.* **2003**, *119*, 12057.
(32) Miller, J. A.; Klippenstein, S. J. *Phys. Chem. Chem. Phys* **2004**, *6*, 1192.
(33) Wang, D. *J. Chem. Phys.* **2006**, *124*, 201105.
(34) Wang, D.; Huo, W. M. *J. Chem. Phys.* **2007**, *127*, 154301.
(35) Letendre, L.; Liu, D.-K.; Pibel, C. D.; Halpern, J. B.; Dai, H.-L. *J. Chem. Phys.* **2000**, *112*, 9209.
(36) Zou, P.; Strecker, K. E.; Ramirez-Serrano, J.; Jusinski, L. E.; Taatjes, C. A.; Osborn, D. L. *Phys. Chem. Chem. Phys* **2007**, *10*, 713.
(37) Balko, B. A.; Zhang, J.; Lee, Y. T. *J. Chem. Phys.* **1991**, *94*, 7958.
(38) Seki, K.; Okabe, H. *J. Phys. Chem.* **1993**, *97*, 5284.
(39) Wodtke, A. M.; Lee, Y. T. *J. Phys. Chem.* **1985**, *89*, 4744.
(40) Satyapal, S.; Bersohn, R. *J. Phys. Chem.* **1991**, *95*, 8004.
(41) Fahr, A.; Laufer, A. H. *J. Photochem.* **1986**, *34*, 261.
(42) Fletcher, T. R.; Leone, S. R. *J. Chem. Phys.* **1989**, *90*, 871.
(43) Lauter, A.; Lee, K. S.; Jung, K. H.; Vatsa, R. K.; Mittal, J. P.; Volpp, H.-R. *Chem. Phys. Lett.* **2002**, *358*, 314.
(44) Hashimoto, N.; Yonekura, N.; Suzuki, T. *Chem. Phys. Lett.* **1997**, *264*, 545.
(45) Magnotta, F.; Nesbitt, D. J.; Leone, S. R. *Chem. Phys. Lett.* **1981**, *83*, 21.
(46) McGhee, T. H.; Weston Jr., R. E.; Flynn, G. W. *J. Chem. Phys.* **1985**, *83*, 145.
(47) Morris, V. R.; Han, K.-L.; Jackson, W. M. *J. Phys. Chem.* **1995**, *99*, 10086.
(48) Huebert, B. J.; Martin, R. M. *J. Phys. Chem.* **1968**, *72*, 3046.
(49) *Infrared Spectra*; Linstrom, P. J.; Mallard, W. G., Eds.; NIST Chemistry WebBook: Gaithersburg, MD 20899.
(50) Continetti, R. E.; Balko, B. A.; Lee, Y. T. *Chem. Phys. Lett.* **1991**, *182*, 400.
(51) van Veen, G. N. A.; Mohamed, K. A.; Baller, T.; de Vries, A. E. *Chem. Phys.* **1983**, *74*, 261.
(52) Xu, Z.; Koplitz, B.; Wittig, C. *J. Chem. Phys.* **1987**, *87*, 1062.
(53) Xie, X.; Schneider, L.; Wallmeier, H.; Boettner, R.; Welge, K. H.; Ashfold, M. N. R. *J. Chem. Phys.* **1990**, *92*, 1608.
(54) Nikow, M.; Wilhelm, M. J.; Dai, H.-L. *J. Phys. Chem. A* **2009**, *113*, 8857.
(55) Hartland, G. V.; Qin, D.; Dai, H.-L. *J. Chem. Phys.* **1993**, *98*, 6906.
(56) Hartland, G. V.; Qin, D.; Dai, H.-L. *J. Chem. Phys.* **1997**, *107*, 2890.
(57) Qin, D.; Hartland, G. V.; Dai, H.-L. *J. Phys. Chem. A* **2000**, *104*, 10460.
(58) Nikow, M.; Wilhelm, M. J.; Smith, J. M.; Dai, H.-L. **to be published.**
(59) Nikow, M.; Smith, J. M.; Wilhelm, M.; Dai, H.-L. *to be submitted* **2009**.
(60) Nikow, M.; Wilhelm, M. J.; Smith, J. M.; Dai, H.-L. *to be submitted.* **2009**.

(61) Lambert, J. D. *Vibrational and Rotational Relaxation in Gases*; Clarendon Press: Oxford, 1977.
(62) Yardley, J. T. *Introduction to Molecular Energy Transfer*; Academic Press: New York, 1980.
(63) Kim, K.; King, W. T. *J. Mol. Struct.* **1979**, *57*, 201.
(64) Herzberg, G. *Molecular Spectra and Molecular Structure*; Krieger Publishing Co.: Malabar, FL, 1966; Vol. III.
(65) Herzberg, G. *Molecular Spectra and Molecular Structure*; Van Nostrand: New York, 1950; Vol. II Infrared and Raman Spectra of Polyatomic Molecules.
(66) Orr, B. J. *Int. Rev. Phys. Chem.* **2006**, *25*, 655.
(67) Trentelman, K. A.; Kable, S. H.; Moss, D. B.; Houston, P. L. *J. Chem. Phys.* **1989**, *91*, 7498.
(68) Busch, G. E.; Wilson, K. R. *J. Chem. Phys.* **1972**, *56*, 3626.
(69) Muckerman, J. T. *J. Phys. Chem.* **1989**, *93*, 179.
(70) Mordaunt, D. H.; Osborn, D. L.; Neumark, D. M. *J. Chem. Phys.* **1998**, *108*, 2448.
(71) Wilhelm, M. J.; Nikow, M.; Letendre, L.; Dai, H.-L. *J. Chem. Phys.* **2009**, *130*, 044307.
(72) Han, Y.-C; Sharma, A.R.; Bowman. Private communication. 2011
(73) Sharma, A.R.; Braams, B.J.; Carter, S.; Shelper, B.C.; Bowman, J.M. *J. Chem. Phys.* **2009**, *130*, 174301.